THE UNIVERSITY
of ADELAIDE

FACULTY OF SCIENCES
DEPARTMENT OF PHYSICS

Development of a high sensitivity absorption measurement system for low-loss novel glasses

---

Sophie K. Muusse

Supervisors:
Prof. Peter J. VEITCH
Dr. Sebastian W. S. NG

March 2023

DECLARATION

I certify that this work contains no material which has been accepted for the award of any other degree or diploma in my name, in any university or other tertiary institution and, to the best of my knowledge and belief, contains no material previously published or written by another person, except where due reference has been made in the text. In addition, I certify that no part of this work will, in the future, be used in a submission in my name, for any other degree or diploma in any university or other tertiary institution without the prior approval of the University of Adelaide and where applicable, any partner institution responsible for the joint award of this degree.

I give permission for the digital version of my thesis to be made available on the web, via the University's digital research repository, the Library Search and also through web search engines, unless permission has been granted by the University to restrict access for a period of time.

I acknowledge the support I have received for my research through the provision of an Australian Government Research Training Program Scholarship.

Signature: ____________________ Date: 12/06/2023

ACKNOWLEDGEMENTS

Foremost, I would like to show my gratitude to my supervisor Peter Veitch for all of his help, time and effort spent on during this masters and before. It was from your efforts that I found my love for optics which I will always be grateful for. Sebastian Ng, I can't overstate how much I've valued you as a co-supervisor and all your help, guidance and advice that came with it. Huy Tuong Cao thanks for being there any second of any day whether in the pursuit yoghurt or correct FEA constraints. Daniel Brown, thanks for having the answers to almost all of my questions, your undying faith in the absorption set-up and making sure I leave the office.

This masters could never have been completed without our collaborators, Heike Ebendorff-Heidepriem, Eric Schartner, Allson Ng and Alex Hemming, and I deeply appreciate all of their help. Nor would it been possible without other school of physics members, such as Dave Ottoway, Gary Hill, Andrew McKinnon, Adrian Giffen, Jackie Hull and Wanye England.

Thank you to OzGrav and all of its members for their help over the years. To everyone in G15, I am very grateful for the support and entertainment in our collective descent into madness, including Thom, Mitchell, Georgia, Madi, Muskan, Darcy, Kendall, Alexei, Zac and Deeksha. To my friends thanks for pretending to care about what happens when glass gets hot and distracting me from the associated problems. So thanks Izzy, Will, Jake, Jas, Hannah, Ethan, Matt, Jack, Seb, Claire, Elaine, Ross, Tarryn, and Kshitjia for all of your efforts on that front.

To my family; thank you all for the support and enthusiasm. Tim thanks for leading by example and being there despite the fact we have no idea what the other is doing past the fact it's science. Finally, thank you to my parents without whom I would never have made it this far.

ABSTRACT

This thesis describes the development of a wavefront measurement system and analysis to quantify absorption in low-loss glasses at 2 μm. Motivated by the proposed gravitational wave detectors at 2 μm and potential glasses which could revolutionise future telecommunication fibres, it will be essential to precisely measure the incredibly small losses due to absorption in the short-wave infra-red.

Key limitations for 2 μm technologies are power loss and the associated reduced transmission distance and absorption induced thermal lens. A solution to these issues is the development and implementation of ZBLAN, a glass which has theoretically predicted losses which are orders of magnitude below the low-loss glasses currently employed. ZBLAN is prevented from reaching the theoretical limits due to extrinsic scatter, resulting from crystallisation in the sample and absorption. Both losses must be understood to improve the glass but the mechanisms for the former are largely unknown and absorption has not been precisely measured. However, if absorption losses can be measured the losses due to scatter can then be inferred.

I describe in this thesis a photo-thermal system to measure the absorption coefficient of a sample independently. This was completed by imaging the thermally induced wavefront distortion of an angled incident beam caused by heating in the glass due to the absorption of a 2 μm laser beam. A value for the bulk and surface absorption coefficients was extracted through comparison to a model which considers the thermo-elastic and thermo-refractive effects.

The multi-parameter model was verified for this system on a N-BK7 glass sample of known parameters as this system does not require calibration and novel glasses may have variations in glass parameters from published values. Furthermore, it was demonstrated that modelling using the incorrect thermo-expansion and thermo-optic coefficients reduces the quality of fit, such that I propose in cases of very high signal to noise the quality of fit could be used determine the correct sample coefficients and limit uncertainty in the absorption coefficients.

Bulk absorption in the 10s of $\mathrm{ppm\,cm^{-1}}$ was measured in ZBLAN and upper bound of surface absorption was determined. Angled incidence of a probe beam was shown to allow errors in bulk absorption to be reduced when surface is not considered as well as enable surface and bulk absorption to be separately measured in a single measurement. These results show that this system can be used as a tool to characterise absorption losses at 2 μm and by increasing the pump beam power to quantify absorption in lowest loss ZBLAN.

TABLE OF CONTENTS

LIST OF FIGURES

LIST OF TABLES

LIST OF SYMBOLS

System Parameters

θ_i	Probe beam incident angle on sample
θ_t	Probe beam transmitted angle in sample
P_{ip}	Plane of incidence of probe beam
$P_{measure}$	Measurement plane, conjugate to DHWS
P_{pp}	Perpendicular plane to plane of incidence P_{ip} rotated by θ_t around the y axis
P_{pump}	Pump beam power
T_0	Environmental Temperature
w_x	Pump beam waist in x axis
w_y	Pump beam waist in y axis
X_o	Distance between centre of end face and probe beam incidence on end face

Sample Parameters

α	Bulk absorption coefficient
α_{CTE}	Thermo-expansion coefficient
β	Surface absorption coefficient
$\frac{\partial n}{\partial T}$	Thermo-optic coefficient
ρ	Density
σ	Poisson's ratio
ε	Surface emissivity
a	Sample radius
C_p	Specific heat capacity
h	Sample length

K	Thermal conductivity coefficient
Y	Young's modulus

Thermal effects

ΔOPL	Change in optical path length
$T(x,y,z)$	Temperature distribution
$u_z(x,y)$	Thermal expansion of end face

List of Acronyms

BS Beam Splitter.

CCD Charge Coupled Device.

CMOS Complementary Metal-Oxide Semiconductor.

CP Compensation Plate.

DHWS Differential Hartmann Wavefront Sensor.

EO Elasto-Optic.

ETM End Test Mass.

FEM Finite Element Model.

GW Gravitational Wave.

HV Hello-Vinet analytical solution.

HWS Hartmann Wavefront Sensor.

ITM End Test Mass.

LIGO Laser Interferometer Gravitational-Wave Observatory.

PCI Photothermal Common-path Interferometry.

PDS Photothermal Deflection Spectroscopy.

PTMS Photo-Thermal Measurement System.

QPD Quadrant Photodiode.

RMSE Root Mean Square Error.

SHWS Shack-Hartmann Wavefront Sensor.

SLED Superluminescent Diode.

SNR Signal to Noise Ratio.

SWIR Short-Wave Infrared.

TE Thermo-Elastic.

TR Thermo-Refractive.

WFD Wavefront Distortion.

CHAPTER 1

INTRODUCTION

1.1 Overview

Optical loss in glass is a fundamental problem for many optical systems, degrading beam quality and causing a loss of power. In this chapter I will discuss why this loss is a significant issue for precision optical measurement systems like gravitational wave detectors and a limiting factor for network internet speed through intercontinental telecom fibre networks.

ZBLAN has been predicted to revolutionise Short Wave Infrared (SWIR) region technologies with theoretical losses much below any glass currently available in this wavelength range, minimising the need for expensive and imperfect compensation methods currently applied [1]. However, these results have not been replicated experimentally. Thus, measuring losses in the SWIR is becoming a necessity, not only to determine loss and predict thermal effects but to inform the development of low-loss glasses.

Optical loss can be separated into a range of mechanisms which will be discussed, with extrinsic scatter and optical absorption dominating at longer wavelengths [2]. ZBLAN is currently believed to be limited by scattering from micro-crystals, but quantifying loss due to scatter is difficult and the mechanisms behind the crystal formation is largely unknown [3]. The other significant source of loss, optical absorption, can be individually quantified by measuring wavefront distortion caused by the consequent heating. By understanding the magnitude of absorption the thermal effects can be determined and the magnitudes of other losses could be inferred.

In this chapter I discuss systems that require the lowest possible losses in the SWIR region and investigate ZBLAN as a future low-loss optical glass for these systems. Previous photo-thermal measurement systems used to measure absorption via its thermal effects will be reviewed and an off-axis wavefront measurement system to measure the absorption induced wavefront distortion will be presented. I will briefly outline the developed model to accurately quantify absorption from this distortion. Finally, the structure of this thesis will be outlined.

1.2 Low-loss glass for short wave infrared technologies

The first published value of loss in silica optical fibres was on the scale of a 1000 $\mathrm{dB\,km^{-1}}$, published 1965 [4]. After only 5 years this value had been decreased to 20 $\mathrm{dB\,km^{-1}}$, enabling the development of telecommunication fibres at 1550 nm [5]. Since then, the losses in silica have been improved until the theoretical low losses in fibre and bulk samples of amorphous fused silica had been achieved, with absorption losses as small as 0.1 $\mathrm{dB\,km^{-1}}$ (0.25 $\mathrm{ppm\,cm^{-1}}$) measured at 1064 nm [6].

Development of low-loss glasses like silica has enabled technologies which previously were implausible. Telecommunication fibres and gravitational wave detectors were both made possible by silica optics and fibres but they are now limited by optical loss. These applications will be discussed below and the current methods used to minimise the effect of optical loss and their limitations will be discussed.

1.2.1 Gravitational wave detectors

The Laser Interferometer Gravitational-Wave Observatory (LIGO) and Virgo gravitational wave detectors are designed to detect the distortion in space time caused by Gravitational Waves (GW) produced by the coalescing of neutron stars and black holes in the distant universe. The detectors are some of the most sensitive measurement systems ever created with the strain sensitivities on the order of $1 \times 10^{-23}\ 1/\sqrt{\mathrm{Hz}}$ at 200 Hz [7], where the strain sensitivity is a measure of the smallest relative change in arm length that can be measured at each frequency.

The detectors are modified Michelson interferometers optimised to measure very small changes in the lengths of the arms shown in the simplified schematic in Fig. 1.1. To be sensitive enough to detected GWs the LIGO detectors require 4km arm lengths and Fabry-Perot cavities in the arms storing an effective power of 250kW, as of the O3 observation run [8].

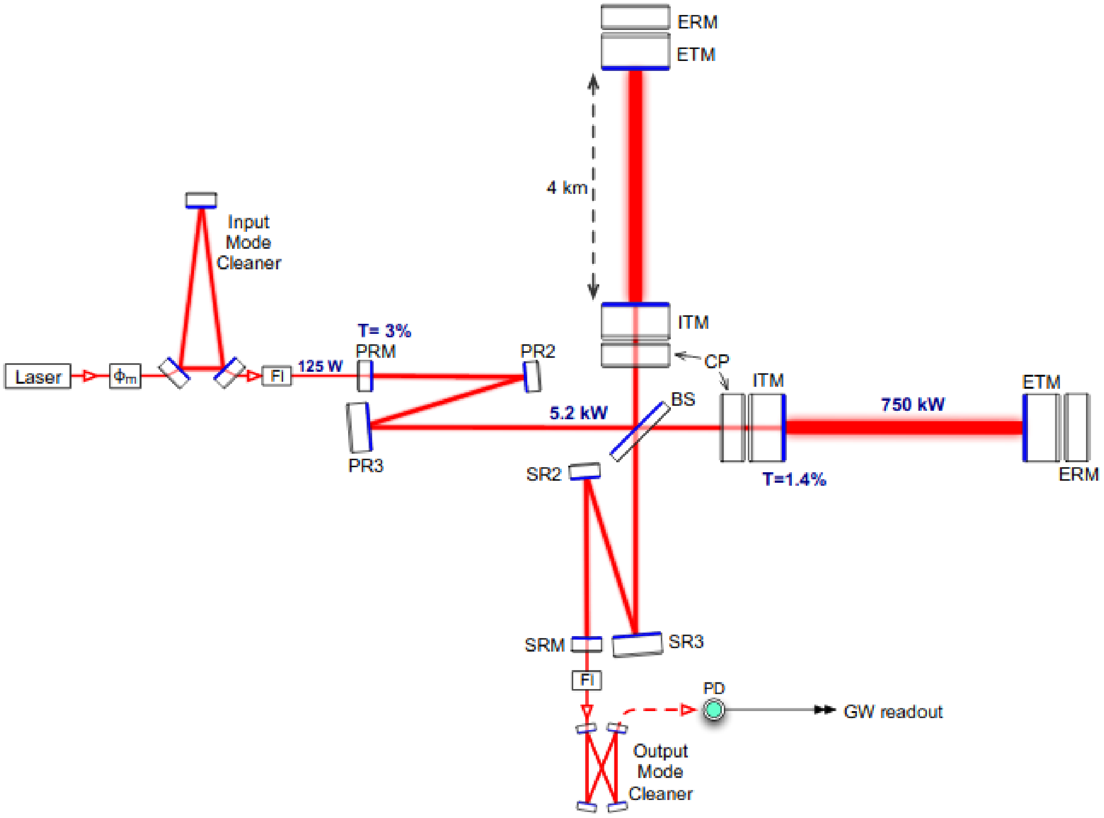

Fig. 1.1 Simplified optical diagram of the LIGO interferometer [9]. The incident laser is shown being split into two beams by the beamsplitter (BS) and separated into each arm where there is a resonance cavity formed using the Internal Test Masses (ITM) and the End Test Masses (ETM).

Despite the end and internal test masses (ETM and ITM) being made of low-loss fused silica and the detector using a 1064 nm laser, the wavelength where silica has 0.25 ppm cm^{-1} absorption, the excessive power within the detector results in significant wavefront distortion. The resulting changes to the beam wavefront disrupts the mode matching of the cavities, reduces the power stored in the arms and degrades the interferometer visibility, reducing sensitivity. The power stored in the arms is also limited by highly absorbing containments in the optical coating which cause significant degradation of the beam wavefront [10].

Multiple methods of thermal compensation are used to combat the thermal aberration of the interferometer beam to prevent the loss of sensitivity. Ring heaters are applied to heat the edge of the test masses such that there is a smaller change in temperature across the test mass. Additionally, a thermal lens is induced in Compensation Plates (CP), using a CO_2 laser, such that its shape and magnitude counteract that caused by the ITM. However, this compensation isn't perfect and the distortion can only be minimised to 5.3 nm [11]. Limiting the power of the interferometer beam reduces the thermal lens but also reduces the sensitivity at high frequencies as the effect of shot noise, the quantum fluctuations in the number of photons hitting the test masses, is increased. Sensitivity in this frequency range can then be improved by the addition of squeezed light, [12], but the effectiveness of squeezed light is significantly reduced by any optical losses, including absorption.

To gain the ability to see more GW events the Voyager upgrade to the LIGO detectors has been proposed [13]. The upgrade aims to increase the range of the detector by a factor of 4-5 across all frequencies as shown in Fig. 1.2. A significant component of the proposed Voyager upgrade is to combat the effects of the thermal wavefront distortion by changing the test masses to cryogenically (123K) cooled silicon. Silicon at this temperature has almost no thermal expansion, minimising the thermal aberration of the beam, and significantly reducing mirror thermal noise [13].

This upgrade necessitates a change in wavelength towards 2 μm as silicon absorbs strongly at 1064nm. To minimise cost and changes to the existing detectors it is proposed that other optics remain as fused silica, such as the beamsplitter. This may prove problematic as fused silica absorbs much more strongly at longer wavelengths, but the exact values have not been determined. Predictions state that 1.1 W would be absorbed in a fused silica beamsplitter which poses significant challenges for thermal compensation as the beamsplitter will experience asymmetric heating. To mitigate these effects fluoride glasses have been considered for the auxiliary optics as they should have lower absorption at these wavelengths due to their heavier molecular mass [13]. Precise knowledge of absorption around 2 μm for all proposed optical glasses is required to determine the viability of Voyager, select the laser wavelength and allow compensation systems, materials and coatings to be modelled and developed.

1.2.2 Telecommunication fibres

Telecommunication fibres distribute information as light across the world through billions of kilometers of glass fibre. Currently, silica fibres are used to transport light at 1550nm where

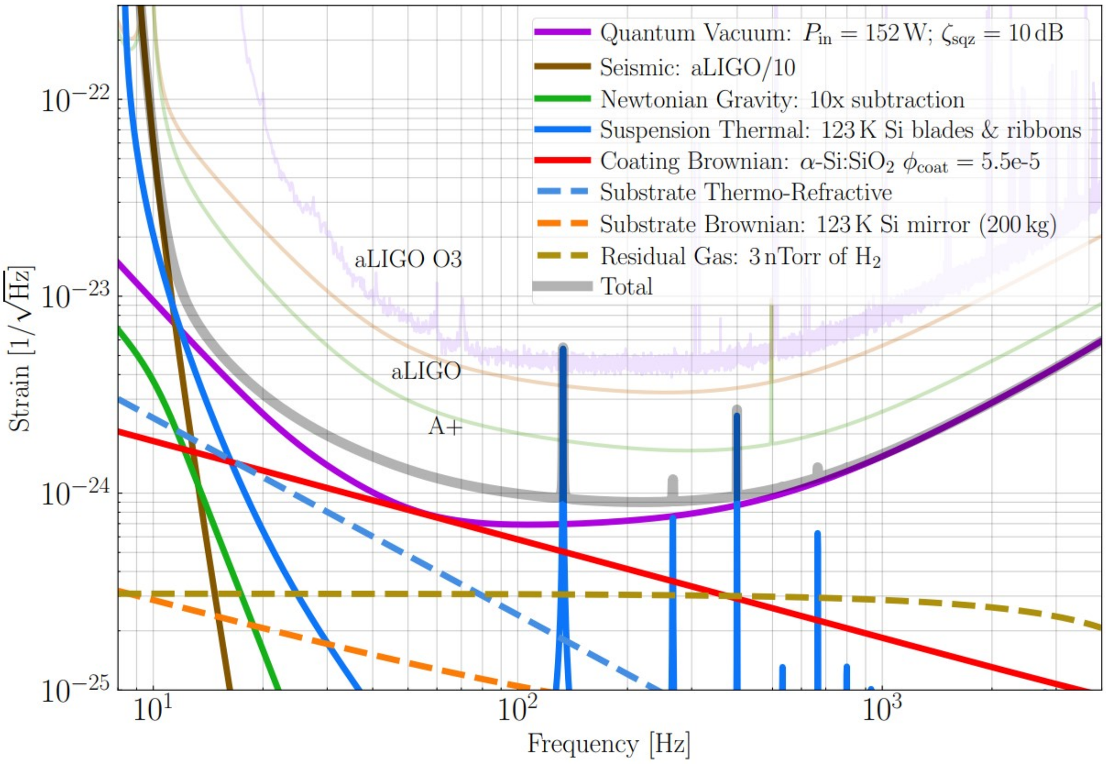

Fig. 1.2 Predicted strain sensitivity for Voyager upgrade to LIGO showing noise sources and total noise for Voyager (grey) against the aLIGO 03 run (light purple) and the modelled predictions for aLIGO (orange) and the A+ update (green) [13].

the typical absorption loss of a standard single mode fibre is 0.2 dB km^{-1} [14]. These fibres are produced at a rate of 400 million kilometres a year making telecom fibre manufacturing a multi-billion dollar industry and improvements to the system of significant consequence [2].

Small amounts of absorption or scatter can cause non-negligible losses in data over the thousands of kilometres travelled by the light in intercontinental telecommunication fibres. Even at 1550nm the absorption losses are at a level that necessitates expensive repeater systems to amplify the signal, commonly, using expensive erbium doped fibres as amplifiers [15]. Decreasing the loss in the fibres to the theoretical limit of ≈ 0.15 dB km would not remove the need for these repeater stations. The total loss required to allow their removal is in the range of 0.01 dB km to 0.001 dB km [2], and thus new glasses need to be developed to at least reduce the number required. In particular much work is being put into developing a fluoride-based glass, ZBLAN [16].

1.2.3 Sources of intrinsic optical loss in a glass sample

The minimum loss in a glass is limited by the intrinsic losses, which are unique to a material, thus, different materials like ZBLAN can have much smaller losses at a different range of wavelengths. The losses can be broken down into 3 dominant processes; electronic absorption, Rayleigh scattering and multi-phonon absorption, which dominate the losses at different sections of the spectrum as shown in Fig. 1.3. These loss mechanisms are described in detail below:

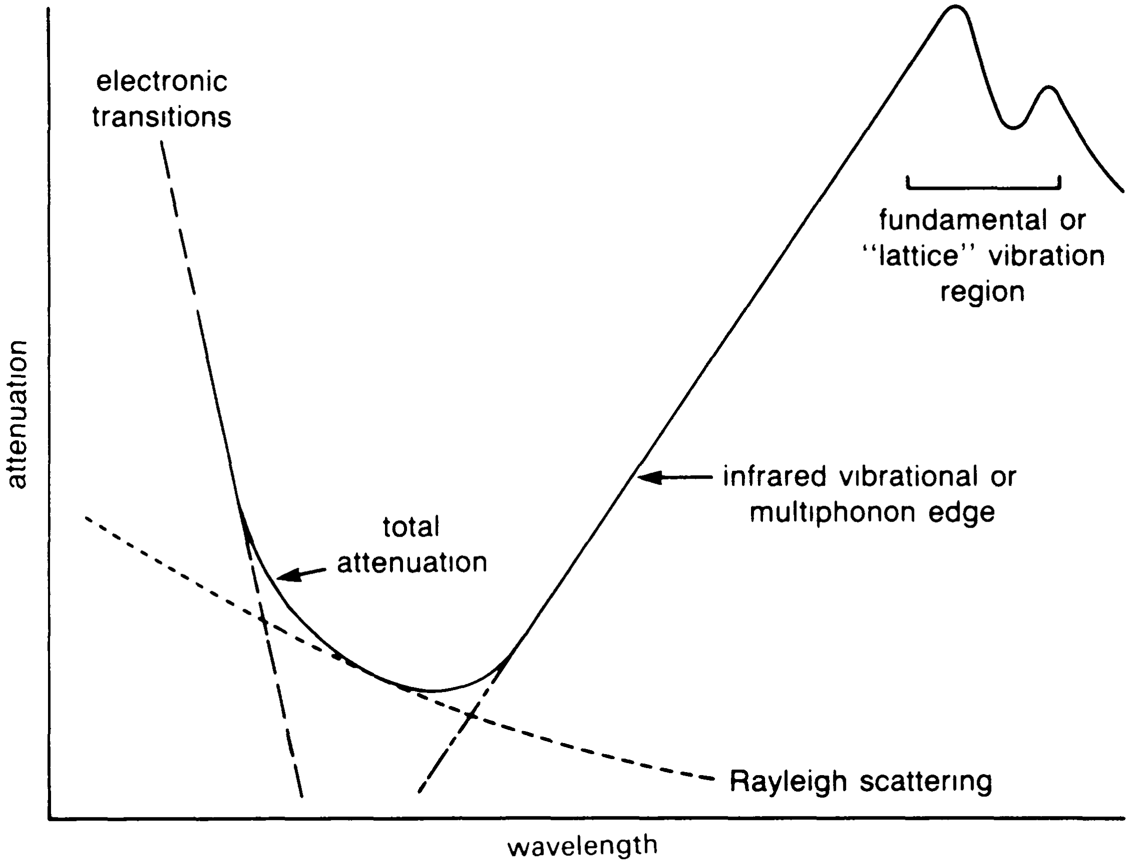

Fig. 1.3 The theoretical intrinsic loss spectrum shows the relationship of the 3 dominant sources of loss, multi-phonon absorption, Rayleigh scatter and electronic absorption to the wavelength of incident light, demonstrating that the minimum loss is determined by the multi-phonon absorption and Rayleigh scatter losses [2].

- **Electronic absorption**

  Shorter wavelengths of light (usually UV) have enough energy to excite electrons in the sample from the valence band to the conduction band. This can result in spontaneous emission in which the photon can be emitted in any direction causing a loss in power or through simulated emission.

- **Rayleigh scattering**
  Rayleigh scattering dominates the centre of the loss spectrum. The intrinsic Rayleigh scattering of a glass is determined by the chemical structure of the glass which has intrinsic variations in the arrangement, density and concentration of atoms. As a result there are microscopic fluctuations in the dielectric susceptibility and thus, refractive index, scattering light [17]. The scattering loss (α_R) is dependent on parameters of the glass, as shown in Equation (1.1),

  $$\alpha_R = \frac{8\pi^3}{3\lambda^4} n^8 p^2 k T_g \beta_T \tag{1.1}$$

  where n is the refractive index, p is the photo-elastic coefficient, k is Boltzmann's constant and β_T is the isothermal compressibility at glass transition temperature T_g. Rayleigh scattering is incredibly sensitive to changes in refractive index with $\alpha_R \propto n^8$. The magnitude of the scattering loss also decreases with wavelength (λ) at a rate of $\frac{1}{\lambda^4}$ thus becomes negligible at larger wavelengths. Other sources of scattering such as Broullion and Raman are negligible in this wavelength range. Minimum intrinsic losses are bounded by Rayleigh scattering, as shown in Fig. 1.3.

- **Multiphonon Absorption**
  Multi-phonon absorption is the result of multiple phonons interacting to create a electromagnetic dipole that incoming electromagnetic fields can couple to. Multi-phonon absorption dominates the loss spectra at higher wavelengths with absorption increasing quickly with wavelength creating what is known as the multi-phonon edge. The wavelength at which multi-phonon absorption begins to dominate the losses, overtaking scattering, is of great interest as it is a theoretical minima of loss.

Optical loss (α_L) in fibre is conventionally stated in units of $\mathrm{dB\,km^{-1}}$, which describes loss over a distance (L) using a base-10 logarithm,

$$\alpha_L(\mathrm{db\ km^{-1}}) = \frac{10}{L(\mathrm{km})} \log_{10}\left(\frac{P_{out}}{P_{in}}\right) \tag{1.2}$$

where P_{out} and P_{in} are the input and output powers. Loss in bulk samples is more commonly referred to in ppm cm^{-1}, which uses a natural log basis per meter, instead described as,

$$\alpha_L(\text{ppm cm}^{-1}) = \frac{1}{L(\text{cm})} \ln\left(\frac{P_{out}}{P_{in}}\right) \tag{1.3}$$

which is easily derived from the Beer-lambert law,

$$P_{out} = P_{in}\exp(-\alpha_L L). \tag{1.4}$$

This is also the standard in the GW community. The conversions between the 2 unit systems are listed below in Equations (1.5) and (1.6).

$$1\text{ppm cm}^{-1} = 0.43\text{db km}^{-1} \tag{1.5}$$

$$1\text{dB km}^{-1} = 2.3\text{ppm cm}^{-1} \tag{1.6}$$

In this thesis I will predominantly state absorption and optical losses in ppm cm^{-1} due to the focus on bulk samples.

1.3 Comparison of low-loss glasses for 2 μm technologies

Silica has reached its theoretical intrinsic loss limits, yet the need for lower losses persists, especially towards 2 µm. In the section above, silicon was described as an ideal material for GW detectors at cryogenic temperatures, with a predicted absorption as low as 1 ppm cm^{-1} [13] and measured as low as 4.3 ppm cm^{-1} [18]. The measured absorption is larger than that of fused silica at the current detector wavelength but is acceptable in light of the significant advantages of almost negligible Brownian motion and thermal expansion. However, this is only true at 123K. Silicon may also cause other unwanted effects such as birefringence as it is a single crystal and cannot be drawn into a fibre.

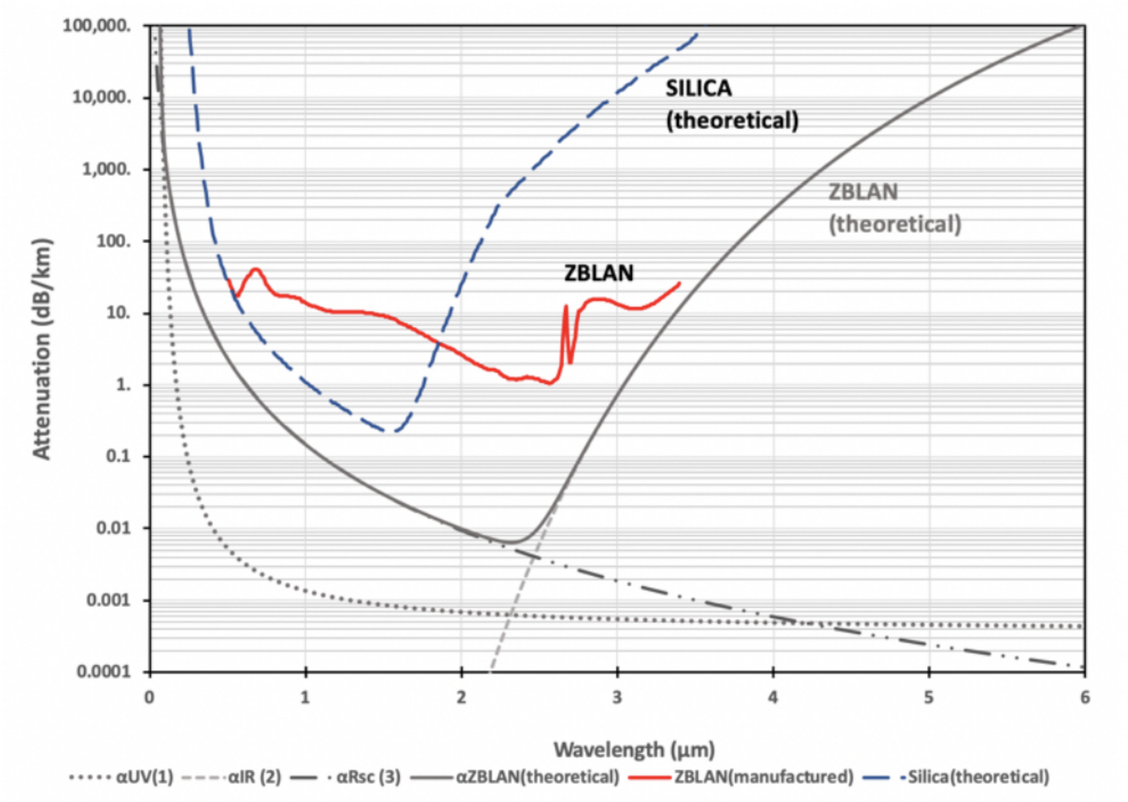

Fig. 1.4 A typical ZBLAN spectra measured in fibre (red) displays significantly more loss than the theoretical curve for silica and ZBLAN [1]. Significantly lower losses are expected from ZBLAN if it could be improved to its theoretical bests like silica.

Alternatively, substituting silica for a fluoride based glass with reduced absorption in the SWIR is in discussion for these applications [1], [13]. One such fluorozirconate glass, ZBLAN (ZrF_4-BaF_2-LaF_3-AlF_3-NaF), is expected to have a minimum loss of approximately 0.014 $\mathrm{ppm\,cm^{-1}}$ (6.4×10^{-3} $\mathrm{dB\,km^{-1}}$) at 2.32 µm [1], over an order of magnitude less than that of silica. If ZBLAN could reach these losses it would surpass fused silica for both future GW and telecommunication applications. The window of low-loss in ZBLAN is significantly larger than that for silica with losses at maximum of 0.05 $\mathrm{ppm\,cm^{-1}}$ (0.02 $\mathrm{dB\,km^{-1}}$) between 1.5-2.5 μm, as shown in Fig. 1.4. A wide loss window strengthens its case as a new optical material for future GW detectors upgrades like Voyager, as well as its use in broadband data transmission, and as optics in IR optical systems for high power delivery and in infrared spectroscopy. However, these incredibly low losses have never been demonstrated.

1.4 The development of ZBLAN glass for low-loss applications and extrinsic loss limitations

Despite investigation into ZBLAN since the 1960s the lowest measured loss is 1.5 ppm cm^{-1} (0.65 dB km^{-1}) at 2.59 µm which is still over a order of magnitude larger than theory [19]. The significant difference between theory and measured absorption, shown in Fig. 1.4, is caused by extrinsic losses due to absorption and scatter.

Extrinsic absorption is caused by the absorption of containments within the sample. Heavy metal containments have a broad electronic absorption spectrum through to IR wavelengths and have been observed in typical ZBLAN fibres. Contaminants can be the limiting source of loss across the spectrum, as shown in Fig. 1.5 [20].

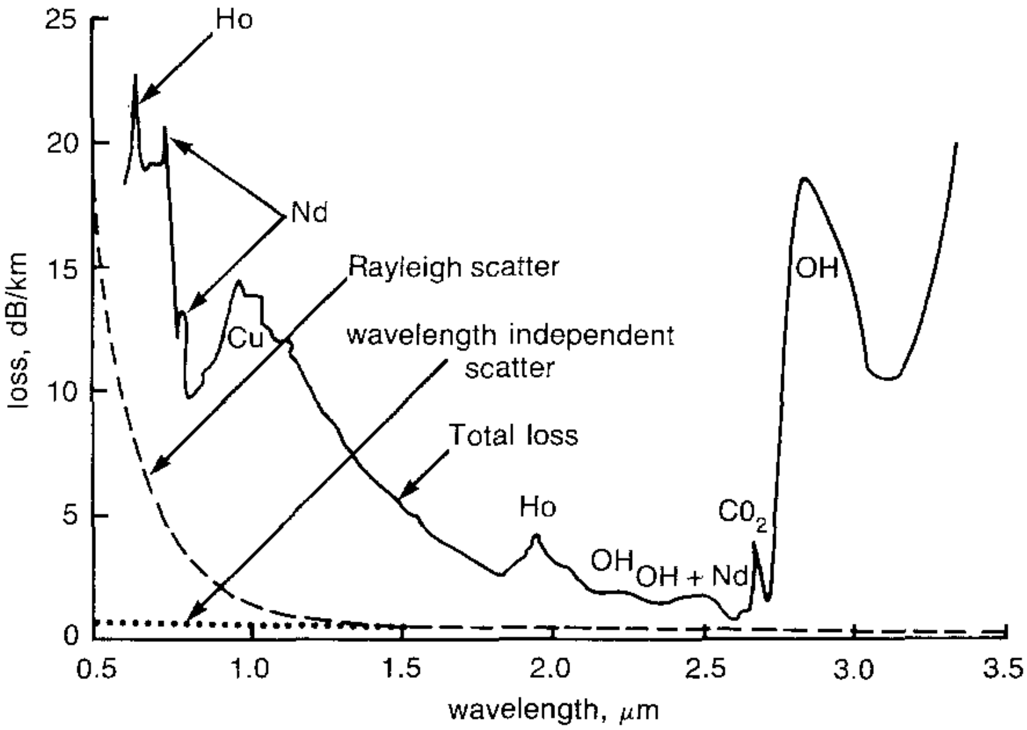

Fig. 1.5 A measured spectrum in ZBLAN (solid line) demonstrates losses orders of magnitude above the theoretical losses. Extrinsic absorption is shown to be a limiting loss source in this spectra due to heavy metals, OH and CO_2. The predicted losses due to scatter, indicted in the dashed and dotted lines [21] are significantly smaller.

In particular, the elements Fe, Cu, Co, Ni and Nd are of concern due to absorption peaks within ZBLAN's low-loss window. Careful treatment during the glass manufacturing process is required to ensure these containments aren't present in the raw materials or that they are oxidised into forms with lower absorption. In particular, Nd^{+3} has an absorption peak at 2.52 µm which is very close to the theoretical minima of ZBLAN. The presence of water as OH^{-1} is also very problematic due to its fundamental absorption peak at 2.8 µm and multi-phonon absorption, reducing the low-loss window [2].

Extrinsic scatter is caused by many effects which result in changes in refractive index. Larger scale refractive index changes can be instilled in the glass during manufacturing causing striations visible to the eye causing. Scattering off unwanted bubbles and crystallisation, is another large source of loss in ZBLAN, across the spectrum. It is currently believed that microcrystals are formed due to heating and cooling of the glass during manufacturing, limiting the size and quality of the sample that can be produced [2]. Additionally, the process of reheating the sample to form a fibre has been shown to increase the amount of scatter suggesting an increase in crystallisation [22]. Great effort has been expended to understand these mechanisms. The effect of gravity on crystallisation during cooling in ZBLAN has been investigated on low gravity flights and in the international space station [23].

This experiment was conducted by heating a ZBLAN fibre above 400 °C, to its glass transformation temperature for 6.5 minutes on earth in comparison to in microgravity aboard a sub-orbital rocket flight [24]. Fig. 1.6 shows the ZBLAN heated in both conditions and visibly demonstrates less crystallisation in low gravity conditions. However, the mechanism responsible for the improvement is unknown and in-depth characterisation is required to understand the causes.

Scatter is difficult and time consuming to measure, but its magnitude can be inferred by measurements of absorption and total loss. However, the predicted losses due to absorption are below 0.06 dB km which is incredibly small and will require an incredibly sensitive absorption measurement system that is insensitive to scatter, if theoretical low-loss ZBLAN is to be achieved.

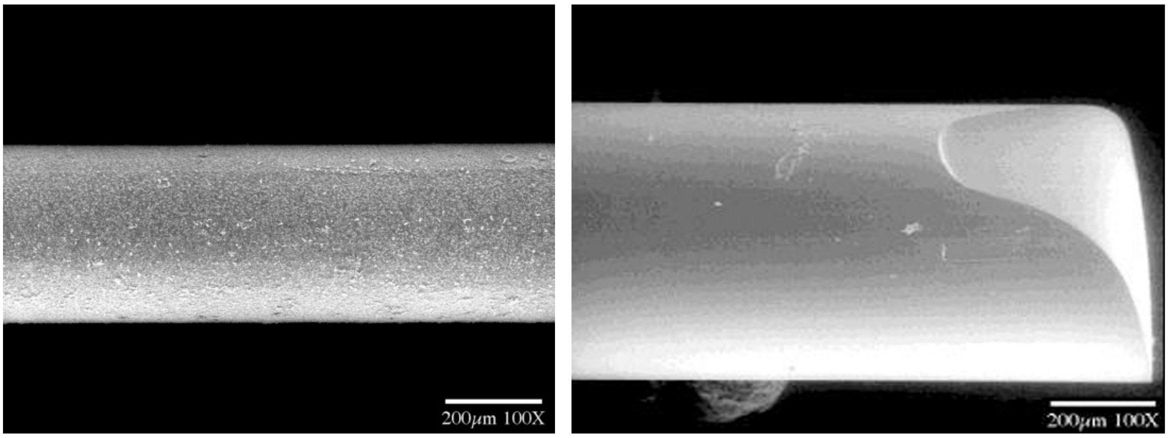

Fig. 1.6 Left: Scanning electron microscope image of ZBLAN fibre after being heated at to 400 °C (above the glass transition temperature) at ground level for 6.5 minutes. Right: Scanning electron microscope image of ZBLAN fibre after being heated at to 400 °C (above the glass transition temperature) in micro gravity for 6.5 minutes

1.5 Independently measuring of absorption loss

I aim to develop a system to measure the absorption coefficient of low-loss glasses at 2 µm, unaffected by scatter loss. This is motivated on 2 fronts. Firstly, to quantify absorption at 2 µm in proposed glasses such as fused silica or cryogenic silicon for 2 µm future GW detectors optics, which is a crucial step in next generation detector compensation and material selection. Secondly, to assist in the improvement of ZBLAN glass by measuring the level of extrinsic and intrinsic absorption to enable loss characterisation and the development of improved glasses for telecommunications. Consequently, I want to develop a highly sensitive measurement system that is capable of measure very small absorptions.

Total optical loss in glass fibre is commonly measured via transmission measurements, such as a cutback measurement in which power before and then after the fibre is measured for decreasing lengths. This allows a loss per meter to be determined, but cannot separate the sources of loss. Alternatively, the wavefront distortion due to absorption can be used to infer the absorption coefficient. Systems that measure absorption via the wavefront distortion are referred to as Photo-Thermal Measurement Systems (PTMS).

PTMS allows the determination of the bulk (α) and surface (β) absorption loss coefficient independently via the thermally induced change in optical path length (ΔOPL). Photo-thermal techniques typically use two beams: a pump and probe beam. The pump beam is absorbed causing a change in temperature and creating a thermal lens. A probe beam is used to measure the thermal lens, the magnitude of which is dependant on the surface and bulk absorption coefficients at the pump beam wavelength. The probe beam is chosen to be highly transmissible through the test sample so its absorption will not cause additional thermal effects. To optimise the sensitivity of the measurement such that small scale absorption coefficients can be observed, the probe beam is usually within the visible wavelengths where sensor and camera technology is well developed, allowing better precision than at 2 µm.

The measured wavefront deformation is the result of the following three effects.

1.5.1 Sources of thermal aberration

Thermo-refractive effect

When a sample is heated a thermal gradient ($T(x,z,y)$) is created inducing a proportional refractive index gradient as shown in Fig. 1.7 which distorts the wavefront of the probe beam. The magnitude and direction of this effect is dependant on the sign and size of the thermo-optic coefficient $\frac{dn}{dT}$.

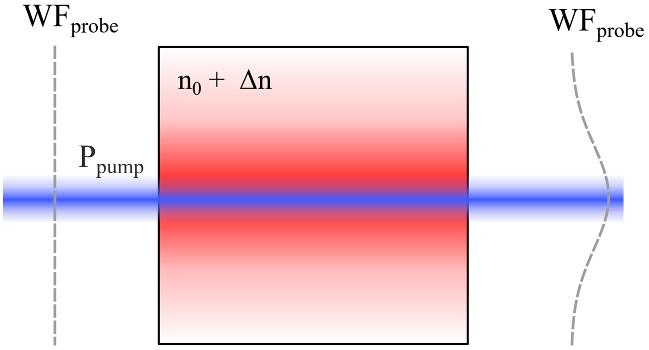

Fig. 1.7 Schematic of the thermal refraction of a beam passing through a sample, centrally heated by absorption of a laser beam with power P_{pump}, due to a refractive index gradient $n_0 + \Delta n$.

Thermo-elastic effect

The thermo-elastic effect describes the ΔOPL resulting from the elastic deformation of the sample. If the heat source is deposited over a small volume, such as absorption of a laser beam, the resulting stresses are not uniform resulting in a piston expansion as well as the

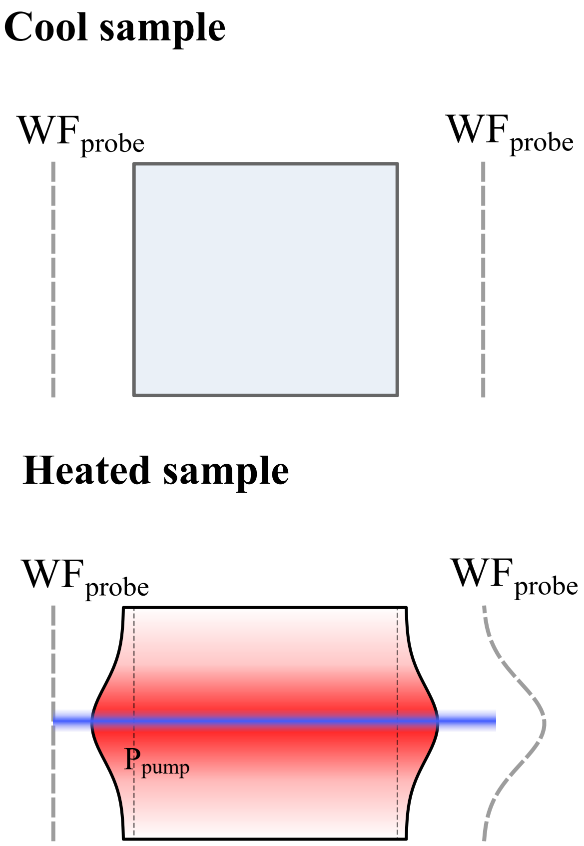

Fig. 1.8 Schematic of the thermal expansion of a sample when centrally heated by a laser beam with power P_{pump}. The thermal expansion from the un-heated end face position, shown by the dashed lines, is exaggerated.

bulging of the incident and exit faces (z) as shown in Fig. 1.8. The wavefront of an incident beam is distorted by the radius of curvature of the thermally expanded end faces and the additional length of the sample the beam must pass though at each end. The magnitude of this effect is defined by the thermal expansion coefficient.

Elasto-optic effect

The elasto-optic effect describes changes in phase due to thermally induced stress within the sample, resulting in a non-uniform refractive index distribution and birefringence. As the stress varies at each point in the sample a slow and fast axis are formed causing a phase change between the polarisations of an incident beam. This results in an ΔOPL for each polarisation which distorts the probe wavefront.

1.6 Review of photo-thermal techniques

Below I will review a series of photo-thermal measurement systems which have been demonstrated to quantify the absorption of glasses with ranging success and accuracy. I will discuss the strength and weaknesses of each system with respect to their capacity to measure very low absorptions at 2 μm, as required for GW and glass development applications.

1.6.1 Interferometric thermal lensing measurement

The GEO 600 interferometer has been used to measure bulk absorption in its fused silica beamsplitter [6]. The interferometer beam acts as both the pump beam and probe beam. Since the path through the beamspilter is different for the beams in each arm, the interference between these two beams at the anti-symmetric port will change. The absorption coefficient is estimated by measuring the interference pattern initially and after reaching thermal equilibrium and comparing to a computational model such as FINESSE. This allowed an upper limit of absorption to be determined with a high uncertainty of $\pm$ 0.1 ppm cm^{-1} [6]. An exact value could not be found as the thermal lens due to surface absorption as it cannot separated from that due to bulk absorption and thermal expansion was neglected.

This method is not easily applicable to a range of samples as it requires a beam splitter to be made for each material and access to a high-power interferometer to achieve high sensitivities. Additionally, to change the wavelength to 2 μm the whole interferometer would have to be reconfigured.

1.6.2 Photothermal Deflection Spectroscopy

Photo-thermal Deflection Spectroscopy (PDS), also sometimes known as a mirage bench measurement, irradiates the sample using a modulated pump beam, modulating its refractive index distribution and elastic-deformation. The probe beam is then refracted by the varying refractive index and deformation, shifting its position on a quadrant detector. To minimise noise this signal can be extracted using a lock in amplifier. A schematic of a typical PDS system is shown in Fig. 1.9. This method has been widely applied in the literature, for

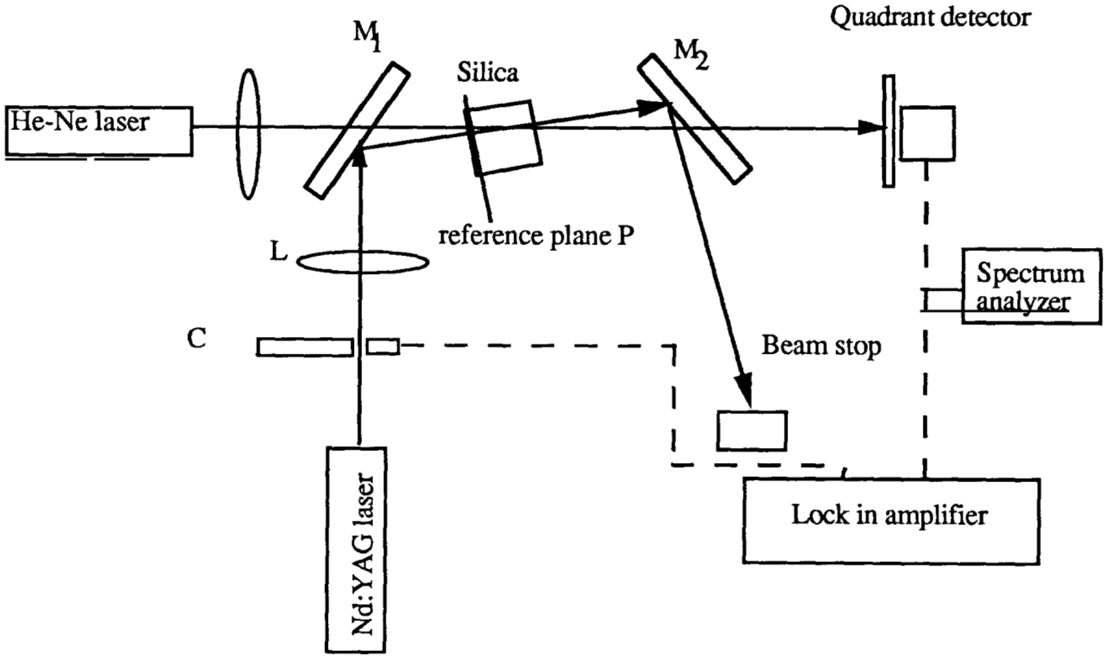

Fig. 1.9 Schematic of a typical photo-thermal deflection setup [25] where an angled incident probe beam passes through a laser heated sample onto a quadrant detector.

wavelengths ranging from the UV to IR [25]–[27]. Jackson *et al.* [26] has shown that absorption (α) through distances (d) can be measured to the limit of $\alpha d = 0.1$ ppm, which is similar to the most sensitive measurements in literature currently. However, the absorption is averaged over the area defined by the volume of the sample the probe beam transmits through and the spatial resolution is defined by the diameters of the pump and probe beams. It has been shown by using PDS, but modulating pump position, instead of power, the sensitivity of the system can be doubled allowing measurement of smaller absorptions [28].

Overall this method is unideal for novel glasses which may not be homogenous and would benefit from knowing if there are anomalous absorbers present in the sample. Due to the small probing area this would take extended time to measure. Furthermore, as the probe beam has to pass through a non-negligible section of the sample this does not allow surface absorptions to be quantified without bulk effects and bulk measurements may be influenced by surface absorptions.

1.6.3 Photo-thermal Common path Interferometry

In Photothermal Common-path Interferometry (PCI), a normally incident, modulated pump beam is focused onto a point in the sample causing a modulated thermal gradient within the surrounding sample, a typical schematic is shown in Fig. 1.10. A larger probe laser beam crosses the heated spot at a slight angle to the pump beam. Due to the changes in refractive index the probe beam experiences differential wavefront distortion and over a distance, self-interference. The amplitude of this modulation is proportional to the phase modulation and thus the optical absorption. Comparing the phase modulation to that predicted by a model allows the magnitude of the absorption to be calculated, after calibration. The sophistication of the model varies between studies, with the most complex using a detailed analytical model considering the phase as a result of thermo-refractive, thermo-elastic and elasto-optic effects [29]. This method is widely applied in low-loss materials [29]–[31].

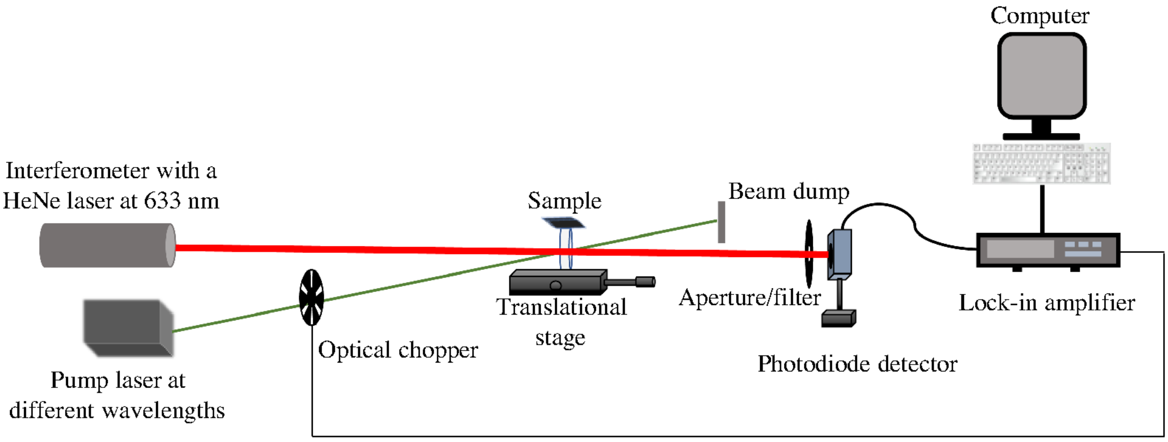

Fig. 1.10 Optical schematic of a typical PCI setup[31]. A small laser beam is focused onto the sample causing heating and self-interference of the probe beam, causes modulating the interference fringes on to appear on a photodiode, changing the measured intensity.

Marchiò *et al.* [30] used PCI to generate a 3D map of the bulk absorption in sapphire at 1 μm by moving the sample in 3D, generating a map of with a resolution of 1mm and sensitivities as low as 1 $\mathrm{ppm\,cm^{-1}}$. Creating a 3D absorption map of a 120x120x100mm sample with this precision requires about 9 hours.

PCI is unsuitable for my proposed application as it yields absorption at one location for each measurement. I aim to determine surface and bulk absorption as measure of the homogeneity of many different samples, which would require full sample scans and thus significant periods of time. Additionally, PCI requires calibration, which is difficult at 2 μm as few materials are sufficiently well characterised.

1.6.4 Photothermal wavefront deformation measurements

The methods outlined above are limited for my application. Interferometric methods are impractical for measurements on numerous samples and are unable to exact surface absorptions. PDS and PCI measurement systems are capable of this applications goals but impractical due to their extremely long measurement times to measure the entire sample. Instead it is possible to extract absorption over a large area of a sample by imaging the wavefront distortion of a probe beam after passing through the heated sample, using a Hartmann Wavefront Sensors (HWS) [32]–[37].

Differential Hartmann Wavefront Sensors (DHWS) and Shack Hartmann Wavefront Sensors (SHWS), which will be broadly referred to as Hartmann Wavefront Sensors (HWS), use an array of uniformly spaced holes or micro-lenses, respectively, to decompose a beam into rays that propagate normally to the wavefront at that point. The rays are incident on a Charge Coupled Device (CCD) or Complementary Metal–Oxide–Semiconductor (CMOS) sensors creating an array of spots, for which a set of centroids are calculated, as shown in figure Fig. 1.11. Changing the shape of the wavefront changes the position of the centroids. The wavefront distortion can be reconstructed from the gradients of the centroid positions before and after the absorption induced distortion using numerical integration or polynomial fitting methods. Consequently, if the sensor is optically conjugate to the sample then the distortion is equivalent to that accumulated through the heated sample and absorption can then be extracted by comparison to a model or via calibration. This method allows a 2D map of the wavefront distortion over a significant portion of a sample, as the probe beam size is only limited by the sample clear aperture. The presence of highly absorbing inhomogeneities in the path of the pump beam are easily identifiable in the map [10].

HWS systems have been widely applied to measure absorption. The measurement noise floor of the DHWS and SHWS can be dramatically reduced by averaging frames to reduce the effect of shot noise, giving similar sensitivities of ca. 100 pm [36], [38].

HWS absorption measurement systems with various configurations of the pump and probe beam have been published. Using a co-linear probe and pump beam, bulk absorption has been measured with an uncertainty of 4 $\mathrm{ppm\,cm^{-1}}$ [32]. However, this method did not allow for surface absorption and bulk absorption to be separated from one measurement. Co-linear

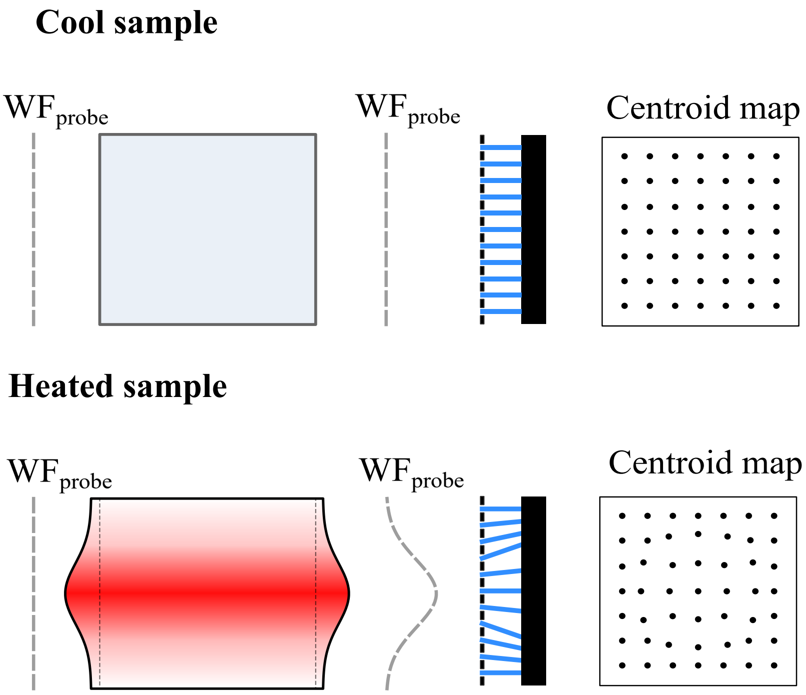

Fig. 1.11 DHWS measure the differential wavefront by decomposing a beam into rays at the Hartmann plate and measuring the change in position of incidence on a sensor. The direction of the rays is defined by the normal to of the wavefront at the plate. This creates a spot pattern on the sensor which is referred to as a centroid map. The effect of the change in wavefront and consequent angle of the rays on the sensor is demonstrated by the position of the centroids measured on the sensor. In this diagram I assume $\frac{dn}{dT}$<0.

measurements also require dichroic mirrors to separate the pump and probe beam which can cause parasitic absorption and distortion as observed in Ingram *et al.* [33].

Brooks *et al.* [34] first suggested measuring absorption by imaging an off-axis probe beam passing through a centrally heated sample using a DHWS in 2005. In Brooks [35] this architecture was used to measure wavefront distortion in BG20 glass at 1064 nm, and a model predicting the total wavefront distortion due to the thermo-refractive effect was created based on the analytical solution for a temperature distribution from Hello *et al.* [39]. However, the absorption coefficient of BG20 was not determined.

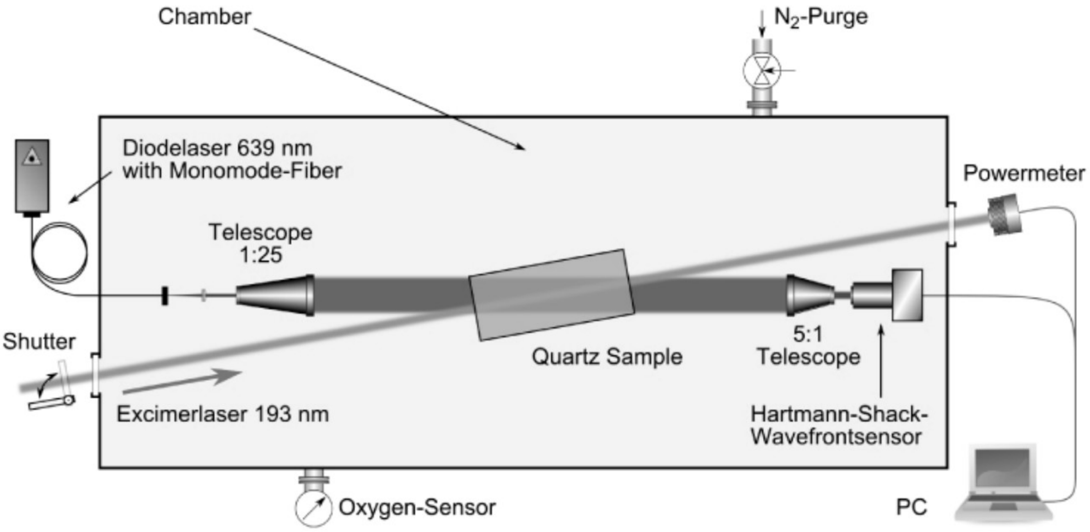

Fig. 1.12 Optical schematic of a system to measure the wavefront deformation of a probe beam passing off-axis through a sample heated by an on-axis heating beam. [36] .

A similar off-axis probe beam setup has also been used for a SHWS absorption measurement system using a 248nm pump beam at a 100 ppm cm^{-1} level in fused silica [36], for which the optical schematic is shown in Fig. 1.12. The wavefront distortion was then reconstructed as a Zernike polynomial. This study compared two methods of calibrating the absorption measurement. The first was to simulate laser heating using a resistor chain and using the peak-valley temperature change at various electrical powers to determine the calibration factors. The second used a Finite Element Method (FEM) that represented the wavefront distortion as a linear expression in terms of surface and bulk absorption and their respective distortion at each point in the sample. The FEM was proven to give a more accurate value, however, it relied upon the assumption that the sample is weakly absorbing and there is negligible power lost over the sample length. The results showed surface absorption could not be extracted due to the small magnitude of the total deformation. While the exact method to determine the deformation was unclear, it was stated that this method considers thermo-expansion and thermo-optic effects.

This system was further modified such that a 50W 1070 nm pump beam and 630 nm probe beam were transmitted through perpendicular faces of the sample, as shown in Fig. 1.13. An analytical model was used to estimate the bulk and surface absorption yielding 11±4 ppm and 74±28 ppm cm^{-1} respectively [40]. This model considered thermo-expansion, thermo-optic

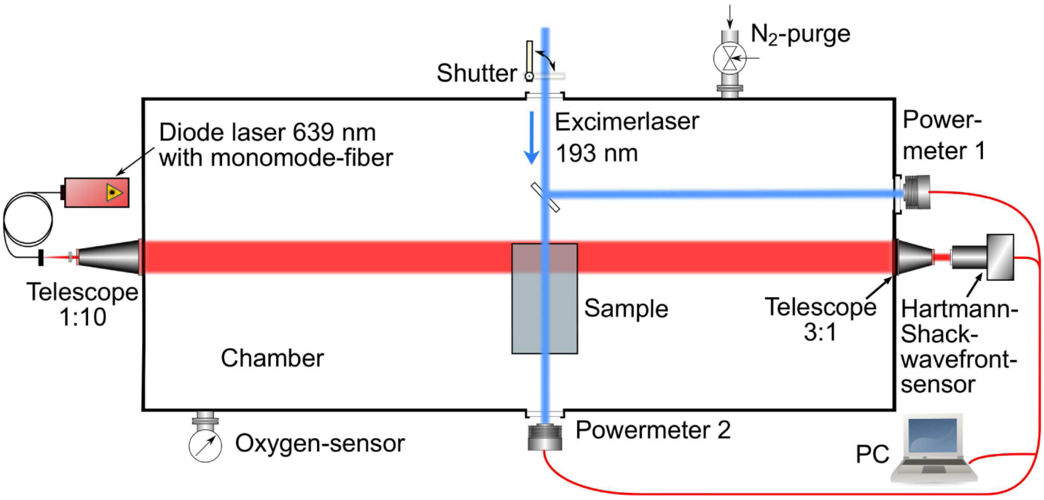

Fig. 1.13 The off-axis probe beam, on-axis pump beam set up can be modified such that the probe beam passes through the perpendicular face. In this case a SHWS is used to measure the wavefront deformation [37]

and elasto-optic effects.

1.7 Requirements of system to measure absorption in low-loss glasses

Measuring absorption accurately is essential to glass development and compensation systems for GW detectors. To create a system to measure low-loss samples but have the adaptability to be used to measure various of novel glasses it must be capable of the following:

1. Sensitivity to absorption coefficients $< 10\,\mathrm{ppm\,cm^{-1}}$.
2. Less than 10% systematic errors.
3. Sensor able to extract surface and bulk absorption coefficients.
4. System can be adapted to different sample size and shapes.
5. Detect inhomogeneity in samples.

In this thesis we aim to develop a system which can measure less than $10\,\mathrm{ppm\,cm^{-1}}$ of bulk absorption whilst extracting surface absorption. This is driven by the long-term aim to measure the absorption losses of fused silica at 2 μm, which can be achieved with this sensitivity, as well as measure the current best available ZBLAN which has absorption of $1.5\,\mathrm{ppm\,cm^{-1}}$

[19]. However, measuring such low levels of absorption is pushing the boundaries of current technology in essential areas like stable high power laser sources at 2 μm, sensor sensitivity and high quality ZBLAN samples of a measurable size. For the initial development of this system, we set this as a reasonable goal which surpasses the current sensitivity of similar methods thus far.

1.8 My project and thesis outline

To fulfill the requirements listed above, in this thesis, I describe an off-axis set-up based upon that in Brooks *et al.* [34], modifying the system to use a 2μm heating beam, as shown in Fig. 4.1, and the FEM model applied to quantify the absorption.

This configuration has been selected to allow surface absorption to be determined and a 2μm heating beam was implemented to measure materials for future GW applications and novel glasses with minimum losses in the SWIR. A FEM model has been selected to allow analysis of all contributing thermal aberration effects described in Section 1.5.1 with high accuracy.

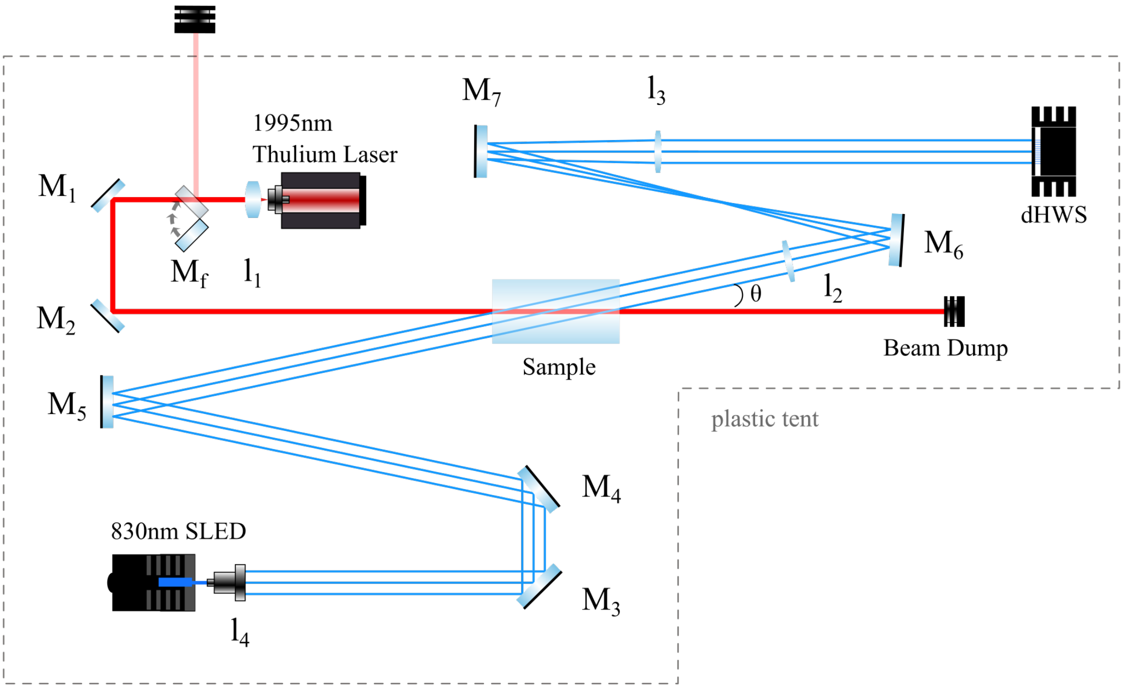

Fig. 1.14 Schematic of my proposed on-axis pump beam, off-axis probe beam DHWS PTMS absorption set-up, described in greater detail in Section 4.2.

My system:

- does not require dichroic optics to combine and separate probe beams,
- can separate surface and bulk absorption coefficients,
- has a larger wavefront distortion than the perpendicular pump and probe configuration as it probes more of the samples heated volume,
- exploits the ultra-high sensitivity and accuracy of the DHWS,
- does not require calibration,
- can identify anomalous localised absorbers,
- can, in principle, determine whether the material parameters used in the FEM are appropriate for the sample.

In this chapter the precision measurement of absorption in glass has been demonstrated to be essential to the development and improvement of novel glasses and their application in high sensitivity systems. ZBLAN has been presented as a future low-loss glass which if theoretical loss limits could be achieved, could be widely applied in SWIR systems like future gravitational wave detector optics and telecommunication fibres. Currently, loss is limited above the theoretical value by extrinsic absorption from impurities in the glass and scattered loss due to these contaminants and crystallization of the glass through mechanisms which are not well understood. Measuring absorption loss can help minimise extrinsic absorption and characterise the sources of loss which is a pathway to achieving the theoretical limit. After reviewing previous photo-thermal techniques a set-up has been proposed to complete this aim.

An accurate model of the centrally-heated ZBLAN sample is described in Chapter 2. Since I wish to measure samples which are rectangular prisms rather than exclusively cylindrical, a finite element model is required. The FEM is validated by comparison of a cylindrical sample with the Hello & Vinet analytical models [39], [41], [42]. The results of the FEM are used in Chapter 3 to determine the off-axis probe wavefront distortion due to the TE, TR and EO thermal effects. Least squares fitting to the experimental data to extract the absorption coefficients and analysis of the effects of inaccurate sample parameters is then described.

Chapter 4 describes the experimental set up used to measure the absorption of a sample. A verification measurement on N-BK7 is completed in this chapter to demonstrate that the model accurately describes the system and can be used to determine surface and bulk absorption. Finally, in Chapter 5 this system is applied to the measurement of a ZBLAN sample to determine the bulk absorption and set limits to the magnitude of the surface absorption. Chapter 6 provides concluding remarks on this body of work.

CHAPTER 2

DETERMINING THE PHYSICAL EFFECTS OF HEATING ON GLASS SAMPLES

2.1 Overview

Optical absorption in glass occurs through the coupling of incident light to the vibrational modes of atoms and bonds in the material. As the excited phonons decay energy is released as heat, heating the bulk glass and changing the physical properties such as the refractive index [2]. Optical beams are sensitive to these changes and are deformed as a result of the thermo-elastic, thermo-refractive and elasto-optic effects. The magnitude of the deformation is dependant on the bulk (α) and surface (β) absorption coefficients of the sample. The measurement system shown in Fig. 4.1 and described in Chapter 4 observes the magnitude of the absorptions via the thermal aberration of a probe beam wavefront as it passes through the sample, as shown in Fig. 2.1. To determine the absorption coefficients, I compare the measured absorption induced wavefront distortion with that predicted by a numerical simulation.

The thermal effects are shaped by the temperature distribution ($T(x,y,z)$). Temperature variations change the density of the glass causing a refractive index distribution ($n(x,y,z)$), producing aberration of incident beams due to the thermo-refractive effect. The change in temperature also produces thermal stresses which induce changes in the refractive index, known as the elasto-optic effect and the expansion of the sample, known as the thermo-elastic effect.

Two models are considered in this chapter, the first is the Hello & Vinet (HV) analytical solutions discussed in Section 2.3 [39], [41], [42]. The second model uses the Finite Element Method (FEM) tool COMSOL Multiphysics described in Section 2.4. Both models consider the thermo-refractive and thermo-elastic effects and the HV model can thus be used to

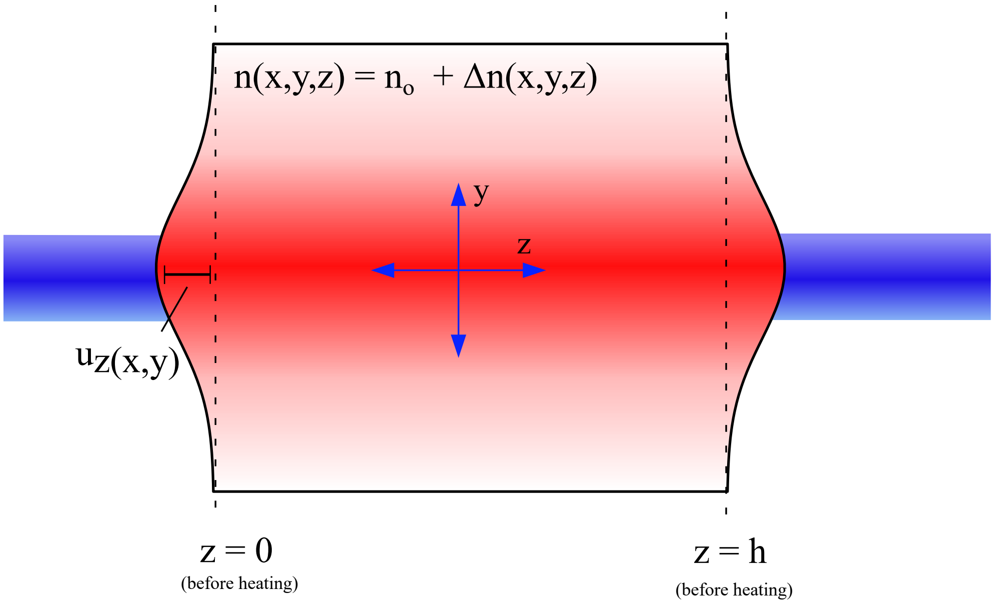

Fig. 2.1 Schematic of the physical effects of centrally heating a sample with a Gaussian beam. The absorption results in a refractive index (n) distribution, where n_o is the refractive index at room temperature and the thermal expansion of the end faces (u_z). The deformation of the end face is exaggerated for clarity.

validate the FEM model for various sample geometries as discussed in Section 2.5. The elasto-optic effect is considered briefly in Section 3.2.3 and in detail in Appendix B.

2.2 Modelling thermal effects on glass samples

The temperature dependent behaviours of glass can be modelled through numerous methods such as analytical and numerical models. A brief description of each is given below:

- An analytical model has an exact solutions to a scenario presented as an equation.
- Numerical models rely on computers to solve complex sets of equations, finding a solution by iterating until it converges. FEM is a common example of a common numerical model for thermal processes.

Numerical models allow significantly more flexibility in what can be modelled as an exact solution does not have to be determined. However, these models can require long computation times dependant on the complexity of the model. Additionally, even if a solution is found with a rational input it may be non-physical.

Analytical models, on the other hand, give a solution which can be more easily analysed, but they may require assumptions to solve complex mathematical equations such as thermo-elastic expansion of a heated sample and become inaccurate when applied to situations in which these assumptions are not valid.

An analytical model for the thermal effects on a glass sample and the subsequent lensing has been developed for applications in gravitational wave detection by Hello & Vinet over a series of works [39], [41], [42]. However, it makes assumptions based on the shape and size of the VIRGO test masses which may not apply to the novel ZBLAN glass geometries I aim to test. In my aims for this project I outlined that a the system should be capable of measuring absorption in almost any sample. Thus, the numerical FEM tool COMSOL will be applied to model the thermal effects on glass for the finalised model.

2.3 Modelling heating of a glass sample using Hello-Vinet analytical solutions

Hello and Vinet (HV) derived equations which describe the thermo-optic and thermo-elastic effects due to weak absorption of a Gaussian laser beam propagating along the cylindrical axis of an isotropic disc with surface coatings [39], [41], [42]. The geometry of the thin disc sample modelled is shown in Fig. 2.2. The equations provide solutions for the temperature distribution ($T(x,y,z)$) of the sample [39] and the displacement of the end faces of the sample u_z [41].

The analytical derivation assumes:

- Absorbed power $\ll$ incident power P_{pump}
- Radiative cooling of all faces
- Surface temperature $\approx$ ambient temperature
- Diameter of the pump beam $2w \ll$ diameter of sample $2a$

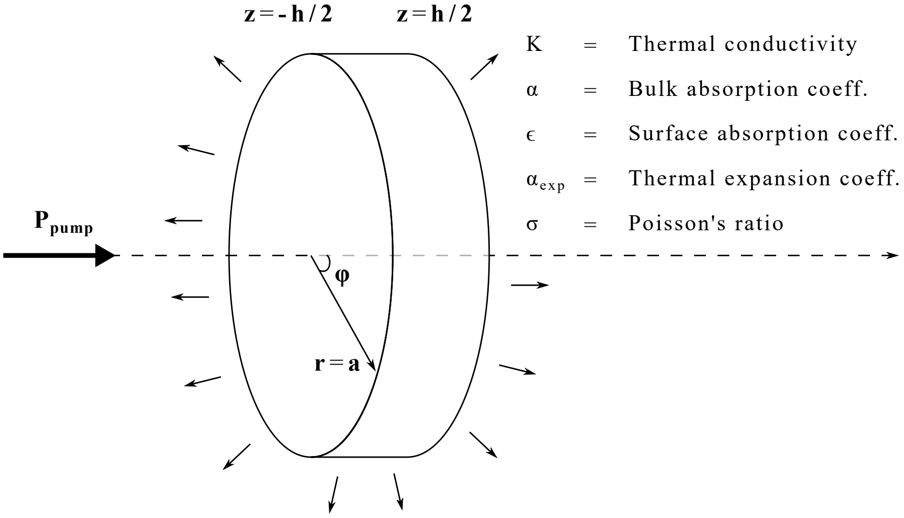

Fig. 2.2 The HV model formulates the change in internal temperature distribution and resulting thermal expansion of a centrally symmetric thin disk of glass with radius (a) and length (h) which is heated along the central z axis by a pump beam (P_{pump}). Arrows indicate radiative cooling.

The heat source assumptions are largely valid for the proposed experimental setup, which centrally heats the weakly absorbing samples using a Gaussian laser beam, as explained in detail in Chapter 4. Thus, the temperature increase in the sample is much less than the ambient temperature. The experiment isn't, as assumed, in a vacuum so there may be losses due to conduction and convention that will primarily affect the thermal gradient near the samples surfaces.

Assumptions about the geometry of the sample create a larger problem as it is convenient to use long rectangular prism samples. Other assumptions such as, $w < a$ can be achieved by choosing of the heating beam's waist to be small, which will also increase the signal size for a given P_{pump}.

2.4 Modelling thermal effects on a glass sample using numerical model

A FEM of the optical absorption in an isotropic solid with surface coatings was developed using the heat transfer and structural mechanics modules in COMSOL Multiphysics [43]. The FEM yields the temperature distribution in the sample. The stresses and the displacements were calculated using the COMSOL Multiphysics tool, Temperature Coupling, to couple the heat transfer and structural mechanics modules [43].

The coordinate system used for the models is shown in Fig. 2.3, where the input face was located at z=0 and the xz and yz planes are assumed to be mirror symmetry planes to simplify the problem and reduce the required computational power, as then only a single quadrant must be considered.

In COMSOL, unphysical expansion and rotational motion, which can result in additional internal stress, was prevented by adding constraints. For my FEA model, the point (0,0,0) was specified to be a Fixed Constraint. Additionally, prescribed displacements specify that nodes on the x(y) axis can't move in the y(x) direction to prevent rotation of the model while allowing free expansion in the radial direction.

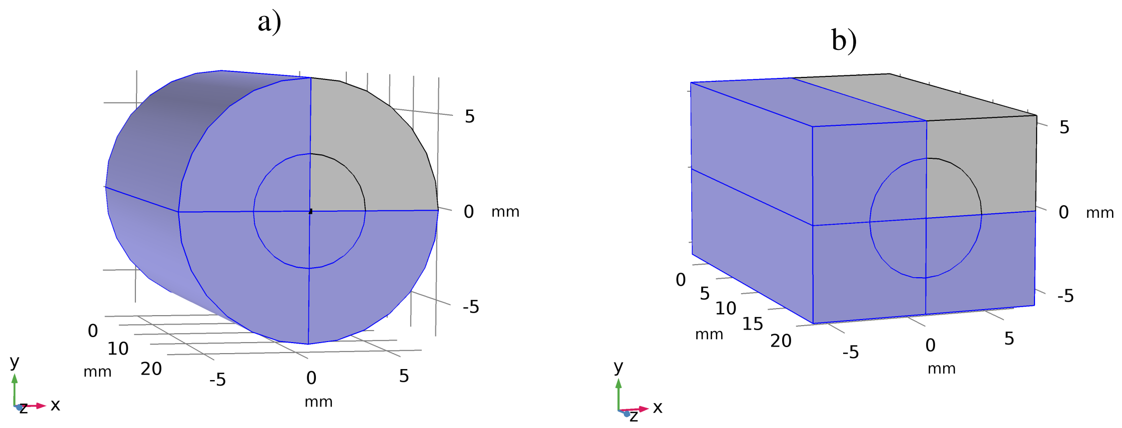

Fig. 2.3 COMSOL allows any sample geometry to be built, such as a cylindrical (a) and rectangular (b) geometry and can be simplified by reducing the model to a symmetric quadrant. The quadrant can then be used in the study to reduce the computational power and recover the total sample solutions post study.

COMSOL iteratively computes the solutions at mesh points in the sample. An example mesh is shown in Fig. 2.4. To accurately describe the thermal gradients a tetrahedral mesh has been used. A finer mesh size was used in the central region of the sample to improve the precision for the larger thermal gradients at the centre of the sample.

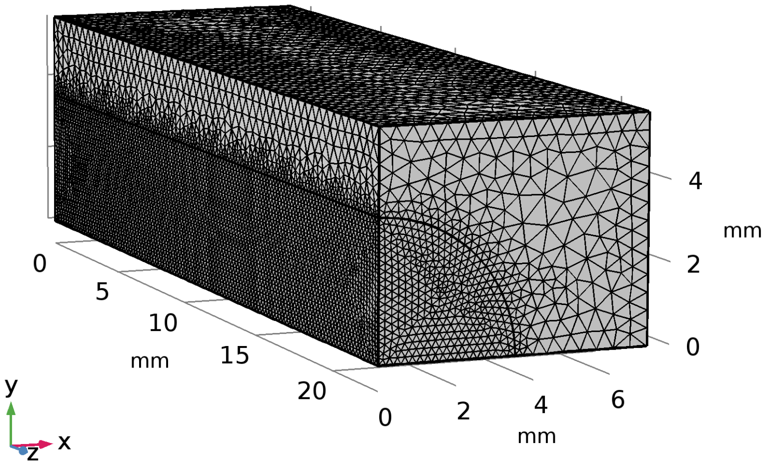

Fig. 2.4 3D COMSOL model showing the mesh points of sample quadrant where a heating beam would pass along the z axis. The density of the mesh grid is increased within a cylindrical centre region of the sample to ensure there are enough data points to see a smooth distribution where there are larger thermal gradients.

2.4.1 Description of heat-transfer

The heat transfer model assumes that the heat source is a collimated laser beam with a beam size w_x and w_y and a Rayleigh range much longer than the sample and that the sample has radiative cooling of all surfaces. Assuming weak absorption, the power of the laser beam at the first surface P_{s1}, in the bulk P_b and at the second surface P_{s2} are given by,

$$P_{s1} = P_{pump} + P_{pump}(1 - R_1)R_2 \tag{2.1}$$

$$P_b = P_{s2} = P_{pump}(1 - R_1) + P_{pump}(1 - R_1)R_2 = P_{pump}(1 - R_2 - R_1 + R_1R_2) \tag{2.2}$$

where P_{pump} is the incident power, R_1 and R_2 are the reflectance of the input and output faces.

The heat load at each point in the sample due to absorption in the bulk, Q_{bulk} is given by,

$$Q_{bulk} = \frac{2}{\pi} \frac{\alpha P_b}{w_x w_y} \exp\left\{ -2 \left(\frac{x^2}{w_x^2} + \frac{y^2}{w_y^2} \right) \right\} \tag{2.3}$$

The heat load due to surface absorption, Q_{fs} and Q_{bs} at the front and back faces is given by,

$$Q_{fs} = \frac{2}{\pi} \frac{\beta P_{s1}}{w_x w_y} \exp\left\{ -2 \left(\frac{x^2}{w_x^2} + \frac{y^2}{w_y^2} \right) \right\} \tag{2.4}$$

$$Q_{bs} = \frac{2}{\pi} \frac{\beta P_{s2}}{w_x w_y} \exp\left\{ -2 \left(\frac{x^2}{w_x^2} + \frac{y^2}{w_y^2} \right) \right\} \tag{2.5}$$

where α is the bulk absorption coefficient and β is the surface absorption coefficient, assumed to be the same at both faces.

The FEM assumes that all surfaces are cooled via radiation, for which the rate of heat loss per unit area, Q_r, is given by,

$$Q_r = \varepsilon\sigma(T_{amb}^4 - T^4) \tag{2.6}$$

where ε is the emissivity of the surfaces, σ is the Stefan-Boltzman coefficient, T is the local temperature of the surface and T_{amb} is the ambient temperature.

2.4.2 Calculating thermal expansion of end-faces

COMSOL returns the displacement from initial points (x, y, z) as (u, v, w). The total displacement consists of an end face deformation and a piston displacement. To evaluate the piston expansion over the whole sample an integration of the displacement in the axial direction, w, can be subtracted to define the origin point from the centre of the sample as opposed to the fixed constraint set at (0,0,0) on the input face. However, only the end face deformation is required in this computation as a differential measurement technique is used.

2.5 Verification of FEM using Hello-Vinet model

In this section, it is shown that the predictions of the FEM model agree with those of HV for a disc sample, thus validating the FEM model. For a rod sample, however, the FEM model predicts that the end-face deformation due to bulk absorption is much smaller than that of HV, due to internal shear stresses that are not significant for thin discs. This severely limits how widely HV can be applied. The sample and system parameters used to generate both models are listed in Table 2.1 and Table 2.2 respectively.

Parameter	Symbol	Value	Unit
Length of rod	h_{rod}	22.805	[mm]
Length of disc	h_{disc}	2.2805	[mm]
Radius_x	a_x	6.975	[mm]
Bulk Absorption Coefficient	α	50	[ppmcm^{-1}]
Surface Absorption Coefficient	β	3	[ppm]
Thermo-optic Coefficient	$\frac{dn}{dT}$	14.75	[10^{-6} K^{-1}]
Thermal conductivity	K	0.628	[Wm^{-1} K^{-1}]
Density	ρ	4330	[kg m^3]
Specific Heat Capacity	C_p	151	[J K^{-1}]
Coefficient of thermal expansion	α_{exp}	17.2	[10^{-6} K^{-1}]
Poisson's Ratio	σ	0.17	-
Young's Modulus	Y	58.5	[GPa]
Surface emissivity	ε	0.9	-
Initial Temperature	T_0	293.15	K

Table 2.1 Table of parameters for the FEM and HV models for a ZBLAN sample.

Parameter	Symbol	Value	Unit
Pump Power	P_{pump}	7.405	[W]
x beam radius	w_x	0.72	[mm]
y beam radius	w_y	0.70	[mm]

Table 2.2 Table of system parameters for the FEM and HV models, replicating that for the experimental set-up in chapter 4.

Both models assume a negligible reduction in power due to absorption. Consequently, for this verification small absorptions of α and β of 50 ppm cm^{-1} and 3 ppm respectively are selected which cause a ≈0.01% reduction of power over the sample, calculated using Beer-lamberts law (Equation (1.4)). Additionally, they are approximately the measured values in chapter 5 and on the order of magnitude of the 10 ppm cm^{-1} absorption aimed to be measured with this system. This allows verification that the FEM model is appropriate for these magnitudes of absorption.

2.5.1 Thermal distributions

Using the methods outlined above, the temperature distribution was produced using the HV and FEM models for a centrally heated ZBLAN disc sample. Comparisons of cross sections of generated $T(x,y,z)$ due to bulk absorption and surface absorption are shown in Fig. 2.5, Fig. 2.6, and Fig. 2.7.

The difference between the FEM and HV temperature distributions for both surface and bulk absorption is greatest where the temperature gradient is largest but is negligible at <0.05% and <0.02% respectively. This agreement also applies to long rod samples (see appendix A). Thus, it can be concluded that the FEM as been formulated to describe the same thermal transfer conditions.

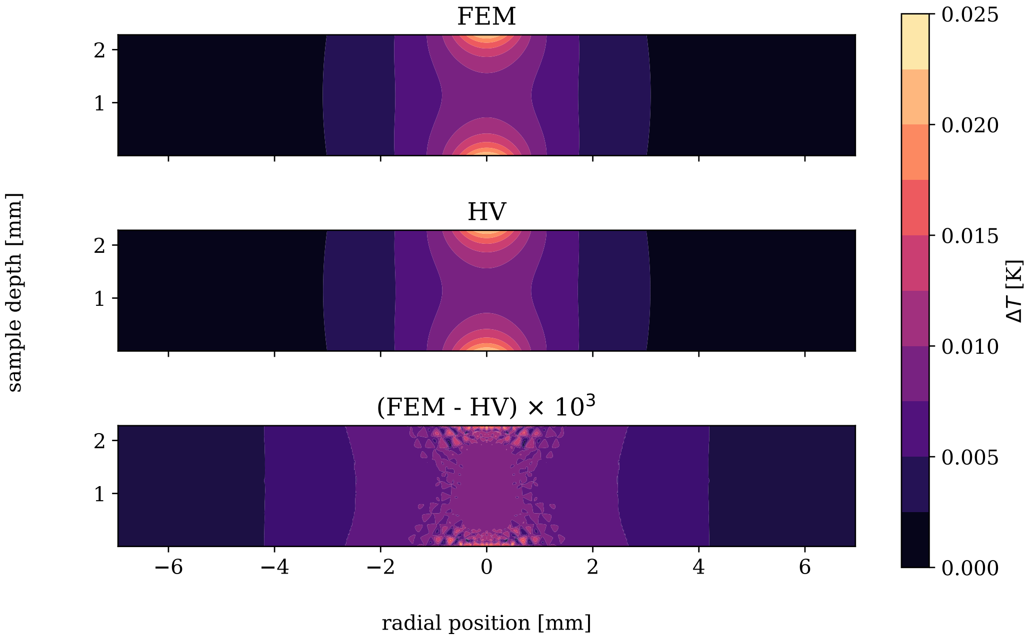

Fig. 2.5 Comparison of FEM and HV $T(x,y,z)$ due to surface absorption using the parameters in Table 2.1. Residual structure due to the COMSOL model mesh structure is observed but is negligible.

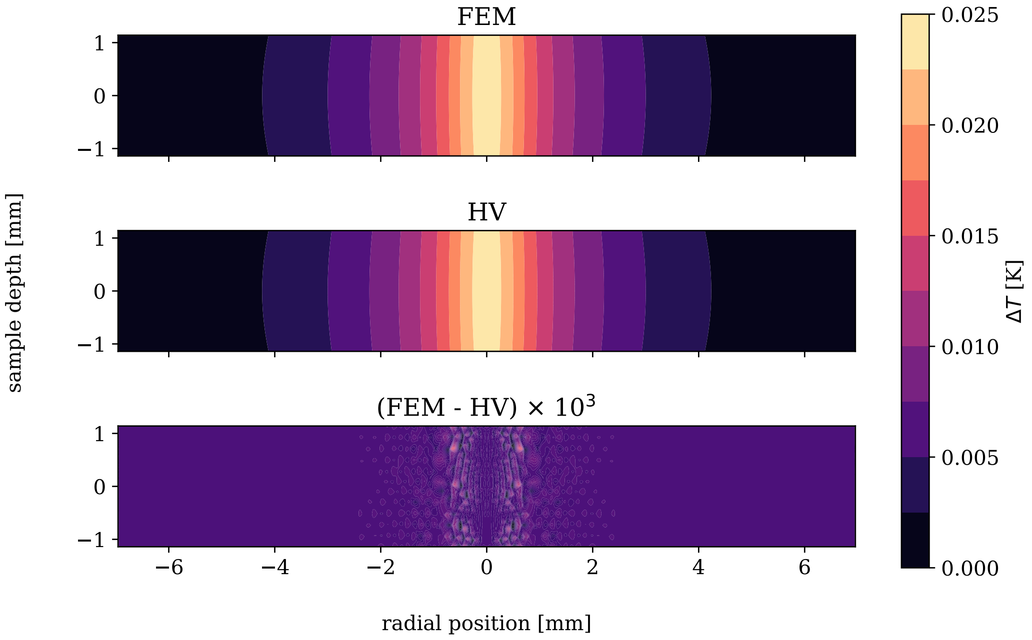

Fig. 2.6 Comparison of FEM and HV $T(x,y,z)$ due to bulk absorption using the parameters in Table 2.1. As above some negligible residual structure is observed.

a) Bulk absorption

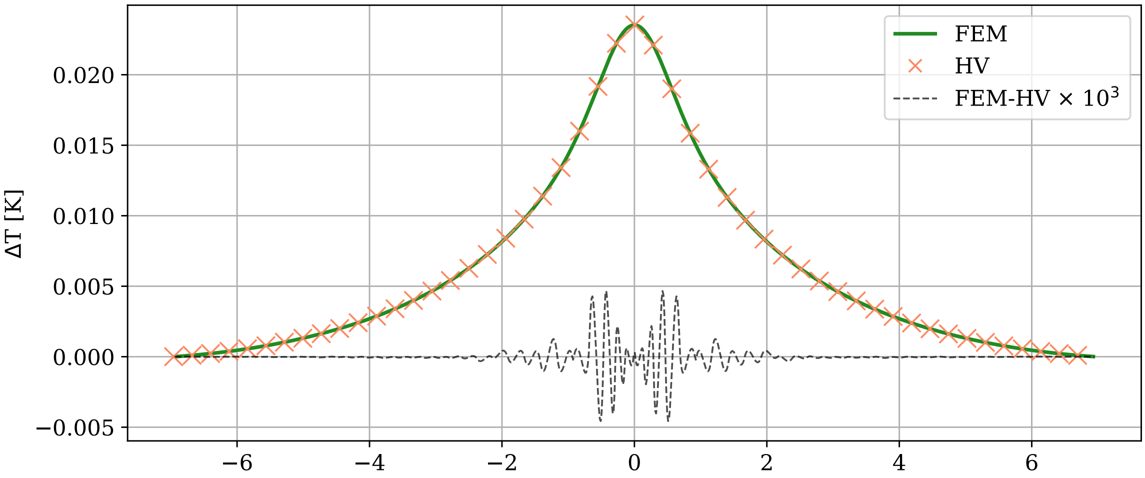

b) Surface absorption

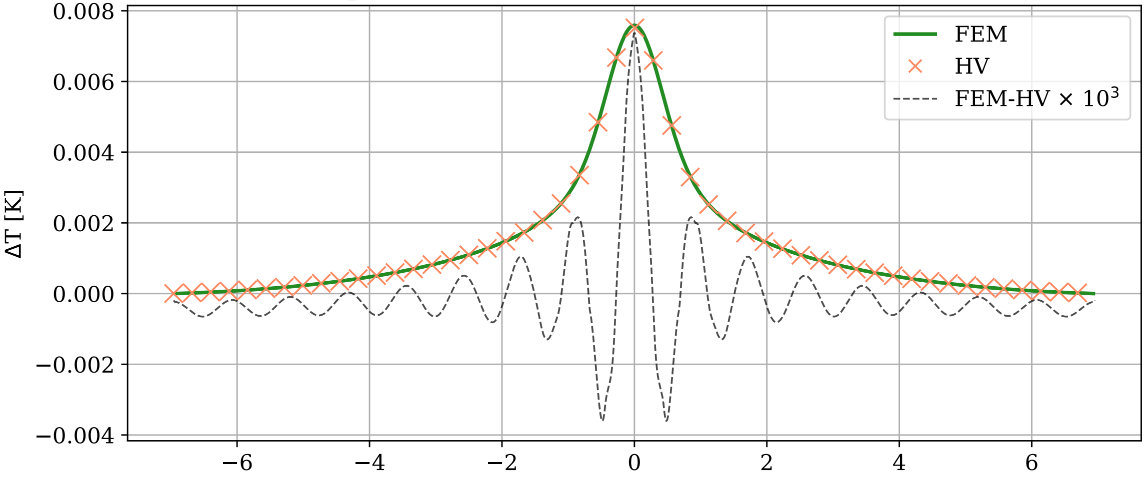

c) Combined absorption

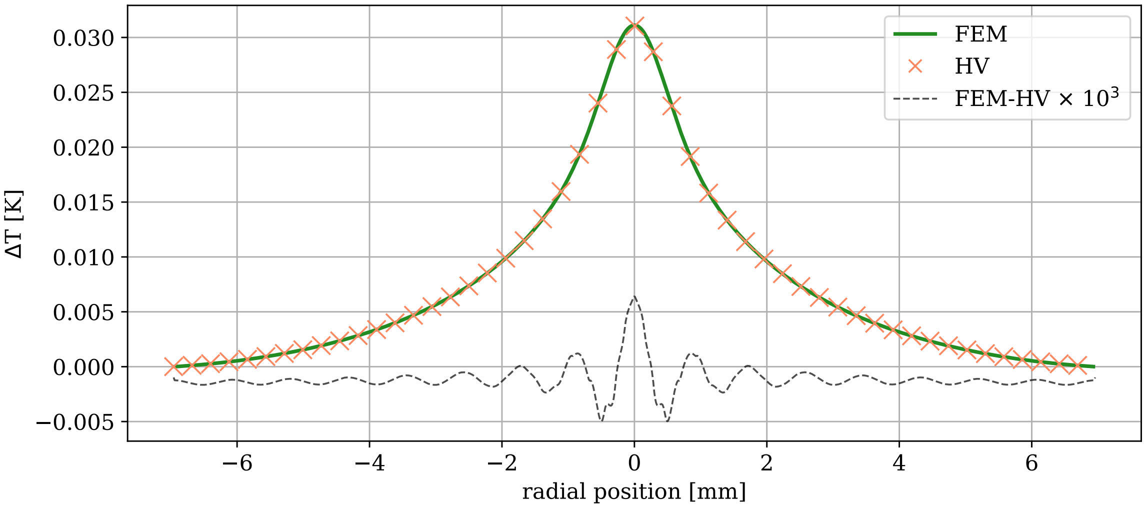

Fig. 2.7 Comparison of temperature profiles at end face of sample generated using FEM (COMSOL) and HV using the parameters from Table 2.1. The residuals of the two plots have been multiplied by 10^3 to show the whilst the structure has a sinusoidal profile it is negligible.

2.5.2 End-face deformation for a thin disc

The end face deformation for a disc sample using the FEM and HV models are plotted in Fig. 2.8.

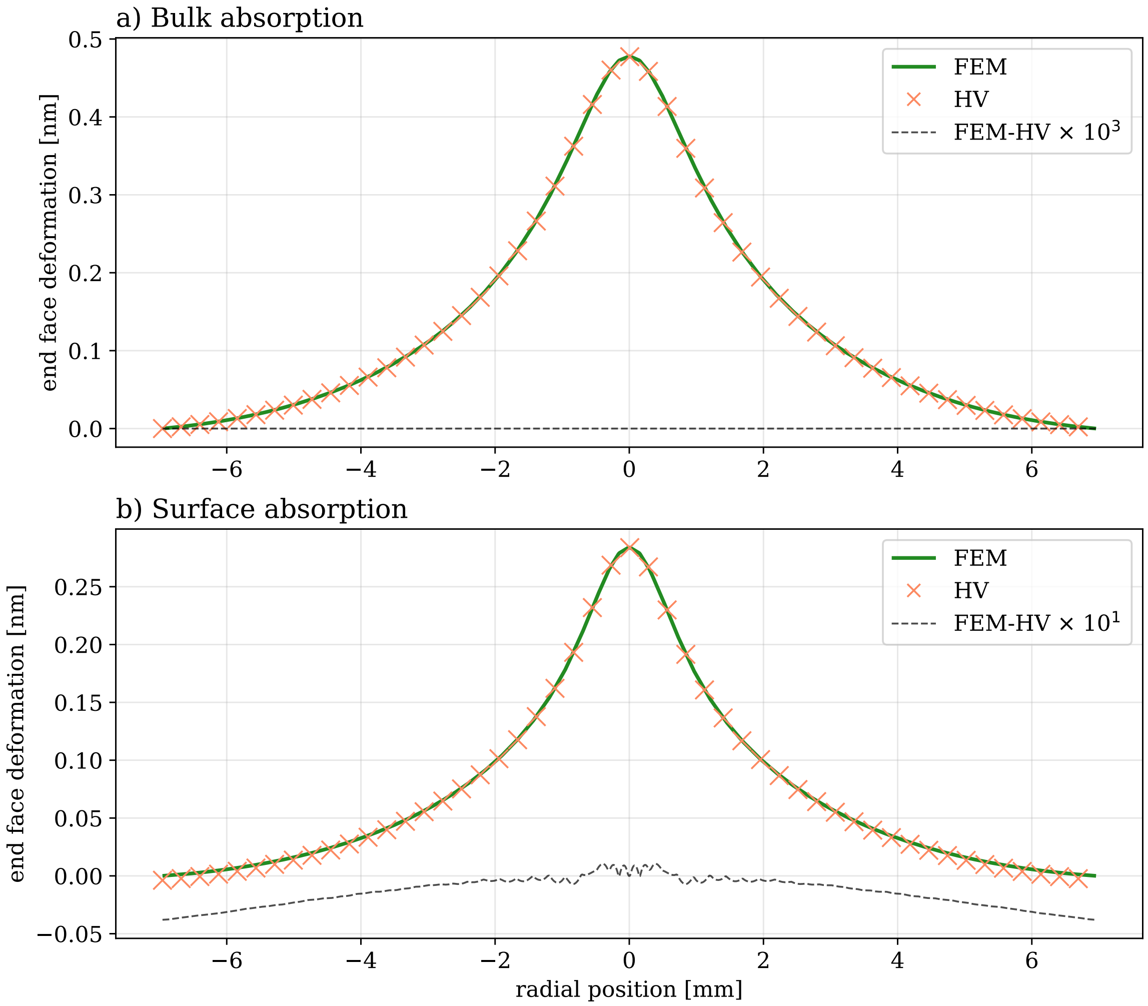

Fig. 2.8 Comparison of thermal deformation of the disc end faces with parameters in Table 2.1.

Excellent agreement is observed for the case of bulk absorption. The u_z for surface absorption also shows good agreement at the centre of the profile but deviates slightly towards the edges of the radial profile. As this variation is small and HV is less accurate towards the edge of the sample, the COMSOL model is considered verified for this geometry.

2.5.3 End-face deformation for long cylinder

The end face deformation for a rod sample using the FEM and HV models are plotted in Fig. 2.9.

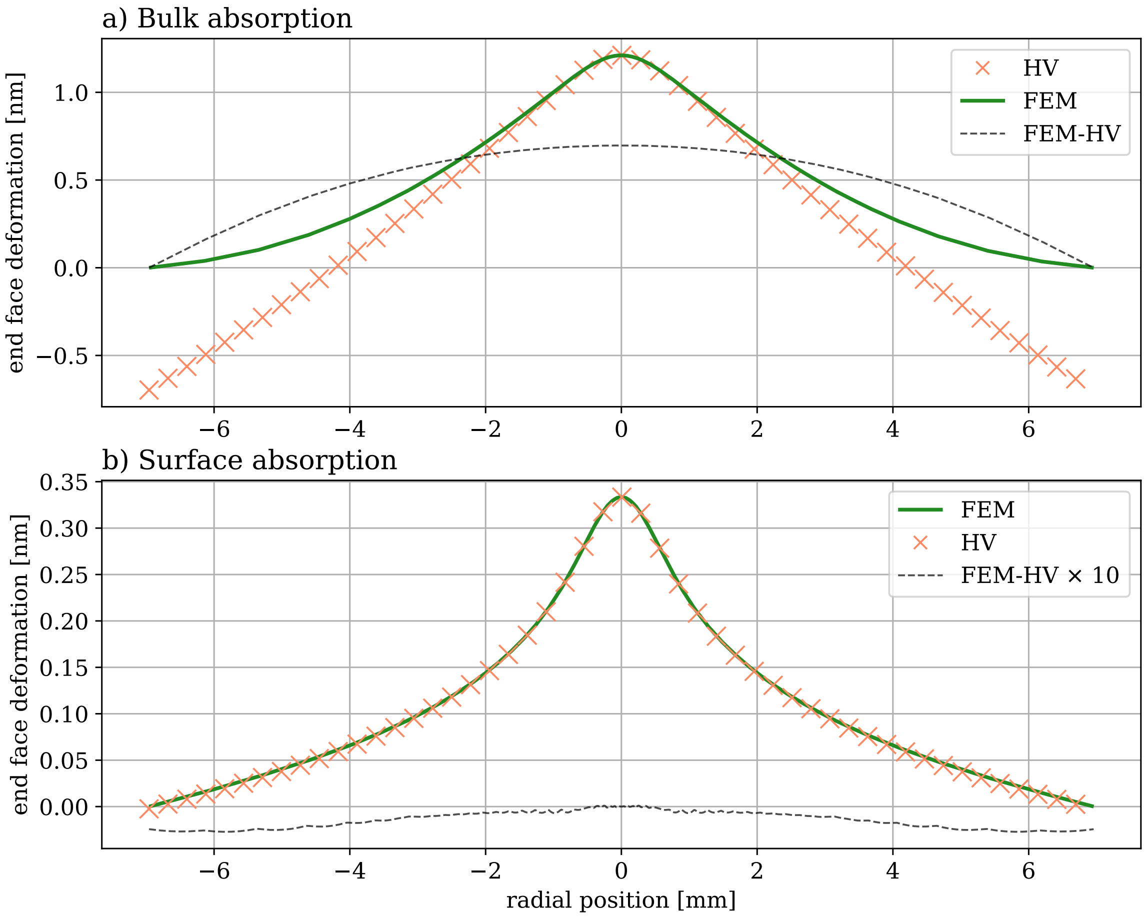

Fig. 2.9 Comparison of end face thermal expansion of a long cylinder using FEM and analytical techniques for (a) bulk absorption and (b) surface absorption. The deformation profiles of the FEM COMSOl model deviates significantly from HV towards the edges of the sample.

The HV and FEM predictions for the surface absorption induced, end face deformation are in good agreement as the heat load is concentrated on the surface and thus the deformation is largely unaffected by the bulk of a long sample. The prediction for the bulk absorption induced end face deformation, however, differ greatly. The large difference between the slopes of the deformation at the outer edge of the end face is particularly notable. The profile of the FEM prediction is consistent with that noted by others [44], [45] for the end face of the rod gain media. The difference is due to the σ_{rz} shear stresses produced as the centre of the sample tries to expand more than the cooler outer areas. These stresses are located mostly near the ends of the rod, modifying the surface deformation. It thus appears that the HV analysis used a "plane strain" approximation, which neglected these stresses.

I test this theory by considering samples with the same material parameters but varying lengths and plot the results in Fig. 2.10. It is thus apparent that the effects of the shear stresses are important if $h > 1.5a$.

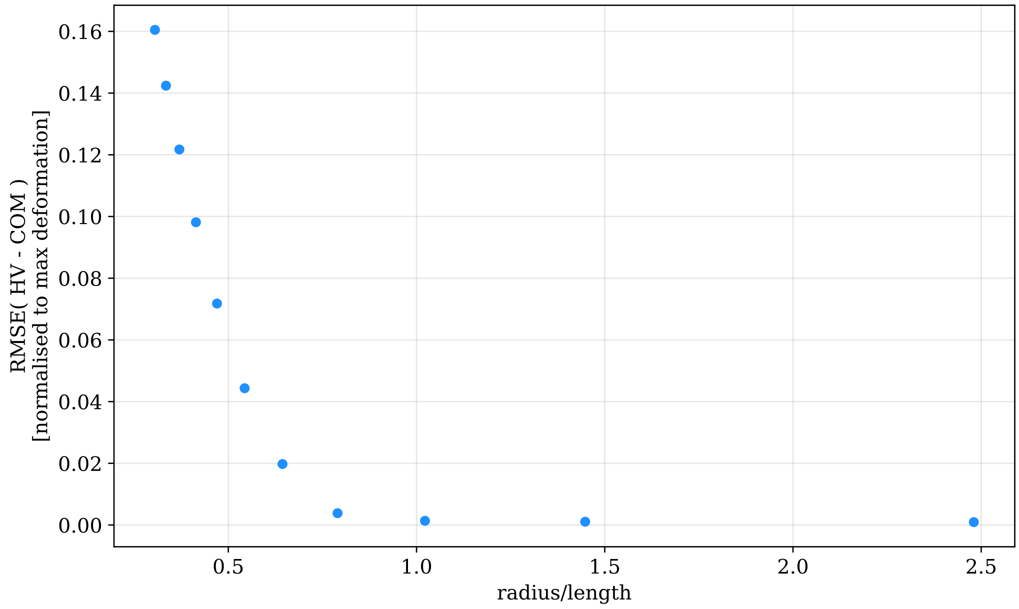

Fig. 2.10 Plot of RMSE difference between the HV and FEM end-face deformation models with increasing radius:length ratio, demonstrating large deviation between the COMSOL and HV models at the radius/length ratio decreases.

This requires us to use the FEM model as I often exploit the increase in wavefront deformation through a long sample to improve the signal to noise ratio of the measurement, as described further in the following chapters.

2.6 Summary

In this chapter the thermally induced physical changes due to the absorption of a Gaussian laser beam were analysed. The underlying physical causes for the dominant thermo-refractive and thermo-elastic effects, the temperature distribution and end face deformations, were focused on. The HV analytical model and an equivalent FEM model were described .

The FEM model was verified through comparison with the HV model for a thin disc sample, but showed deviations when modelling long cylinders, which I predict to be due to the HV model assumption ignoring shear stresses. The FEM is not limited by sample size as it iteratively solves the thermal boundary conditions at each point in the sample and does not use the same assumptions. However, this is at the cost of more time expensive calculations required for FEM than HV.

I have now shown a verified COMSOL model to determine physical changes in a range of samples. The next chapter considers how these effects deform a incident beam wavefront to allow the experimental wavefront deformation to be predicted and absorption to be inferred.

CHAPTER 3

DETERMINING ABSORPTION BY PREDICTING WAVEFRONT DISTORTION

3.1 Overview

The previous chapter presented a FEM of a sample heated via weak surface and bulk absorption of a pump beam propagating along its central z axis. The aim of this chapter is to describe how the FEM predicted temperature distributions, stress distributions and end-face deformations can be used to determine the absorption-induced wavefront distortion of an off-axis probe beam. The probe beam is incident on the sample at the angle θ_i such that it is displaced from the centre of the pump beam by the distance X_o, as shown in Fig. 3.1, and passes through the centre of the sample as shown in Fig. 3.2a and Fig. 3.2b.

The thermo-refractive (TR), thermo-elastic (TE) and elasto-optic (EO) contributions to the change in optical path length will be described in Sections 3.2.1, 3.2.2 and 3.2.3. The magnitude of each wavefront distortion will be compared in Section 3.3 and combined to produce a model for the total wavefront distortion.

Using the completed wavefront distortion model, I begin in Section 3.4 describing the least-squares fitting method used to determine the surface and bulk absorption and verifying that the analysis can correctly reproduce these values for modelled distortions. The effect of Gaussian noise on the fit is investigated in Section 3.5 and followed by methods to observe small surface absorption using different sample orientations and probe beam angles in Section 3.5.1.

The proposed system describes a method of determining absorption without calibration causing the best fit values to be highly dependant on the parameters used in the FEM. In Section 3.6 the effect of incorrect sample parameters is analysed and finally, the quality of fit to a model built with incorrect sample parameters is investigated as a method to determine the accuracy of the parameters.

3.2 Modelling thermally induced changes in optical path length

The total change in optical path length of the probe beam, ΔOPL, after passing through a heated sample is the sum of the TR, TE and EO effects and is given by,

$$\Delta\mathrm{OPL}_{tot}(x_h, y_h) = \Delta\mathrm{OPL}_{TE}(x_h, y_h) + \Delta\mathrm{OPL}_{TR}(x_h, y_h) + \Delta\mathrm{OPL}_{EO}(x_h, y_h) \tag{3.1}$$

where x_h,y_h are coordinates at the DHWS, and (0,0) corresponds to the ray that passes through the centre of the sample. The wavefront distortion due to each effect will be modelled individually and then combined to determine the total distortion using Equation (3.1).

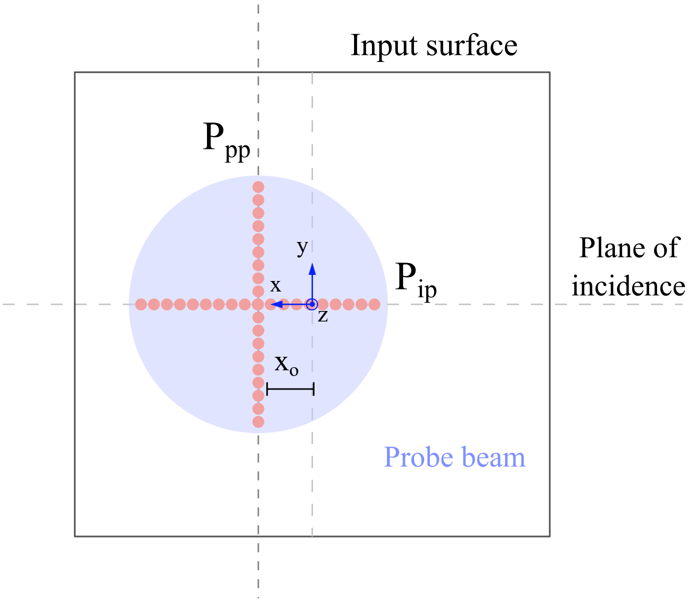

Fig. 3.1 The off-axis probe beam is incident on the sample, displaced from the centre of the face where the heating beam is incident, by a distance X_o. The wavefront will be modelled as rays propagating in the plane of incidence (P_{ip}) and in a plane perpendicular to the plane of incidence (P_{pp}), which are indicated as dots on the cross-sections of the probe beam.

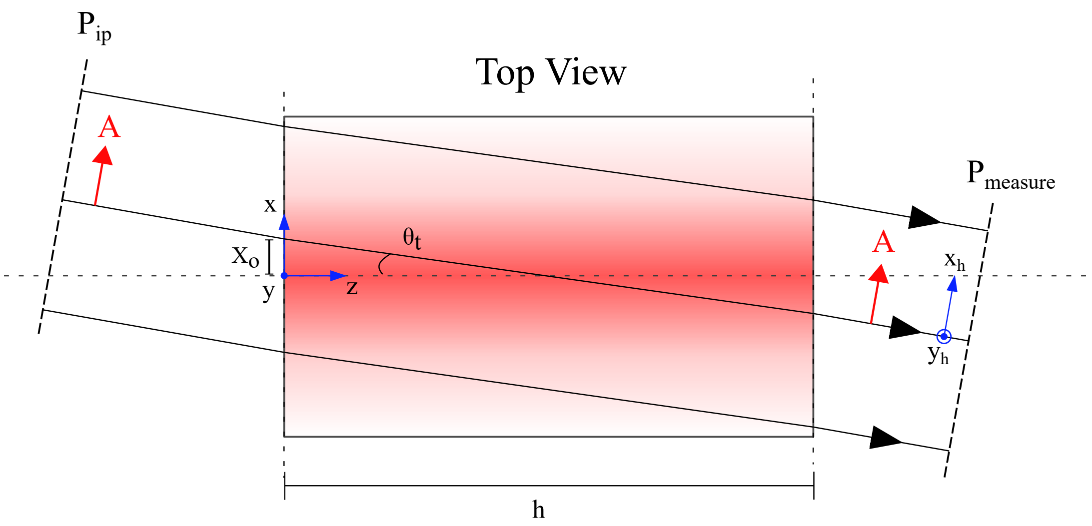

(a) Plane P$_{ip}$

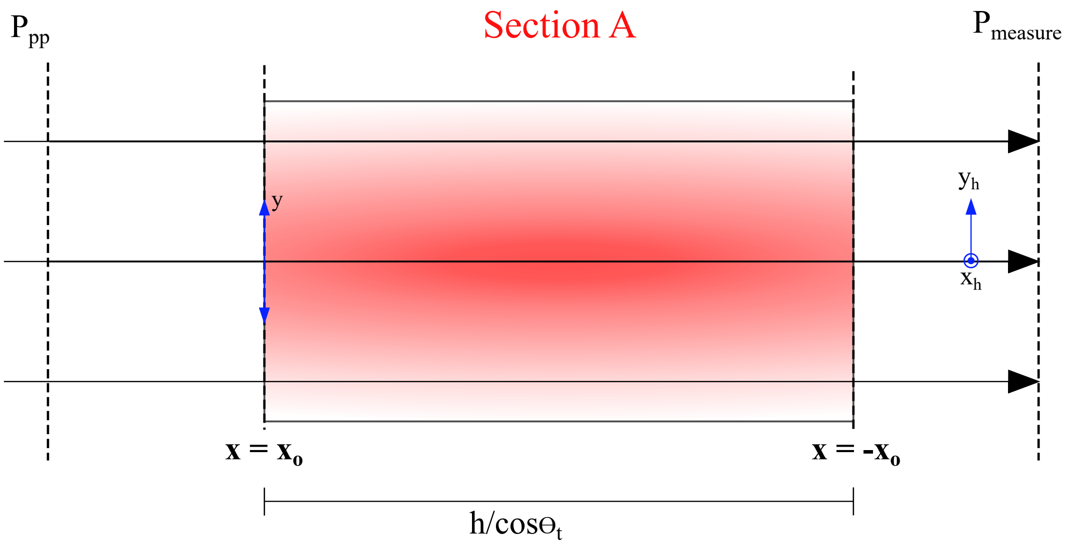

(b) Plane P$_{pp}$

Fig. 3.2 Schematic of the probe beam rays propagating through a sample heated along the z axis with a temperature distribution $T_0 + \Delta T(x,y,z)$ at angle θ_t in the planes P$_{ip}$ and P$_{pp}$.

The wavefront change is determined by calculating the change in optical path length of a set of probe beam rays propagating through the sample. In this analysis, I consider rays propagating in the plane of incidence (P_{ip}), and in a plane perpendicular to the plane of incidence (P_{pp}), rotated by θ_t about y axis, as shown in Fig. 3.2a and Fig. 3.2b. These rays have been selected as they experience the maximum and minimum ΔOPL due to the surface absorption, respectively. I model ΔOPL at the plane $P_{measure}(x_h, y_h)$, which is the projection of the distortion at output face of the sample onto the plane measured by the DHWS.

For a typical ZBLAN sample and pump beam with parameters listed in Table 3.1 and Table 2.2, the best-fit focal lengths for the TR thermal lens and TE end-face distortion were estimated to be 4000m and 258m, respectively, using the models below. As these are much larger than the sample length I assume the change in refraction of the rays as they enter and exit the sample and the refractive bending of the rays within the sample are negligible.

Parameter	**Symbol**	**Value**	**Unit**
Length	h	22.81	[mm]
Height	$2a_y$	13.96	[mm]
Width	$2a_x$	11.31	[mm]
Bulk Absorption Coefficient	α	50	[ppm cm^{-1}]
Surface Absorption Coefficient	β	3	[ppm]
Thermo-optic Coefficient	$\frac{dn}{dT}$	14.75	[10^{-6} K^{-1}]
Thermal Conductivity	K	0.628	[Wm^{-1} K^{-1}]
Density	ρ	4330	[kg m^{3}]
Specific Heat Capacity	C_p	151	[J K^{-1}]
Coefficient of Thermal Expansion	α_{exp}	17.2	[10^{-6} K^{-1}]
Poisson's Ratio	σ	0.17	-
Young's Modulus	Y	58.5	[GPa]
Surface Emissivity	ε	0.9	-
Ambient Temperature	T_0	293.15	K
Refractive index (@ 830 nm)	n	1.495	-

Table 3.1 Table of parameters for the FEM model for a rectangular ZBLAN sample.

The modelling in this chapter will continue to use $\alpha = 50\,\mathrm{ppm\,cm^{-1}}$ and $\beta = 3\,\mathrm{ppm}$, approximately the measured values for the ZBLAN sample in chapter 5, to closely model the experimental effects. However, to show the linearity of fitting will use $\alpha = 30\,\mathrm{ppm\,cm^{-1}}$ and β =1 ppm which chosen to show the model is linear over absorptions of the similar magnitude.

Below I describe the model techniques used for the TR, TE and EO effects before demonstrating the consolidated model which is fit to the experimental data to determine absorption coefficients in future chapters.

3.2.1 Thermo-refractive effect

The change in optical path length of a ray due to the TR effect (ΔOPL_{TR}) is calculated using the coordinate system and symbols shown in Fig. 3.2a and Fig. 3.2b, and the path integral,

$$\Delta OPL_{TR} = \frac{dn}{dT} \int_L \Delta T(\vec{r}_L(s))ds \tag{3.2}$$

where $\vec{r}_L(s)$ describes the path L of the ray, ΔT is the temperature change predicted by the FEM, and $\frac{dn}{dT}$ is the thermo-optic coefficient.

Since the refraction of the probe rays is negligible, the path L can be described by a straight line path as shown in Fig. 3.3. Thus,

$$\Delta OPL_{TR}(x_{out}, y_{out}) = \frac{1}{\cos\theta_t} \frac{dn}{dT} \int_0^h \Delta T(x_{out} + (h-z)\tan\theta_t, y_{out}, z)dz \tag{3.3}$$

where (x_{out}, y_{out}) is the location of the probe ray at the output face.

The $\Delta\mathrm{OPL}_{TR}$ in eq. (3.3) must be projected onto the plane normal to the probe beam and conjugate to the plane of the DHWS. The change in optical path length recorded at the DHWS is given by,

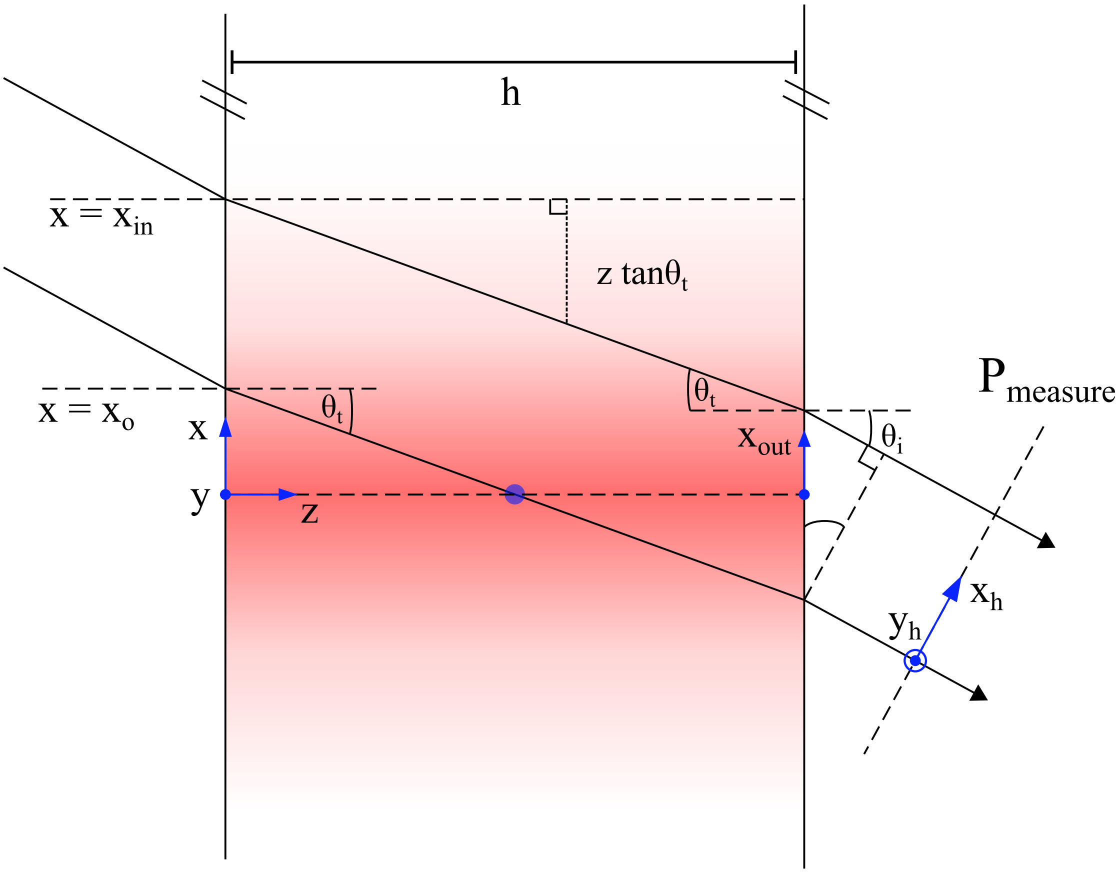

Fig. 3.3 Schematic of the path of rays through the temperature distribution of a sample in P_{ip}. The ray passing through the centre of the sample defines the origin in the plane of measurement $P_{measure}$.

$$\Delta\mathrm{OPL}_{TR}(x_h, y_h) = \Delta\mathrm{OPL}_{TR}(x_{out} + \frac{h}{2}\cos\theta_i, y_{out}) \tag{3.4}$$

A plot of the TR wavefront distortion modelled for the P_{ip} and P_{pp} rays using the FEM temperature distribution and parameters listed in Table 3.1 and Table 2.2 is shown in Fig. 3.4. $\Delta\mathrm{OPL}_{ip}$ has a slightly broader profile as a larger section of the probe beam intersects with the pump beam over the length of the sample, which increases with angle.

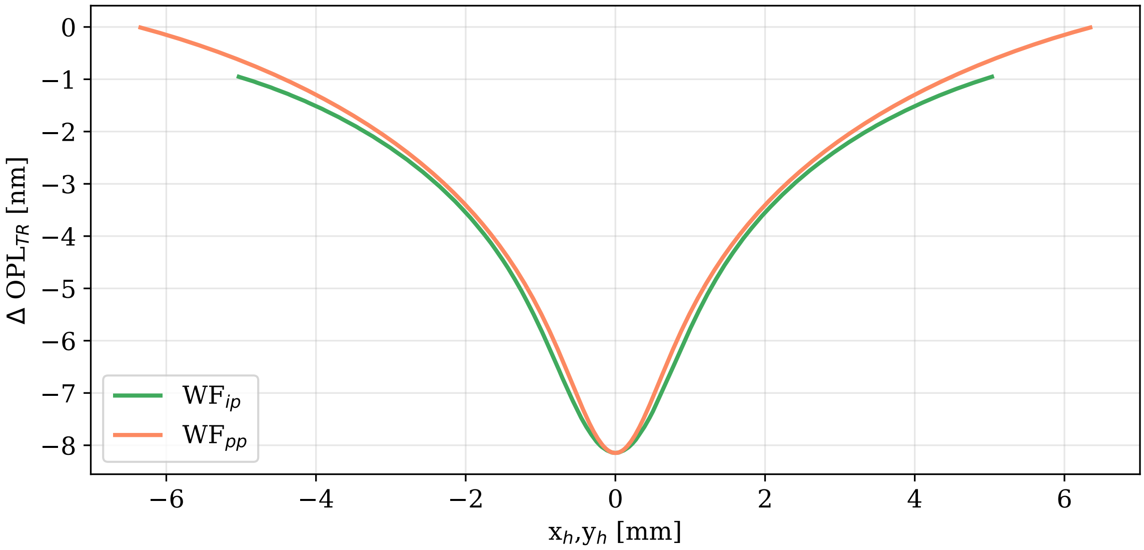

Fig. 3.4 Plot of optical path length change due to thermo-optic effect for the $P_{ip}(x_h)$ and $P_{pp}(y_h)$ rays using parameters given in Table 3.1 and Table 2.2 and θ_i =0.074 rad.

3.2.2 Thermo-elastic effect

The thermo-elastic (TE) effect results in bulging of the input and output faces, demonstrated in Fig. 3.5. Its magnitude scales with the thermo-expansion coefficient (α_{exp}) and can be negligible for low-loss, low expansion glasses such as fused silica. However, in glasses such as ZBLAN, α_{exp} is an order of magnitude larger and must be considered.

In response to the thermally-induced stress, the sample experiences a piston expansion along the z-axis and a non-uniform deformation (u_z) of the input and output faces. Both cause a change in the optical path length of the probe ray but only the effects of u_z are recorded by the DHWS as it is insensitive to piston wavefront change.

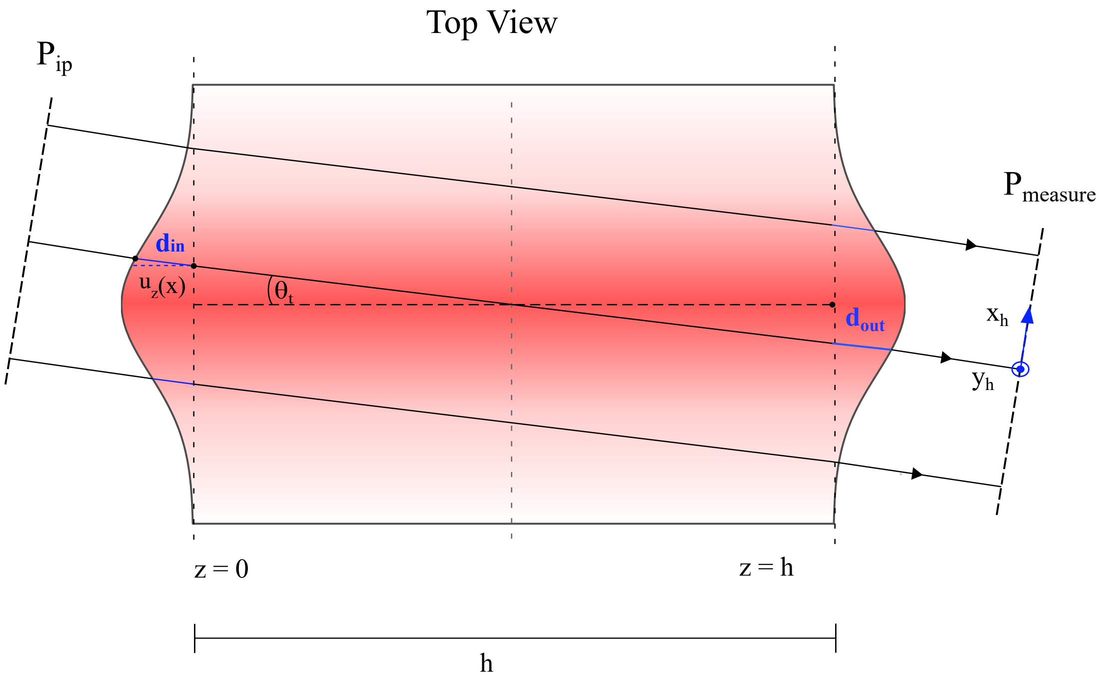

Fig. 3.5 Diagram showing the propagation of a P$_{ip}$ ray through the sample, demonstrating the additional distance (d_{in}, d_{out}) travelled through the deformed faces.

The ΔOPL_{TE} is given by,

$$\Delta\text{OPL}_{\text{TE}}(x_{out}, y_{out}) \approx (d_{in} + d_{out}) \times (n_s - n_{air}) \tag{3.5}$$

$$d_{in} = u_z(x_{out} + h\tan\theta_t, y_{out}, 0)/\cos(\theta_t) \tag{3.6}$$

$$d_{out} = u_z(x_{out}, y_{out}, h)/\cos(\theta_t) \tag{3.7}$$

This ΔOPL_{TE} is then projected onto the measurement plane using the transform in Equation (3.4).

The $\Delta\text{OPL}_{\ TE}$ for rays in the planes $\Delta\text{OPL}_{\ ip}$ and $\Delta\text{OPL}_{\ pp}$, with parameters in Table 3.1, Table 2.2 and $\theta_i = 0.074$ rad and $\theta_i = 0.284$ rad are plotted in Fig. 3.6. A contour map of the predicted wavefront distortion with $\theta_i = 0.284$ rad is also shown.

ΔOPL_{ip} is broader than ΔOPL_{pp} as rays on different sides of the centre of the probe beam in P_{ip} pass through the maximum surface displacements on each face. At larger angles this results in the separation of the deformation due to the input and output surfaces.

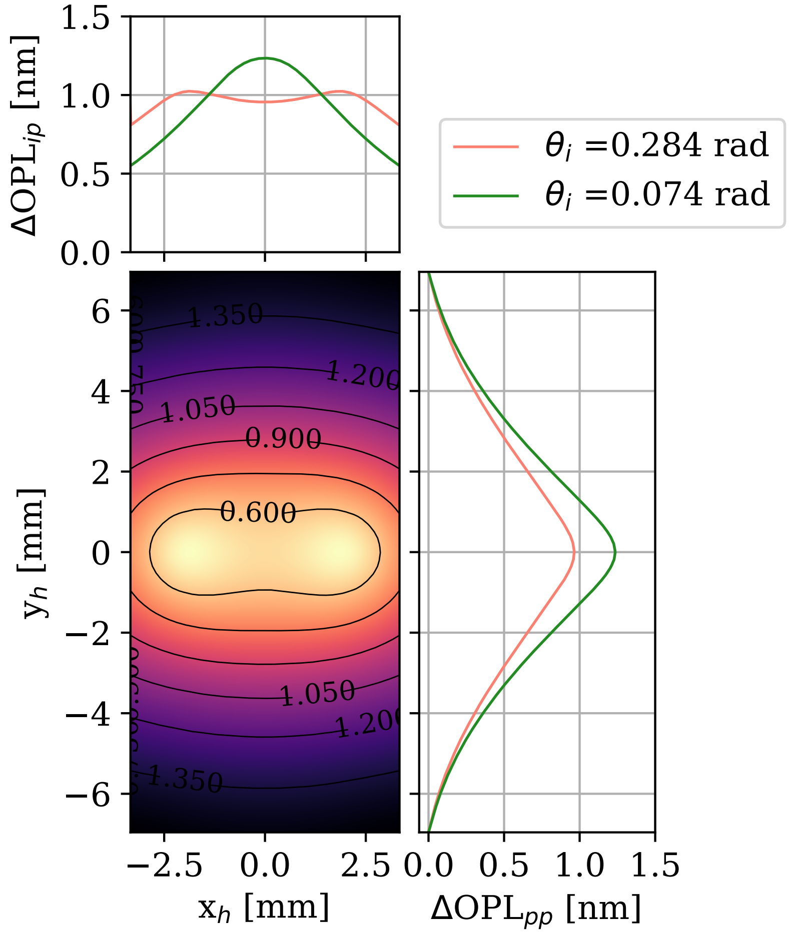

Fig. 3.6 Contour plot of $\Delta\mathrm{OPL}_{TE}$ calculated at the output face for ZBLAN parameters listed in Table 3.1 and Table 2.2 and $\theta_i = 0.284$ rad. Above and to the right $\Delta\mathrm{OPL}_{ip}$ and $\Delta\mathrm{OPL}_{pp}$ are shown for the cases $\theta_i = 0.074$ rad and $\theta_i = 0.284$ rad. Limits of the figure are given by the clear aperture when $\theta_i = 0.284$ rad.

3.2.3 Elasto-optic effect

The elasto-optic effect, or photo-elastic effect, describes the change in permittivity, and thus refractive index, due to an applied stress which typically results in stress-induced birefringence. In this case I am considering the thermally-induced stress due to the pump beam absorption within the test sample which leads to an additional change in optical path length, $\Delta\mathrm{OPL}_{EO}$.

The calculation of $\Delta\mathrm{OPL}_{EO}$ used the stress tensor predicted by the FEM and is described in detail in Appendix B. Briefly, it includes the following steps:

- Rotate the stress tensor distribution from the FEM by angle θ_t about the y-axis.
- Apply principal component analysis to determine the direction of the principal axes and their refractive index at each node.
- Construct the index ellipsoid at each node.
- Calculate the refractive index for s and p-polarised input light.
- Calculate ΔOPL_{EO} using Jones calculus for both s and p-polarised input light, assuming the SLED is 50:50 polarised.

The resulting ΔOPL_{EO} assuming $\theta_t = 0.074$ rad and the material and beam parameters in Tables 3.1 and 2.2, are plotted in Fig. 3.7.

The ΔOPL_{EO} is 2 orders of magnitude smaller than the other effects. Thus, it is apparent that ΔOPL_{EO} is negligible in ZBLAN, as was observed by Matusita *et al.* [46]. Consequently, as it falls below the DHWS sensitivity it will be ignored in further modelling.

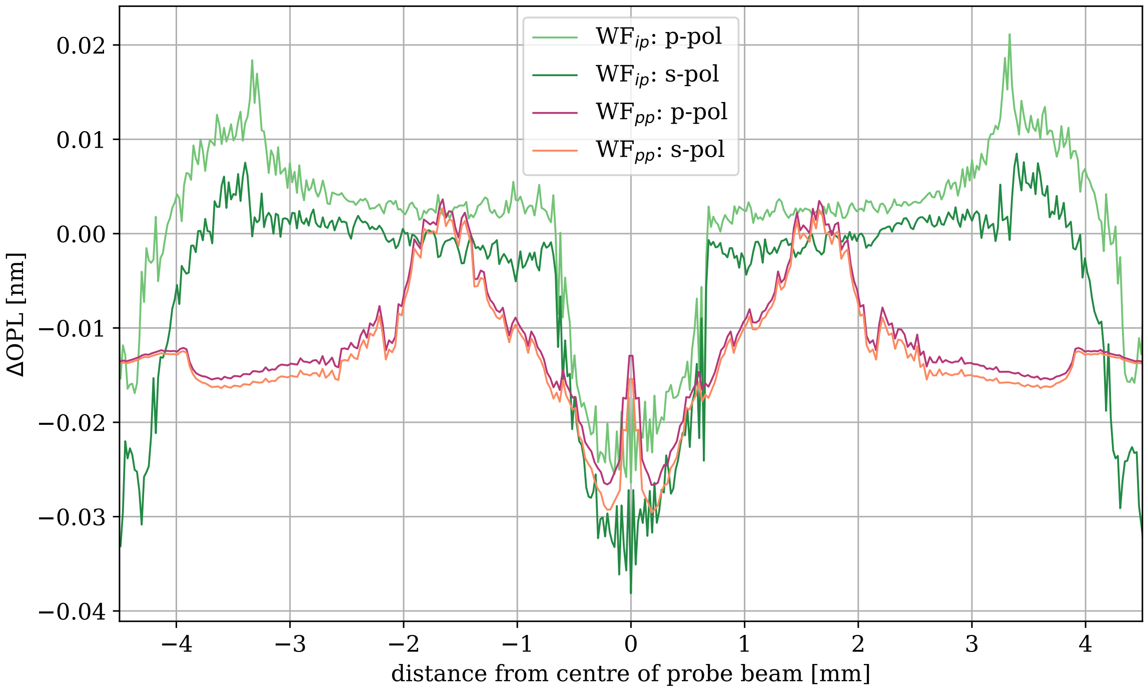

Fig. 3.7 Plot showing ΔOPL_{EO} for both slices of interest WF_{ip} in green and WF_{pp} in pink, the final ΔOPL of the s and p polarisation components is shown for the case where $\theta = 0.074$ rad and $\alpha = 50\,\text{ppm}\,\text{cm}^{-1}$.

3.3 Predicted total in change in optical path length for ZBLAN

The wavefront distortion measured by the DHWS is the sum of each of the thermal effects. As stated above due to the sensitivity of the camera this can be defined as is the sum of ΔOPL_{TR} and ΔOPL_{TE}, excluding ΔOPL_{EO}. Below I will demonstrate the variation between ΔOPL_{ip} and ΔOPL_{pp} due to each effect and the effect of angle on the total optical path length change.

The ΔOPL_{TR} and ΔOPL_{TE} for $\theta = 0.074$ rad and parameters from Table 3.1 and Table 2.2 are plotted in Fig. 3.8 where $\alpha = 50\ \text{ppm}\,\text{cm}^{-1}$. Note that TR and TE contributions have opposite signs for ZBLAN due to the negative thermo-optic coefficient reducing the overall magnitude of the ΔOPL. Additionally, the shape of ΔOPL_{total} in the ip and pp planes are different due to the use off-axis probe beam.

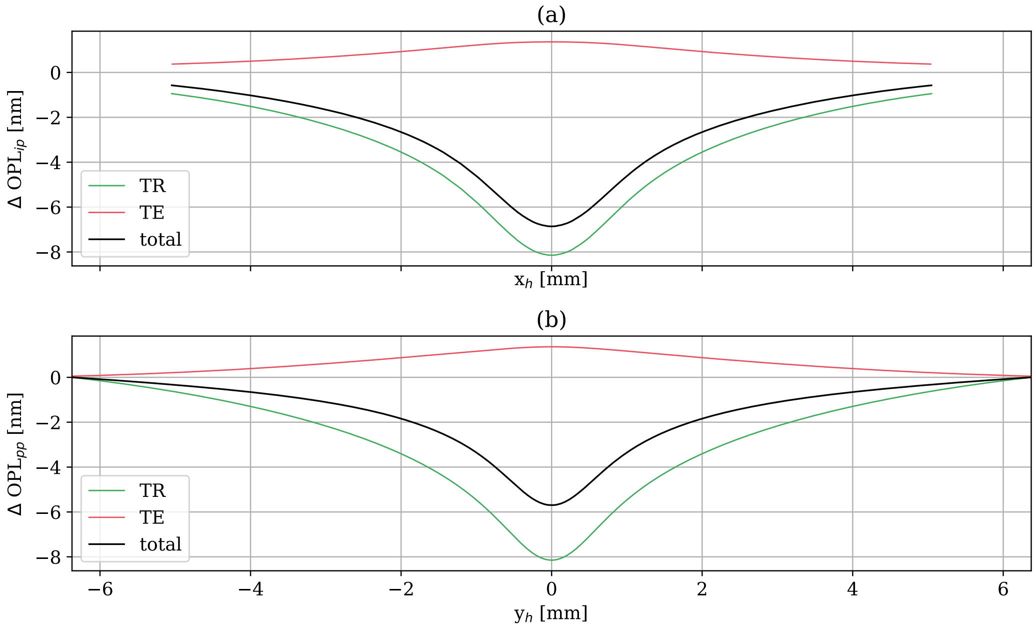

Fig. 3.8 Plots of modelled total ΔOPL for (a) P_{ip} and (b) P_{pp} for $\theta_i = 0.074$. This demonstrates the opposing TR and TE effects and that the former is the dominate effect for a ZBLAN sample of this geometry. The range of plots is limited by the clear aperture.

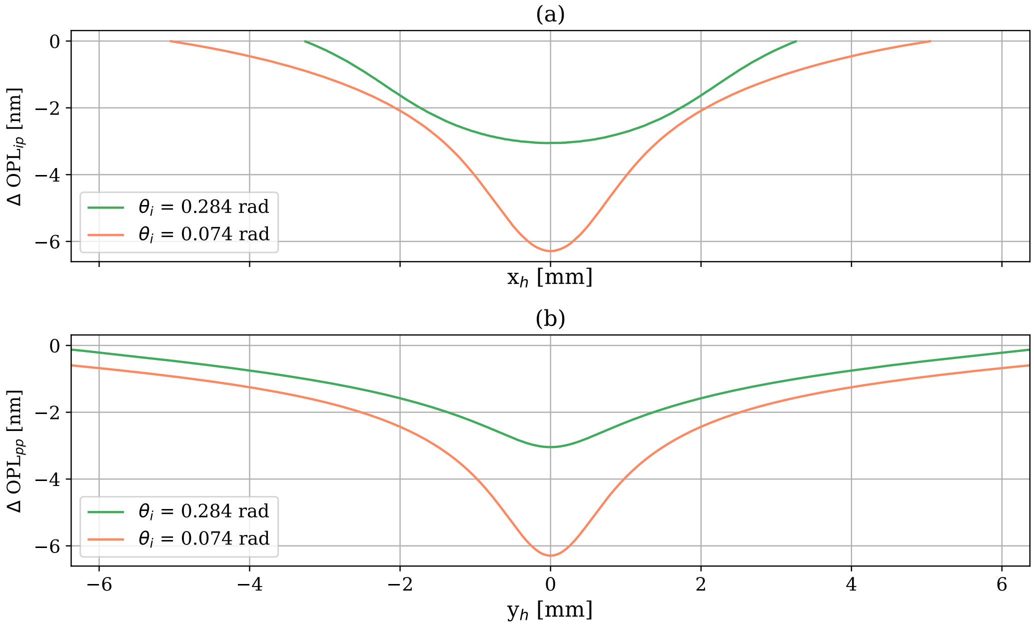

Fig. 3.9 The profile of the predicted (a) ΔOPL$_{ip}$ and (b) ΔOPL$_{pp}$ for the bulk absorption contribution to the wavefront distortion is highly dependant on θ_i. At small angles, $\theta = 0.074$ rad, the centre of the beam is most deformed as it passes through the highest temperatures section of the sample and deformed end sections, whereas, at larger angles,$\theta = 0.284$ rad, these effects are spread across the P$_{ip}$ slice of the probe beam. The range of plots is limited by the clear aperture.

The profile of the bulk absorption contribution to the distortion is affected by the angle of incidence as demonstrated in Fig. 3.9 by comparing ΔOPL$_{ip}$ and ΔOPL$_{pp}$ using $\theta = 0.074$ rad and $\theta = 0.284$ rad. Increasing the angle, causes the probe beam to be incident on the front surface further from the pump beam. The magnitude of the WF$_{pp}$ slice is decreased but the profile is largely unchanged as the same section of the probe beam passes through the highest temperature throughout the sample. At large angles more of the rays in P$_{ip}$ cross the axis of heating along the length of the sample causing the TR aberration to be distributed across x_h, shown in Fig. 3.2a. Additionally, the rays which pass through the largest end face deformation are separated by a greater distance. Consequently, both slices of the wavefront experience a reduced maximum distortion at larger angles and the ΔOPL$_{ip}$ has a distinct and much broader profile at larger angles.

The change in profile of ΔOPL$_{ip}$ is much more significant for surface absorption, showing two distinct peaks as the effects are localised at the surfaces, as shown in Fig. 3.10.

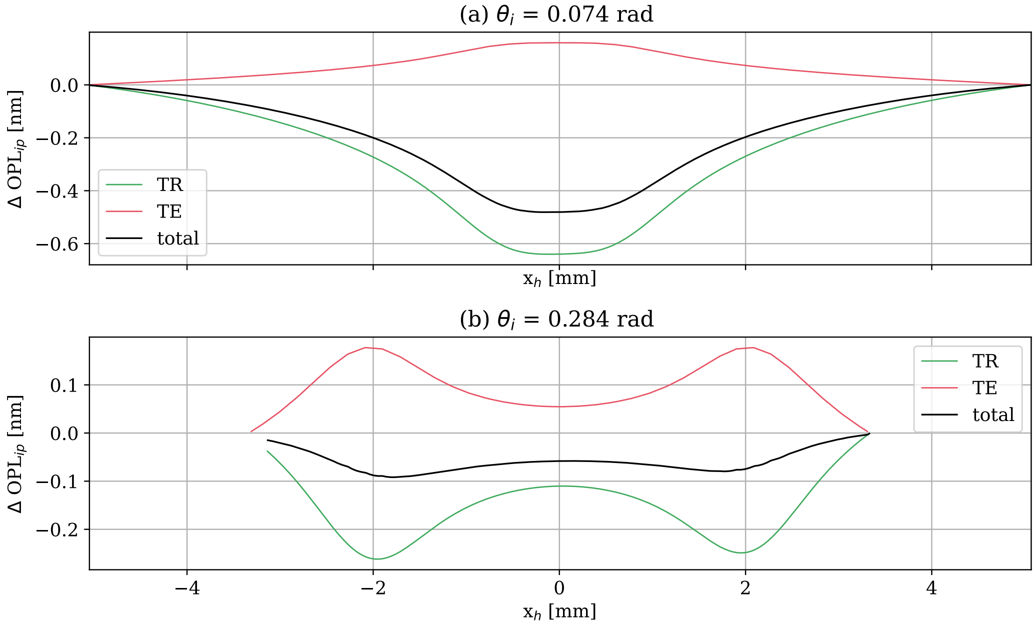

Fig. 3.10 The profile of the predicted wavefront distortion in P$_{ip}$ due to the TE and TR caused by $\beta = 3$ ppm surface absorption is dependant on θ_i, demonstrated for θ_i = 0.074 rad (a) and θ_i = 0.284 rad. The model uses parameters from Table 3.1 and Table 2.1.

By comparing Fig. 3.9 and Fig. 3.10 it can be observed that distortion due to surface and bulk absorption coefficients at larger angles are distinct from one another. This will allow the component of distortion due to surface absorption to be discerned from that due to bulk absorption during fitting, which will be described in detail in Section 3.5.1.

For both bulk and surface absorption, the overall wavefront deformation for ZBLAN is reduced due to the opposing TE and TR effects, decreasing the SNR, as shown in Fig. 3.8 and Fig. 3.10. The reduction in signal will reduce the smallest absorption coefficients that could be measured. To maximise the measurable wavefront distortion longer samples could be used as ΔOPL_{TR} would increase while ΔOPL_{TE} would not change significantly as shown in Fig. 3.11.

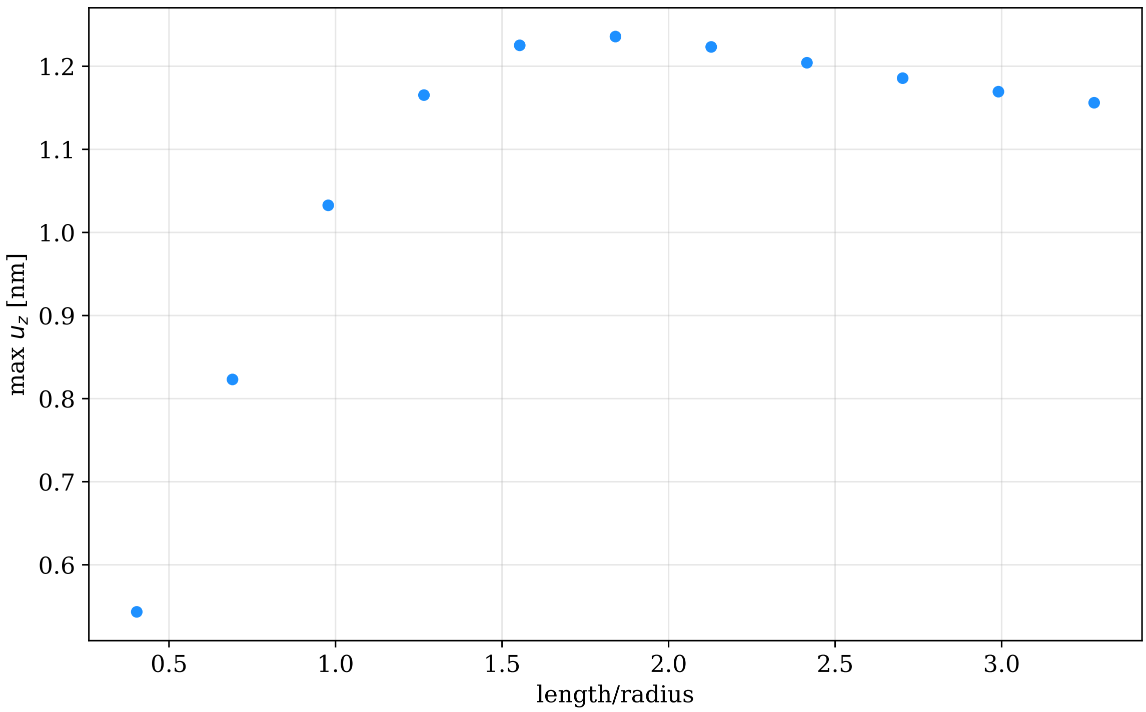

Fig. 3.11 The maximum TE distortion of a probe beam through a sample of length h initially increases as h is increased. However, as the h approaches the radius of the sample the maximum distortion begins to decrease as a greater amount of stress is required to deform the end surfaces at greater distances.

3.4 Determining α and β

The sample α and β values are determined using an ordinary least-squares fit process, comparing the wavefront change measured by the DHWS to that predicted by the FEM for any angle of incidence. The accuracy depends on the assumption that the measurement system and model parameters are correct and that α and β are homogenous across the sample.

The least-squares fit process is:

1. Determine the origin of the (x_h, y_h) coordinate system by fitting Gaussian wavefront shapes to the semi-major (P_{ip}) and semi-minor (P_{pp}) cross-sections of the measured wavefront.

2. Determine the measured $\Delta\mathrm{OPL}(x_h)$ and $\Delta\mathrm{OPL}(y_h)$.

3. Calculate the least-squares best-fit absorption coefficients α_{bf} and β_{bf} values using,

$$\begin{aligned}\chi^2(\alpha,\beta,c) \quad &= \sum[(\text{predicted } \Delta\text{OPL}_{ip}(\alpha,\beta,x_h)+c)-\text{measured } \Delta\text{OPL}_{ip}(x_h)]^2 \\ &+[(\text{predicted } \Delta\text{OPL}_{pp}(\alpha,\beta,y_h)+c)-\text{measured } \Delta\text{OPL}_{pp}(y_h)]^2\end{aligned} \tag{3.8}$$

where c is an arbitrary constant (as DHWS doesn't detect piston and noise can cause the wavefront deformation to be shifted) and $\Delta\text{OPL}_{ip}(\alpha,\beta,x_h)$ and $\Delta\text{OPL}_{pp}(\alpha,\beta,y_h)$ are calculated assuming linearity, using

$$\begin{aligned}\Delta\text{OPL}(\alpha,\beta) \quad &= [\Delta\text{OPL}_{TR\,bulk}+\Delta\text{OPL}_{TE\,bulk}](\alpha/50\text{ppm cm}^{-1}) \\ &+[\Delta\text{OPL}_{TR\,surf}+\Delta\text{OPL}_{TE\,surf}](\beta/3\text{ppm})\end{aligned} \tag{3.9}$$

Linearity was confirmed by:

- Calculating the total bulk and surface contributions for $\Delta\text{OPL}(50,3)$ and $\Delta\text{OPL}(30,1)$ using the FEM with Table 2.2 and Table 3.1.
- Using Equation 3.9 and $\Delta\text{OPL}(50,3)$ to calculated the extrapolated values for $\Delta\text{OPL}(30,1)$.
- Comparing the FEM and extrapolated values of $\Delta\text{OPL}(30,1)$

The normalised differences are 6 and 9 orders of magnitude smaller than the wavefront distortion (WFD) for surface and bulk absorption, respectively, as shown in Fig. 3.12.

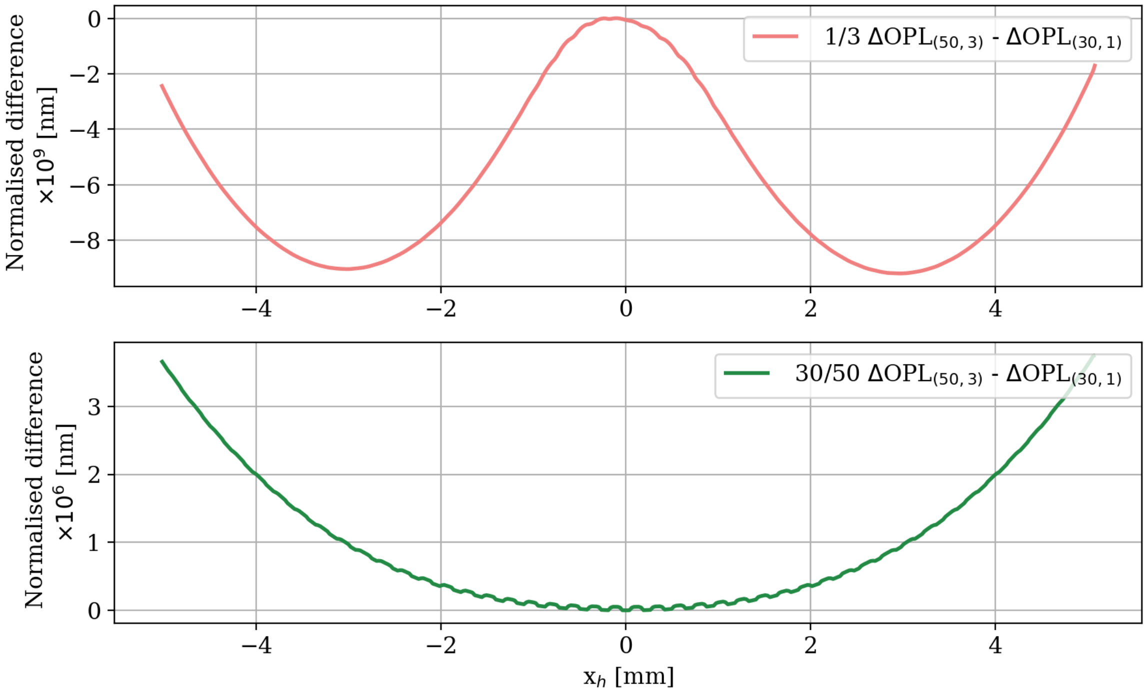

Fig. 3.12 Plot of the normalised differences between the FEM and extrapolated $\Delta\mathrm{OPL}(30,1)$ values, demonstrating that the WFD where $\alpha = 30\mathrm{ppm\,cm}^{-1}$ and $\beta = 1\mathrm{ppm}$ calculated using FEM is equivalent to that calculated using Equation 3.9.

The relative error in the parameters determined by the least-squares fit are given by the square root of the diagonal of the covariance matrix, which provides a relative variance of each estimated parameter [47]. As α, β, c is fit for, a vector of $(\sigma_\alpha, \sigma_\beta, \sigma_c)$ is returned. This allows the quality of fit for the given parameter to be determined.

This fitting process was tested by generating and fitting to $\Delta\mathrm{OPL}(50,3)$ using the parameters from Table 3.1 and Table 2.2 and $\theta_i = 0.074$ rad. To replicate the size of the probe beam used in the measurement system a modelled wavefront with 5mm diameter was used. As expected, the method outlined above yielded $\alpha = 50.00\,\mathrm{ppm\,cm}^{-1}$ and $\beta = 3.00\,\mathrm{ppm}$.

3.5 Effect of measurement noise on least-squares fit

I have shown that this fitting method is able to return the α and β used in the model. However, weakly absorbing samples produce very small wavefront deformations which can approach the noise floor of the DHWS. The effect of measurement noise on the least-squares fit to the total wavefront distortion was investigated by adding noise, informed by the DHWS noise floor, to the predicted ΔOPL. The following procedure was used:

- Measure the fluctuations in the local wavefront gradients between 2 subsequent sets of 1000 averaged frames taken on the DHWS, the number of averages used in the experimental procedure (see Section 4.5). A normal distribution with $\bar{x} = 0$ nrad and $\sigma_x = 0.083$ nrad was yielded.
- Calculate the noise gradients at each point of the probe wavefront by sampling from a normal distribution using $\bar{x}$ and σ_x.
- Numerically integrate the noise gradients using the same code as for experimental gradients to create a 2D noise map.
- Cross-sections of noise wavefront were added to predicted $\Delta\mathrm{OPL}_{ip}$ and $\Delta\mathrm{OPL}_{pp}$.

Plots of a typical measured and modelled noise floor and wavefront cross section are shown in Fig. 3.13 and Fig. 3.14. In both cases $\theta_i = 0.074$ rad and the modelled noise assumes $\alpha = 50\,\mathrm{ppm\,cm^{-1}}$ and $\beta = 0$ using parameters from Table 3.1 and Table 2.2. On visual inspection the noise appears to be accurately described by the process above, but some difference should be expected as a nominal α and β are used for the model.

The effect of the noise on the least-squares fit process was investigated by generating 1000 random noise floors, which were added to a FEM wavefront distortion for which $\alpha = 50\,\mathrm{ppm\,cm^{-1}}$ $\beta = 0$ppm and determining the best-fit α. The average α was $50.03\,\mathrm{ppm\,cm^{-1}}$ with a standard error of $0.02\,\mathrm{ppm\,cm^{-1}}$, shown in Fig. 3.15.

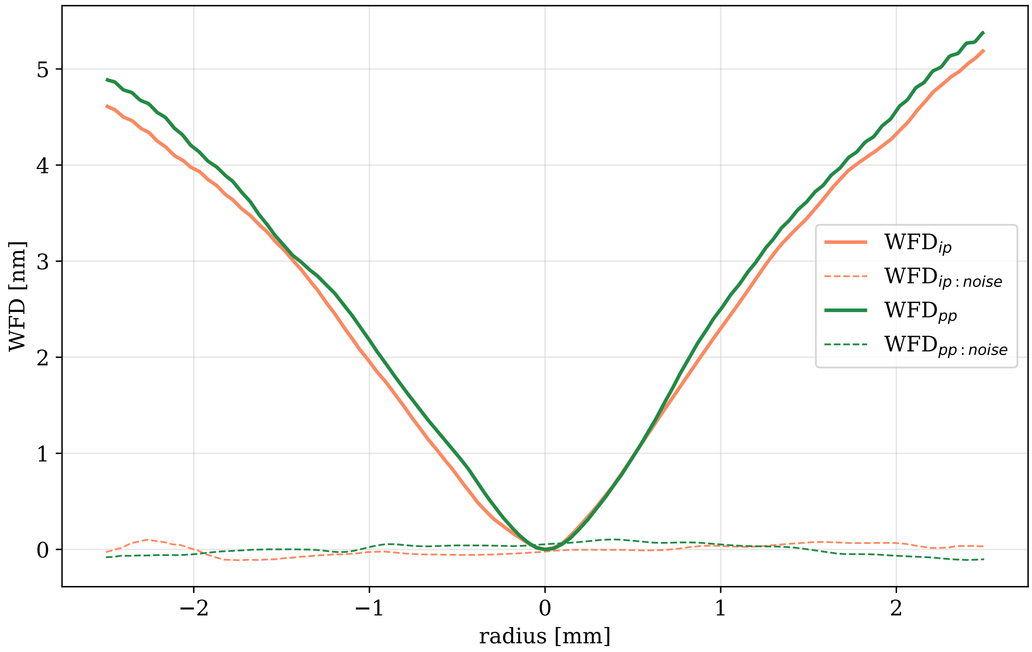

Fig. 3.13 Plot of measured wavefront deformation in ZBLAN and noise floor using system described in chapter 4.

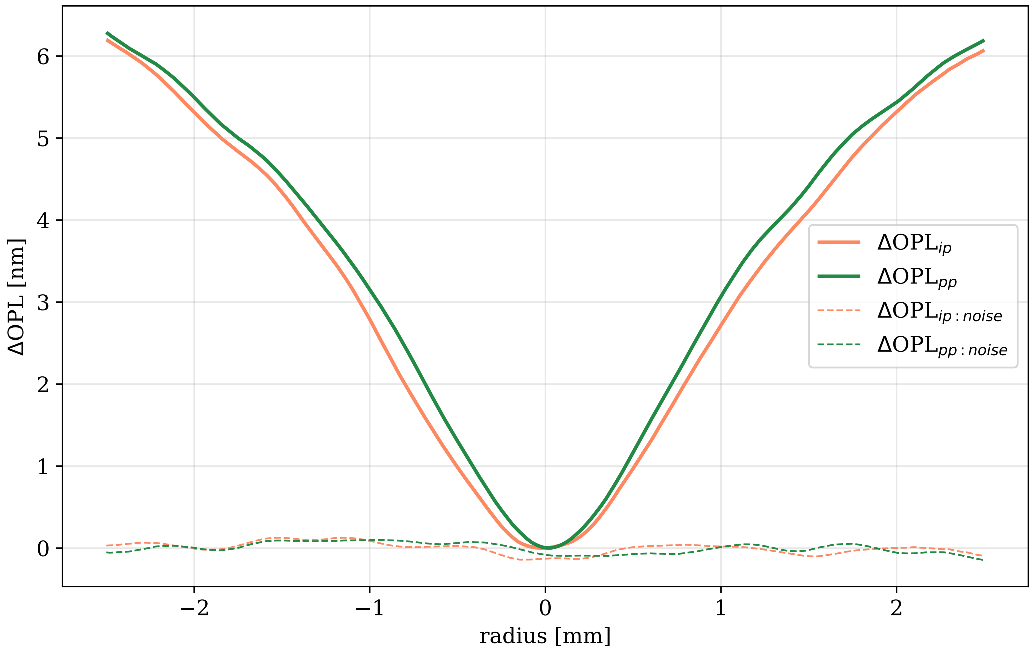

Fig. 3.14 Plot of simulated wavefront deformation with Gaussian noise where $\sigma = 0.083$ nrad and $\bar{x} = 0$ nrad.

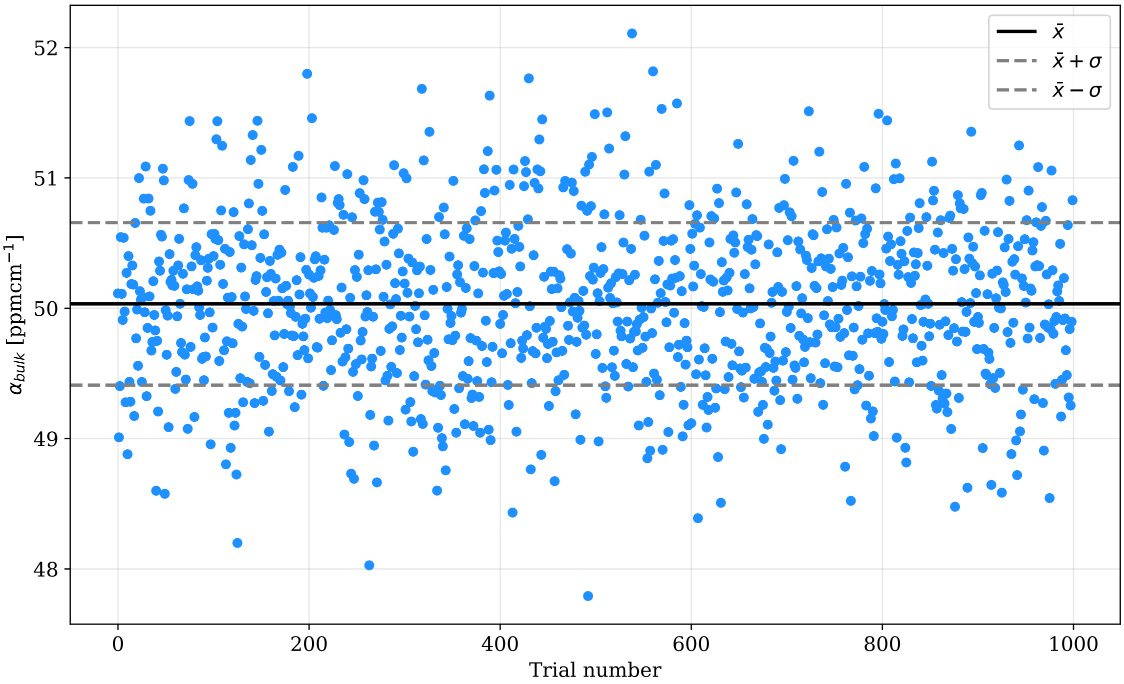

Fig. 3.15 Plot of best-fit α for a FEM model with $\beta = 0$ ppm and $\alpha = 50\,\mathrm{ppm\,cm^{-1}}$ and added noise. 1000 iterations were completed to demonstrate the random fluctuation of the best fit α.

This process was repeated with 3 ppm of surface absorption added to the model and fitting now for α and β. A 2D histogram contour of the best fit α and β is plotted in Fig. 3.16 for the case where $\theta_i = 0.074$ rad.

While most of the best-fit α values were close to the correct value ($50\,\mathrm{ppm\,cm^{-1}}$), usually corresponding to a negligible value for β, surface absorption was sometimes over estimated by up to 2000%. In this case α is underestimated by up to 30%. Thus, allowing the least-squares fit to determine the best-fit β when the surface induced WFD is similar to the measurement noise floor can produce very large errors.

The best-fit α for this data assuming that $\beta = 0$ are plotted in Fig. 3.17 , which has a mean of $50.7\,\mathrm{ppm\,cm^{-1}}$. While this value is offset from the correct value, the difference is less than the magnitude of β due to the use of an off-axis angle probe beam.

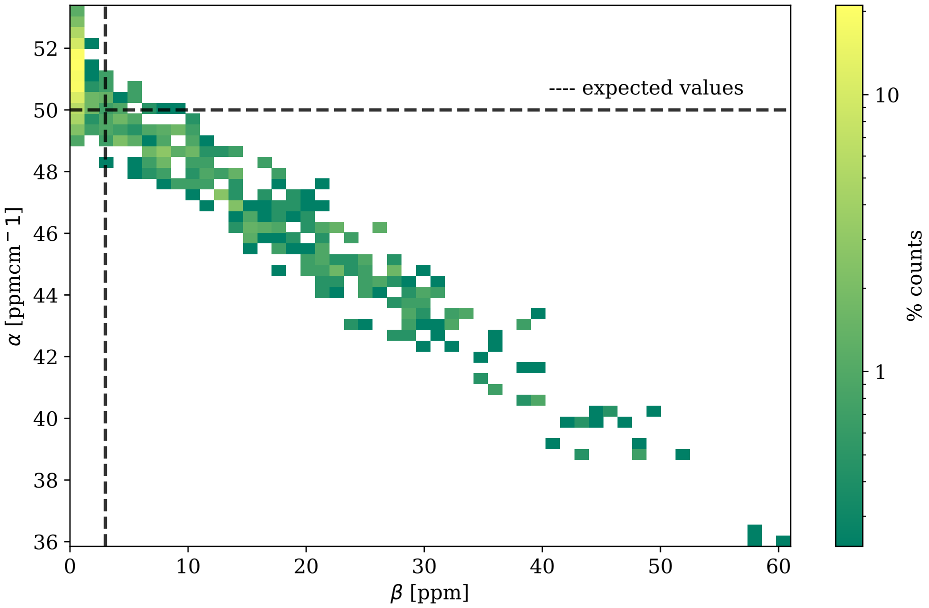

Fig. 3.16 2D histogram showing distribution of fitted values of bulk and surface absorption to FEM wavefront with simulated experimental noise using $\theta_i = 0.074$ rad.

The reduction in variation suggests that when surface and noise effects are a similar magnitude, fitting for just bulk absorption produces a more consistent solution but induces a systematic increase in α. Alternatively, increasing the angle of incidence causes the distortion of the probe beam to be more distinct and better constrains the least-square fit, as shown in Fig. 3.18 for which the average $\alpha = 50.00$ ppm cm^{-1} and $\beta = 3.33$ ppm. These values vary within a range of 5% and 160%, respectively, which is dramatically reduced from small angles.

Thus, the most effective method to extract surface absorption is to measure the sample using a large off-axis angle. However, large angles might not be viable for certain sample geometries due to clipping of the probe beam on the sample edges and the reduction in signal size as the probe beam passes through less of the heated area in the sample. I discuss below another method for determining surface absorption by considering the profile of the induced distortion for different sample/angle orientations and in the P_{ip} and P_{pp} cross-sections.

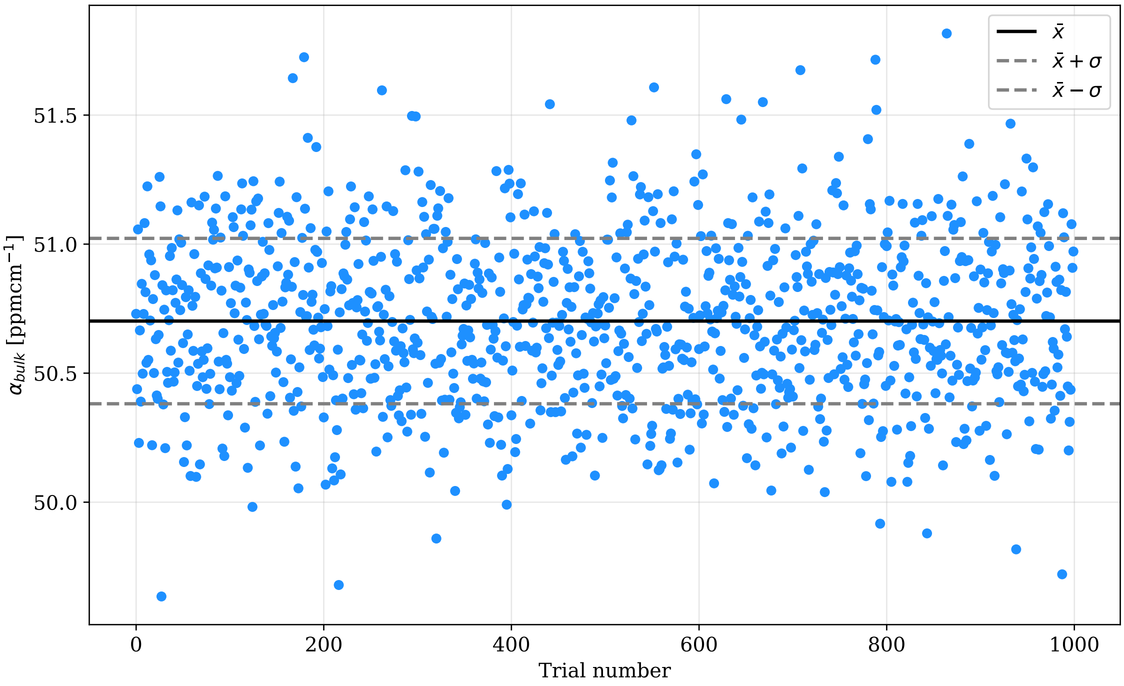

Fig. 3.17 Plot of α of 1000 iterations of fitting to a model where $\beta = 0$ ppm and $\alpha = 50\,\mathrm{ppm\,cm^{-1}}$ with random noise added to the wavefront deformation, demonstrating the random fluctuation of the best fit α.

3.5.1 Extracting surface absorption with low SNR

If surface absorption is incorrectly assumed to be negligible then the best-fit α deviates from the true value by an amount dependant on how a sample is being probed. This difference could be decreased by using a longer sample with the same probe beam offset as this would increase the WFD due to bulk absorption without changing that due to surface absorption. Increasing the angle of incidence would decrease the magnitude of the effects of surface absorption as the passage of the probe beam through the sample would be less affected by surface heating. Additionally, it would create a larger difference between the $\Delta\mathrm{OPL}_{pp}$ and $\Delta\mathrm{OPL}_{ip}$, which would yield incorrect best-fit α values unless the best-fit β value was correct, as discussed below.

Consider the three cases in Fig. 3.19, in which the orientation of the sample and/or probe beam angle is varied for a sample of dimensions given in Table 3.1. In case 1 the initial layout is replicated, where the sample is heated along its longest axis h and the probe beam is at a small angle of incidence, 0.074 rad. Case 2 has the sample rotated such that the heating

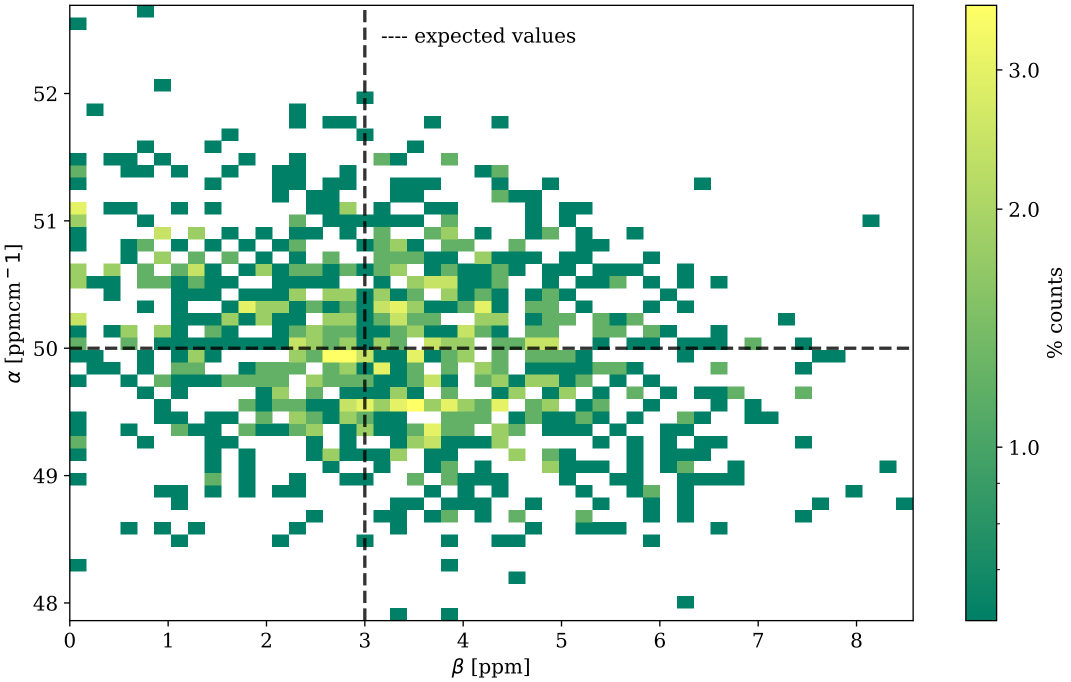

Fig. 3.18 2D histogram showing distribution of fitted values of bulk and surface absorption to FEM wavefront and simulated noise where $\theta_i = 0.284$ rad.

axis is along the 11.3 mm length. Finally, case 3 modifies case 2 by increasing angle of incidence to 0.284 rad.

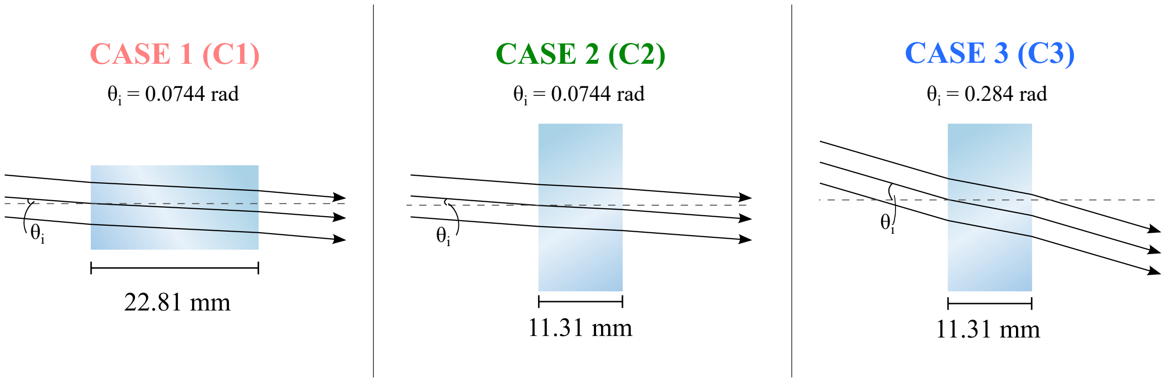

Fig. 3.19 Schematic of the three cases of sample orientation and angles of incidence of the probe beam that will be used to investigate the effects of surface absorption.

For each case a FEM wavefront was generated where α =50 ppm cm^{-1} and β=3 ppm. A best-fit α was then calculated for β in the range $\beta \in [0,10]$ ppm. The best-fit α was determined for each slice and for the combined fit and the results are shown in Fig. 3.20. As expected there is a linear relationship between α and β for each case and slice and all lines intersect at the expected values α =50 ppm cm^{-1} and β=3 ppm.

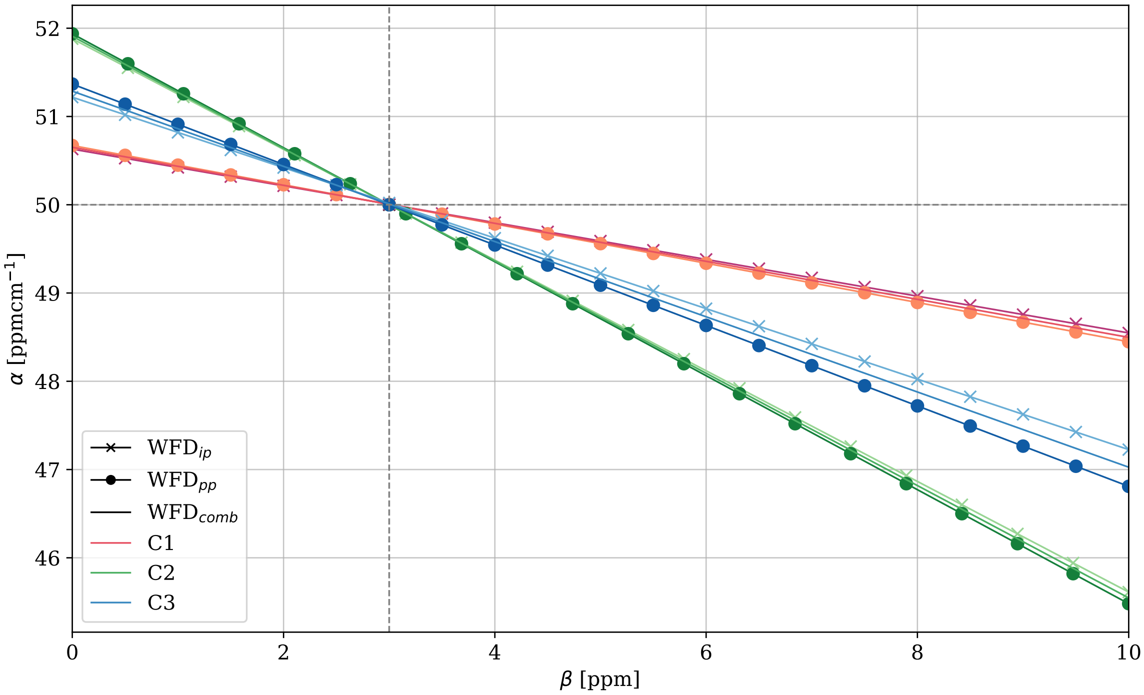

Fig. 3.20 The best-fit α values plotted as a function of the assumed β value for each slice independently and for the combined fit. All lines intersect at the β and α used in the FEM.

Thus, assuming a good SNR, the surface absorption could be determined using one measurement by finding where $\alpha_{ip} = \alpha_{pp}$. Case 3 would be the best orientation for this measurement as the greatest differences are observed due to the large angle of incidence. Alternatively, using two angles of incidence and requiring that the best-fit α and β values agree could improve the estimate of the surface absorption. The quality of the fit could also be used to determine the correct beta value, as shown in Fig. 3.21. In each case, P$_{ip}$ has the greatest sensitivity to an incorrect β value, as the effect of surface absorption is more apparent in that slice and is less amenable to an incorrect value of α. This is the result of the ΔOPL$_{ip,surf}$ shape being more distinct from the ΔOPL$_{ip,bulk}$ and thus, it can't be as strongly attributed to α as for ΔOPL$_{pp,surf}$.

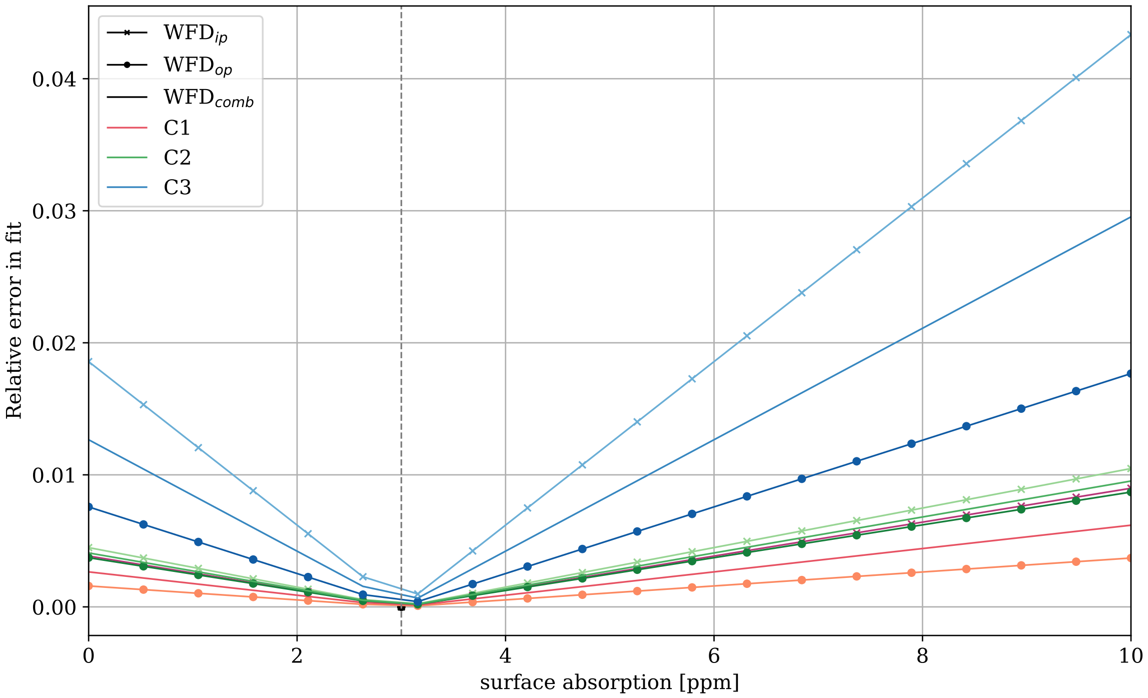

Fig. 3.21 The error in fit for α whilst sweeping the value for β against a modelled wavefront where α =50 ppm cm^{-1} and β = 3 ppm.

This analysis was repeated with the addition of random noise yielding Fig. 3.22, showing the results of one iteration. Once again there is linear dependence between α and β but the intersection of the lines has shifted from the α and β values used in the FEM.

This test was repeated 1000 times and the averages and standard errors for the intersection point for each pair of cases are listed in Table 3.2.

Pair of Cases	avg intersection α [ppm cm^{-1}]	$\sigma_\alpha/\sqrt{n}$	avg intersection β [ppm]	$\sigma_\beta/\sqrt{n}$
C1-C2	49.88	0.07	3.6	0.1
C1-C3	49.42	0.10	3.9	0.3
C2-C3	49.08	0.20	4.7	0.3

Table 3.2 Table of averaged intersection points for 1000 iterations of fitting for α to a predicted wavefront with simulated random noise whilst sweeping the β value for each of the cases C1, C2 and C3. The standard error in this value is also listed.

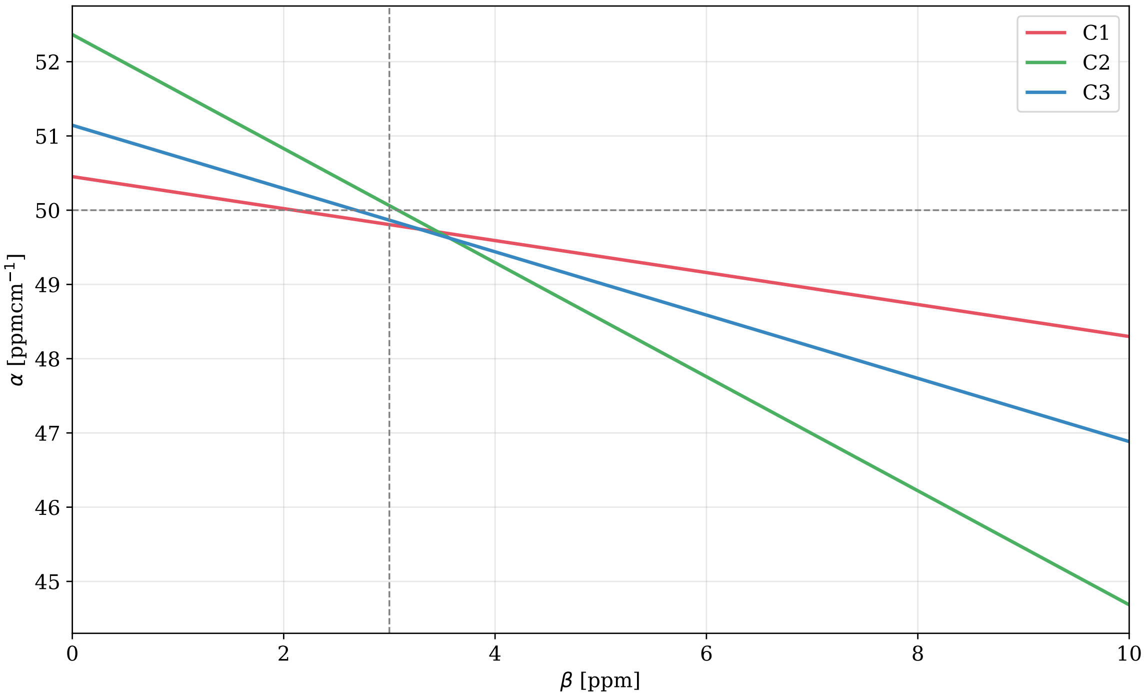

Fig. 3.22 The best-fit α values plotted as a function of the assumed β value for each slice independently and for the combined fit with added noise. All lines intersect at the β and α used in the FEM.

The addition of noise to the model did not significantly vary the average intersection position in α for each pair of cases, which deviated by <2% from the value used in the FEM. β showed more variation a standard error of up to 50%. The C1-C2 pair yielded the best results as C1 maximizes the SNR due to the longest overlap of the probe and heated region while C2 is most effected due to the surface heating. Thus, there is the greatest relative effect of surface absorption between these cases.

It can be concluded that β and α are most accurately determined using the cross-sections at large angles as any noise is consistent between the slices. However, due to sample constraints also measuring through a long sample with both small and large off-axis angles will provide the best estimate of α and β.

3.6 Systematic errors due to incorrect material parameters

Quantifying absorption in novel glasses such as ZBLAN is of interest to developers who aim to improve and characterise the material. My method uses a self-calibrating approach reliant on the accuracy of the glass parameters, such as the thermo-optic ($\frac{dn}{dT}$) and thermal-expansion coefficients (α_{exp}), which in development glasses may not be reliable. If either are incorrect the profile of the predicted wavefront will be incorrect and the absorption coefficients will be inaccurate.

I describe below the effect of inaccurate parameters on α and the quality of the fit is investigated as a means of analysing the correctness of the fitting parameters. In the following analysis a ZBLAN sample will be analysed using parameters from tables 3.1 and 2.2 and assuming an angle of incidence of 0.074 rad.

3.6.1 Thermo-optic and thermal expansion coefficients for ZBLAN

There has not been extensive work on quantifying the thermal expansion coefficient, α_{exp}, and the thermo-optic coefficient, $\frac{dn}{dT}$, in ZBLAN. Most papers studying ZBLAN thermal effects cite Izumitani's 1987 paper in which α_{exp} =17.2×10^{-6} K^{-1} and $\frac{dn}{dT}$ = -14.75×10^{-6} K^{-1} which were measured at 633 nm [48].

These parameters will vary with the percentage of each heavy metal group used in a ZBLAN sample [2]. Izumitani's ZBLAN sample had the mole percentages ZrF_4 53,BaF_2 20,LaF_3 4,AIF_3 3,NaF 20, but the ZBLAN label describes only which heavy metals are present not necessarily their mole percentage which can vary as ZBLAN is still under development. The range of published parameter values are listed in Table 3.3 and Table 3.4.

The measurements of $\frac{dn}{dT}$ vary by about 10% and alpha varies by about 5%, but with fewer independent measurements. Additionally, from [51], $\frac{dn}{dT}$ decreases slightly as the wavelength decreases, as expected, but that change is negligible compared to the variation in the values at 633nm. Thus, I assume below that the FEM parameters might be incorrect by +/- 10%.

$\frac{dn}{dT} \times 10^{-6}$ [k^{-1}]	λ [nm]	ref
-14.75	633	[48]
-14.45	633	[49]
-13.6	633	[50]
-15.5	633	[51]
-15.3	1150	[51]

Table 3.3 Literature values for the thermo-optic coefficient for ZBLAN at a range of wavelengths

$\alpha_{exp} \times 10^{-6}$ [K^{-1}]	Temperature [K]	ref
17.2	243.15 - 343.15	[48]
16.5	$\approx$ 293.15	[49]

Table 3.4 Literature values for the thermal expansion coefficient for ZBLAN and the range of temperatures

3.6.2 Sweeping thermo-optic and thermal expansion coefficient values to estimate uncertainty

To determine the inaccuracy in α due to incorrect thermo-optic and thermal expansion coefficients I will fit to $\Delta\mathrm{OPL}_{(50,0)}$ calculated using the nominal values $\alpha_{exp_{FEM}} = 17.2\mathrm{K}^{-1}$ and $\frac{dn}{dT}_{FEM}$ = -14.75 K^{-1} whilst sweeping the α_{exp} and $\frac{dn}{dT}$ used in the FEM over the 10% range determined from literature. Non-negligible changes in α were observed over this range, with α increasing as $\frac{dn}{dT}$ decreases and the opposite effect occurring for α_{FEM}, as shown in Fig. 3.23.

This simulation shows that an error in the assumed material parameters results in a similar relative error in the best-fit α and that the resulting variation in the quality of the fit is much less than the uncertainty due to the measurement noise, as shown in Section 3.6.3. The quality of the fit is best when correct coefficients are used as shown in Fig. 3.23 (b). However, there is a linear function of α_{exp} and $\frac{dn}{dT}$, where the ratio $\alpha_{exp_{FEM}} / \frac{dn}{dT}_{FEM}$ is conserved with only a fractionally larger error, shown in Fig. 3.23. This is when the changes in lensing due to TR and TE compensate for each other. Thus, there are many combinations of coefficients which minimise the relative error in the fit and the correct values can't be easily found.

This observation is valid for each of the three combinations of sample length and angle, C1, C2, and C3 defined in Fig. 5.2. The variation in α due to incorrect parameters depends on

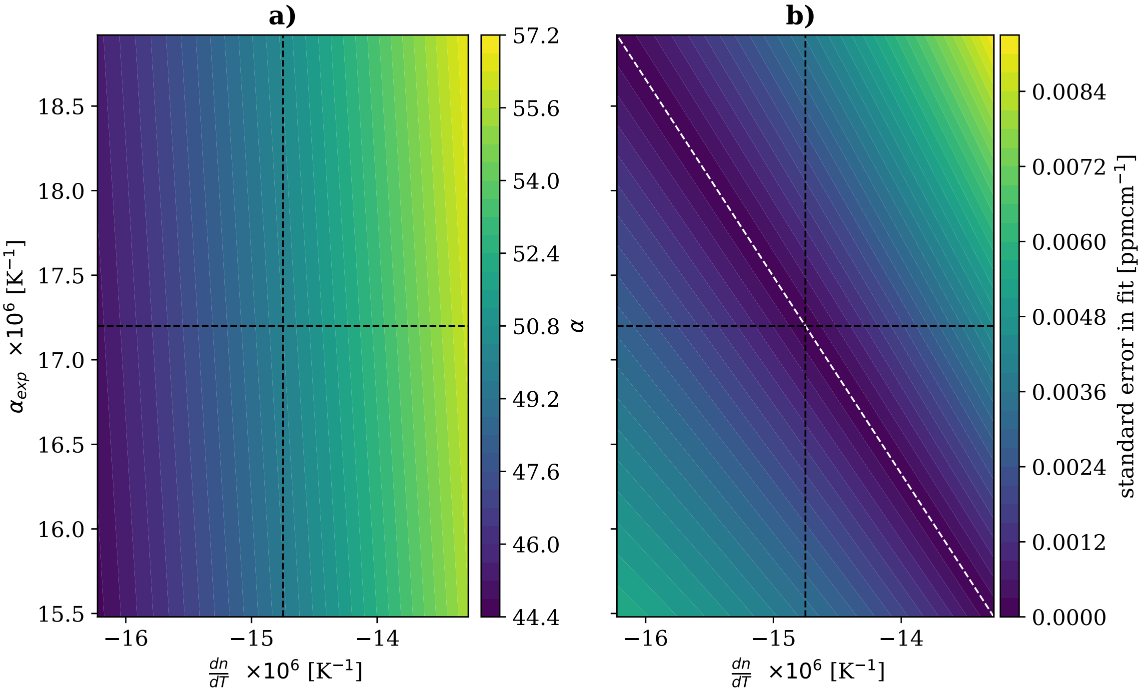

Fig. 3.23 a) The magnitude of α is sensitive to the inaccuracies in the thermal-expansion and thermo-optic coefficients used in the model, shown in plots (a) of the expected change in best-fit alpha value, and (b) the standard error in alpha due to the use of incorrect material parameters. The black dashed lines indicate the nominal material parameters and the white dashed line has slope $\alpha_{exp}/\frac{dn}{dT}$

sample lengths, probe beam angles and has a different effect on each cross-section of the probe beam as shown in Fig. 3.24. All best-fit α will only agree if the material parameters used in the FEM are the correct parameter values. The same effect is observed when surface absorption is considered as the best fit α varies linearly with added β.

The deviation of α is smallest for $C1$ with a 10% change in $\frac{dn}{dT}$ or α_{exp} resulting in approximately 10% and 2% change in α respectively. The thermo-optic coefficient causes the greatest change as it is the dominant effect. For C3 the TE and TR effects have similar magnitude and their contributions have more distinct profiles, due to the large angle of incidence, causing the errors in $\frac{dn}{dT}$ and α_{exp} to have a more significant effect.

Thus, it has been demonstrated that if one of the coefficients is known accurately then the other can be determined from the intersection point and minimum error, but not if both are unknown due to the degeneracies of the minimum fitting error. However, by limiting the

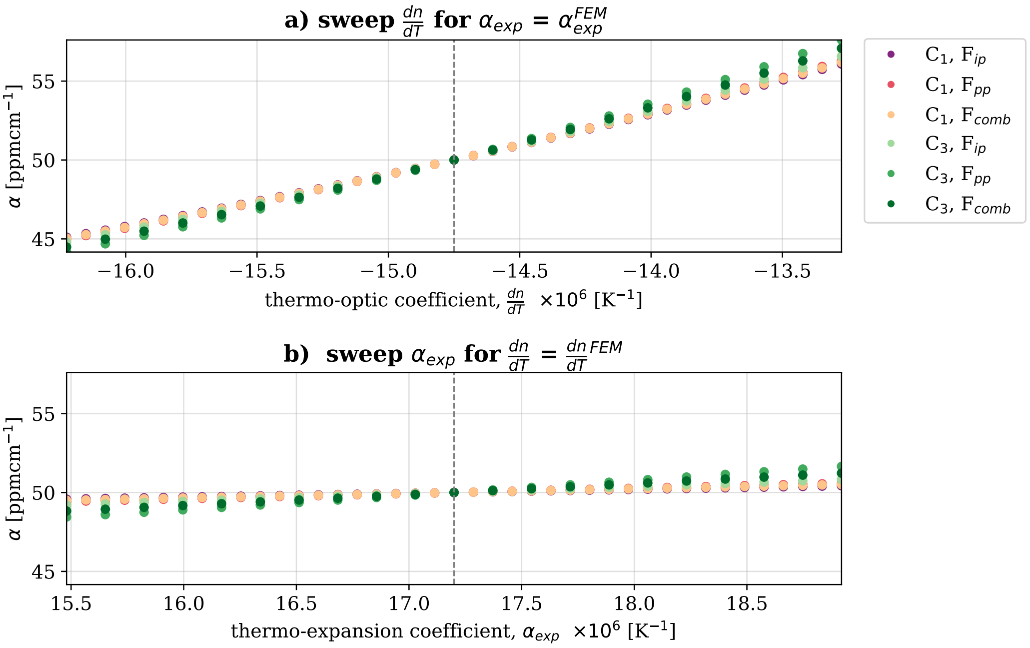

Fig. 3.24 Figure (a) shows the change in absorption coefficient (α) as $\frac{dn}{dT}$ is swept when α_{exp} is known. Figure (b) shows the change in absorption coefficient (α) in the alternative case when α_{exp} is swept and $\frac{dn}{dT}$ is known.

possible values of α to those that fall along the minimum error line $\left(\frac{\alpha_{exp}}{\frac{dn}{dT}}\right)$ the variation in α can be constrained to 5%. To most effectively use the standard error to determine if α_{exp} or $\frac{dn}{dt}$ used in modelling are accurate, shorter samples with larger angles of incidence should be used as greater deviation will be observed. However, this is more likely influenced by noise due to the smaller signal size.

3.6.3 Effects of noise on coefficient uncertainty

Once again the experimental noise floor will effect how much information about the coefficients can be extracted from measured data. In fact, by adding randomly sampled noise on a scale expected in experimentation as described in Section 3.5 all fitting error information is obscured, shown for C1 which has the highest SNR in Fig. 3.26.

However, if the noise is reduced by a factor of 10 the error in fit begins to show the $\alpha_{exp}/\frac{dn}{dT}$ minimum structure, shown in Fig. 3.27. Thus, if the experimental SNR could be increased the accuracy of the coefficients could be analysed experimentally.

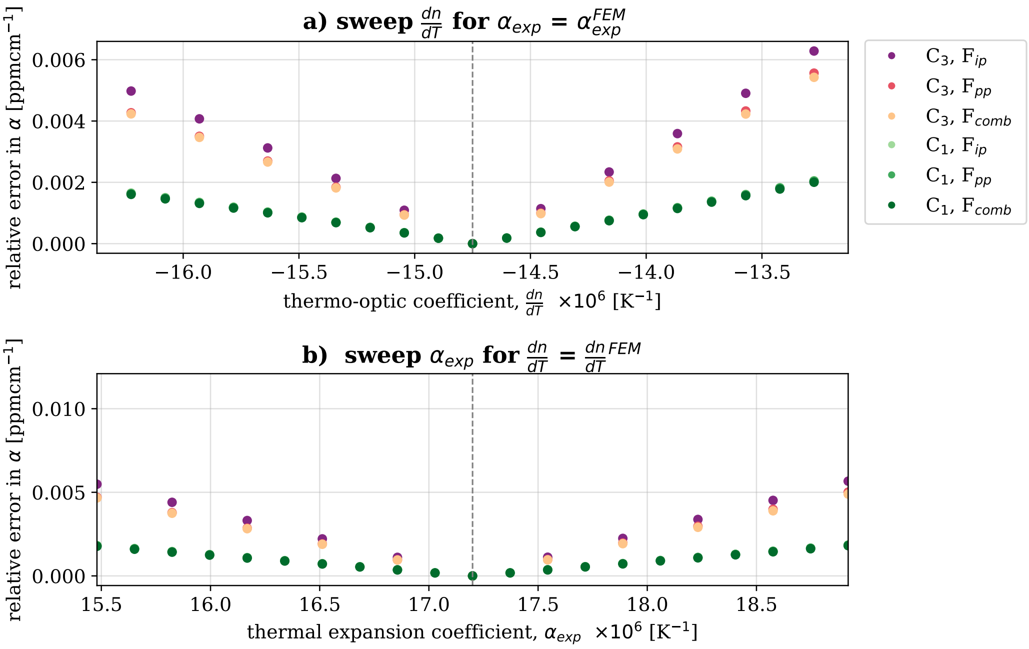

Fig. 3.25 Plot of the change in the goodness of fit for cases C1 and C3 and P_{ip} and P_{pp} cross-sections, as $\frac{dn}{dT}$ and (b) α_{exp} are varied. This demonstrates that the highest quality fit is observed when the accurate value is used and that a at large angles (C3) more significant changes in profile are observed with coefficient variance leading to greater error.

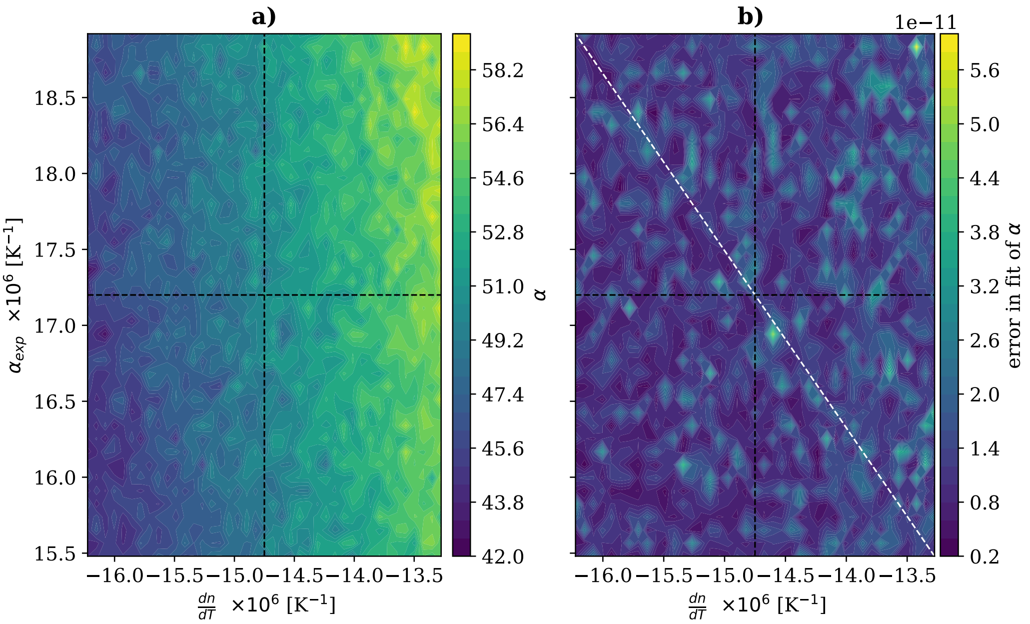

Fig. 3.26 Added noise to the coefficient sweep causes significant noise structure in the fit for α when sweeping the thermo-optic and thermal expansion coefficients (a) and obscures any structure in the error in the fit shown in figure (b). The dashed white line indicates the slope $\alpha_{exp}^{FEM} / \frac{dn}{dT}^{FEM}$, where without noise a minimum error was observed.

Increasing the laser power is a method of improving the SNR without significant modification to the system.

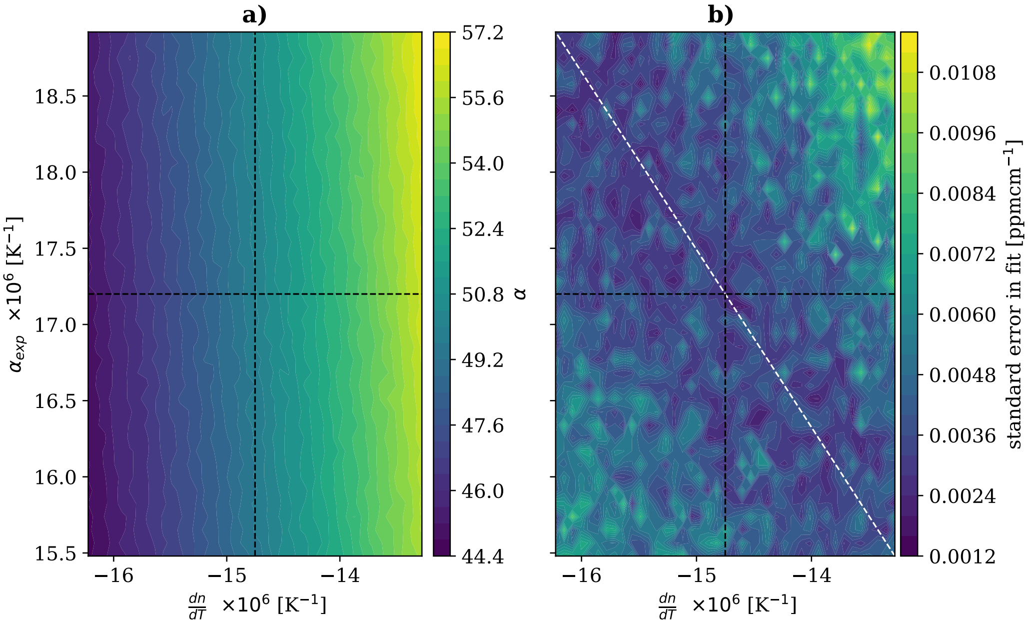

Fig. 3.27 Reducing the noise added to the model by factor of 10 less than experimental noise visibly improves the fit for α when sweeping the thermo-optic and thermal expansion coefficients (a) and minimises the relative error in the fit (b) compared to Fig. 3.25. The dashed white line indicates the slope $\alpha_{exp}^{FEM} / \frac{dn}{dT}^{FEM}$, where a noisey minimum error is once again visible.

3.7 Summary

In this chapter a model has been developed to determine the ΔOPL of an off-axis probe beam after propagating through a sample centrally heated by the absorption of laser light. The model calculates deformation due to the thermo-elastic, thermo-refractive and elasto-optic effects using data taken from the FEM described in the previous chapter. Through this analysis the electro-optic effect was shown to be negligible.

A fitting process has been defined to determine α and β using a least squares fit of a linearised equation for $\Delta\mathrm{OPL}(\alpha,\beta)$ to the wavefront. It was demonstrated that using large angles of incidence surface and bulk absorption could be extracted, even in the presence of noise with a small error. However, if large angles are impractical, fitting for α to the P_{ip} and P_{pp} slices of the probe beam and the combined fit for an assortment of angles of incidence or sample lengths, and sweeping for β until the α values agreed could reproduce the α and β with a slightly reduced accuracy.

Finally, it was determined that differences in the thermal expansion and thermo-optic coefficients from the actual properties of the glass lead to inaccuracies in the calculated values of absorption and increases in the fitting error. However, in the cases where the ratio $\alpha_{exp} : \frac{dn}{dT}$ is preserved this error is minimised. Using this linear set of minimums the variation in α due to inaccurate coefficients could be constrained to 5% of the total absorption. However, with the current level of experimental noise this fitting error is obscured and it can only be concluded that there could be a 2% and 10% variation in α due to inaccuracies in the thermal expansion and thermo-optic coefficients respectively. Noise must be reduced by a factor of 10 to be able to observe fitting errors due to incorrect coefficients and constrains their effect on α to 5%.

This developed model was fit to the experimental data measured using the system in Chapter 4 to determine absorption losses in ZBLAN in Chapter 5.

CHAPTER 4

MEASUREMENT OF WAVEFRONT DEFORMATION USING AN OFF-AXIS HWS

Measuring absorption by imaging wavefront deformation has been previously conducted using many photo-thermal measurement systems [33], [34], [36], [37]. Brooks *et al.* [34] proposed that an off-axis probe beam system could be used to measure absorption for the applications in gravitational wave instrumentation but stopped short of determining the absorption coefficients. Schäfer *et al.* [36], [37] constructed a similar system measuring bulk and surface absorptions 1000s of times larger than our aim of $10\,\mathrm{ppm\,cm^{-1}}$ in the UV. Stubenvoll *et al.* [40] adapted the system to employ perpendicular probe and pump beams to measure absorptions in anisotropic crystals where $\alpha = 11 \pm 4$ $\mathrm{ppm\,cm^{-1}}$ and $\beta = 74 \pm 28$ $\mathrm{ppm\,cm^{-1}}$ which in both cases is approximately 40% error. Additionally, the perpendicular beams limits the maximum deformation the system can measure and how small of an absorption coefficient can be quantified.

In this chapter I present an optimised off-axis system based on that suggested by Brooks *et al.* [34], allowing surface and bulk absorption to be determined at levels of $10\,\mathrm{ppm\,cm^{-1}}$ and 1 ppm without significantly sacrificing signal and reducing error. To improve on the previous measurements in low-loss glasses the system must be optimised for high signal to noise and accuracy.

4.1 Objective

In the previous chapter the effects of heating a sample were investigated and a generalised model was created for the optical path length change of a beam transmitted through the sample at an angle, θ_t. In this chapter, I will describe a system to measure the Wavefront Distortion (WFD) of an off-axis probe beam using a differential Hartmann Wavefront Sensor (DHWS), detailed in Section 4.2. Through the combination of this system and the model, the absorption coefficients can be extracted. The measurement system allows uses multiple angles of incidence, allowing the bulk (α) and surface (β) coefficients to be determined with decreased uncertainty.

Measuring the absorption coefficients in low-absorption ZBLAN or other low-loss materials, such as fused silica requires a system that is optimised for α's of 10s of ppm cm^{-1}. Thus to limit the effects of noise I selected the power and profile of the pump beam to maximise the signal which is discussed and characterised in Section 4.3. The sensitivity of the measurement is limited by the DHWS noise floor which is investigated in Section 4.4. After which the measurement procedure will be stated in Section 4.5.

The multi-parameter nature of the model requires verification to ensure the experimental set-up is accurately described. The objective of the remainder of this chapter, beginning in Section 4.6 is to verify this measurement system using a N-BK7 sample.

4.2 Experiment design

The absorption induced WFD is measured using an on-axis pump and off-axis probe beam, shown in Fig. 4.1. This orientation was selected as a large probe beam angle of incidence allows separation of bulk and surface effects, whilst still probing a significant portion of the heated sample in comparison to perpendicular beams.

The sample is mounted on a podium on cloth with low thermal conductivity to reduce conductive cooling and secured such that there is no added stress. The 1995 nm pump beam was selected due to its relatively high power and closeness to the proposed wavelength for GW detectors. It is aligned to the central axis of the sample using mirrors, M_1 and M_2. The probe beam is aligned such that it passes through the centre of the sample at angle θ_t. Off-axis incidence ensures the probe beam will not pass through any other optics heated by the pump beam and experience other sources of thermal lensing. The probe beam was selected to be a low power 830nm superluminescent diode (SLED) beam as this sample is highly transmissive at this wavelength and so a Si CCD DHWS camera can be used. The SLED's short coherence length prevents spurious interference fringes. The probe beam was expanded and collimated to 7.8mm using a fibre coupled doublet (L_4) so that a large volume

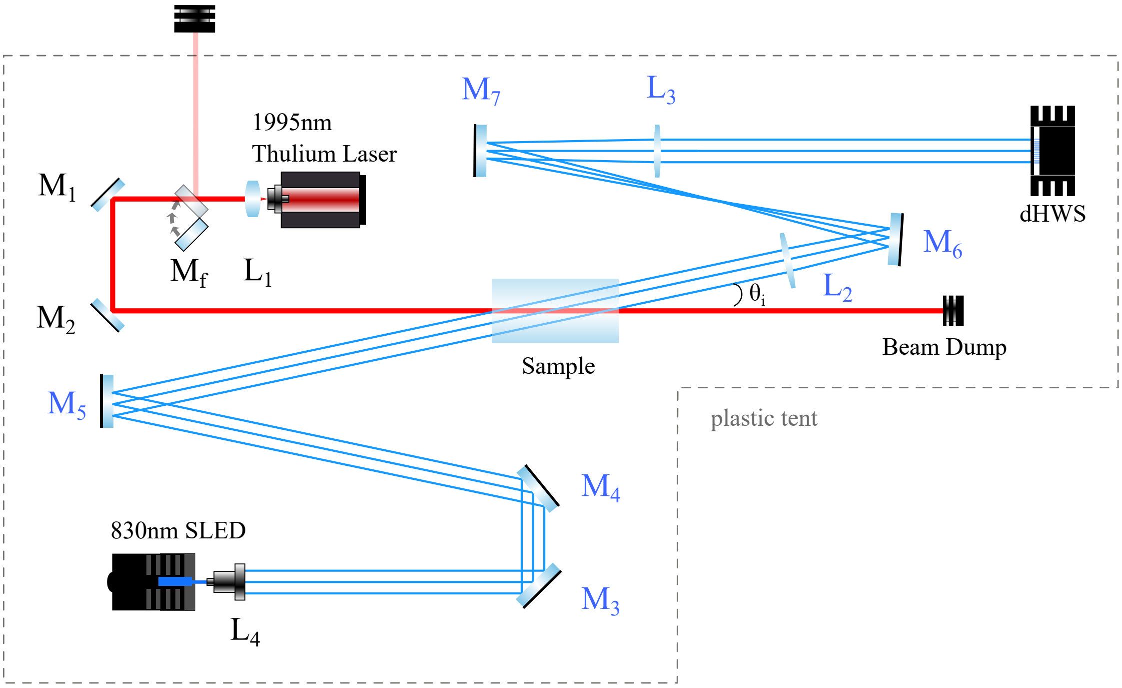

Fig. 4.1 Schematic of the on-axis pump beam, off-axis probe beam DHWS photo-thermal absorption measurement system. The red beam depicts the on-axis heating beam which is absorbed in the sample and the blue beam is the off-axis probe beam which transmits through the sample. In this figure optics labelled L denotes lenses and M denotes mirrors. The optics labelled in blue represent the two sets of optics used to modify the angle of incidence, θ_i.

of the sample is imaged without clipping. The probe wavefront at the sample exit face is imaged by a relay telescope (L_2 and L_3) with a 2x magnification to ensure the DHWS sensor screen is filled. This set-up is placed in a tent to reduce convective cooling and prevent the associated turbulence from disrupting the probe beam.

In the previous chapter it was highlighted that the use of large and small θ_t was essential to determine both surface and bulk absorption. Thus, this measurement system is designed to be operated using two angles of incidence which are switched using a flip mount mirror in place of M_4 directing the beam onto an alternative set of optics. The magnitude of the angles are limited by the restriction that the probe beam must be larger than the pump beam and pass through the sample without clipping, which will be discussed in detail in the next chapter for a ZBLAN sample.

The pump beam size is informed by the model requirement to have a collimated beam and the required SNR to measure low-loss samples. Using the model developed in chapter 2 and 3, for a heated thin disc of fixed geometry, it was demonstrated that by reducing the pump beam size the signal is increased as shown in Fig. 4.2. Thus, experimentally the beam radius was reduced to the smallest size where there was no significant divergence over the sample.

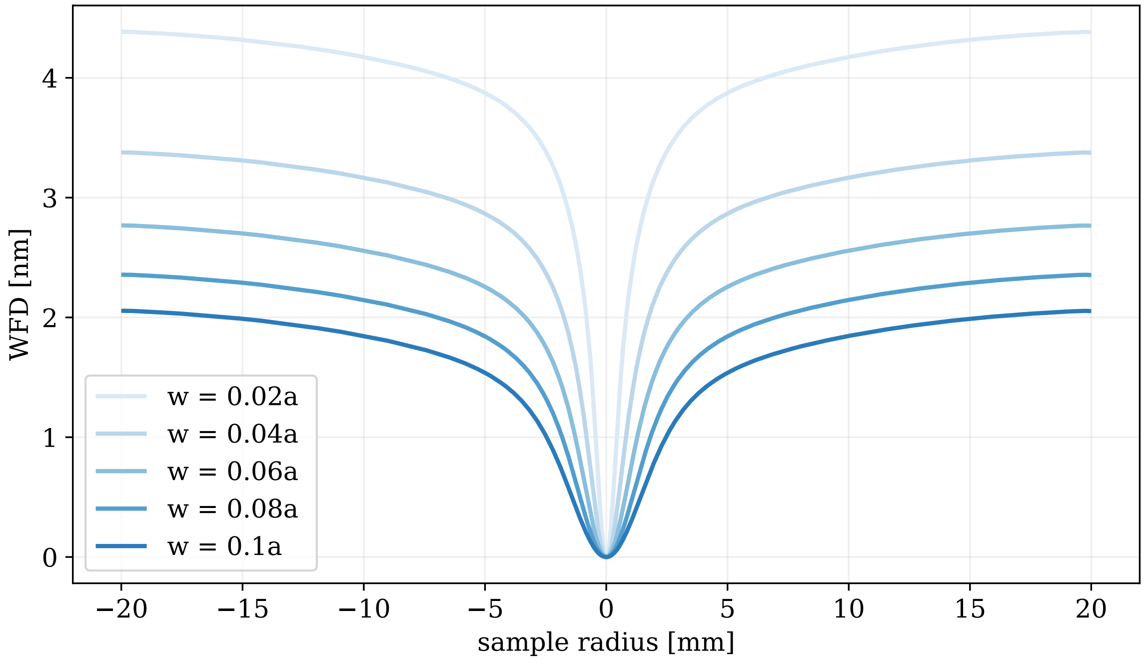

Fig. 4.2 Modelling the WFD of a probe beam using a variation of pump beam sizes (w) demonstrates that by decreasing the pump beam radius the maximum deformation is increased. The modelled WFD used sample parameters given in table 4.1 and the dimensions of length = 10mm and radius = 20mm.

4.3 Pump beam characterisation

The pump beam is a key component of the system, defining the wavelength of absorption measured and the magnitude and profile of the probe beam wavefront distortions. Furthermore, as I calculate the absorption coefficients by comparison to a model the precision and uncertainty in all pump beam parameters will effect the uncertainty in α. In particular, power is proportional to the wavefront distortion and its uncertainty will be carried through to the absorption coefficient. Maximising the pump power will also allow the signal to be increased which is essential for a system designed to measure low-loss glasses which will not cause very large distortions. Thus, in this section I describe the thulium laser pump beam parameters in great detail to ensure it will produce the largest signal and can be defined with low uncertainties in the model.

4.3.1 Wavelength characterisation

The choice of laser defines the wavelength of absorption investigated. For the measurements reported here, I used a Tm:fiber laser, with the spectrum shown in Fig. 4.3. This spectrum shows it has a wavelength of 1995.5 nm and a narrow line-width, limited by the 4 GHz resolution bandwidth of the Bristol spectrum analyser. For this measurement I aim to measure the absorption at a discrete wavelength. However, the changes in absorption coefficients are expected to be minimal and vary smoothly over the small range, thus this bandwidth should not cause a significant deviation. The signal was measured to be 30dB above the noise floor, thus, absorption at other wavelengths will not effect this measurement.

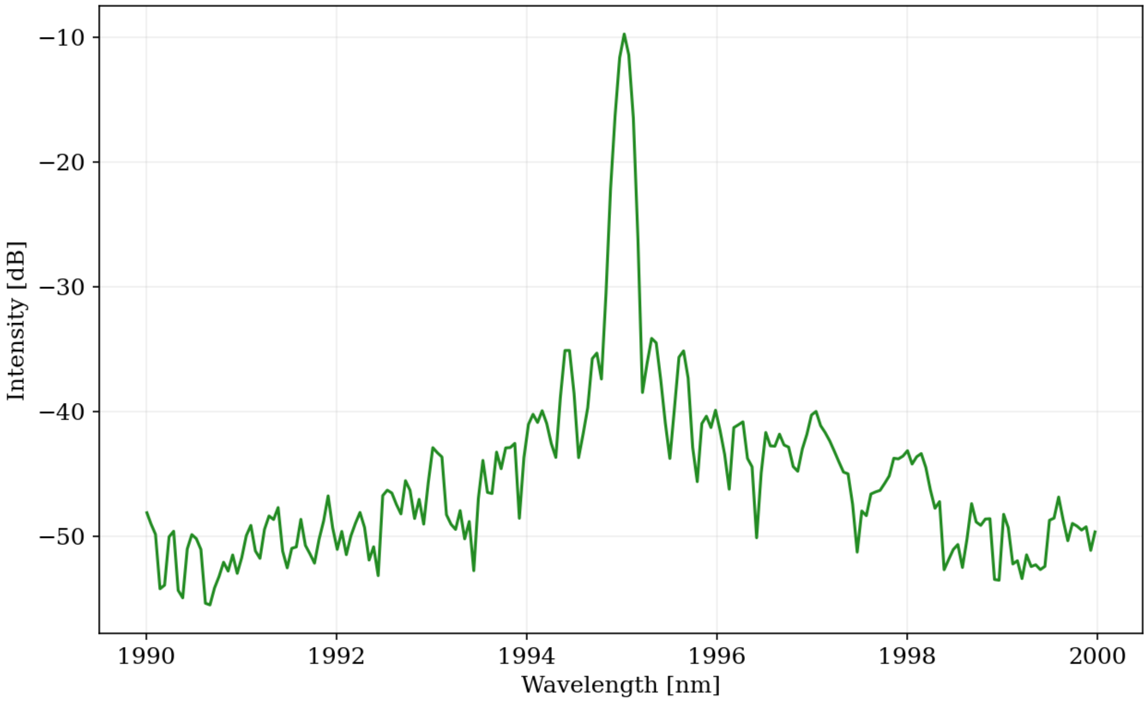

Fig. 4.3 Spectrum of 1995 nm pump beam.

4.3.2 Power and stability of the pump beam

For weakly absorbing samples the magnitude of the measured WFD is linearly proportional to pump beam power, thus, the maximum stable pump power of approximately 7.4W will be used. The power is limited by thermal cooling systems ability to transfer heat from the diode.

The pump beam power was measured using two thermal power heads, each with a calibration uncertainty of 5%, which is consistent with the 4.5% difference between the recorded values. Additionally, there is a random variation of 5mW listed by the manufacturers and both uncertainties are carried through the fit causing inaccuracies in β and α.

Further uncertainty can be caused by power drift, which is problematic due to the averaging of multiple frames used to reduce shot noise in this measurement. The beam power over an hour at 0.84 W was measured on a Quadrant Photodiode (QPD) sensor giving a relative power and pointing noise of the beam, shown in Fig. 4.4 and Fig. 4.5.

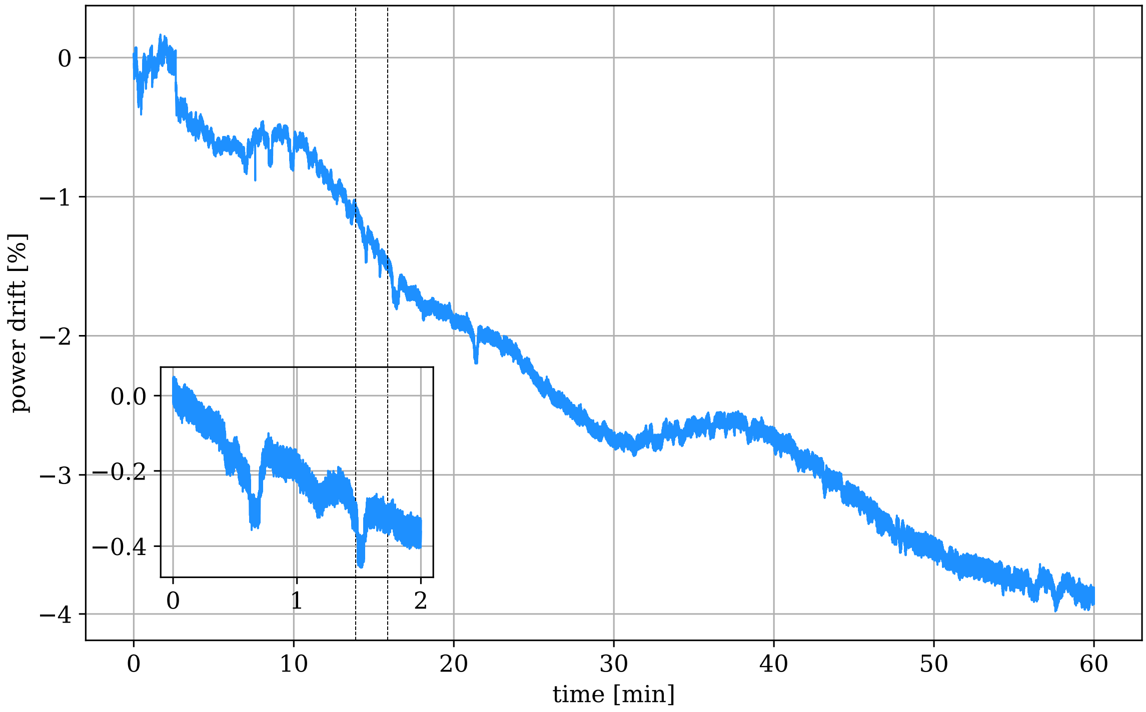

Fig. 4.4 The relative intensity of the 2 μm pump beam was measured over 1 hour demonstrating a 4% reduction in relative intensity over this time. The insert shows 2 minutes (approximate measurement time) where there is the highest rate of change.

Over an hour an intensity drop of 4% is observed, as shown in Fig. 4.4. The power fluctuation over a measurement period (approx 2 minutes) is just over 0.4% percent, considering the highest rate of change measured, as shown in the insert in Fig. 4.4. The small change over the measurement is acceptable but will propagate through to α proportionally. However, the drift in power over a longer period may cause errors between datasets as the laser power was controlled by the current supplied to the diode. This is considered in more detail in Appendix D.

Additional to power drift, variation in the pump beam position in the sample will broaden the WFD by increasing the area heated by the beam. Over a period of 60 minutes the beam position on the QPD was measured to drift 25 µm in the y axis and 10 µm in the x axis. The QPD was bolted in position, however, the strain from the cord could cause a constant drift in either axis, but this can't be confidently concluded. Like the power drift, the measurement is only sensitive to pointing noise whilst the sample is being heated. In this time frame there is an oscillation over a range of 1 μm with standard deviation of 0.4 µm and 0.3 µm for the x and y axis of the beam, as shown in the insert in Fig. 4.5. This is consider negligible as it is significantly below the uncertainty in the beam size of 40 µm which corresponds to a 1% error in α, as discussed in Section 4.3.3 and Appendix D.

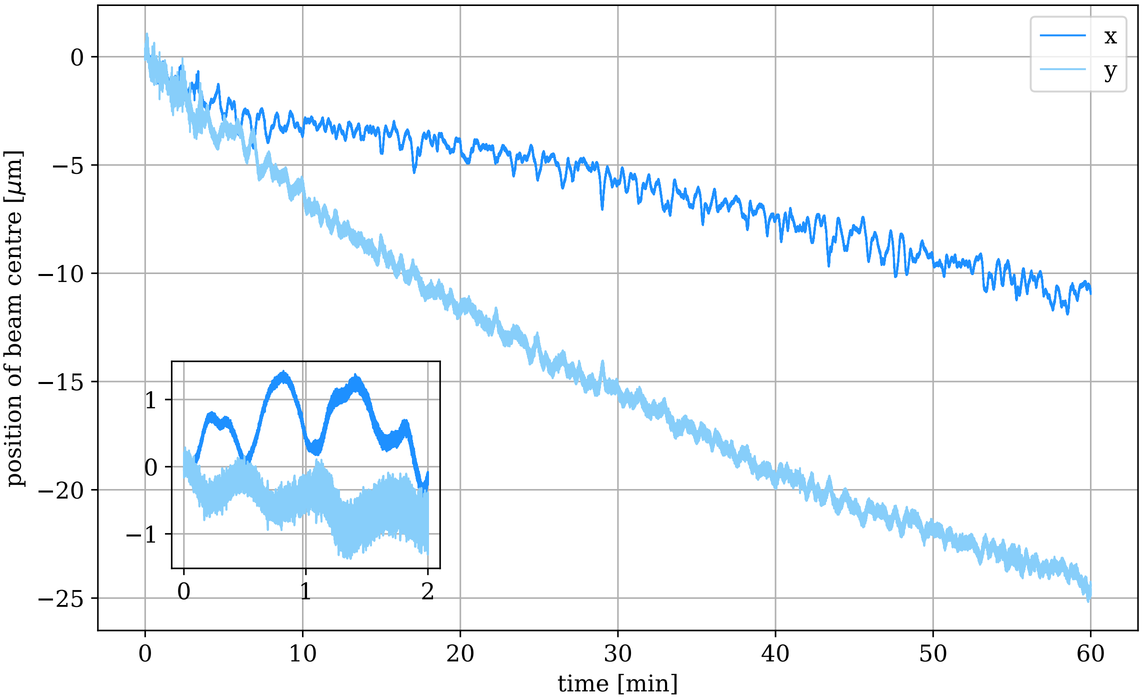

Fig. 4.5 The measured beam pointing noise in pump beam in the x (dark blue) and y (light blue) axis. The insert shows the deviation over a single measurement period which for both axis oscillates over a 1 µm range.

4.3.3 Profile of the pump beam

The pump beam size was selected by determining the smallest beamsize which will not considerable diverge over the ZBLAN sample length measured in Chapter 5. The profile of the pump beam at the center of the sample was measured prior to inserting the sample, using the knife edge technique. The results plotted in Fig. 4.6 indicate that the pump beam is slightly elliptical, with $w_x = 0.72 \pm 0.04$ mm, $w_y = 0.70 \pm 0.04$ mm. The waist was located before the sample to reduce the effect of suspected cladding modes on the beam profile causing the beam to diverge through the sample. This divergence was measured to be 0.02mm over the length of the sample by measuring at the input and output faces, thus satisfying the assumption that the pump beam was collimated within the sample.

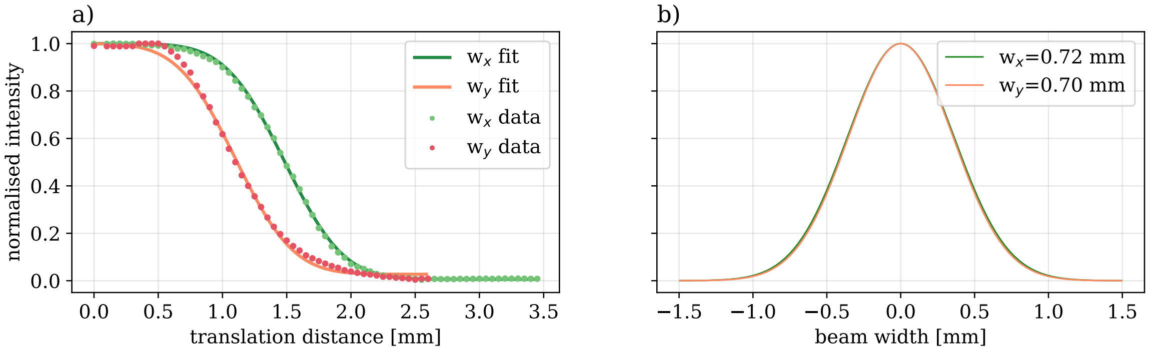

Fig. 4.6 a) Plot of the error signal measured when translating knife edge across pump beam in the x and y axis at central plane of sample and the fit. b) Plot of the normalised heating beam profile at the sample centre plane reconstructed from the fit to the knife edge technique.

The determined beam size is slightly elliptical. If the ellipticity of the beam is not considered, the predicted WFD will not accurately predict the experimental deformation as demonstrated in Appendix C. In fact, in Appendix D a 40 μm uncertainty in beam-size (as given by the knife edge measurement) was determined to a 1% uncertainty in α. Hence, any undiagnosed ellipticity larger than this value will lead to significant variation in α. Additionally, the best fit α will vary for the P_{ip} and P_{pp} slices impairing the ability to determine surface absorption from these slices as proposed in Section 3.5. For this reason the beam was made as circular possible and was input into the COMSOL model as a function of its x and y cross-sections.

Above, I have shown that our system is very sensitive to the pump beam parameters and that changes in power, beam shape and wavelength will significantly effect the best fit absorption coefficients. I have demonstrated that the pump beam power has a direct effect on the magnitude of the wavefront deformation and can be used to increase the signal. However, the laser is operating at its maximum power, thus, to further increase the SNR the noise measured by the DHWS must be reduced, which will be discussed in the following section.

4.4 Hartmann wavefront sensor

The DHWS used in this experiment uses a Dalsa 1M60 Charge Coupled Device (CCD) camera with an invar Hartmann plate suspended by a lever arm (L) of 10.43mm over the sensor array. The invar plate has 850 holes of diameter 150 µm arranged in a hexagonal configuration with a spacing of 430 µm. These parameters were selected to optimise the spatial sensitivity whilst minimising cross talk of the centroids [35].

When a beam is incident on the DHWS, each hole in the Hartmann plate produces a ray propagating normal to the beam at that point, forming an array of spots on the camera. The DHWS can be used to determine the change in the wavefront (W) from the shifting in position of these dots using the following steps:

- Take two images using the CCD.
- Determine the centre of each spot on the Hartmann array to produce an array of centroid positions, in terms of pixels, for the first c_1 and second frame c_2.
- Calculate the wavefront gradients ($\frac{dW}{dx}$) in radians as the change in position of the centroids between the two frames in x and y using,

  $$\frac{dW}{dx} = \frac{p_s(c_{2x} - c_{1x})}{Lm}$$

  where p_s is the pixel size, m is the inverse of the magnification of the image relay telescope and x can be replaced with y to determine $\frac{dW}{dy}$.
- Remove tilt from wavefront by subtracting the average gradient in x and y.
- Numerically integrate gradients to produce measured wavefront distortion.

To apply this system to measure the distortion of the probe beam wavefront due to the absorption DHWS takes images before and after the absorption induced heating of sample. The differential system removes common mode distortions in the beam leaving the differential component of the absorption induced change in wavefront.

The sensitivity of the DHWS can be degraded by;

- Photo-electron shot noise.
- Air currents in the measurement system.
- Sensor readout and digitization noise.
- Excess heating of the CCD sensor.
- "Coherence noise" due to interference fringes caused by stray reflections of the probe beam and cross-talk between spots.

The coherence noise was minimized by using a SLED light source and the temperature of the sensor was actively cooled and stabilised using a TEC PID system [35]. Shot and readout noise were reduced by averaging multiple CCD images. Air current noise was minimized by enclosing the measurement system in a tent and turning off the air-conditioning during measurements.

The temperature of the CCD was monitored over a period of 5 hours whilst taking images, using the internal digitizer temperature sensor and a thermistor attached to the external casing as is plotted in Fig. 4.7. Unfortunately, the digitizer sensor resolution is only 0.3 K. The thermistor, which has a much better sensitivity, measured a variation with a standard deviation of 0.01K, as shown in Fig. 4.7 and observes a slow sinusoidal temperature change. The sinusoidal behaviour of the temperature is attributed to the thermal controller.

The combined effect of the noise was evaluated by taking two images without changing the system producing a RMSE of 30 nm. This is consistent with what is expected if the DHWS was shot noise limited [38], but is significantly larger than the signals expected for thermal aberration due to absorption in low-loss samples.

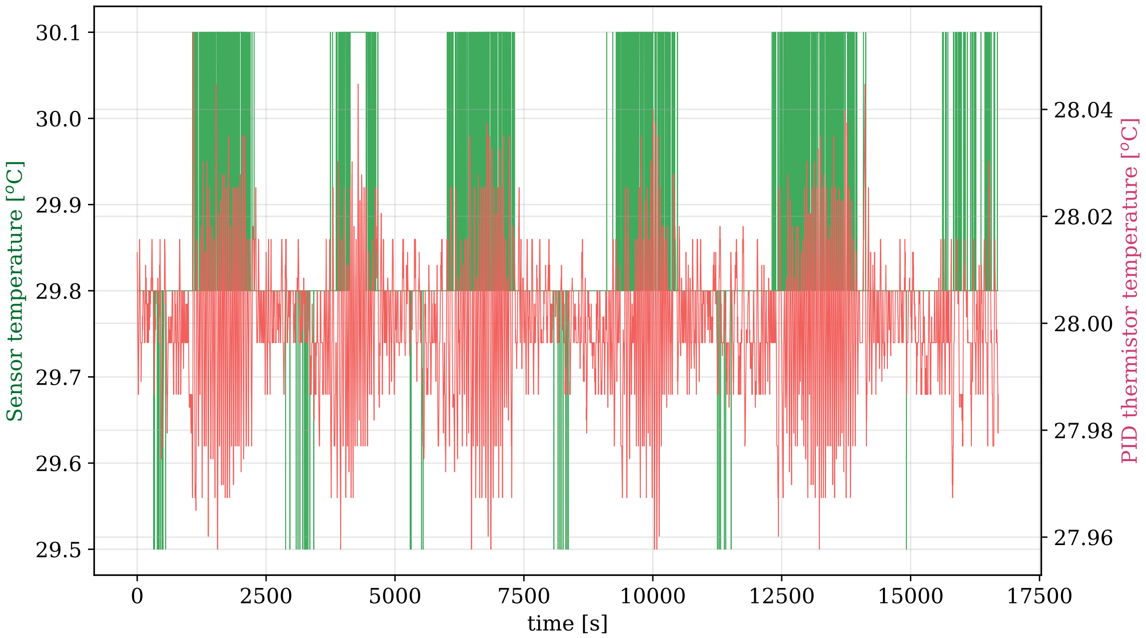

Fig. 4.7 Plot of the temperature of the sensor DHWS measured using the internal digitizer sensor (green curve) and a thermocouple attached to the external casing (red curve), while recording images. The thermistor has a much improved precision compared to the digitizer which operates over discrete 0.3 K increments.

For example, the predicted WFD in Chapter 3 in ZBLAN using where $\alpha = 50\,\mathrm{ppm\,cm^{-1}}$ has a maximum deformation between 2 nm to 5 nm for ZBLAN depending on alignment and angle, requiring improved sensitivity.

4.4.1 Reducing noise floor of the DHWS with averaging

Since the reproducibility of the DHWS centroid positions in each image is expected to be shot-noise limited [38], its effect can be reduced by a factor $N^{1/2}$ by averaging over N frames. Thus, below I will demonstrate the extent of the SNR improvement with averaging and selection a number of frames to average in measurements.

To quantify the noise in a differential wavefront measurement, two images are taken without changing the system. The root-mean square (RMS) variation of the centroids between the images one direction σ_x is given by,

$$\sigma_x = \sqrt{\frac{\sum_m^{j=0}(c_{x2j} - c_{x1j})^2}{m}} \tag{4.1}$$

where c_{x1j} is the location of the j-th centroid in the initial image, c_{x2j} is the location of the j-th centroid in the second image and m is the number of centroids.

The total wavefront error (σ_W) is determined by the product of the variance between adjacent centroids ($\sigma_{\Delta w}$),

$$\sigma_{\Delta w} = \left[\frac{h_p}{L} \left(\frac{\sigma_x + \sigma_y}{2} \right) \right] \tag{4.2}$$

where h_p is the spacing of holes on the Hartmann plate, and the Southwell noise coefficient ($C_{\Delta}^{1/2}$), as given in Brooks [35].

To investigate the improvement in $\sigma_{\Delta W}$ with averaging, a 830 nm SLED beam was allowed to freely expand onto the DHWS camera as shown in Fig. 4.8. This removed any changes due to the surface quality of additional optics and ensured the sensor is overfilled so that the average is over all the centroids.

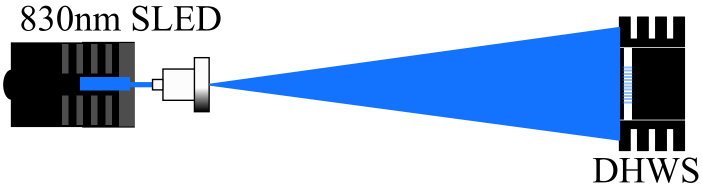

Fig. 4.8 Schematic of the apparatus to measure sensitivity of DHWS.

A set of 5000 images were recorded with an exposure time of 30ms to allow averaging to occur until limited by a systematic effect. The first and last 500 images were averaged to yield reference centroid locations which were not significantly effected by random fluctuations. A second set of centroids were then calculated using an average of N frames from the remaining 4000 images and σ_W was determined as above. The results are plotted in Fig. 4.9, demonstrating a decreasing noise floor with averaging.

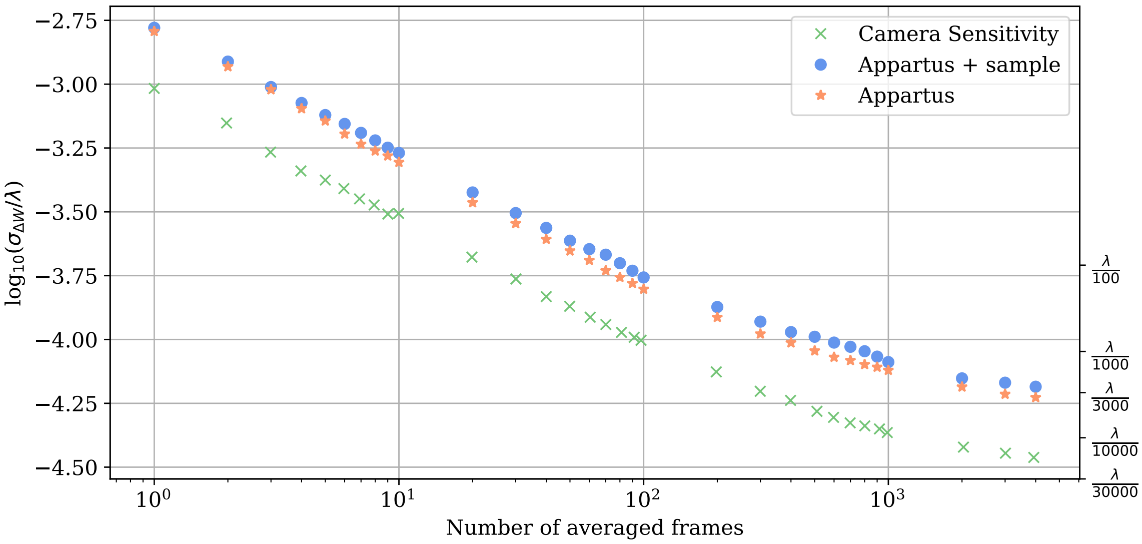

Fig. 4.9 The DHWS sensitivity increases with the number of averaged frames, shown for the cases of free expansion of a beam onto the DHWS, the DHWS in the optical set up and the DHWS in the optical set up with the addition of a ZBLAN sample in the measurement position.

The test was repeated with the probe beam aligned through the measurement system apparatus without a sample in place. The results plotted in Fig. 4.9 indicate that additional optics degraded the reproducibility of the centroid positions, which I attribute to scattering off dust on optics and poor surface quality. A further loss in sensitivity is observed after inserting the ZBLAN sample, which is likely due to the hand polish quality, as well as potential scattering sites inside the sample. Nevertheless, averaging up to 1000 images recorded over 30s, still improves the sensitivity. The improvement in sensitivity when averaging more than 1000 frames begins to plateau, indicating systematic structure beginning to appear in the measured gradients. Thus, 1000 images were recorded and averaged for each measurement, with 500 reference images recorded before and after sample heating to minimize the effect of slow drift during the measurement.

The limiting noise source of the DHWS has been demonstrated to initially be random noise sources allowing the sensitivity to be improved by averaging. Due to this analysis a 1000 frame average was selected, where the noise floor is approximately $\frac{\lambda}{2500}$ or 0.33nm, such that the expected distortion through a ZBLAN, or equivalently low-loss, sample can be measured.

4.4.2 Measured noise floor

A typical measurement noise floor was imaged using a 1000 frame average as discussed above, where the sample was cold for both sets of images, is plotted in Fig. 4.10. The noise floor appears random in structure and has an average of 0.3 nm of wavefront distortion, which is consistent with the data in Fig. 4.9.

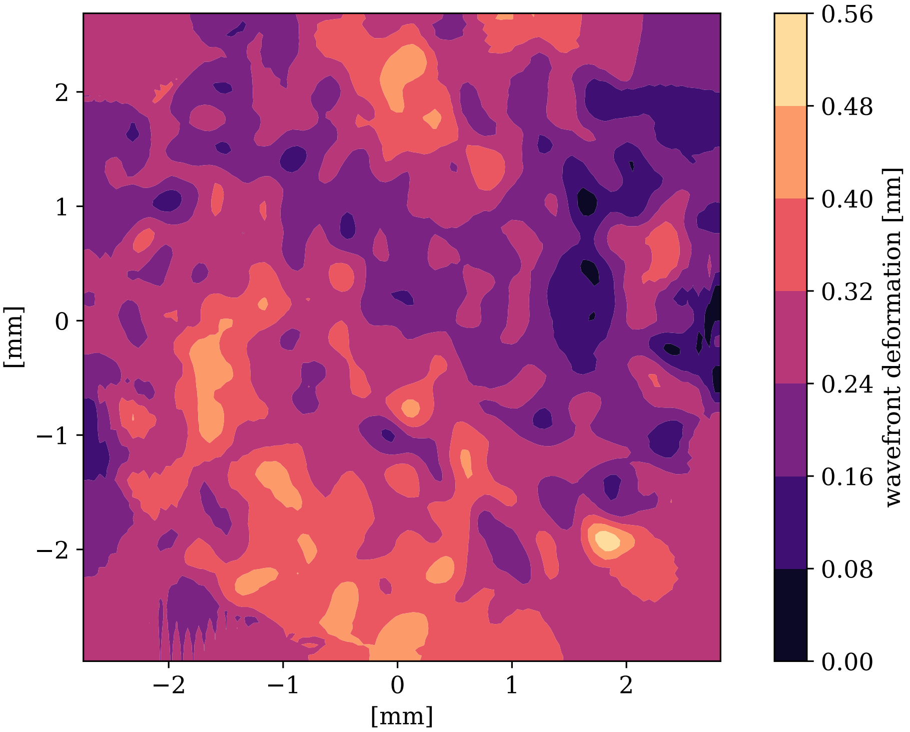

Fig. 4.10 A typical measurement noise floor taken through a ZBLAN sample, demonstrating that the structure appears random in nature and has a magnitude which is below the expected WFD.

This noise floor is a factor of 6 lower than the WFD expected for a ZBLAN sample with 50 ppm cm^{-1} when measuring through the shorter axis. This SNR could be improved in the future by implementing a laser with increased power or an increased sample length. Furthermore, taking and averaging multiple wavefront measurements may also allow the effects of noise to be further reduced.

4.5 Measurement Procedure

To ensure accuracy and reproducibility of each measurement, when a new sample is placed in the set-up these steps are followed:

1. Place sample in set-up such that the front face is perpendicular to the propagation of the heating beam.
2. Align the image relay telescope using L_2 and L_3 and characterise magnification at back face of sample.
3. Take 500 reference images with pump beam blocked so there is no heating of the sample.
4. Unblock the pump beam and wait 30s to establish thermal equilibrium of the sample.
5. Take 1000 images while the sample is heated.
6. Again block the pump beam and wait 30s for sample to cool before taking the final set of 500 images.

In order to take multiple measurements for a sample without realignment steps 3-6 are repeated. A noise measurement is run immediately before and after each measurement, which is discarded if there is significant systematic structure or noise observed. This ensures no systematic noise is present in the wavefront measurement. It was determined that 30s is sufficient to return the sample to thermal equilibrium by measuring the deformation ranging this waiting time from 30 s to 360 s in the N-BK7 sample and there was no observable difference in the measured deformation. Thus, this method will be used to measure the thermally induced WFD.

4.5.1 Effect of scatter on measurement

A significant source of optical loss in the current quality of ZBLAN is extrinsic scatter. Small contaminants, bubbles and crystallization can act as scattering points, disrupting a small region the wavefront. Small scattering points are unlikely to affect the wavefront as single extraneously large gradients are removed before processing. However, this system is sensitive scattering points large enough to noticeably scatter light from reaching the end of the sample and require samples without large scatterers, or measure regions free of these scatters.

Another source of scatter is striations which are large scale changes in density, can cause larger regions of the wavefront to be distorted. An example of the appearance of the wavefront after passing through a ZBLAN sample with striations is shown in Fig. 4.11.

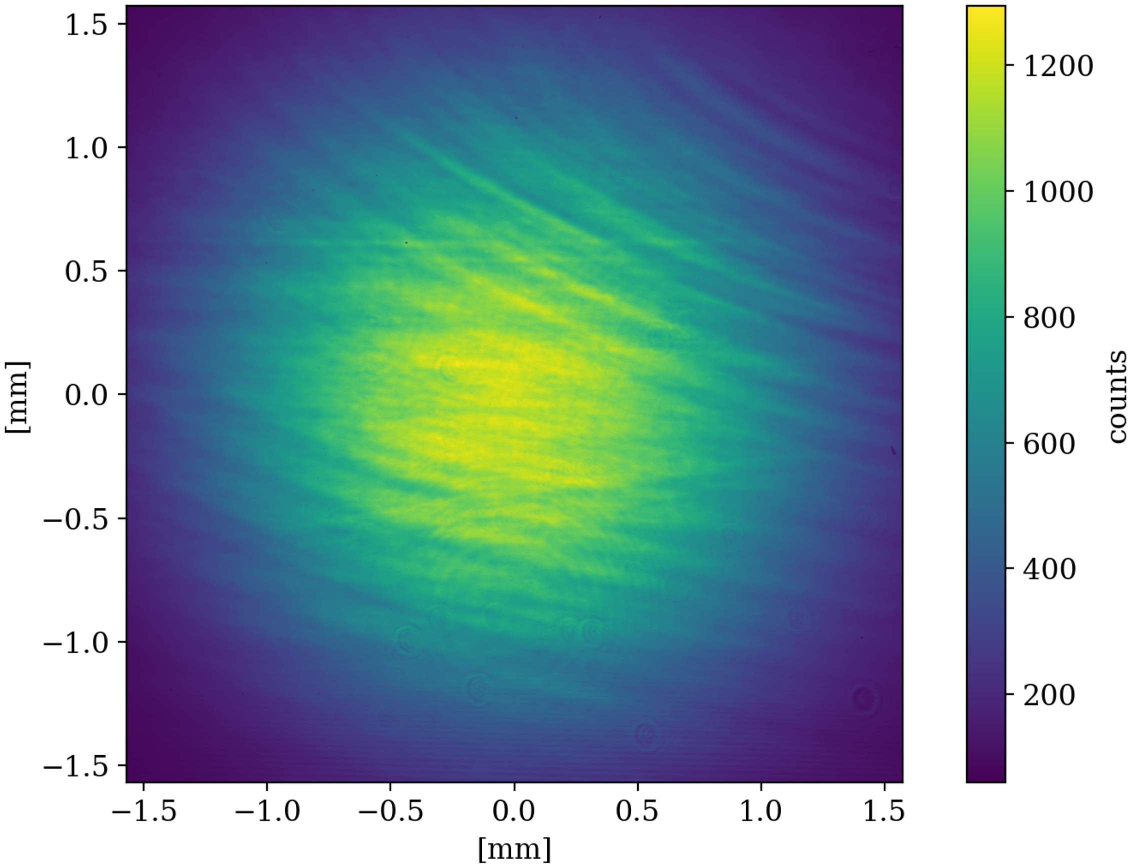

Fig. 4.11 Image of the deformed probe beam wavefront after passing through ZBLAN sample with striations, imaged at the back face of the sample.

Without heating the sample, the effects of striations are minimal as this measurement is differential. When the sample is heated the path of the probe beam which goes through the striation is minutely changed with comparison to wavefront after an unheated sample. This can cause striation like structure to appear in the differential wavefront. If the change in refractive index is small the probe beam may become diffused by fluctuations through the sample broadening the bulk absorption and noise features of the profile. Due to the quality of the fits demonstrated in chapter 5 this effect seems unlikely.

I use samples without observable striations on the probe beam, when imaging the probe beam through the sample. Furthermore, we do not notice in the measured wavefront deformation that there is consistent structure on the wavefront that could be due to the striations, which we would expect to move with the sample. Thus a full analysis of the effects is outside the scope of this work.

4.6 Measurement system validation using N-BK7

I aim to use the measurement system outlined in this chapter to determined the absorption coefficients accurately in low-loss glasses by fitting the imaged WFD to the predicted WFD described in chapter 3. The accuracy of model is dependant on the system and glass parameters used to predict the WFD and does not use calibration. To verify the model and system a Schott N-BK7 glass sample, with known parameters, was measured and the best fit α were determined.

N-BK7, a borosilicate glass, was selected for this verification measurement as all parameters required for modelling are given by the manufacturer, it is transmissive at the probe beam wavelength of 830 nm and has a large enough absorption that the noise floor will not limit this measurement. The increased absorption, however, requires extra considerations to ensure my model is applicable.

In this section, I first determined the expected absorption at 1995.5 nm by completing a fit to the Schott data informed by Rayleigh scattering and multi-phonon absorption losses. Then using the off-axis measurement system described above the thermally induced WFD was imaged and fit to the model developed in chapters 2 and 3 to determine α and β. To investigate the reproducibility and accuracy of the system and model measurements was conducted at multiple powers.

4.6.1 Expected absorption in N-BK7

NBK-7 was selected as its parameters are well known, including the internal transmission (T). Schott gives T at a discrete range of wavelengths [52]. Assuming all loss behaves exponentially, like absorption, it can be converted into a total loss coefficient (α_{tot}) using,

$$\frac{P_{out}}{P_{in}} = T = \exp(-\alpha_{tot} l) \tag{4.3}$$

where l is the length of the sample, shown in Fig. 4.12.

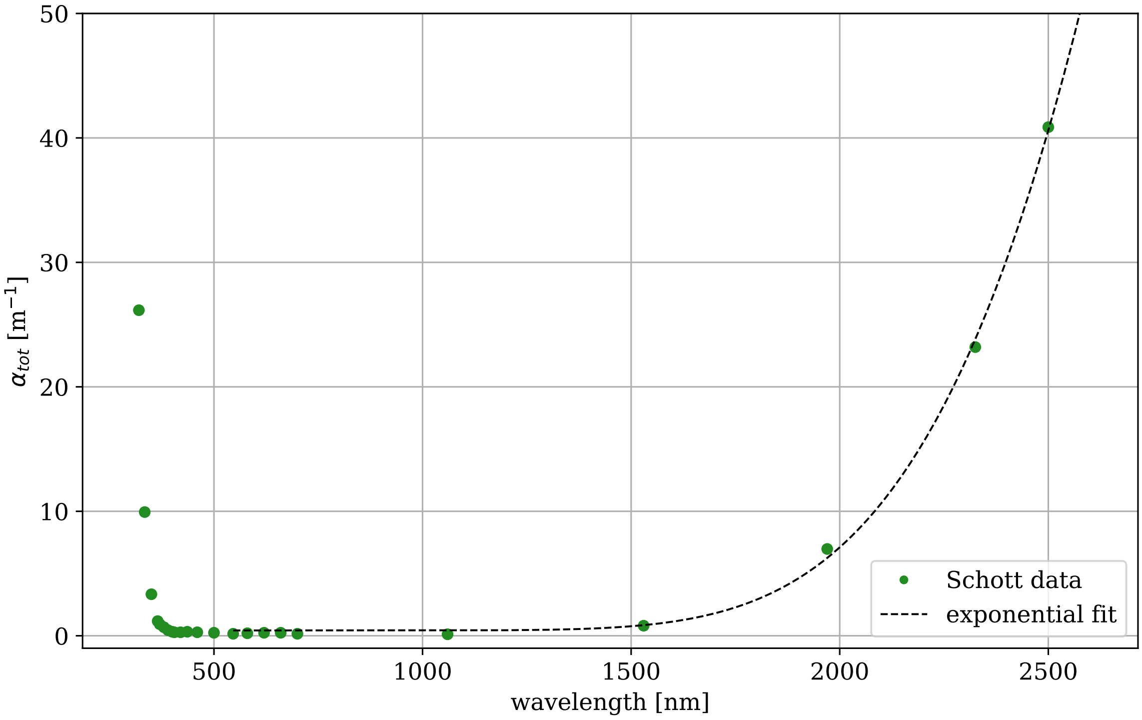

Fig. 4.12 Plot of the Schott N-BK7 loss spectrum derived from internal transmission data from the manufacturer data sheet (green dots) [52] and a fit using Equation (4.5) and Equation (4.4) fitting from where scattering became dominant (plateau).

To determine the absorption coefficient at 1995.5 nm it is assumed that the spectra towards the IR is dominated by Rayleigh scattering and multi-phonon absorption. This is fit to the data as the sum of the Rayleigh scattering loss($\alpha_R(\lambda)$),

$$\alpha_R = \frac{B}{\lambda^4} \tag{4.4}$$

where B is a constant term and the multi-phonon absorption loss($\alpha_M(\lambda)$, which can be simplified to an exponential term with the form,

$$\alpha_M = a\exp\left(-\frac{b}{\lambda}\right) \tag{4.5}$$

where a and b are material constants France *et al.* [2]. At 1995.5 nm the loss is predicted to be $6.93\,\mathrm{m}^{-1}$.

The loss at this wavelength maybe in part due to scattering but is likely dominated by multi-phonon absorption at the wavelength of interest, thus, it is assumed $\alpha = 6.93\,\mathrm{m}^{-1}$. Furthermore, the loss at exactly 1995.5 nm was not measured and there could be other absorption peaks due to contaminants at this wavelength or variations in absorption between batches. Other measured spectra of N-BK7 do not demonstrate any large structure in this wavelength range so it is expected that the true value is approximately $6.93\,\mathrm{m}^{-1}$.

4.6.2 Considerations for modelling a strongly absorbing glass

The N-BK7 and ZBLAN parameters which describe the effects of heating are of a similar order of magnitude, as shown in Table 4.1. N-BK7 has a smaller and positive thermo-optic coefficient and conversely to ZBLAN the TE effects will dominate. N-BK7 is also a significantly stronger absorber by 3 orders of magnitude at 1995.5 nm . The N-BK7 sample is uncoated but may have some surface absorption due to contamination on the surface such as water due to unideal and unknown storage conditions.

Parameter	**Symbol**	**ZBLAN**	**N-BK7**	**Unit**
Absorption Coefficient	α	≈ 0.005	7.67	$[\mathrm{m}^{-1}]$
Thermal conductivity	K	0.628	1.114	$[\mathrm{Wm}^{-1}\,\mathrm{K}^{-1}]$
Density	ρ	4330	2510	$[\mathrm{kg\,m}^{3}]$
Thermo-optic Coefficient	$\frac{dn}{dT}$	14.75	≈ 1.07	$[10^{-6}\,\mathrm{K}^{-1}]$
Specific Heat Capacity	C_p	151	858	$[\mathrm{J\,K}^{-1}]$
Coefficient of thermal expansion	α_{exp}	17.2	7.1	$[10^{-6}\,\mathrm{K}^{-1}]$
Poisson's Ratio	σ	0.17	0.206	-
Young's Modulus	Y	58.5	82	[GPa]

Table 4.1 Table comparing of parameters used to model thermal effects for ZBLAN and N-BK7, showing similar magnitude glass parameters with the exception of absorption which is measured to be much larger in BK7.

To apply my model, which assumes weakly absorbing glasses, the measurement was run at less than 30% of the power than used for ZBLAN. Despite this two further considerations are taken for N-BK7 due to its large absorption. Foremost, the absorption through the sample is not considered negligible on the power of the beam with beer-lamberts law,

$$P_{beer}(z) = P_{pump}\exp\{-\alpha z\} \tag{4.6}$$

predicting a 7.3% loss over the length of the sample. Instead the power at any point z along the axis of heating will be described as the first order Taylor expansion of $P_{beer}(z)$,

$$P_{beer}(z) \approx P_{pump}(1-\alpha z) \tag{4.7}$$

which predicts a 7.5% loss over the sample length, attributing only 0.2% error to the best fit α for N-BK7, which is below the error in the fit, discussed below.

To ensure the profile of WFD is still proportional to power when the absorbed power is larger, the measurements were taken at the powers 0.57 W, 0.84 W and 1.115 W, which I will refer to as P_1, P_2 and P_3. Normalising each of these deformations with power gives an identical profile which is demonstrated in Fig. 4.13 showing the residuals of the deformation cross-sections using P_1 and P_2 against P_3.

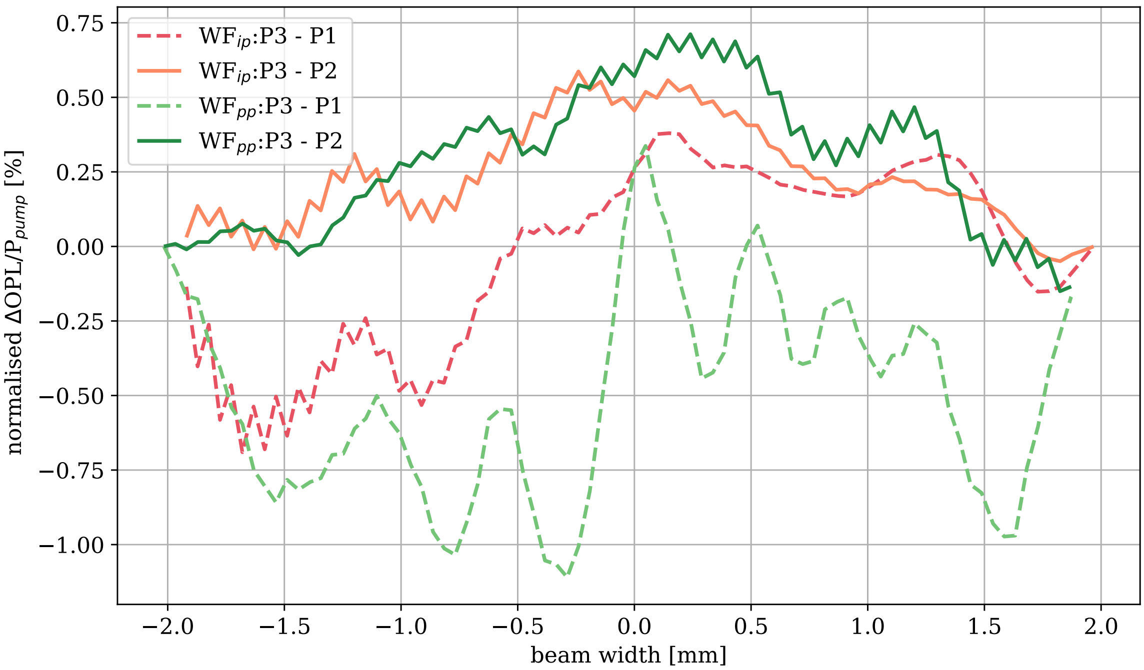

Fig. 4.13 Plot of the normalised wavefront deformations that were measured in BK7 at the powers 0.57 W, 0.84 W against the deformation at 1.115 W, for the probe beam cross-sections. All profiles are normalised with respect to the pump power used. Small fluctuations over 1% of the deformation profile are observed but do not have significant structure.

Additionally, due to the higher absorption the thermo-optic coefficient $\frac{\partial n}{\partial T}$ cannot be considered constant as the maximum ΔT is 13 K which increases $\frac{\partial n}{\partial T}$ by 14% from ambient temperature, for a N-BK7 sample modelled with the parameters in Table 4.1. The $\frac{\partial n}{\partial T}$ at each point of the COMSOL generated temperature distribution is calculated using,

$$\frac{\partial n}{\partial T} = \frac{n^2(\lambda,T_0)-1}{2n(\lambda,T_0)}\left(D_0+2D_1\Delta T+3D_2\Delta T^2+\frac{E_0+2E_1\Delta T}{\lambda^2-\lambda_{tk}^2}\right) \tag{4.8}$$

where, n is the refractive index at the wavelength λ, T_0 is the ambient temperature and D_0,D_1,D_2,E_1,E_2 and λ_{tk} are coefficients given by the Schott datasheet [52]. The WFD will be most effected at the centre, the section of the probe beam which transmits through the hottest section of the sample, creating a narrower deformation profile.

With these consideration in mind the described PTMS system can be adapted for the N-BK7 sample.

4.6.3 Model and system optimization for N-BK7

The N-BK7 sample is a thin disc of radius 24.5 mm and average width of 9.88 mm. The sample is slightly wedged with the largest width of 10.22 mm and shortest of 9.50 mm. FEM models were created for a the wedged geometry and cylinder with length 9.88 mm, using the values for N-BK7 in Table 4.1. Residuals between the ΔOPL_{ip} and ΔOPL_{pp} calculated using each model is 0.2% and 0.4% respectively, thus the wedged surface does not have a significant effect and a cylindrical model will be used.

The N-BK7 sample was mounted in ring mount ensuring consistent boundary conditions. Conduction from the contact of the mount is assumed to not influence the results as the sample size is much larger than the heating beam (w_x,w_y = 1.065 mm,1.06 mm) and probe beam (w=7.8 mm).

The sample was measured using a pump power of 2.20W with a probe beam angle of incidence of $\theta_i = 0.284$ rad, to allow surface absorption to be distinguished, using the method described in section 4.5.

4.6.4 Absorption measured in N-BK7

The WFD was measured using a pump power of 2.20W, taking 8 measurements over 2 days. An example wavefront and measurement noise floor is shown in Fig. 4.14.

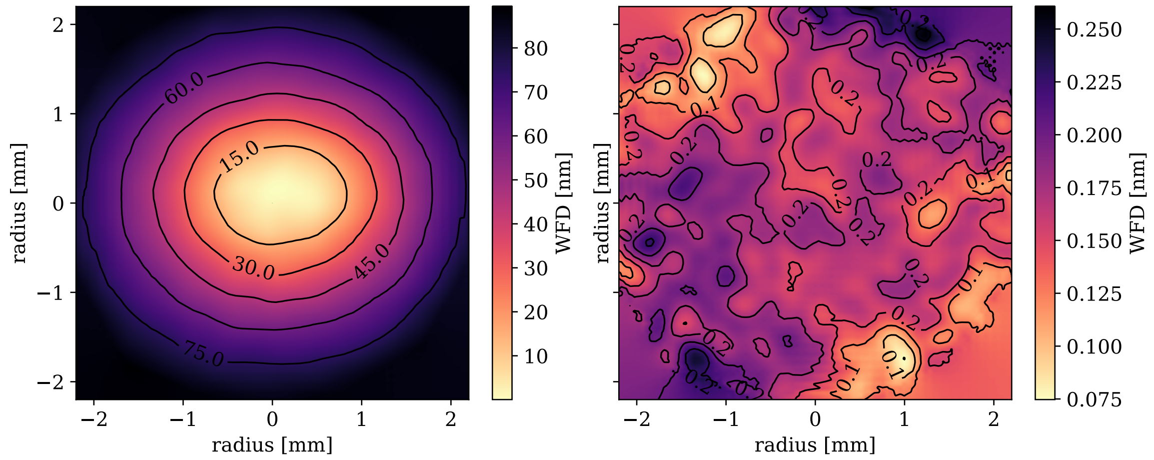

Fig. 4.14 Plot of the WFD of the probe beam measured on the DHWS (left) and the noise floor measured immediately before taking data (right). The signal to noise for this measurement is demonstrated to be approximately 343:1.

The cross-sections of the WFD corresponding to the plane of incidence, WFD$_{ip}$, and the perpendicular slice, WFD$_{pp}$, were extracted as the horizontal and vertical slices corresponding the maximum given by a 2D Gaussian fit to the centre of the deformation. From visual inspection WFD$_{ip}$ is the x axis of the wavefront map as expected. This is consolidated by a measurement in Section 5.4 that shows that translating the sample in x direction moves an anomalous absorber along the x axis in the measured wavefront map. The regions of the wavefront map less than the noise floor were removed from the radial extents before fitting.

The WFD$_{ip}$, and WFD$_{pp}$ slices were fit to by a predicted WFD, using the parameters in Table 4.1, as shown in Fig. 4.15.

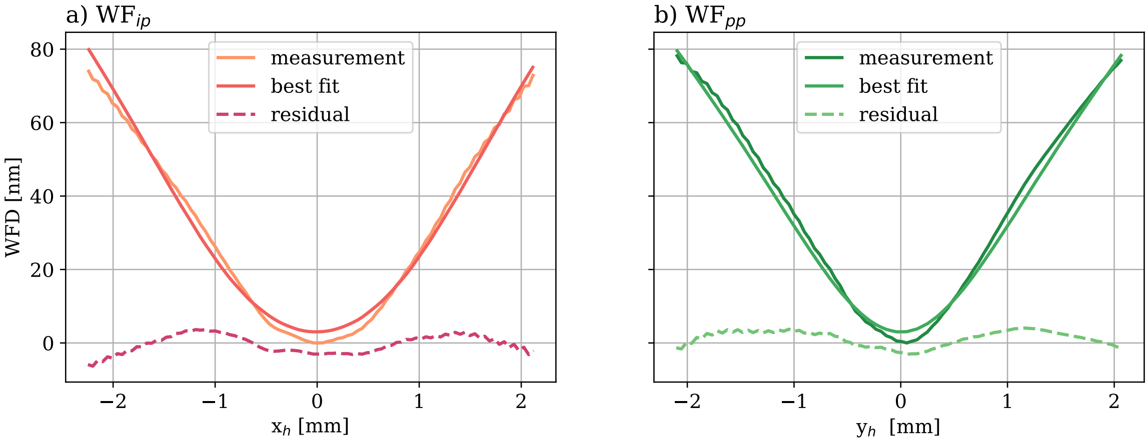

Fig. 4.15 Plot of the average of 3 WFD slices $WF_{ip}(x_h)$ (a) an $WF_{ip}(y_h)$ (b) and the fitted curve using the model outlined in chapter 3, for $\theta_i = 0.284$rad and $P_{pump} = 2.20\,$W.

For each of the 8 measurements α and β were fit for and the averages were found to be α = 6.95 m^{-1} with a standard error in the mean of 1.1% and β = 2800 ppm with a standard error in the mean of 8.2%. The variation in both values is due to the relatively small deformation due to surface absorption compared to bulk absorption, causing the surface or bulk contributions to be assigned to the other. I have also calculated a $\pm^{7.7}_{7.6}\%$ error due to the uncertainties in the parameters used in the fit for bulk absorption and calibration error in the power meter used to determine pump power, described in appendix D.

As discussed in the previous chapter, under the assumption of homogenous surface and bulk absorption, the best fit α value calculated using different angles of incidence should give the same values of α when fitting using the accurate value of β. Thus, I will additionally take and average 4 measurements at $\theta = 0.074$ rad and the first day averaged measurements at $\theta = 0.284$ rad and sweep surface absorption fitting for α to determine where ($\alpha_{\theta=0.284}$,$\beta_{\theta=0.284}$) =($\alpha_{\theta=0.074}$,$\beta_{\theta=0.074}$), as shown in Fig. 4.16.

Whilst there is no intersection there is significant overlap of the uncertainty bounds. The uncertainty bounds consider the random errors which effect the fit and would cause variation between measurements which were determined to be $^{+2.7}_{-2.6}\%$ where $\theta_i = 0.284$ rad and $^{+2.5}_{-3.1}\%$ where $\theta_i = 0.074$ rad. The stated uncertainty bounds are the maximum bound and are examined in greater detail in appendix D. By determining the edge of the uncertainty overlap I set a maximum limit of surface absorption to 3200 ppm corresponding to a bulk absorption of $6.6\,\mathrm{m}^{-1}$. If surface absorption was negligible the value determined does not agree with the theoretical absorption within the uncertainty bounds but based on the low error in the fit using β and α this is unlikely. I predict the cause of the lines separation to be due to systematic factors between the measurements such as power fluctuations. There is additional uncertainty in α determined using this intersection method due to the 5% inaccuracy of the power meter which would act as a scaling factor for both geometries, thus, would only effect the α term of the intersection point not β.

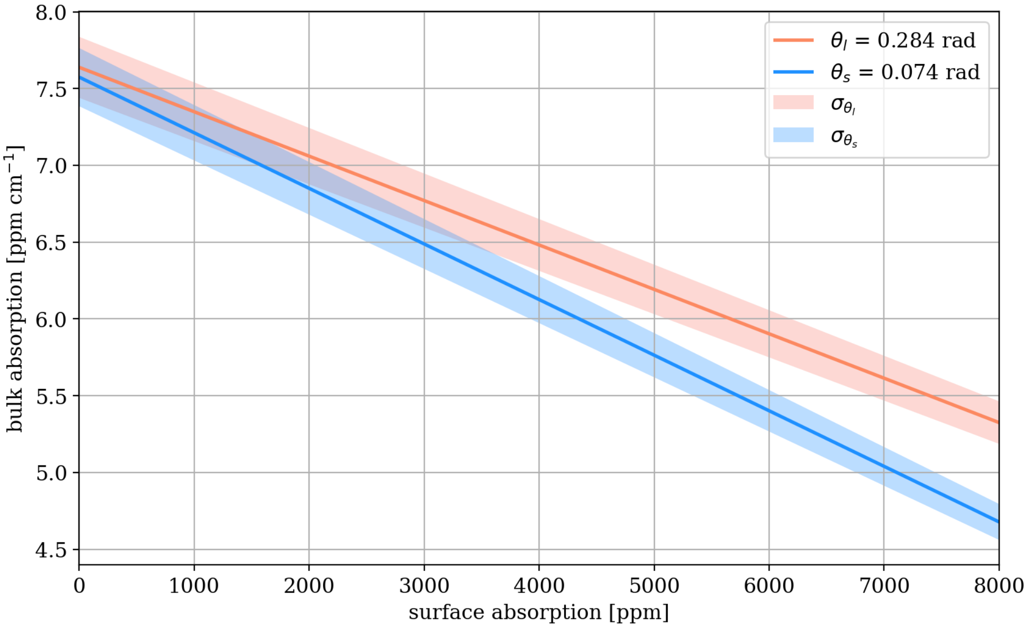

Fig. 4.16 Plot of the fitted value of α for swept values of β using $\theta_i = 0.074$ rad and $\theta_i = 0.284$ rad. The uncertainty in these values is dictated by the shaded areas.

Thus, I have determined, with considerations for surface absorption, that the absorption in NBK-7 is $6.95\,\mathrm{m}^{-1}$ with a standard error of 1.1%, which is very similar to the value predicted above from the loss spectrum, $6.93\,\mathrm{m}^{-1}$. This verifies that the model accurately describes the PTMS described above as the sample parameters are well known, thus only system parameters should cause significant errors.

4.7 Summary

The chapter describes an off-axis probe beam system as a tool to measure the WFD due to heating by a laser beam. This system was optimised for the case of a 2 µm beam in the aim to measure low-loss samples.

In the second half of this chapter I aimed to verify whether the model developed in chapters 2 and 3 accurately describe this system and can be used to determine α. However, for samples with unknown absorption this is difficult to determined, but, by using N-BK7, a sample with known parameters I could conclude that within the uncertainty bounds α could be determined. Thus, it has been demonstrated that β and α can be determined with high reproducibility and accuracy.

CHAPTER 5

ABSORPTION IN ZBLAN

5.1 Introduction

ZBLAN is predicted to have losses as low as $0.014\,\mathrm{ppm\,cm^{-1}}$ at $2.32\,\mu\mathrm{m}$, which would enable its use in future generation 2 μm gravitational wave detectors and as vastly improved telecommunication fibres [1]. However, currently ZBLAN's lowest published losses are approximately $1.5\,\mathrm{ppm\,cm^{-1}}$ at $2.56\,\mu\mathrm{m}$ [19]. To achieve these theoretically low losses the loss mechanisms must be understood and characterised independently

The absorption losses in a ZBLAN sample are measured in this chapter in the aim to determine the quality of the glass sample and demonstrate that the proposed system can measure the current quality of ZBLAN being produced. The absorption coefficients are quantified by imaging the induced wavefront deformation using the system described in chapter 4 and determine the absorption coefficients through the modelling and fitting procedures described in chapters 2 and 3.

Measuring absorption in ZBLAN is difficult. Even the current standard of ZBLAN has very small absorption losses. The measurable distortion is further limited as the size of the sample is constrained by the rate of crystallisation while heating and cooling in manufacturing [16]. Additionally, the opposing TR and TE effects reduce the total wavefront distortion. To ensure high signal to noise as well as the ability to measure surface absorption, three probe beam angle and sample orientation combinations will be used as discussed in Section 5.2. The measured wavefront distortion and noise floors for each case will be shown in Section 5.3 and the bulk absorption coefficient are determined in each case. In one orientation the ability of the system to detected homogeneities in absorption was demonstrated by the measurement of an anomalous absorber which is investigated in Section 5.4.

In section 5.3.4 I discuss how the varying profile of the distortion caused by surface absorption for different orientations, different incident angles and the cross-section of the probe beam allows the surface absorption coefficient to be determined. The uncertainty in α and β due to variation in system parameters and sample parameters used in the model was investigated and estimated in Section 5.5.

Finally, I will discuss modifications to this system to allow theoretically low absorption ZBLAN to be measured in Section 5.6.

5.2 Optimisation to quantify weak absorption in small samples

In this chapter I quantify the absorption coefficients of ZBLAN sample with the dimensions shown in Fig. 5.1. The small dimensions are a trade-off for a high quality bulk ZBLAN sample, constrained by the crystallisation rate during cooling [16]. Large samples cool slower resulting in more crystallisation and scatter leading to larger losses. The small sample size limits how easily surface absorption can be quantified by restricting the angles of incidence and reduces the signal to noise ratio.

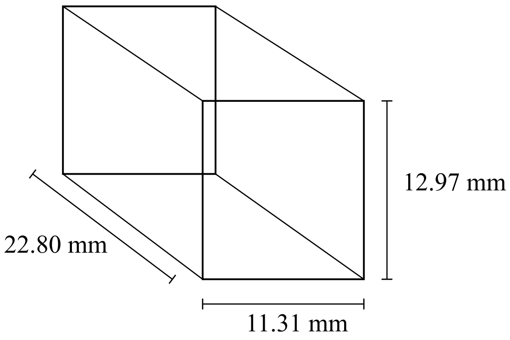

Fig. 5.1 Schematic of ZBLAN sample showing dimensions

The surface absorption is expected to be small as the sample faces were polished which should remove contaminants imbued in the surface during manufacturing, but polishing can incorporate OH^{-1} into the surface, made worse by prolonged exposure to moisture in air [2]. To prevent additional surface contamination the ZBLAN sample is stored in a box with desiccant.

Three sample measurement configurations were used, as shown in Fig. 5.2.

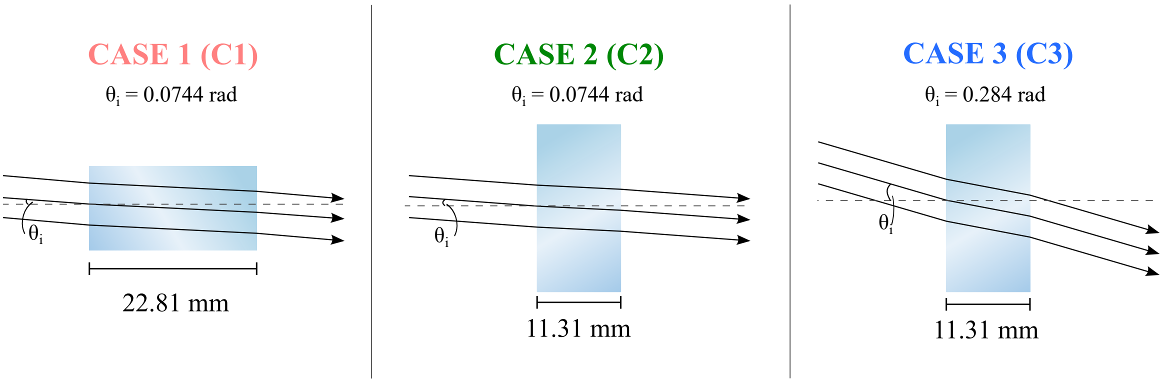

Fig. 5.2 Schematic showing the three angle and sample orientation combinations of the ZBLAN sample measured.

and defined in Table 5.1.

Geometry	angle [rad]	face width [mm]	face height [mm]	z axis [mm]
C1	0.0744	11.31	13.915	22.81
C2	0.0744	22.81	13.915	11.31
C3	0.274	22.81	13.915	11.31

Table 5.1 Description of the three angle and sample orientation combinations for the ZBLAN sample measurement. The face width dimension is in the plane of incidence and the z axis is the direction of propagation of the heating beam.

Configuration C1, heats along the longest axis causing the largest signal and makes the measurement less sensitive to surface absorption, but only a small θ_i could be used. Modelling in Chapter 4 demonstrated that with a small angle of incidence surface absorption induced distortion in C1 is too similar to bulk thus β can't be accurately determined in this case. Configuration C2, had exactly the same optical layout as C1 but the sample was rotated about vertical axis, which will reduce the signal size, but surface absorption will account for a larger proportion of the WFD. Configuration C3 used a larger θ_i and thus enabled a better measurement of β, as at greater angles the distortion due to surface effects becomes more distinct. The results for each configuration are presented in the next section.

5.3 Quantifying bulk absorption through the measurement of wavefront deformation

5.3.1 C1 Configuration

Using the C1 configuration the wavefront deformation was measured in blocks of 4 measurements that were repeated over 4 consecutive days to investigate reproducibility. The measurement system was not changed during this data collection but the sample was removed and stored in a moisture free environment at the end of each days measurements. Thus, there may be small changes in the sample orientation.

The average wavefront distortion and the measurement noise floor for the 4 measurements on day 1 is plotted in Fig. 5.3. The major and minor axis cross-sections for the average of the day 1 data and the best fit is shown in Fig. 5.4.

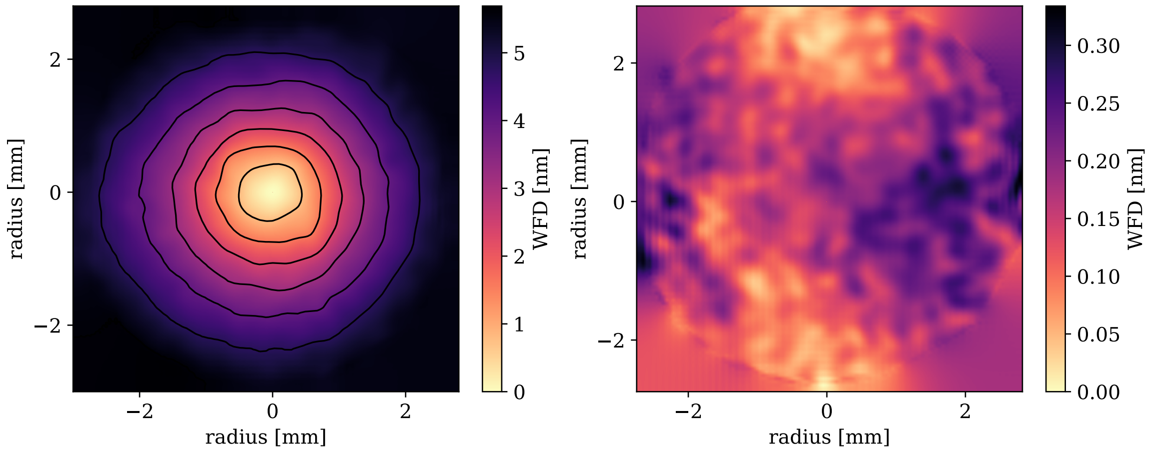

Fig. 5.3 The average wavefront distortion from 4 measurements taken in the C1 alignment show a smooth deformation, without obvious noise structure, plot on the left. The measurement noise is as expected for the 1000 averaged frames taken yielding a 16:1 SNR, shown in the right figure.

As in this configuration β cannot be found through fitting, the data from each day was analysed by setting $\beta = 0$ ppm and β = 3.5 ppm, the maximum bound of surface absorption β from Section 5.3.4, in the model. The resulting bulk absorption coefficients are plotted in Fig. 5.5a and Fig. 5.5b. The averaged best-fit α for both β values and the standard error in the mean are given in Table 5.2.

β [ppm]	best fit α [ppm cm^{-1}]	standard error in the mean [ppm cm^{-1}]
0	47.2	0.4
3.5	46.2	0.4

Table 5.2 The average α for the 12 wavefront distortions measured over 4 days for C1 for $\beta = 0$ ppm and $\beta = 3.5$ ppm

Despite not being able to determine surface absorption in this configuration, it can be seen that even using a small θ reduces the effect of undiagnosed surface absorption from ca. 7% if $\theta_i = 0$ of the bulk absorption to 2%.

The variation in both Fig. 5.5a and Fig. 5.5b is very similar, represented by the approximately equal standard errors. The small standard errors in the fit show that the measurement system is reproducible despite environmental, power and random noise effects. Uncertainty in the system parameters used in the fit approximately adds an additional ±8.5% error which is discussed in Section 5.5.

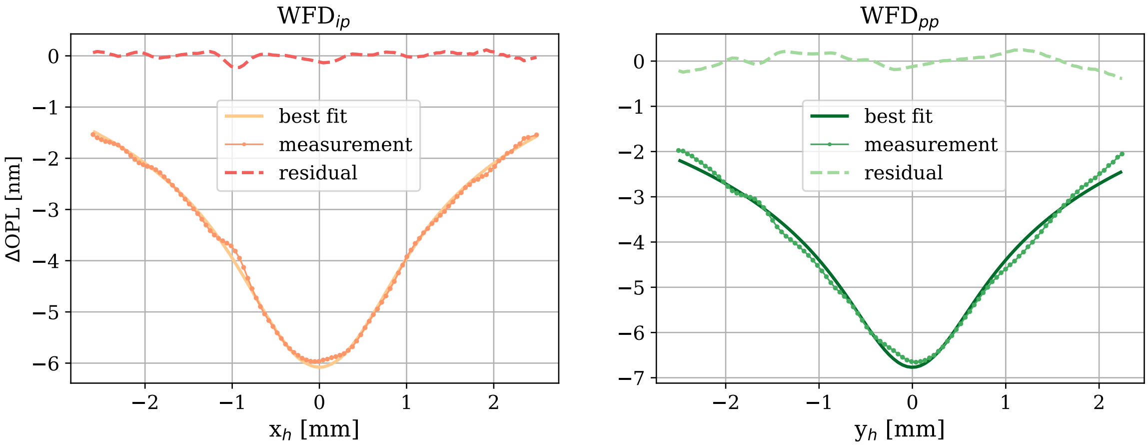

Fig. 5.4 Fitting to 1st day average WFD$_{ip}$ (left) and WFD$_{pp}$ (right) cross-sections using β=0 ppm showing the measured deformation is well described by the model.

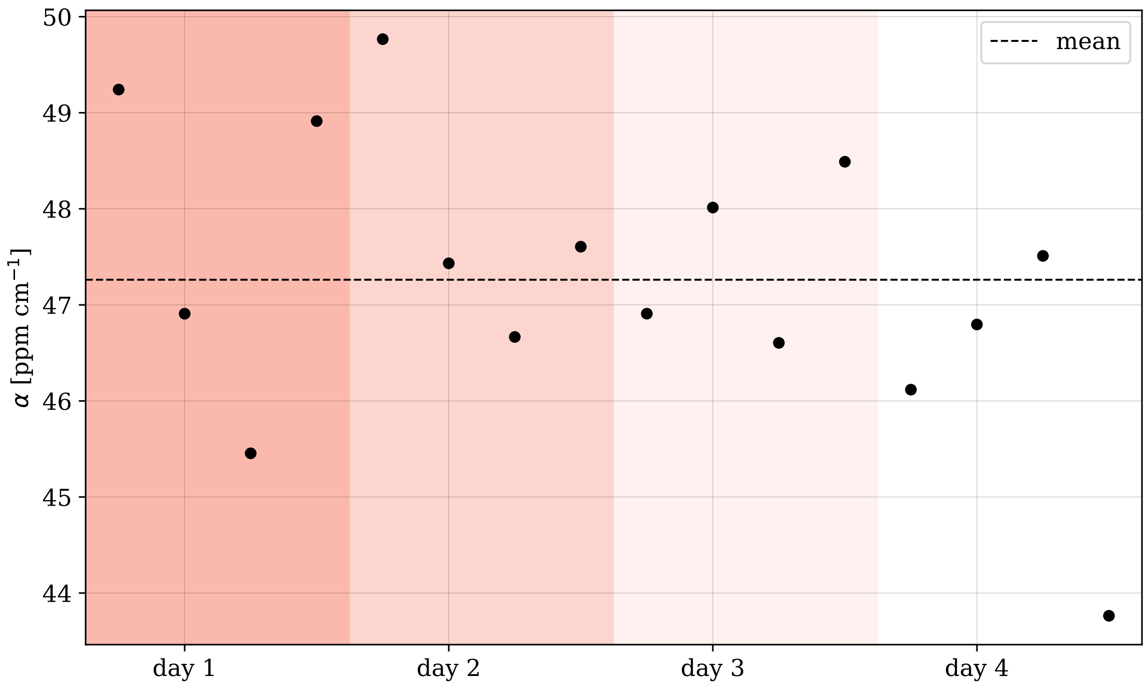

(a) β = 0 ppm

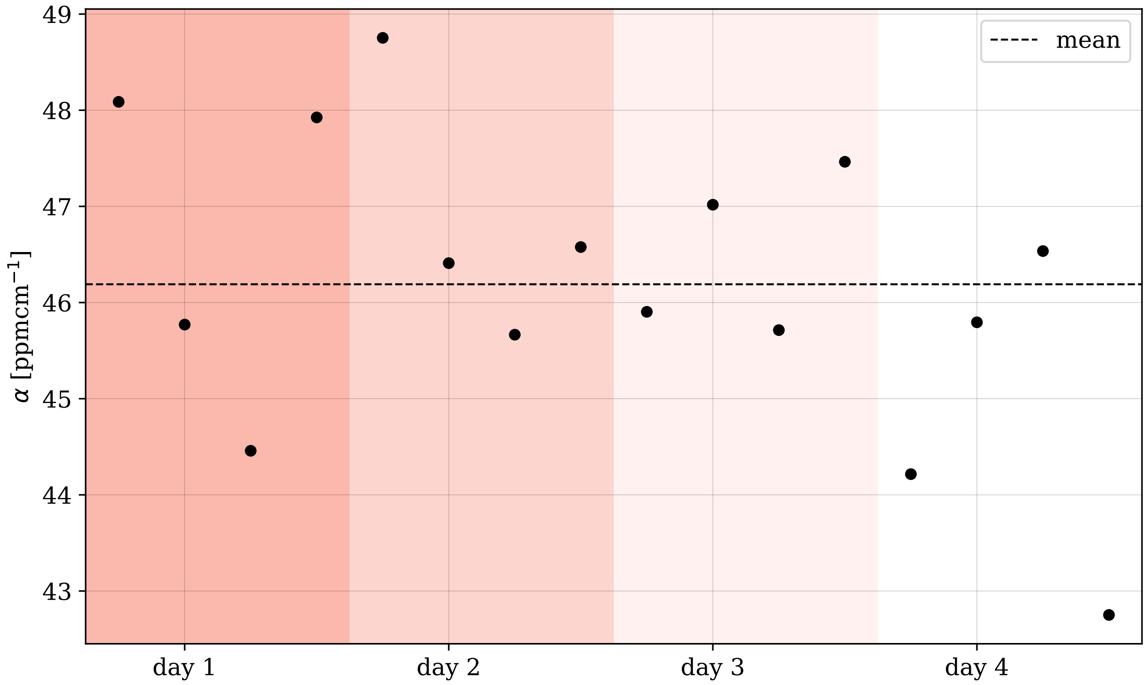

(b) β = 3.5 ppm

Fig. 5.5 The best fit α values for measurements taken over 4 days, using (a) β= 0 ppm and (b) β= 3.5 ppm demonstrate random variation around the mean value consistent with that expected for data effect by random noise. Thus the uncertainty in this measurement can be represented as the standard error in the mean.

5.3.2 C2 Configuration

Once again 4 measurements were taken in this configuration and the 4-measurement average wavefront distortion and best fit, assuming $\beta = 0$ ppm for C2 are plotted in Fig. 5.6 and Fig. 5.7.

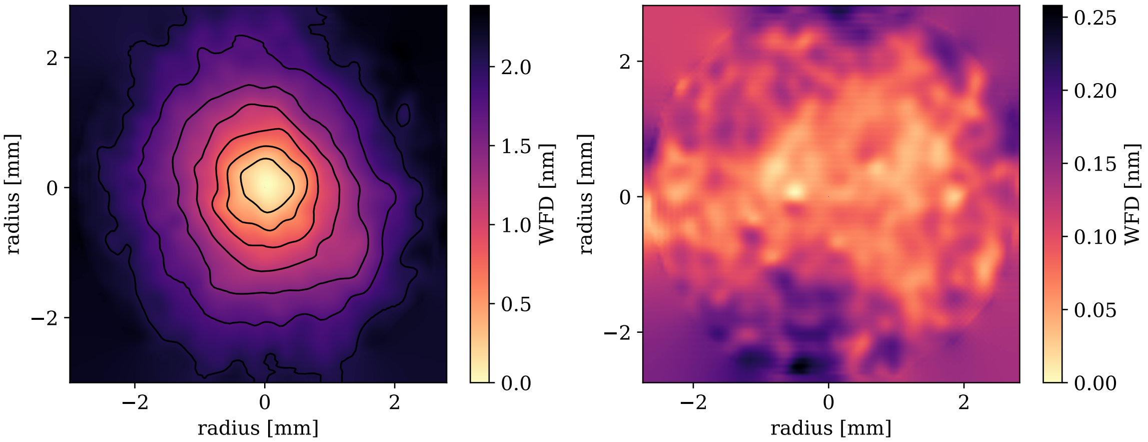

Fig. 5.6 The average wavefront distortion of the 4 measurements taken in ZBLAN (left) and the noise floor for C2 (right).

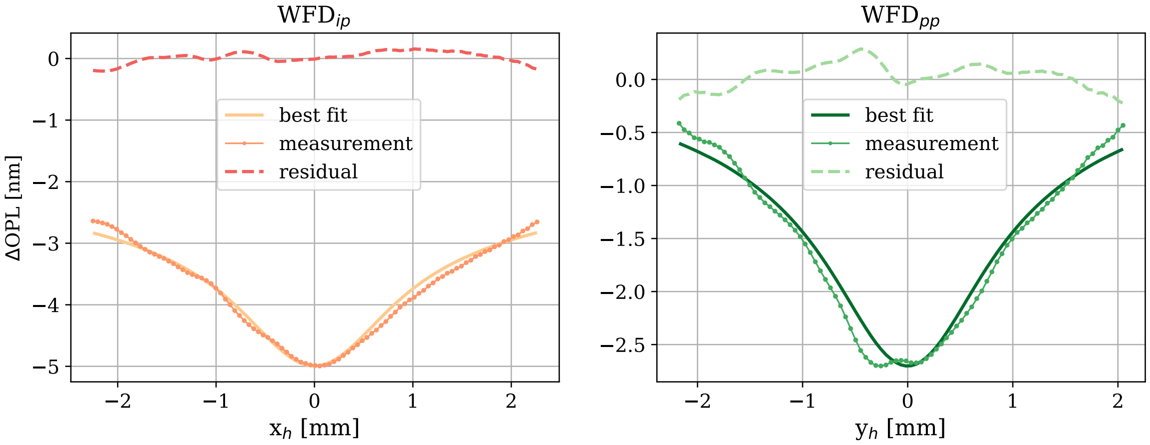

Fig. 5.7 The FEM fit to the day 1 averaged wavefront measurements for the cross-sections WFD$_{ip}$ (left) and WFD$_{pp}$ (right) in C2 are shown in this figure, allowing it to be observed that there is an anomalous absorber in the WFD$_{pp}$ slice.

As expected, there is less distortion and a worse SNR than for C1 and the least-squares fit is poorer. The C2 measurement orientation was selected as it should be most effected by surface absorption due to heating along the shorter axis and small θ_i, thus through comparison with the other orientations surface absorption could be inferred with the least uncertainty. However, there is evidence of an anomalous absorption in the WFD$_{pp}$ cross-section thus data taken using this configuration will not be used for further analysis. An investigation of this anomaly is described in Section 5.4.

5.3.3 C3 Configuration

Data for this orientation was once again taken in blocks of 4 and repeated for 2 consecutive days. A typical averaged wavefront distortion is given in Fig. 5.8. The fits to WFD$_{ip}$ and WFD$_{pp}$ for the day 1 data and the fits are shown in Fig. 5.9.

Each of the 8 wavefront distortions were again analysed using $\beta = 0$ ppm and β = 3.5 ppm. The resulting bulk absorption coefficients are plotted in Fig. 5.10a and Fig. 5.10b.

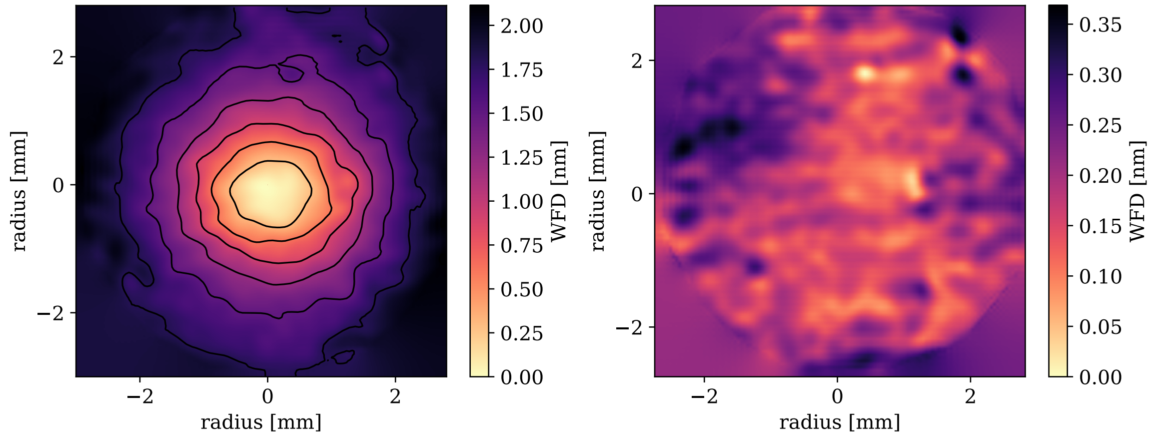

Fig. 5.8 The average of the wavefront deformation measurements taken on day 1 for C3 demonstrated a broadened distortion in the x-axis due to a larger angle of incidence, shown in the figure on the left. The average measurement noise floor is the same magnitude as in C1 but the SNR is reduced to 6:1 causing the wavefront deformation to be noticeably noisier than Fig. 5.4, shown in the figure on the right.

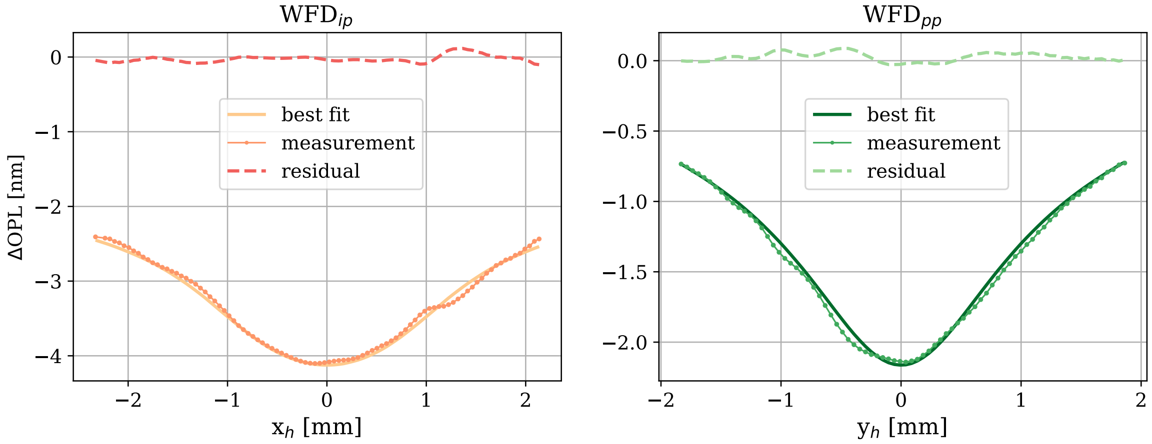

Fig. 5.9 The FEM fit to the day 1 averaged wavefront measurements for the cross-sections WFD$_{ip}$ and WFD$_{pp}$ in C3 shown in this figure. The residuals have no structure and appear to be random noise, demonstrating a high quality of fit.

A larger fluctuation is observed for C3, as expected, due to the lower SNR resulting from the smaller propagation length and larger angle, both of which reduce the magnitude of the TR distortion. The 2-day average values for $\beta = 0$ ppm and $\beta = 3.5$ ppm are shown in Table 5.3.

β [ppm]	best fit α [ppmcm^{-1}]	standard error in the mean [ppmcm^{-1}]
0	46.8	0.4
3.5	45.2	0.3

Table 5.3 Table of averaged best fit α considering different values for β for the 8 measurements taken over 2 days in C3.

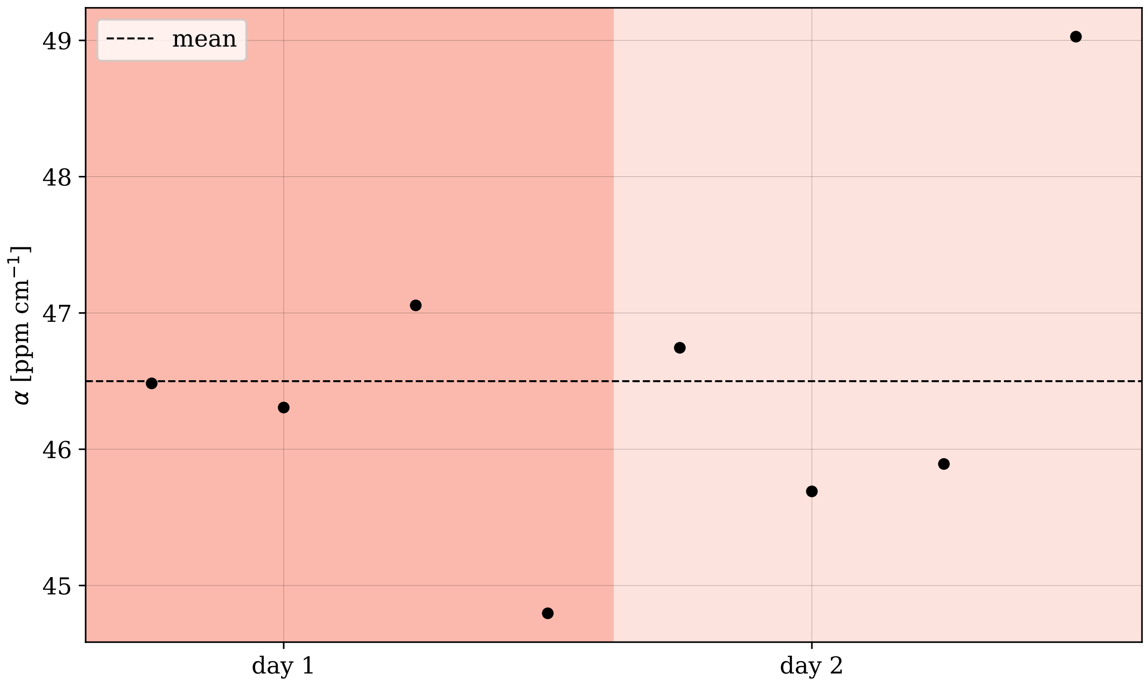

(a) $\beta = 0$ ppm

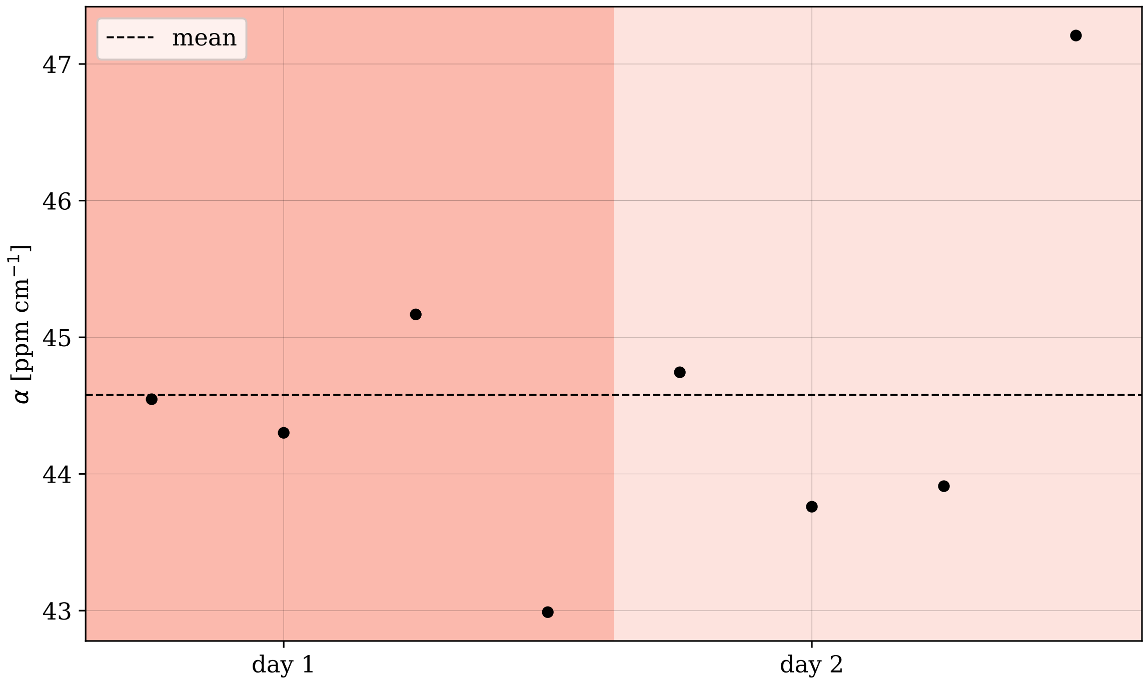

(b) $\beta = 3.5$ ppm

Fig. 5.10 Similar to Fig. 5.5 but using the 8 measurements taken over 2 days for C3, using (a) β= 0 ppm and (b) β= 3.5 ppm.

The best fit values of α for C1 and C3 are very similar for both values of β, varying by approximately 1% and are in both cases reproducible over multiple days. This variation is small and falls within the uncertainty bounds described in Section 5.5. The measured value of α for this sample is significantly above the theoretical value but within an order of magnitude of the best bulk measurement of ZBLAN currently 1.5 ppm cm^{-1} at 2.56 µm [19]. Thus, it can initially be concluded that this system can detect bulk absorptions at the 10 ppm cm^{-1} scale, which is the order of magnitude expected for absorption in samples of interest like fused silica for GW applications. However, individually quantifying surface absorption is essential for these applications and allows α to be more accurately determined. In chapter 3 modelling showed that there will be variation between the best-fit αs for C1 and C3 if there is a non-negligible β, which is observed experimentally. Thus, in the next section the presence of surface absorption is investigated.

5.3.4 Quantifying surface absorption

The results presented in the previous section suggested that the surface absorption was small. In this section I will bound the surface absorption using the results of the model in chapter 3, which states that for each angle of incidence, orientation and cross-section of the probe wavefront the best fit α will only agree when the model considers the correct value of β.

Initially, I will consider variations in WFD$_{ip}$ and WFD$_{pp}$ in C3. As described in chapter 3, the larger separation between the centres of the heating beam and the probe beam at the input and output faces (X_0 = 1.55 mm for C3 and 0.85 mm for C1) will result in more distinct differences in WFD$_{ip}$ and WFD$_{pp}$, with the former experiencing more distortion due to surface heating.

The best-fit α for WFD$_{ip}$ and WFD$_{pp}$ as a function of β for C3 day 1 and day 2 are plotted in Fig. 5.11a and Fig. 5.11b.

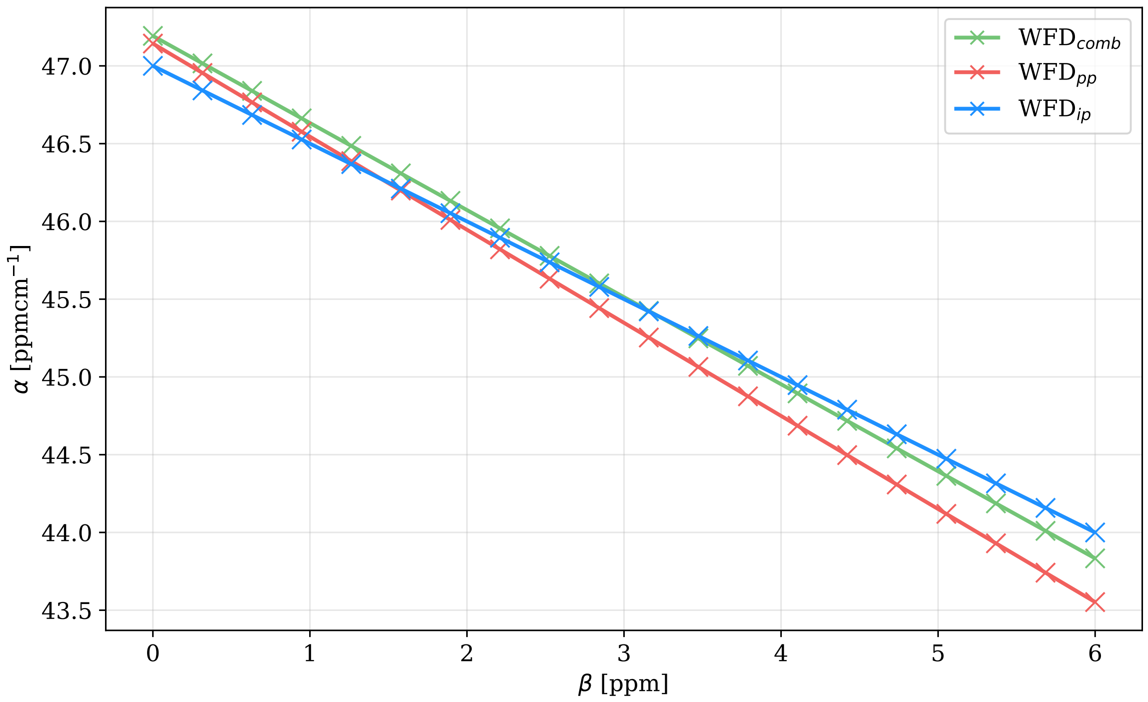

(a) day 1

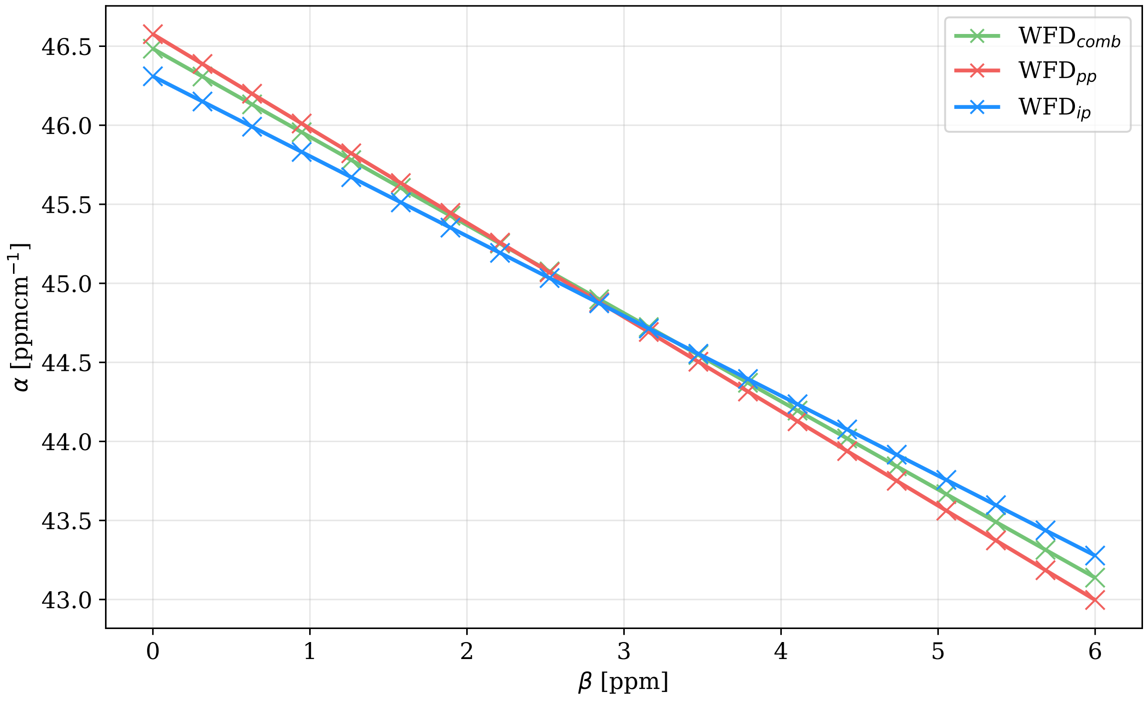

(b) day 2

Fig. 5.11 Fitting to a wavefront distortion for the best fit values for the cross-sections WFD$_{ip}$ and WFD$_{pp}$ and the combined fit, α_{pp}, α_{ip} and α_{comb} while sweeping surface absorption (β) considered in the model for day 1 and 2 demonstrates a linear relationship. The slope of the linear trend line varies for each fit and the intersection point should indicate the β and α values for the sample based on modelling in Chapter 3.

I expect from modelling in chapter 3 that each line would intersect at the point given by the surface and bulk absorption coefficients of the sample. However, it was observed that one intersection point appears in the experimental data on day 2, but day 1 data has individual intersection points for each set of lines. Thus, this analysis suggests the optimum β value is within the range 2-3.5 ppm bounded by the observed intersections from each day and that there were random noise sources effecting the data on day 1. The result of the noise is a shift in the position of the lines in terms of α. On average the values of α_{ip} and α_{comb} on day 1 are $\approx 0.7\,\mathrm{ppm\,cm^{-1}}$ larger than day 2 but α_{pp} is only shifted by $0.5\,\mathrm{ppm\,cm^{-1}}$ between days causing it to intersect at different points. The slopes for α_{pp}, α_{ip} and α_{comb} with β are constant between days. As the cross-sections are taken from one averaged image, systematic fluctuations in power or angle should effect each fit equally thus the β value is only sensitive to variations within a wavefront measurement.

It is also expected that the quality of fit would be best when surface absorption is accurately considered due to the difference in the profile of the bulk and surface induced WFD. The uncertainty in the value of α for the ordinary least squares analysis can be estimated from its covariance matrix [47] and is plotted as a function of β for C3 day 1 and day 2 in Fig. 5.12a and Fig. 5.12b. Day 1 shows the optimum β values is <6 ppm, while the day 2 suggests the optimum β is approximately 0 ppm. Thus, the previous approach in which the best fit α_{pp}, α_{ip} and α_{comb} are used to determine β appears to be more precise than using the errors in the fit.

Finally, if the absorption in the sample is uniform, then, much like for WFD_{ip} and WFD_{pp} the best fit α for the C1 and C3 measurements will only agree when the correct value of surface absorption is considered. Thus, I also plot the best-fit α as a function of β for each day in the C1 and C3 datasets shown in Fig. 5.13. Due to a systematic variation between measurements there is not a singular intersection point. In fact, not every C1 trend-line even intersects with C3 line and there is a shift in α between days of up to a 4% range for each orientation. Thus, all that can be concluded is that surface absorption is small and likely <3.5 ppm based on the largest intersection point, which is consistent with the above analysis.

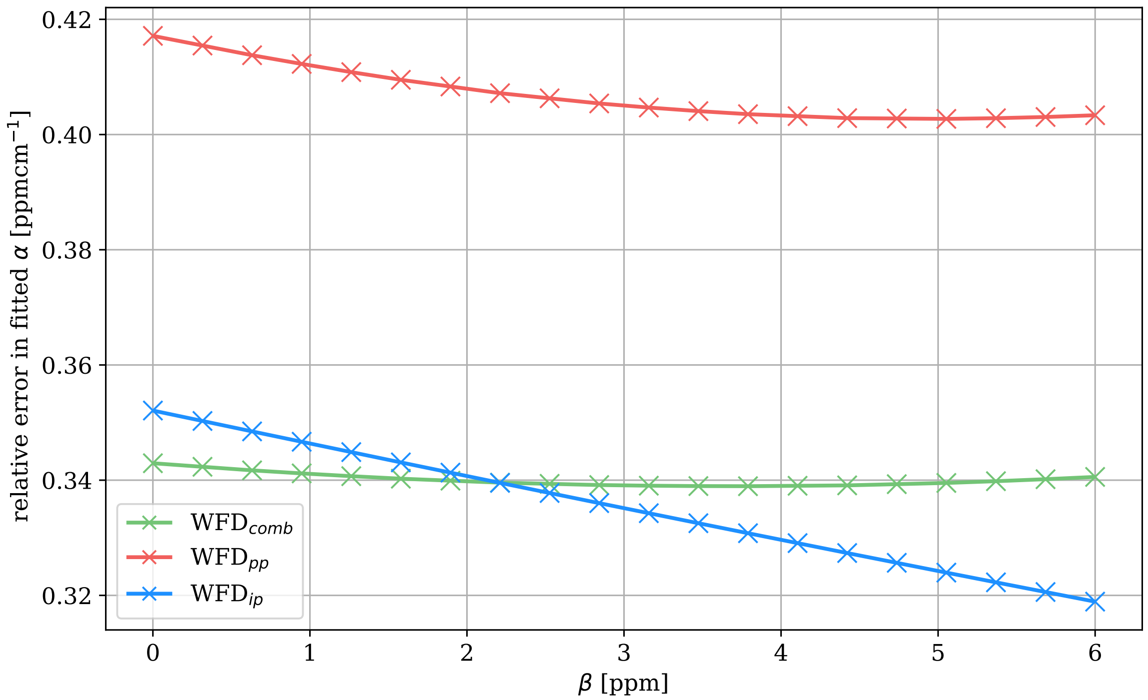

(a) day 1

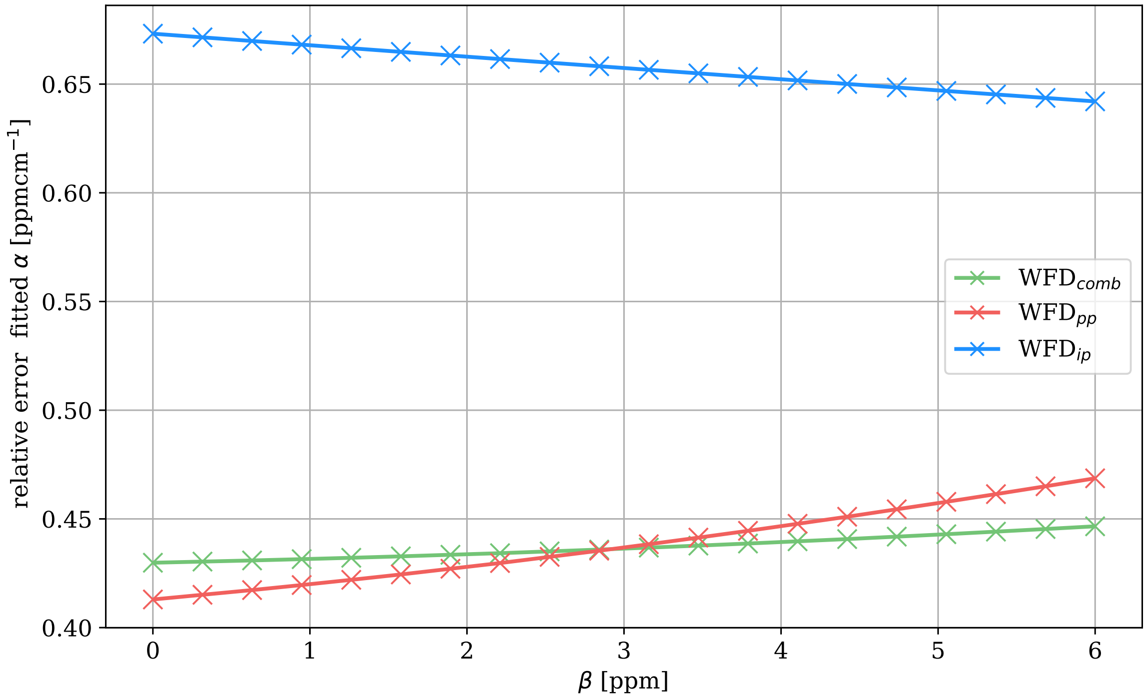

(b) day 2

Fig. 5.12 The relative error in fit the for α_{pp}, α_{ip} and α_{comb}, for the 4 measurement average taken on days 1 and 2 in C3 for a range of β, calculated as the square root of the covariance matrix.

As the slope of the change in α with increased β is constant but shifted in α the increase in variation is attributed to a combination of fluctuating power between days, as the current for the diode-pumped heating laser was controlled rather than its output power, random noise and realignment errors.

To lower the uncertainty this method could also be applied to another configuration, such as C2, which was unable to be completed for this sample due to an anomalous WFD. The initial method, using the cross-sections of averaged wavefront, is less sensitive to systematic changes and consequently is the preferable method.

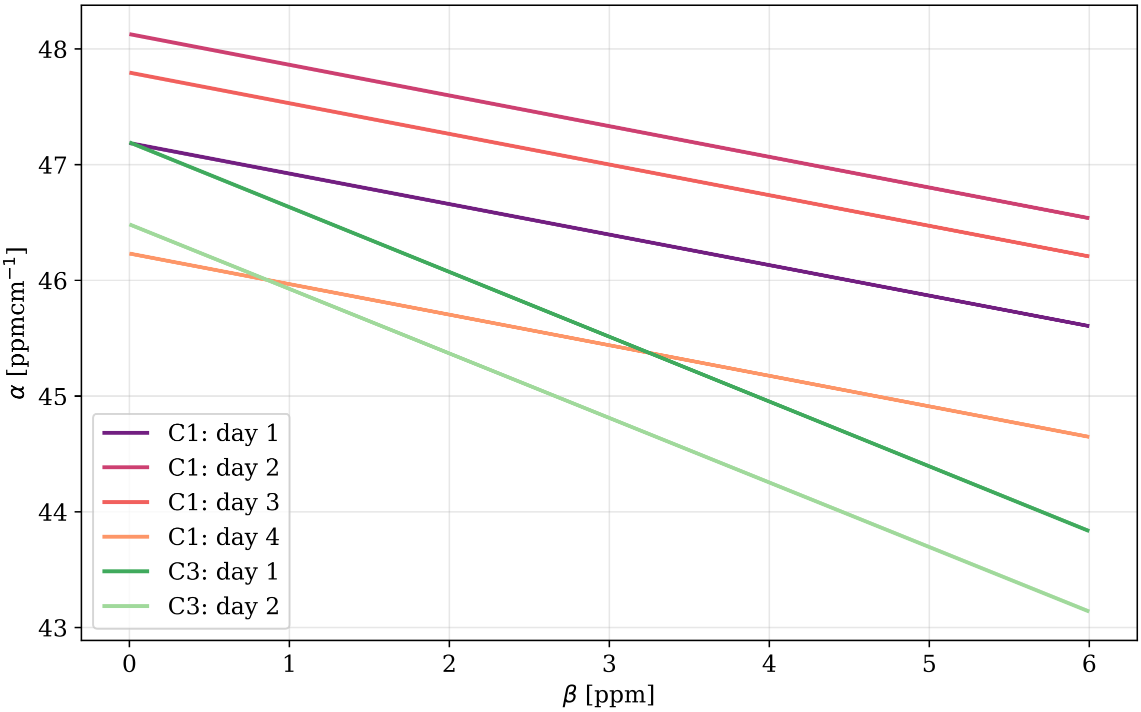

Fig. 5.13 The best fit α to the experimental data scales linearly with the surface absorption considered in the model (β) with a slope that is dependant on the optical configuration, in this case C1 and C3. The shift in terms of α is predicted to result from power fluctuations and other systematic noise effects. The surface and bulk WFD are modelled using FEM and the material parameters given in Table 3.1.

In this section I have determined that there appears to be a small amount of surface absorption with a maximum bound of 3.5 ppm, corresponding to a reduced bulk absorption coefficient of 45.5 ppm cm^{-1}. I have shown that determining the surface absorption by probing the heated sample at a large angle of incidence and fitting to WFD_{ip}, WFD_{pp} and WFD_{comb} of one wavefront measurement is less effected by noise and thus, the preferable method. Surface absorption should be able to be quantified by fitting to C1, C2 and C3 whilst sweeping β, however, the fluctuations in system parameters between measurement days causes large uncertainty in this techniques. The point absorber observed in C2 also reduced the effectiveness of the technique by removing another data point.

5.4 Investigating the C2 anomalous absorber

In the analysis above, only C3 and C1 were used to determine α and β as a anomalous point in the wavefront was observed in measurements of C2 in Section 5.3.2. In this section, I describe an investigation of this anomaly, to determine the whether it will influence the other measurement cases and estimate the strength of the absorber.

To determine the localisation of the anomalous absorber the sample was translated by 0.5 mm steps in the plane of incidence for the C1 configuration, as shown in Fig. 5.14.

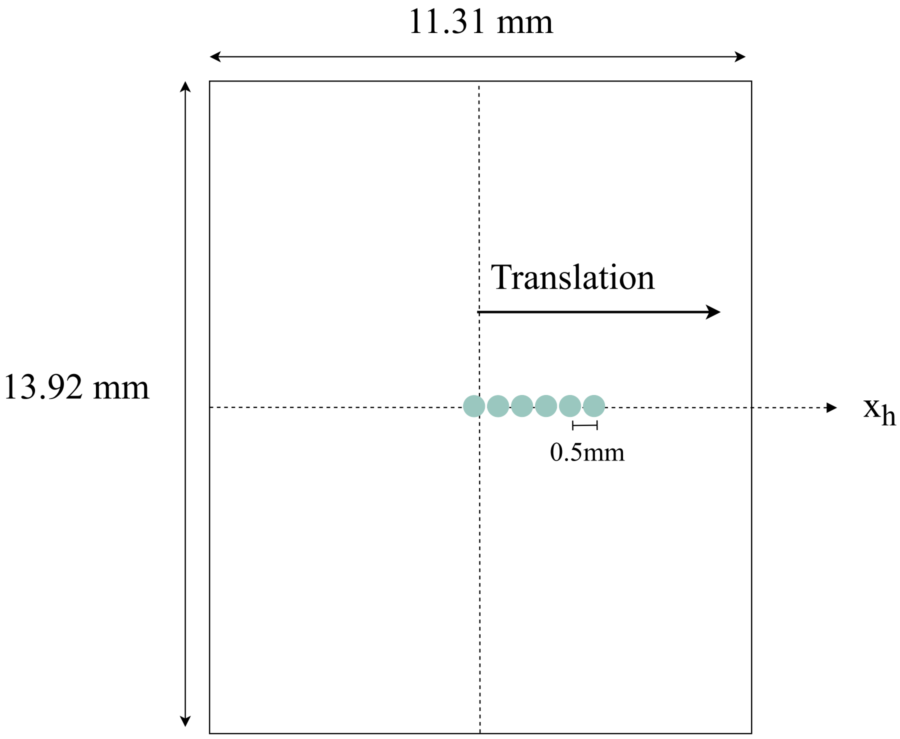

Fig. 5.14 Schematic of the slab translation along x_h where each dot indicates the position of the pump beam on the sample.

This orientation was chosen to determine if the C1 data was affected by the anomaly and demonstrate that the anomaly is localised. The change in measured wavefront in response to the translation is shown in Fig. 5.15. An additional narrow distortion, is observed in each frame and increases in magnitude with translation until a much larger distortion than is measured for C1 is observed when the absorber is centred on in the probe beam, in the third-from-bottom measurement.

The right column in Fig. 5.15 shows the difference between the measured distortion and that observed for the C1 measurement, demonstrating in each frame a distortion with a maximum amplitude much larger than the measurement noise and the residual for the C1 best-fit. These plots show that the anomalous absorber moves laterally by about the same amount as the translation of the sample, thus, it cannot be a random noise artefact.

The absence of localised anomalies in the wavefront best-fit distortion for C1 and the residuals appearing to be random noise suggests that the anomalous absorption observed in Section 5.3.2 has not significantly affected the C1 measurement.

The magnitude of the absorption and size of the anomalous absorber was estimated under the assumption it was a point absorber, using the HV analytical solution for temperature distribution due to heating at one surface [42]. Fitting to the predicted $\Delta \mathrm{OPL}_{TR}$, shown in Fig. 5.16, yields an absorption of 192 ppm and suggests that the size of the anomalous absorber is ca. 0.6mm. Thermal expansion is not included in this fit as it has a small contribution for a localised internal heat source.

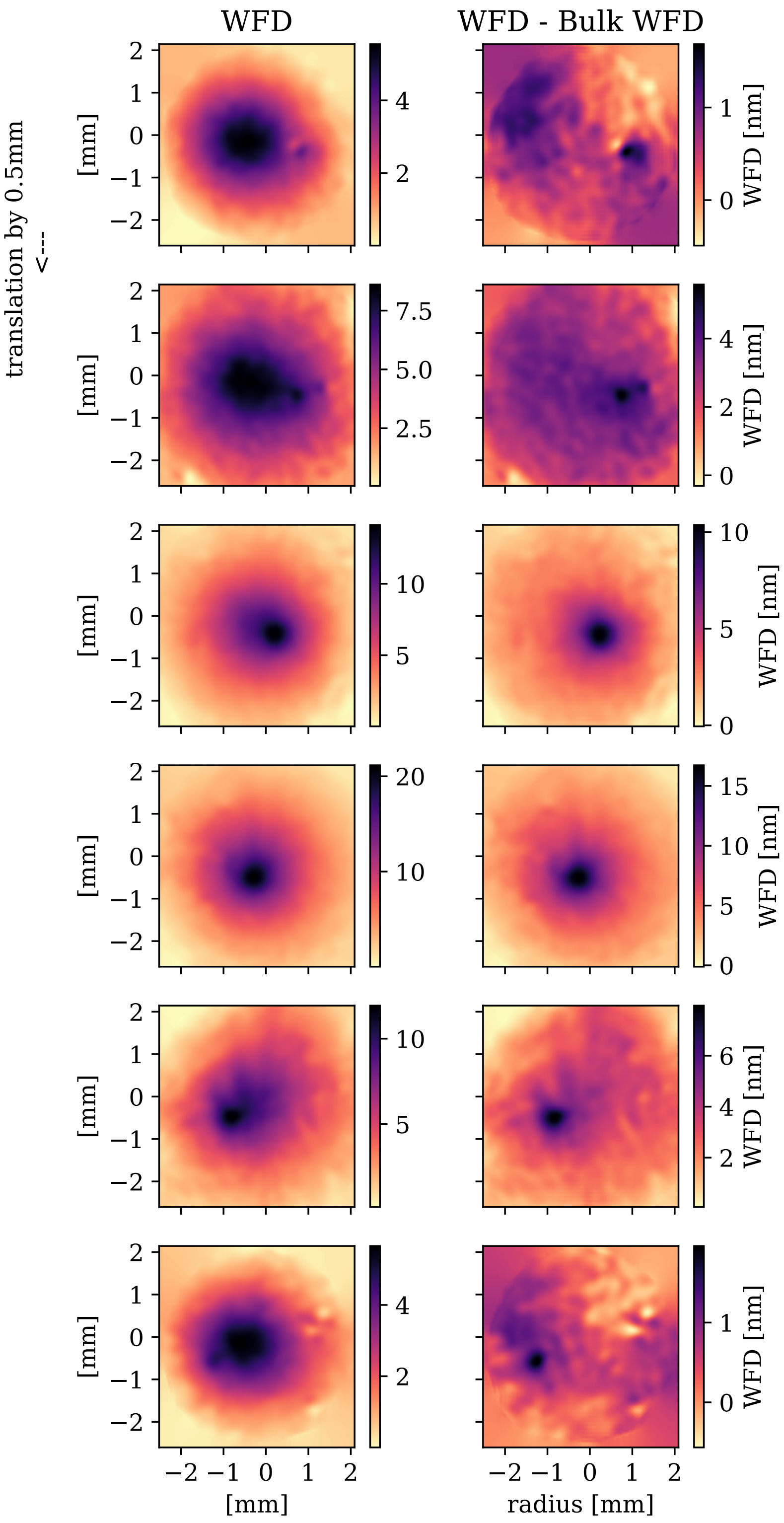

Fig. 5.15 The measured wavefront distortions (a) display an additional wavefront distortion which shifts with the sample as it is translated by 0.5mm increment. This indicated the presences of a localised absorber. Plot b) shows the subtraction of the measured distortion (WFD) and that observed for the C1 measurement (Bulk WFD).

I conclude this anomalous deformation is the result of an absorbing material as the magnitude of the deformation increases with laser beam proximity to the point. This is observable in the fourth image in Fig. 5.15 where the anomalous distortion is maximized when it is centred over the bulk absorption deformation peak. A non-absorbing discrete scatterer would be expected to have a less significant response to the position of the heat source. However, a localised defect, like a nano-particle which exhibits both scattering and absorption properties could be the cause. For example, platinum's, high refractive index causes observable scatter off points at small as 0.005 μm and is a common contaminant in ZBLAN [2]. This is possible as some scattering points can be observed when high intensity light is shone through the sample.

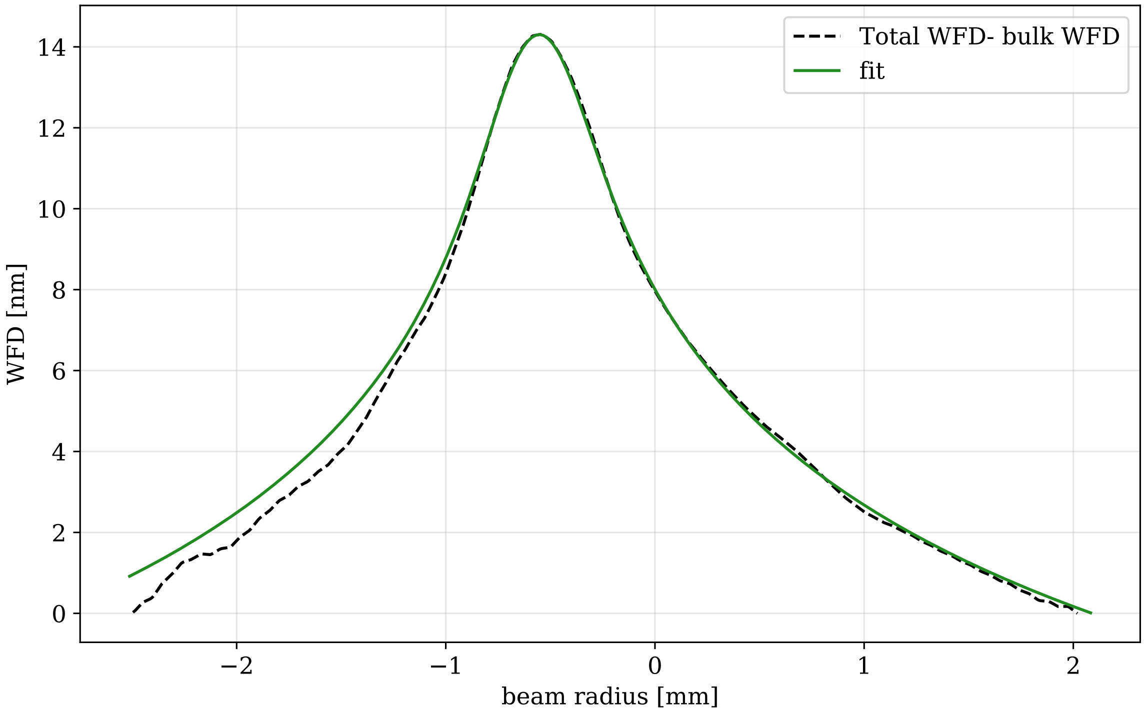

Fig. 5.16 The additional WFD due to the anomalous absorber fit to under the assumption it is a point absorber using the HV surface absorption temperature distribution and parameters in Table 3.1 and Table 2.2, its absorption and size could be predicted.

To conclude the deformation is due to a point absorber and identify if it corresponds to a visible scattering point a scan would have to be conducted through each face to ensure the absorption is localised in each axis. An optimised system for this purpose is a potential future step for this set-up as verifying the existence of extrinsic absorbers is incredibly useful for glass development. This will inform the manufacturing process on the source of the contaminants which could be imbued into the glass from unoptimised manufacturing processes or impure materials. Thus, the ability to discern inhomogeneities, is not only essential to determine α and β accurately, but to inform on the manufacturing process for the glass.

5.5 Effect of parameter uncertainty on best-fit α

The α and β values determined above assume that the measurement system and material parameters accurately describe the experimental system and sample. The aim of this section is to quantify impact of the parameter uncertainties on the absorption coefficients.

The considered sources of errors are listed below and the quantification of each uncertainty is described in Appendix D:

- A systematic inaccuracy due to the calibration of the power meter used to measure pump power.
- Random uncertainties in the measured system parameters listed in Table 5.4
- Differences between material parameters extracted from literature and those of the sample, due to difference in ZBLAN composition and probe beam wavelength.

The impact of the uncertainties in the system parameters was estimated by varying each parameter in the model by $\pm$ the variance and finding the percentage change in the best-fit α to give an upper and lower bound, rather than an extensive Monte-Carlo simulation. The random effects were added in quadrature.

Photo-thermal measurement systems measure absorption through the effects of deposited power and thus the uncertainty in the calibration of the power meter will directly effect the absorption coefficients. The maximum error in the calibration of the power head was specified to be 5% and a 4.5% difference was observed between two power meters. This uncertainty was added to that calculated for the random errors giving the results shown in Table 5.4 and total errors listed in Table 5.5 for C1 and C3 configurations.

Parameter	**Units**	C1 **% change in α [%]***	C3 **% change in α [%]***
Power variation, P	[w]	1.0	1.0
Angle, θ_i	[rad]	4.0	2.0
Pump beam size, w	[mm]	1.9	1.9
Length, h	[mm]	1.1	1.1
width, a_x	[mm]	1.2	1.2
height, a_y	[mm]	1.2	1.2
x pump beam offset from centre	[mm]	1.4	2.2
y pump beam offset from centre	[mm]	1.0	2.2
Magnification	-	1.0	1.0

Table 5.4 Table listing the variance in each system parameter and the % change in the best fit α due to this variance for C1 and C3. * signifies that this is the total of the upper and lower variances in α.

The errors were dominated by uncertainty in the angle of incidence and the position of the heating beam and probe beam intersection in the XY plane. The later is due the change in temperature conditions towards the boundary of the sample.

Case	Random uncertainty [%]	Total uncertainty [%]
C1	$^{+2.9}_{-3.6}$	$^{+7.9}_{-8.6}$
C3	$^{+2.1}_{-2.8}$	$^{+7.7}_{-8.3}$

Table 5.5 Table listing the random uncertainty and the total uncertainty for the measurement systems in C1 and C3.

The errors in the assumed material parameters are unknown but any variation from the value used in the model will cause inaccuracy in the determined absorption coefficients. In principle these errors and the system parameters errors, may introduce non-random structures into the best-fit residuals. In chapter 3, it was demonstrated that a 10% variation in each of the thermo-optic and thermal expansion coefficient would result in at least 10% and 2 % errors in α respectively. Furthermore, my analysis predicted that the effect of the sample parameter error could be reduced, if the measurement SNR was improved.

5.6 Future optimization to detect loss in theoretically small ZBLAN sample

I have demonstrated the ability to measure ZBLAN samples bulk absorption coefficient of approximately 47 $\mathrm{ppm\,cm^{-1}}$ @2 μm which is three orders of magnitude larger than the theoretical losses. However, this measurement approaches the limits of the systems sensitivity. To measure improved ZBLAN samples down to the theoretical α value or gain an improved SNR, this sensitivity must be dramatically improved. Using the current system and assuming the same parameters listed in Table 3.1 and Table 2.2 but using the theoretical absorption coefficient $\alpha = 0.01\,\mathrm{ppm\,cm^{-1}}$ the expected wavefront deformation is modelled to have a maximum of 1e-3 nm, as shown in Fig. 5.17, well below the current noise floor of 0.3 nm.

Currently, the wavefront distortion measured on the DHWS uses an average of 1000 reference frames and the average of 1000 frames taken while heating the sample to minimise the effect of random noise. However, this averaging is bounded by a systematic noise floor which becomes prominent in the 1000s of averaged frames, likely due to thermal effects. If this sensitivity cannot be increased instead the magnitude of the deformation must be increased. As stated above the ZBLAN sample size is restricted and can't be made considerably larger, thus, either the laser power or beam size must be optimised.

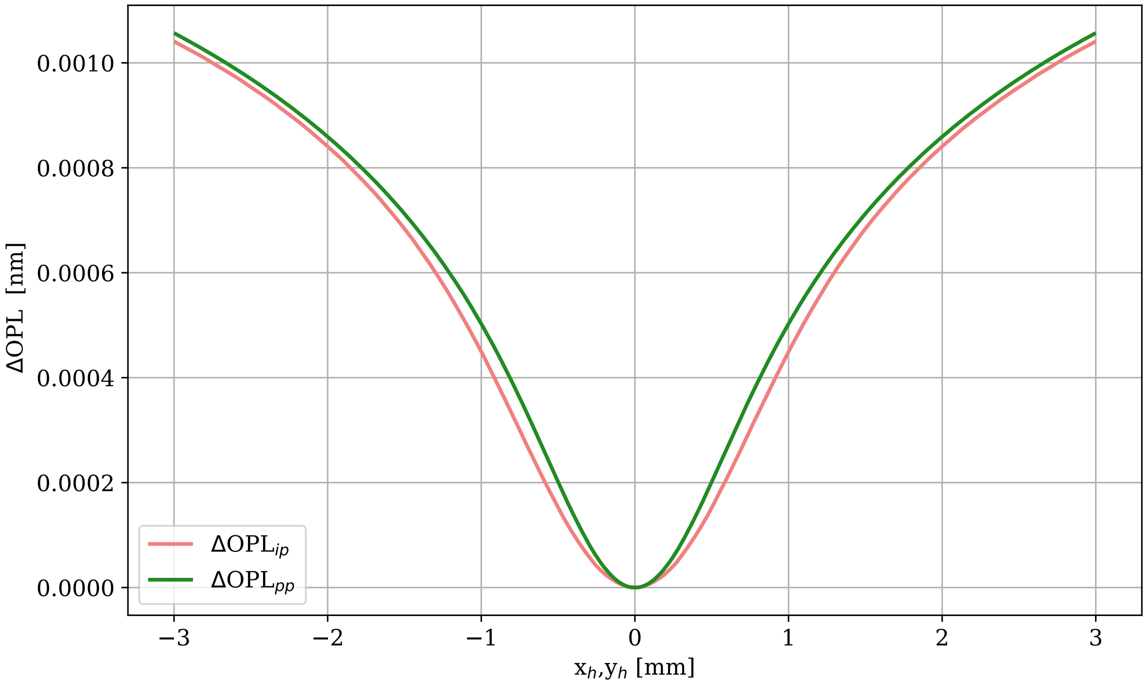

Fig. 5.17 The modelled wavefront deformation expected using the developed system for theoretically low-loss ZBLAN where α = 0.01 ppm cm^{-1} produces a significantly smaller deformation than measurable with this system. The predicted wavefront distortion was calculated using θ_i=0.074 rad and the parameters in Table 3.1 and Table 2.2.

Beam size can only be slightly reduced at this wavelength without significant divergence over the sample. A minimum beam size to ensure a less than 1% change over the sample would be limited at $\approx$ 0.3 mm, calculated using the Raleigh range, however, this only increases the signal size by a factor of 1.3, as shown in Fig. 5.18.

The only feasible way to produce an observable signal when $\alpha = 0.01$ ppm cm^{-1} is to increase the laser power over 1000 fold at which point an 1.06 nm wavefront deformation that is just within the range of measurement will be produced. However, creating a 7 kW, or ideally more powerful, laser at this wavelength is not a insignificant task with the highest power ≈ 2 μm lasers published being 885 W @2050 nm and 608 W @2040 nm [53], [54]. A resonate cavity may be a viable way to achieve this incident power with a lower power laser.

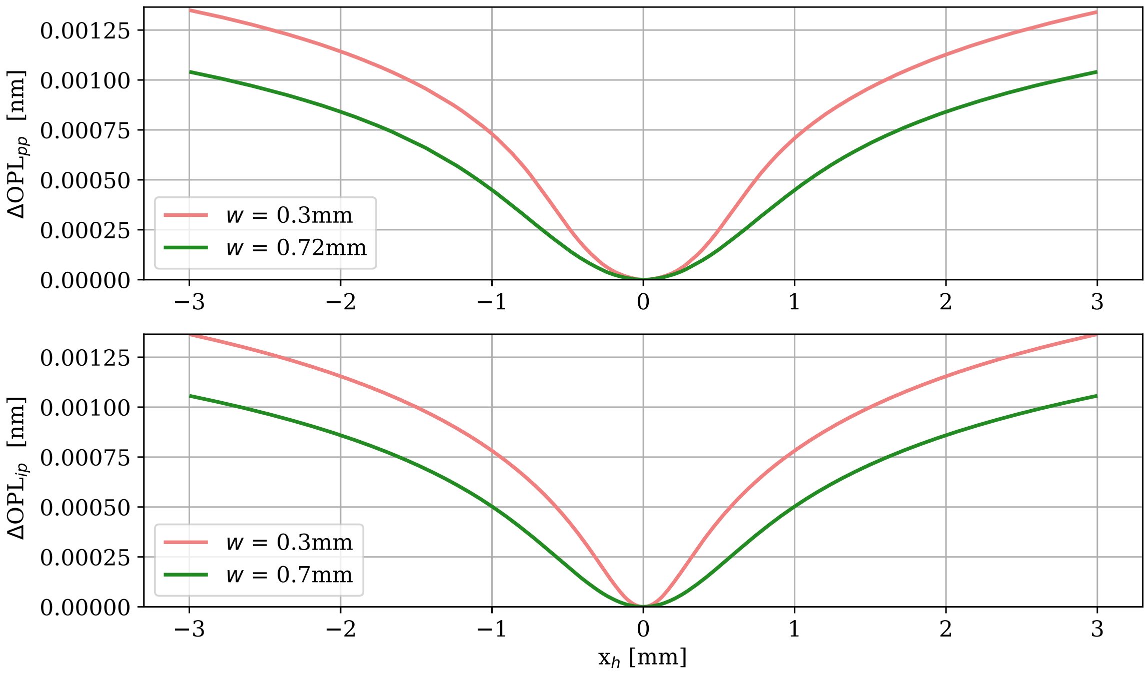

Fig. 5.18 Decreasing the size of the laser beam causes a greater amount of heat to be deposited in the sample over a smaller area increasing the wavefront deformation. In this plot the increase in magnitude is demonstrated for theoretically low-loss ZBLAN using w=0.7 mm in comparison to w=0.3 mm for the WFD_{ip} and WFD_{pp} deformation slices.

5.7 Conclusions

This chapter has described the measurement of the bulk optical absorption coefficient, α, at 1995 nm for a small ZBLAN sample, using several measurement orientations. Transmitting the heating beam along the long axis yielded $\alpha = 47.2 \pm 0.4\,\mathrm{ppm\,cm^{-1}}$ assuming $\beta = 0$ ppm and $46.2 \pm 0.4\,\mathrm{ppm\,cm^{-1}}$ assuming $\beta = 3.5$ ppm. Using a large off-axis angle for the probe beam enabled an estimate of the upper limit of $\beta = 3.5$ ppm, with α between $46.8 \pm 0.4\,\mathrm{ppm\,cm^{-1}}$ and $45.2 \pm 0.4\,\mathrm{ppm\,cm^{-1}}$. I also described an investigation of the effect of errors in the measurement system, which suggested an uncertainty in the fit of up to 8.5% and inaccuracies in the material parameters used in the FEM which could cause up to an additional 12% systematic error.

The absorption measured in ZBLAN is substantially above the total theoretical loss predicted at 1995 nm which suggest there is extrinsic absorption due to containments in the sample. There has been evidence of the contaminants acting as absorbers in the hundreds of ppm also described in this chapter. Improving ZBLAN such that it can be used as a revolutionary low-loss glass for internet transmission or precision sensing would require the sensitivity of the measurement system to be reduced by 3 orders of magnitude and these containments removed. Measuring such low losses would require the system to be upgraded to higher sensitivities, which would require higher power pump solutions.

CHAPTER 6

CONCLUSION

6.1 Summary of the aims of this work

This thesis described the development of a photo-thermal measurement system and accompanying model that uses the thermal lensing of a probe beam to quantify absorption. The motivation of creating this system is two-fold;

- To allow precise measurement of absorption in low-loss optical materials proposed to be used as test masses and auxiliary optics in future 2μm gravitational wave detectors, informing the choice of specific wavelengths and the design of thermal compensation systems.
- To quantify and qualify the sources of loss in novel glasses such as ZBLAN in the aim to help developers understand the mechanisms of the loss and improve the glass. Achieving ZBLAN's low-loss glass would be beneficial for many applications including gravitational wave detector optics and telecommunication fibres. By measuring absorption losses the loss due to scatter, which is difficult to independently measure, can be inferred from the total loss.

To achieve these aims a measurement system was designed which fulfils the following goals:

1. The system is sensitive to absorption coefficients of $\approx 10\,\mathrm{ppm\,cm^{-1}}$ to allow measurement of the current quality of ZBLAN and 2 μm GW optical materials.
2. The system is able to extract surface and bulk absorption coefficients quickly.
3. There are less than 10% systematic errors due to the system.
4. The system is insensitive to sample size and shape allowing measurement of a range of samples.

5. The system is able to detect homogeneity in the sample and point absorbers, allowing investigation of their source and minimise inaccuracies in bulk measurements.

6.2 Summary of the results

In this thesis I have achieved the aims outlined above by creating a model and analysis technique to predict the wavefront distortion of a beam through a heated sample and an optimised experimental system to measure this wavefront distortion. By comparison of the predicted and measured wavefront distortion, I have demonstrated for a ZBLAN and N-BK7 sample that this system can reproducibly measure bulk and surface absorption coefficients, as low as 10s of $\mathrm{ppm\,cm^{-1}}$ and ppm scales respectively, and can measure samples of different geometries. This system was also demonstrated to be sensitive to anomalous absorbers which could be localised along an axis of the sample. Thus, an understanding of the level of contamination in the sample was gained which is very valuable for glass developers.

The validity of these results is dependant on the quality of the COMSOL FEM describing the heating of the sample, which was verified through comparison to the Hello & Vinet analytical solutions for a thin disc geometry. In the process the limitations of the HV model's thermal expansion solution when modelling samples which deviate from this thin disc geometries was discovered. Thus, FEM model must be used as it can be applied to any geometry and it will not be effected in the same manner.

A model of the change optical path length ΔOPL of a probe beam incident on the heated sample at an angle was formulated in chapter 3, using the FEM. The thermo-elastic, thermo-refractive and elasto-optic effects were considered with the latter proven to be negligible in glass samples. Thermo-elastic and thermo-refractive effects were demonstrated to counteract each other reducing the observable distortion in ZBLAN, highlighting the advantages of measuring longer samples where thermo-refractive effects dominate. A linearised function in terms of α and β for the ΔOPL was then formed allowing the absorption coefficients to be found by completing a least-squares fit.

The accuracy of the fit was dependant on the sample parameters which may vary in novel development glasses due to changes in the composition and the system parameters. Thus, a verification measurement using a N-BK7 sample, which has well documented parameters, was conducted in chapter 4, measuring bulk absorption accurate to the predicted value within 0.3%. Varying sample parameters such as the thermo-optic and thermal expansion coefficients was, however, demonstrated to have a proportional effect on the value of α and increases the error in the fit. Modelling demonstrated that by sweeping the coefficients and finding the minimum error, the uncertainty in α could be reduced and even allow determination of the correct coefficients. However, the experimental noise floor must be reduced by a factor of 10 to recover this information experimentally.

This thesis introduced an off-axis probe, on axis pump photo-thermal measurement system which was optimised to measure small, low-loss samples. In chapter 5, this system was demonstrated to be able to reproducibly measure bulk absorption as small as 47.2 $\pm 0.4\,\mathrm{ppm\,cm^{-1}}\ ^{+7.9}_{-8.6}\%$ when the system was configured for the highest SNR, however, β could not be determined due to the small angle required. It was demonstrated that at large angles the bulk and surface distortion profiles become very distinct allowing an upper limit of $\beta = 3.5$ ppm to be determined. Consequently, when assuming this maximum surface absorption in the highest SNR configuration the bulk absorption is bound to α = 46.2 $\pm 0.4\,\mathrm{ppm\,cm^{-1}}\ ^{+7.9}_{-8.6}\%$. Thus, this demonstrates that this system is able to quantify bulk absorption of a magnitude expected for fused silica at 2 μm for GW applications and currently available ZBLAN, and with improvements to increase signal size could be used to measure the intrinsic losses in ZBLAN.

6.3 Future work

I aim for this system to be used to measure samples with absorptions approaching the lowest predicted theoretical losses. Whilst it has been demonstrated that ZBLAN samples of the current quality can be quantified this system will need to be improved to reach this goal. Thus, it is essential that future work is done to obtain a higher power pump beam or build a resonate cavity system to increase the effective power by approximately 1000 times. The uncertainty in the fit and the noise floor of the DHWS also limits how well surface and bulk absorption could be quantified. Additionally, to increasing the signal, fitting to the whole wavefront deformation map instead of just the cross section will reduce the uncertainty.

I envision that the methods of formation of crystals in ZBLAN can be investigated in future work. By determining the absorption loss and total loss in bulk glass the loss due to scatter could be inferred and then verified using an integrating sphere. Crystallisation in ZBLAN increases during fibre drawing, but absorption should not be significantly increased in this process. Using cutback measurements to determining total loss and finding the difference from absorption loss I predict to be able to infer an increase in crystallisation and scatter during the drawing process.

This system was built to be capable of measuring many samples with small realignments so that it could be used not only for ZBLAN parametrisation but the precision measurement of optics for gravitational wave detection. Future work in this field aims to measure fused silica and silicon at this wavelength. Silicon in particular will require an increase pump power due to a larger thermal conductivity than ZBLAN and upgrading the system to include a cryogenic tank to replicate the desired 127 K environment in the proposed detectors.

Whilst I have identified a number of areas in which this measurement system and associated model can be improved, I have up to this point verified that this system can measure absorption on the order of magnitude 10s of ppm cm^{-1} and ppm surface absorptions. Successfully completing future work will allow absorption coefficients to be quantified below anything currently published whilst helping determine the wavelengths and materials for future GW detectors and develop low-loss ZBLAN to revolutionise telecommunications.

BIBLIOGRAPHY

[1] I. Cozmuta, S. Cozic, M. Poulain, S. Poulain, and J. R. Martini, *Breaking the silica ceiling: ZBLAN-based opportunities for photonics applications* (SPIE OPTO). SPIE, 2020, vol. 11276 (cit. on pp. 1, 9, 99).

[2] P. W. France, Drexhage, J. M. M. G. Parker, M. W. Moore, S. F. Carter, and J. V. Wright, “Perspective and overview,” in *Fluoride Glass Optical Fibres*, P. France, Ed., Boca Raton, Florida: Springer Dordrecht, 1990 (cit. on pp. 1, 5, 6, 11, 25, 66, 91, 101, 117).

[3] S. Shibata, M. Horiguchi, K. Jinguji, S. Mitachi, T. Kanamori, and T. Manabe, “Prediction of loss minima in infra-red optical fibres,” *Electronics Letters*, vol. 17, no. 21, pp. 775–777, 1981 (cit. on p. 1).

[4] G. P. Agrawal, *Fiber-Optic Communication Systems*, Fourth Edition. Hoboken, New Jersey: A JOHN WILEY and SONS, INC., PUBLICATION, 2010 (cit. on p. 2).

[5] F. P. Kapron, D. B. Keck, and R. D. Maurer, “Radiation losses in glass optical waveguides,” *Applied Physics Letters*, vol. 17, no. 10, pp. 423–425, 1970 (cit. on p. 2).

[6] S. Hild, H. Lück, W. Winkler, *et al.*, “Measurement of a low-absorption sample of oh-reduced fused silica,” *Applied optics*, vol. 45, pp. 7269–72, 2006 (cit. on pp. 2, 15).

[7] D. V. Martynov, E. D. Hall, B. P. Abbott, *et al.*, “Sensitivity of the advanced ligo detectors at the beginning of gravitational wave astronomy,” *Physical Review D*, vol. 93, no. 11, p. 112 004, 2016 (cit. on p. 2).

[8] A. Buikema, C. Cahillane, G. L. Mansell, *et al.*, “Sensitivity and performance of the advanced ligo detectors in the third observing run,” *Physical Review D*, vol. 102, no. 6, p. 062 003, 2020 (cit. on p. 3).

[9] J. Aasi, B. Abbott, R. Abbott, *et al.*, “Advanced ligo,” *Classical and Quantum Gravity*, vol. 32, 2015 (cit. on p. 3).

[10] A. Brooks, G. Vajente, H. Yamamoto, *et al.*, *Point absorbers in Advanced LIGO*. 2021 (cit. on pp. 3, 18).

[11] A. F. Brooks, B. Abbott, M. A. Arain, *et al.*, “Overview of advanced LIGO adaptive optics,” *Applied Optics*, vol. 55, no. 29, p. 8256, 2016. DOI: 10.1364/ao.55.008256. [Online]. Available: https://doi.org/10.1364%2Fao.55.008256 (cit. on p. 4).

[12] M. Tse, H. Yu, N. Kijbunchoo, *et al.*, “Quantum-enhanced advanced ligo detectors in the era of gravitational-wave astronomy,” *Physical Review Letters*, vol. 123, no. 23, p. 231 107, 2019 (cit. on p. 4).

[13] R. X. Adhikari, K. Arai, A. F. Brooks, *et al.*, “A cryogenic silicon interferometer for gravitational-wave detection,” *Classical and Quantum Gravity*, vol. 37, no. 16, p. 165 003, 2020. DOI: 10.1088/1361-6382/ab9143 (cit. on pp. 4, 5, 8, 9).

[14] M. Li and T. Hayashi, *Optical Fiber Telecommunications VII: Advances in low-loss, large-area, and multicore fibers*. Academic Press, 2019 (cit. on p. 5).

[15] A. E. W. Ivan P Kaminow Tingye Li, in *Optica Fibre Telecommunications VII*, ell Laboratories, Alcatel-Lucent, Academic Press, 2013, pp. 1–13 (cit. on p. 5).

[16] X. Zhu and N. Peyghambarian, “High-power zblan glass fiber lasers: Review and prospect,” *Advances in OptoElectronics*, vol. 2010, p. 501 956, 2010 (cit. on pp. 5, 99, 100).

[17] V. G. Tsoukala, J. Schroeder, G. A. Floudas, and D. A. Thompson, "Intrinsic rayleigh scattering in fluoride glasses," *Materials Science Forum*, vol. 19-20, pp. 637–646, 1987 (cit. on p. 7).

[18] J. Degallaix, J. Komma, D. Forest, *et al.*, "Measurement of the optical absorption of bulk silicon at cryogenic temperature and the implication for the einstein telescope," *Classical and Quantum Gravity*, vol. 31, no. 18, p. 185 010, 2014 (cit. on p. 8).

[19] S. Carter, M. Moore, D. Szebesta, J. Williams, D. Ranson, and P. France, "Low loss fluoride fibre by reduced pressure casting," *Electronics Letters*, vol. 26, no. 25, 1990 (cit. on pp. 10, 22, 99, 109).

[20] C. R. Day, P. W. France, S. F. Carter, M. W. Moore, and J. R. Williams, "Overview of fluoride glass fibre optics," in *Proc.SPIE*, vol. 0799, 1987, pp. 94–100 (cit. on p. 10).

[21] S. F. Carter, J. R. Williams, M. W. Moore, D. Szebesta, and S. T. Davey, "Prospects for ultra-low-loss fluoride fibres at btrl," *Journal of Non-Crystalline Solids*, vol. 140, pp. 153–158, 1992 (cit. on p. 10).

[22] H. Tokiwa, Y. Mimura, O. Shinbori, and T. Nakai, "Scattering characteristics in reheated fluorozirconate glasses," *Journal of Lightwave Technology*, vol. 3, no. 3, pp. 574–578, 1985 (cit. on p. 11).

[23] D. S. Tucker and M. SanSoucie, "Production of zblan optical fiber in microgravity," in *Optical Fiber Sensors Conference 2020 Special Edition*, G. W. A. D. M. Cranch and P. Dragic, Eds., ser. OSA Technical Digest, Washington, DC: Optica Publishing Group, 2020, T2B.1 (cit. on p. 11).

[24] D. S. Tucker, E. C. Ethridge, G. A. Smith, and G. Workman, "Effects of gravity on zblan glass crystallization," *Annals of the New York Academy of Sciences*, vol. 1027, no. 1, pp. 129–137, 2004 (cit. on p. 11).

[25] P. Y. Baurès and C. N. Man, "Measurements of optical absorption at 1.06 μm in low-loss materials," *Optical Materials*, vol. 2, no. 4, pp. 241–247, 1993 (cit. on p. 16).

[26] W. B. Jackson, N. M. Amer, A. C. Boccara, and D. Fournier, "Photothermal deflection spectroscopy and detection," *Applied Optics*, vol. 20, no. 8, pp. 1333–1344, 1981 (cit. on p. 16).

[27] H. Piombini, A. Guediche, D. Picart, and G. Dammame, "Absorption measurement of layers or materials: How to calibrate?" *Results in Physics*, vol. 14, 2019 (cit. on p. 16).

[28] V. Loriette and C. Boccara, "Absorption of low-loss optical materials measured at 1064 nm by a position-modulated collinear photothermal detection technique," *Applied Optics*, vol. 42, no. 4, 2003 (cit. on p. 16).

[29] K. V. Vlasova, A. I. Makarov, N. F. Andreev, and A. Y. U. Konstantinov, "High-sensitive absorption measurement in transparent isotropic dielectrics with time-resolved photothermal common-path interferometry," *Applied Optics*, vol. 57, no. 22, pp. 6318–6328, 2018 (cit. on p. 17).

[30] M. Marchiò, M. Leonardi, M. Bazzan, and R. Flaminio, "3d characterization of low optical absorption structures in large crystalline sapphire substrates for gravitational wave detectors," *Scientific Reports*, vol. 11, no. 1, 2021 (cit. on p. 17).

[31] J. Ma, M. Thomas, P. McGuiggan, and J. Spicer, "Weak absorption and scattering losses from the visible to the near-infrared in single-crystal sapphire materials," *Optical Engineering*, vol. 59, no. 8, p. 087 101, 2020 (cit. on p. 17).

[32] S. Yoshida, D. H. Reitze, D. B. Tanner, and J. D. Mansell, "Method for measuring small optical absorption coefficients with use of a shack-hartmann wave-front detector," *Applied Optics*, vol. 42, no. 24, p. 4835, 2003 (cit. on p. 18).

[33] C. Ingram, H. T. Cao, S. Ng, *et al.*, “High precision measurement of optical absorption in low-oh fused silica at 2 micron,” in *ANZCOP*, vol. 11200, SPIE, 2019 (cit. on pp. 18, 19, 73).

[34] A. Brooks, P. Veitch, J. Munch, and L. Kelly, “An off-axis hartmann sensor for the measurement of absorption-induced wavefront distortion in advanced gravitational wave interferometers,” *General Relativity and Gravitation*, vol. 37, pp. 1575–1580, 2005 (cit. on pp. 18, 19, 22, 73).

[35] A. F. Brooks, “Hartmann wavefront sensors for advanced gravitational wave interferometers,” Ph.D. dissertation, University of Adelaide, 2007 (cit. on pp. 18, 19, 81, 82, 84).

[36] B. Schäfer, J. Gloger, U. Leinhos, and K. Mann, “Photo-thermal measurement of absorptance losses, temperature induced wavefront deformation and compaction in duv-optics,” *Optics Express*, vol. 17, no. 25, pp. 23 025–23 036, 2009 (cit. on pp. 18, 20, 73).

[37] B. Schäfer, M. Schöneck, A. Bayer, and K. Mann, “Absolute measurement of surface and bulk absorption in duv optics from temperature induced wavefront deformation,” *Optics express*, vol. 18, pp. 21 534–9, 2010 (cit. on pp. 18, 21, 73).

[38] A. F. Brooks, T.-L. Kelly, P. J. Veitch, and J. Munch, “Ultra-sensitive wavefront measurement using a hartmann sensor,” *Optics Express*, vol. 15, no. 16, pp. 10 370–10 375, 2007 (cit. on pp. 18, 82, 83).

[39] P. Hello and J.-Y. Vinet, “Analytical models of thermal aberrations in massive mirrors heated by high power laser beams,” *Journal de Physique*, vol. 51, no. 12, pp. 1267–1282, 1990 (cit. on pp. 19, 23, 25, 27).

[40] M. Stubenvoll, B. Schäfer, K. Mann, and O. Novak, “Photothermal method for absorption measurements in anisotropic crystals,” *Review of Scientific Instruments*, vol. 87, no. 2, p. 023 904, 2016 (cit. on pp. 20, 73).

[41] P. Hello and J. Vinet, “Analytical models of transient thermoelastic deformations of mirrors heated by high power cw laser beams,” *Journal de Physique*, vol. 51, no. 20, pp. 2243–2261, 1990 (cit. on pp. 23, 25, 27).

[42] J.-Y. Vinet, “On special optical modes and thermal issues in advanced gravitational wave interferometric detectors,” *Living Reviews in Relativity*, vol. 12, no. 1, p. 5, 2009 (cit. on pp. 23, 25, 27, 115).

[43] *Comsol multiphysics: Reference manual cm020005*, 2019 (cit. on p. 29).

[44] W. Koechner, “Thermal lensing in a nd:yag laser rod,” *Applied Optics*, vol. 9, no. 11, pp. 2548–2553, 1970 (cit. on p. 37).

[45] J. D. Mark and S. H. Joseph, “Thermal lensing of laser materials,” in *Proc.SPIE*, vol. 9237, 2014, p. 923 710 (cit. on p. 37).

[46] K. Matusita, H. Kato, T. Komatsu, M. Yoshimoto, and N. Soga, “Photoelastic effects in some fluoride glasses based on the zrf4baf2 system,” *Journal of Non-Crystalline Solids*, vol. 112, no. 1, pp. 341–346, 1989 (cit. on p. 50).

[47] G. D’Agostini, “On the use of the covariance matrix to fit correlated data,” *Nuclear Instruments and Methods in Physics Research Section A: Accelerators, Spectrometers, Detectors and Associated Equipment*, vol. 346, no. 1, pp. 306–311, 1994 (cit. on pp. 56, 111).

[48] T. Izumitani, T. Yamashita, M. Tokida, K. Miura, and H. Taima, “New fluoroaluminate glasses and their crystallization tendencies and physical-chemical properties,” *Materials Science Forum*, vol. 19-20, pp. 19–26, 1987 (cit. on pp. 66, 67).

[49] J. M. Jewell, C. Askins, and I. D. Aggarwal, “Interferometric method for concurrent measurement of thermo-optic and thermal expansion coefficients,” *Appl Opt*, vol. 30, no. 25, pp. 3656–60, 1991 (cit. on p. 67).

[50] J. M. Jewell and I. D. Aggarwal, “Thermal lensing in heavy metal fluoride glasses,” *Journal of Non-Crystalline Solids*, vol. 142, pp. 260–268, 1992 (cit. on p. 67).

[51] P. Greason, J. Dietro, B. Bendow, and D. J. Martin, “Temperature dependence of the refractive index of fluorozirconate glass,” *Materials Science Forum*, vol. 5-6, pp. 607–610, 1985 (cit. on pp. 66, 67).

[52] *Data sheet: Schott n-bk7*, 517642.251, Schott Glass, 2021 (cit. on pp. 90, 93).

[53] D. G. Gregory, D. B. Lewis, and E. R. Joshua, “600-w single-mode single-frequency thulium fiber laser amplifier,” in *Proc.SPIE*, vol. 7195, 2009, 71950Y (cit. on p. 121).

[54] S. Karsten, L. Samir, K. Philipp, and F. Peter, “2 μm laser sources and their possible applications,” in *Frontiers in Guided Wave Optics and Optoelectronics*, P. Bishnu, Ed., Rijeka: IntechOpen, 2010, Ch. 21 (cit. on p. 121).

[55] J. F. Nye, *Physical properties of crystals their representation by tensors and matrices*. Oxford: Clarendon, 1979 (cit. on pp. 140, 142, 143).

[56] H. Aben and C. Guillemet, “Basic photoelasticity,” in *Photoelasticity of Glass*, H. Aben and C. Guillemet, Eds., Berlin, Heidelberg: Springer Berlin Heidelberg, 1993, pp. 51–68 (cit. on pp. 142, 146).

[57] E. E. G. Pericles S. Theocaris, *Matrix Theory of Photoelasticity* (Springer Series in Optical Sciences). Berlin, Heidelberg: Springer, 1979, vol. 11 (cit. on p. 146).

[58] Z. D. Pan and J. P. Wicksted, “Rayleigh-brillouin scattering studies of thoriated fluoride and fluorozirconate glasses,” *Optical Engineering*, vol. 31, no. 1, pp. 116–120, 1992 (cit. on p. 150).

APPENDIX A

FEM TEMPERATURE DISTRIBUTION VERIFICATION FOR LONG CYLINDER

Using the formulations described in Chapter 2 the temperature distribution was produced using the HV and FEM models for a centrally heated ZBLAN long rod sample with a length of 22.803mm and radius of 6.96mm. The cross sections for surface and bulk absorption and the end face profiles are plot in Fig. A.1, Fig. A.2, and Fig. A.3.

The generated $T(x,y,z)$ are identical for bulk with the residual of the two models 3 orders of magnitude smaller and 30 times smaller for the surface absorption.

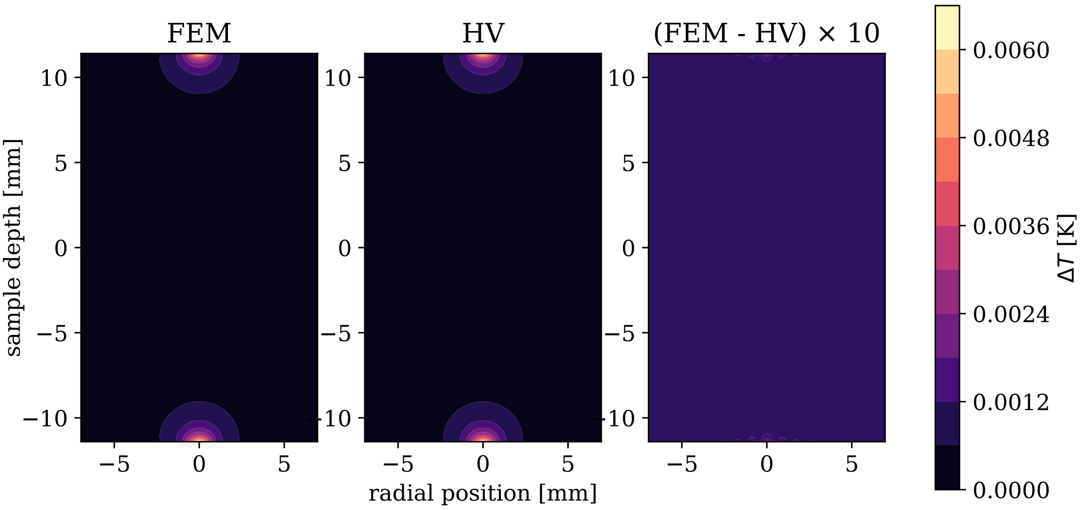

Fig. A.1 Comparison of FEM and HV temperature distributions due to surface absorption using the parameters in Table 2.1.

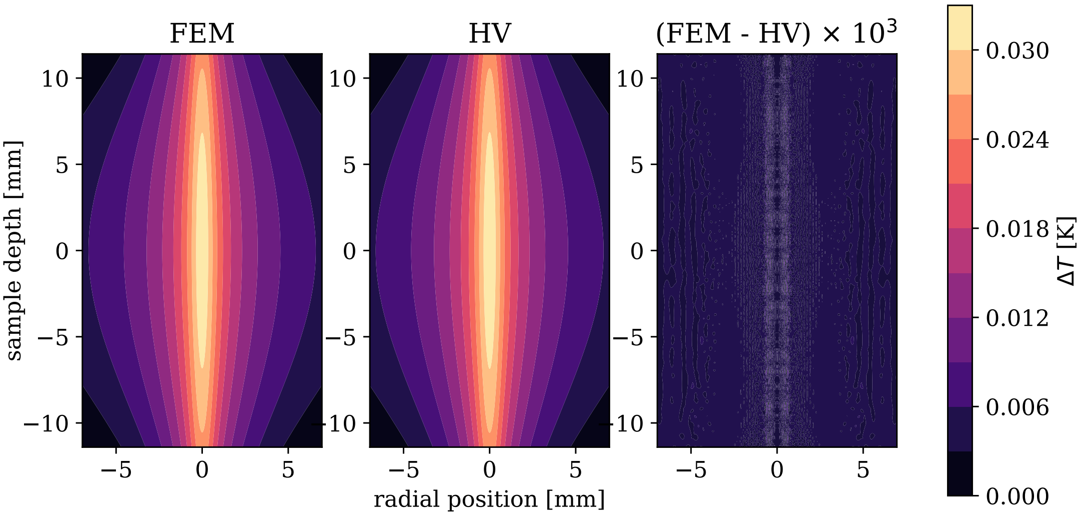

Fig. A.2 Comparison of FEM and HV temperature distributions due to bulk absorption using the parameters in Table 2.1 .

a) Bulk absorption

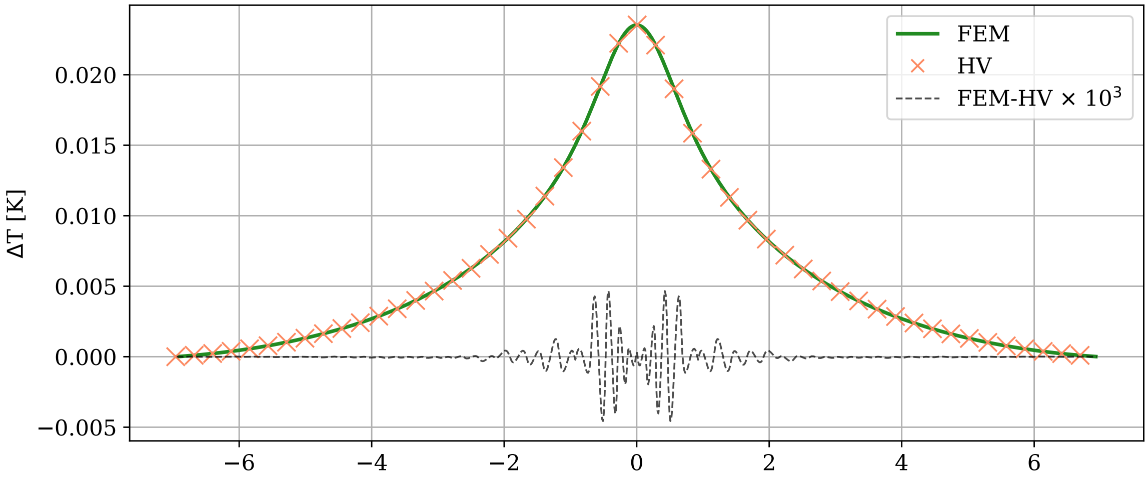

b) Surface absorption

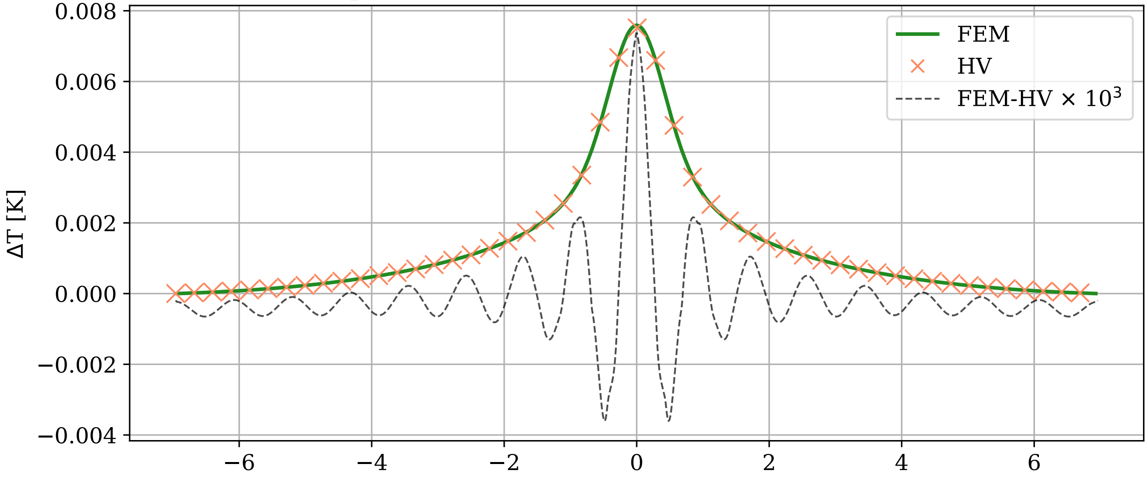

c) Combined absorption

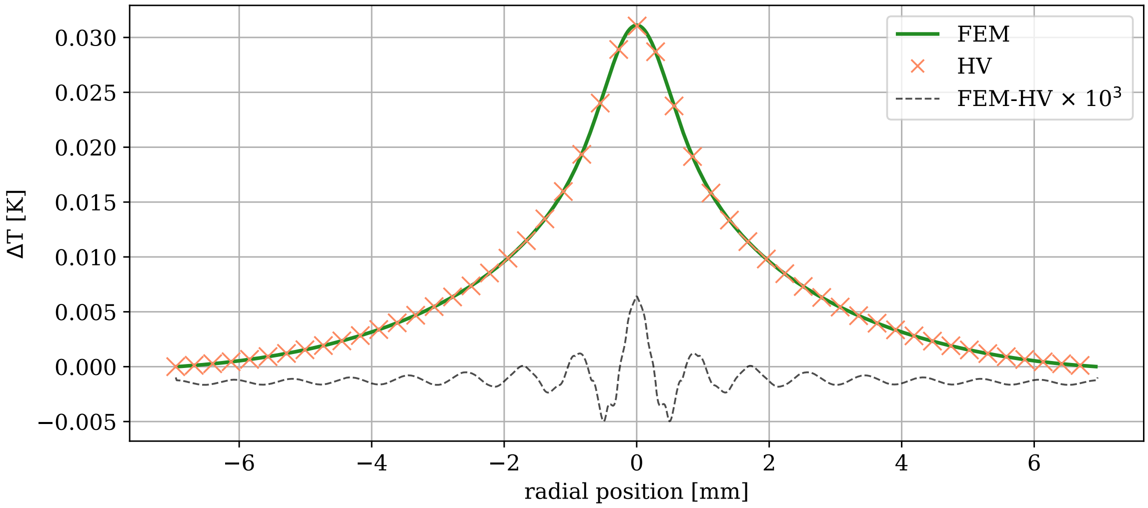

Fig. A.3 Comparison of temperature profiles at end face of sample generated using FEM (COMSOL) and HV using the parameters from Table 2.1.

APPENDIX B

A1: APPENDIX 1 - BIREFRINGENCE

The elasto-optic effect, or photo-elastic effect, describes the phase change of light due to stress induced birefringence. This is caused by the introduction of an external stress to a sample leading to changes in the permittivity and the dielectric constants of the material. As the refractive index is derived from these properties it too is modified by applied stress. Subsequently, there will be varying fast and slow refractive index at each point in the sample. As a result different polarisation's of incident light will experience different effective optical path lengths, inducing a phase difference.

The magnitude of this effect varies between samples. It scales with the thermo-expansion coefficients (α_{TE}) magnitude, the thermal conductivity and the absorption. Such an effect is often cited as negligible for other low loss glasses such as silica which boasts a α_{TE} on the order of magnitude of $1 \times 10^{-7}\,\mathrm{K}^{-1}$. However, in glasses such as ZBLAN α_{TE} is an order of magnitude higher and might result in non-negligible changes in the wavefront. Thus it is imperative that this effect is modelled and proven to be negligible in this sample.

In this study we measure the deformation of a SLED beam which by definition is an unpolarised beam. Consequently, we assume that there is 50:50 ration of s and p polarisation in the beam. The issue which may arise is that the s and p components experience significant differences in polarisation which results in net phase change of a large magnitude. Thus in the section below we will consider the effects of stress in the s and p polarisation to determine the total phase change through the x and y slice of interest.

B.1 Modelling process

B.1.1 Calculating stress

The thermally induced stress was modelled using the FEM program COMSOL, formulated as described in chapter 2 We export the stress tensors at each point in the sample and use post processing to extract the principal stresses due to the sharp variations in magnitude and orientation which causes interpolation errors when exported from COMSOL.

The stress tensor is a second-rank tensor corresponding to the normal and shear stresses.

$$\mathbf{S} = \begin{bmatrix} \sigma_{xx} & \sigma_{xy} & \sigma_{xz} \\ \sigma_{yx} & \sigma_{yy} & \sigma_{yz} \\ \sigma_{zx} & \sigma_{zy} & \sigma_{zz} \end{bmatrix} \tag{B.1}$$

This tensor is simplified the symmetry argument $\sigma_{ij} = \sigma_{ji}$ leaving 6 individual stress tensors.

$$\mathbf{S} = \begin{bmatrix} \sigma_{xx} & \sigma_{xy} & \sigma_{xz} \\ \sigma_{xy} & \sigma_{yy} & \sigma_{yz} \\ \sigma_{xz} & \sigma_{yz} & \sigma_{zz} \end{bmatrix} \tag{B.2}$$

In Fig. B.1 examples of typical stress tensor components taken from COMSOL are shown for a slice of a rectangular ZBLAN sample. It can be seen that the radial shear stresses on the slice are negligible as the corresponding components are minimal. The only non-negligible shear term is xz as z corresponds to the direction of the heating propagation and significant axis of thermal expansion.

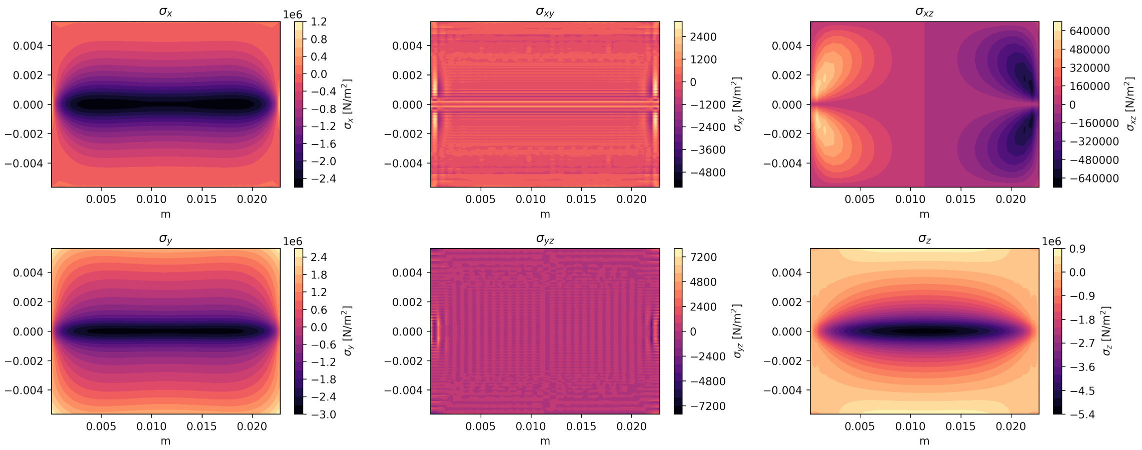

Fig. B.1 The stress tensor components for the modelled ZBLAN sample for the case where α = 1 m^{-1} through the central horizontal slice of the sample. As the stress tensor is symmetrical only 6 components of the tensor must be calculated as $\sigma_{ij} = \sigma_{ji}$. It can be seen that σ_{xy} and σ_{yz} are negligible as we are evaluating the slice perpendicular to the y axis. These components were set to 0 to avoid numerical noise.

The magnitude and direction of the principal stresses can be determined by viewing the matrix of stress tenors as an eigenvalue/eigenvector problem. The invariants of the stresses tensor describe the principal stresses, as the eigenvalues and the corresponding eigenvectors build an orthogonal coordinate system with respect to the sample geometry. The first principal stress in a slice of a ZBLAN sample, is shown in Fig. B.2, with arrows dictating the direction of the stress. This coordinate system is selected such that the each principal stress vector is normal to a plane with no shear stress. The principal stresses by convention are assigned such that the first principal stress corresponds to the largest magnitude.

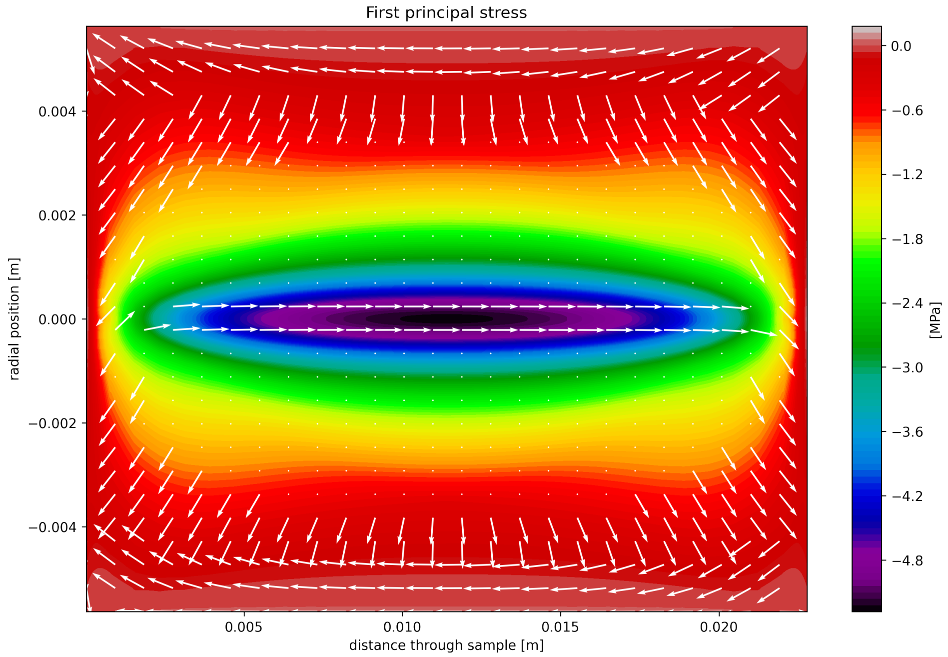

Fig. B.2 The first principal stress in a horizontal slice of the sample. The quivers dictate the direction of the stress and the contours show the magnitude. In the case the quivers appear like a dot the vector is pointing into/from the plane of the page.

B.1.2 Calculating the change in refractive index in each principal stress axis

The change in refractive index due to added stress is a product of the relative dielectric impermeability (B) changing. This value is the reciprocal of the refractive index.

$$B = \frac{1}{n^2} \tag{B.3}$$

We will use the relative dielectric impermeability tensor (B_{ij}) to quantify the effects on refractive index. This analysis to determine the refractive indices in the principal stress axis is following the formulation given in Nye [55]. The components of this tensor define the coefficients of an ellipsoid known as the indicatrix.

$$B_i j x_i x_j = 1 \tag{B.4}$$

Each of the perpendicular axes in the indicatrix are defined by the magnitude of the refractive index in the 3 principle stress axis,

$$B_1x_1^2 + B_2x_2^2 + B_3x_3^2 = \frac{x_1^2}{n_1^2} + \frac{x_2^2}{n_2^2} + \frac{x_3^2}{n_3^2} = 1 \tag{B.5}$$

The principle stresses axis are often rotated with respect to the sample geometry, therefore so is the indicatrix.

ZBLAN is an isotropic glass with a uniform refractive index. In which case the indicatrix is a sphere defined as

$$B^0(x_1^2 + x_2^2 + x_2^2) = 1 \tag{B.6}$$

where $B^0 = n_0$ and n_0 is the initial refractive index of the sample. However, the addition of a thermal stress due to an applied electric field cause changes in B_1, B_2 and B_3 by determining these changes the refractive index can be determined. Photo-elasticity is first order effect on B_{ij} defined in Equation (B.7).

$$\Delta B_{ij} = z_{ijk}E_k + \pi_{ijkl}\sigma_{kl} \tag{B.7}$$

The first term on the RHS of Equation (B.7) describes the electro-optical effect whose magnitude depends on z_{ijk}. We are interested in the second term which describes the effect of an external stress (σ_{kl}) on B with a magnitude given by the piezo-optic coefficients (π_{ijkl}). This is visualised on the indicatrix as each axis being compressed relative to the magnitude of the applied stress.

Thus we are interested in the change in B described as

$$\Delta B_m = \pi_{mn}\sigma_n \qquad (m, n = 1, 2..6) \tag{B.8}$$

Which has been simplified using symmetry arguments similar to the stress tensor above.

To quantify B_1, B_2 and B_3 when have to determine $\Delta B_1, \Delta B_2$ and ΔB_3. This requires solving Equation (B.8). Displayed in matrix form

$$\begin{bmatrix} \Delta B_1 \\ \Delta B_2 \\ \Delta B_3 \\ \Delta B_4 \\ \Delta B_5 \\ \Delta B_6 \end{bmatrix} = \begin{bmatrix} B_1 - B_0 \\ B_2 - B_0 \\ B_3 - B_0 \\ B_4 \\ B_5 \\ B_6 \end{bmatrix} = \begin{bmatrix} \pi_{11} & \pi_{12} & \pi_{13} & 0 & 0 & 0 \\ \pi_{21} & \pi_{22} & \pi_{23} & 0 & 0 & 0 \\ \pi_{31} & \pi_{32} & \pi_{33} & 0 & 0 & 0 \\ 0 & 0 & 0 & \pi_{44} & 0 & 0 \\ 0 & 0 & 0 & 0 & \pi_{55} & 0 \\ 0 & 0 & 0 & 0 & 0 & \pi_{66} \end{bmatrix} \begin{bmatrix} \Delta\sigma_1 \\ \Delta\sigma_2 \\ \Delta\sigma_3 \\ 0 \\ 0 \\ 0 \end{bmatrix} = \begin{bmatrix} \pi_{11}\sigma_3 + \pi_{12}\sigma_2 + \pi_{13}\sigma_3 \\ \pi_{21}\sigma_3 + \pi_{22}\sigma_2 + \pi_{23}\sigma_3 \\ \pi_{31}\sigma_3 + \pi_{32}\sigma_2 + \pi_{33}\sigma_3 \\ 0 \\ 0 \\ 0 \end{bmatrix} \tag{B.9}$$

We can see that $\Delta B_4, \Delta B_5$ and ΔB_6 are equal to 0 as the glass is isotropic and will not influence the refractive indices [55]. The equations for the first 3 components of B_i are simplified using the fact that $B_i = \frac{1}{n_i^2}$ and $\Delta B_i = \left(\frac{-2}{n_i^3}\right)(\Delta n_i)$ for i =1,2,3 and the assumption that the sample is isotropic. This allows us to assume $\pi_{11} = \pi_{22} = \pi_{33}$ and all the shear terms are equal ($\pi_{ij} = \pi ij$ for all $i \neq j$). Finally, using the approximation $n_i = n_0$ the following equations can be derived for the refractive indexes in each principal stress direction,

$$n_1 = n_0 + C_1\sigma_1 + C_2(\sigma_2 + \sigma_3) \tag{B.10}$$

$$n_2 = n_0 + C_1\sigma_2 + C_2(\sigma_3 + \sigma_1) \tag{B.11}$$

$$n_3 = n_0 + C_1\sigma_3 + C_2(\sigma_1 + \sigma_2) \tag{B.12}$$

where σ_i corresponds to the magnitude of stress in the i-th principal stress direction. The C_1 and C_2 coefficients are constants for the material such that $C_1 - C_2 = C$ where C is the stress-optic coefficient and can be calculated from the piezo-optic coefficients [56].

B.1.2.1 Finding incident ellipse

The determined refractive indices are not defined such that they align with the samples axis or the probe beam coordinates. Consequently, the fast and slow axis in the plane of the probe beam must be determined. This can be determined as the cross-section of the ellipsoid and the plane corresponding to this normal vector of the probe beam as shown in Fig. B.3.

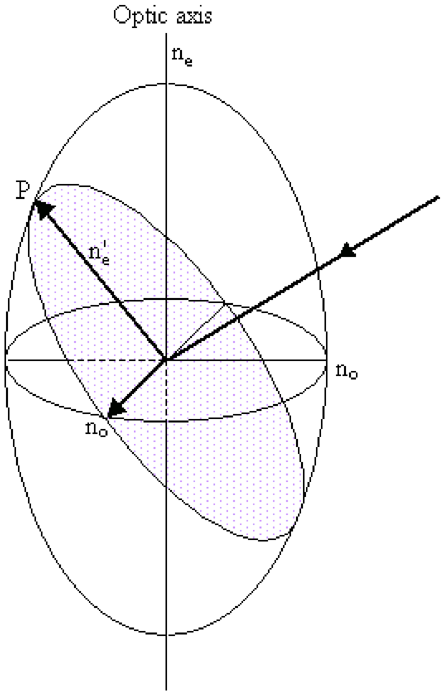

Fig. B.3 The incident ellipse described is by cross-section of the normal of the probe beam with the indicatrix of the sample.

Nye [55] has shown the major and minor axis of this ellipse corresponds to the fast and slow refractive indexes in the plane of incidence. Thus, we must find this ellipse. In the section above we calculated the refractive index in the principal stress frame, X'= (x',y' z').

In the X' frame the ellipse equation is,

$$\frac{x'^2}{n_1^2}+\frac{y'^2}{n_2^2}+\frac{z'^2}{n_3^2}=1 \tag{B.13}$$

We can also write a parametric form this equation for any point on the surface of the ellipsoid as,

$$x_e' = n_1 \cos\theta \sin\phi \tag{B.14}$$

$$y_e' = n_2 \sin\theta \sin\phi \tag{B.15}$$

$$z_e' = n_3 \cos\phi \tag{B.16}$$

(B.17)

At this point the incident light normal vector is in the sample space coordinates, X= (x,y,z), which we will label $k = (k_x, k_y, k_z)$. However, we now need to be able to relate this to positions in our principal stress space. A transformation matrix (M) can be constructed out of the principal stress vectors (sp_1,sp_2,sp_3) which describe the principal stress axis in the sample space to transform coordinates in X to X'.

$$M = [sp_1.\mathrm{T}, sp_2.\mathrm{T}, sp_3.\mathrm{T}] \tag{B.18}$$

thus we can describe X' as,

$$X' = MX \tag{B.19}$$

Therefore k can be defined in the X' frame as k_x using the following formula.

$$k_{X'} = Mk_X = (k_{x'}, k_{y'}, k_{z'})$$

The plane normal to this vector which cuts through the ellipsoid making a ellipse would then be defined as,

$$k_{x'}x' + k_{y'}y' + k_{z'}z' = 0 \tag{B.20}$$

using the requirement that the plane cuts through the centre of the ellipsoid. The following equations derived from the parametric equation in Equation (B.17),

$$u = \frac{x'}{n_1} \tag{B.21}$$

$$v = \frac{y'}{n_2} \tag{B.22}$$

$$w = \frac{z'}{n_3} \tag{B.23}$$

which allows the ellipsoid to be transformed into a unit sphere and the plane of intersection is now described as,

$$k_{x'}un_1 + k_{y'}vn_2 + k_{z'}wn_3 = 0 \tag{B.24}$$

This can be written in a normalised hessian form of $[m_u, m_v, m_w]$ where each m component describes a normalised coefficient of the normal to the plane. Under this transformation our ellipse will be a unit circle which can be defined by the equation,

$$e_1 \sin t + e_2 \cos t \tag{B.25}$$

where t is within the range $[0{,}2\pi]$. Thus, if we can find two vectors orthogonal to each other and the normalised normal vector we can define this cross section. We must consider two cases.

1. First when m_w approaches 0 so the max is between the v and u components. We define e_1 as,

   $$e_1 = \frac{1}{\sqrt{m_u^2 + m_v^2}}[m_v, -m_u, 0] \tag{B.26}$$

   and to find the vector orthogonal to both m and e_1,

   $$e_2 = m \times e_1 \tag{B.27}$$

2. when $|m_w| \approx 1$

   $$e_1 = \frac{1}{\sqrt{m_u^2 + m_w^2}}[m_u, 0, -m_w] \tag{B.28}$$

   and, e_2, the vector orthogonal to both m and e_1,

   $$e_2 = m \times e_1 \tag{B.29}$$

To convert this back to a distance in the ellipse space e_1 and e_2 are scaled by Equation (B.32), which is a rearrangement of Equation (B.23) which previously converted points on the ellipsoid to points on a unit sphere, to give the vectors f_1 and f_2.

$$x' = u\, n_1 \tag{B.30}$$

$$y' = v\, n_2 \tag{B.31}$$

$$z' = w\, n_3 \tag{B.32}$$

The magnitude of the vectors f_1 and f_2 give the major and minor axis of the ellipse. We have now obtained the major and minor axis of the ellipse defined by the incident beam normal and calculate this at each point in the sample. These lengths correspond to the largest (slow axis) and smallest (fast axis) refractive index in that plane of the sample. Using these values we are now able to calculate the birefringence.

B.1.3 Jones Calculus

To model the change in phase through a birefringent material we rely on Jones Calculus. The incoming light is represented as a vector split into its 2 polarisation components, the Jones vector, and any optical element as a matrix, Jones matrix. The vector product of their multiplication describes the change in polarisation through the sample.

The wave vector as can be described as [56]:

$$\mathbf{E} = \begin{bmatrix} E_x(t) \\ E_y(t) \end{bmatrix} = \begin{bmatrix} E_{0x}\mathrm{e}^{i\phi_x} \\ E_{0y}\mathrm{e}^{i\phi_y} \end{bmatrix} \mathrm{e}^{i(wt-kz)}$$

In the final formulation shown we have separated the time and frequency dependence from the ϕ term, the additional phase term, which represents the change due to polarisation. Thus we can extract the Jones vector,

$$\mathbf{J} = \begin{bmatrix} E_{0x}\mathrm{e}^{i\phi_x} \\ E_{0y}\mathrm{e}^{i\phi_y} \end{bmatrix} \tag{B.33}$$

The magnitude of the vector is equal to one and describes the total intensity of the incident beam. In the case where there is linearly polarised light in the x and y directions the Jones vectors are [1,0] and [0,1] respectively.

The Jones matrix (T) is defined as [57]:

$$T = e^{-\frac{i\eta}{2}} \begin{bmatrix} \cos^2\theta + e^{i\eta}\sin^2\theta & (1-e^{i\eta})e^{-i\phi}\cos\theta\sin\theta \\ (1-e^{i\eta})e^{i\phi}\cos\theta\sin\theta & \sin^2\theta + e^{i\eta}\cos^2\theta \end{bmatrix}$$

where:

θ describes the angle between the x axis of the incident beam and the fast axis.

η is the phase difference between the fast and slow axis.

ϕ is the circularity of the polarisation, which is assumed to be 0.

Thus to find the Jones vector after the polarising media the vector product must be calculated as such,

$$\mathbf{J}_f = \mathrm{T}\mathbf{J}_i \tag{B.34}$$

In the case of a uniform polariser this can be used to calculate the polarisation change through the sample. However, if the change in refractive index isn't consistent through the sample this no longer holds. In which case we have to formulate a Jones matrix each point in the sample. The Jones vector after passing through the sample is given by the vector product of the initial Jones vector and matrix formed by the multiplication of each n unique Jones matrix corresponding to points in the sample the beam passes through.

$$\mathbf{J}_f = [\mathrm{T}_1\mathrm{T}_2\mathrm{T}_3........\mathrm{T}_\mathrm{n}]\,\mathbf{J}_i \tag{B.35}$$

Thus to define a whole wavefront is must be deconstructed into rays and this calculation must be completed for each ray.

B.1.3.1 Applying Jones calculus

To determine the overall birefringence we must calculate the Jones matrices at every point in the sample and multiple the matrices down the path of each ray to determine its phase change. As stated above this requires the calculation of 2 parameters at each point.

- The phase difference between the fast and slow axis (η)
- The angle between the fast axis and x axis of the incident beam (θ)

Phase difference

The phase difference is calculated by converting the change in refractive index into change in optical path length, calculated using Equation (B.36).

$$\eta = kdl(n_s - n_f) = \frac{2\pi dl}{\lambda}(n_s - n_f) \tag{B.36}$$

The phase difference is the optical path difference over a distance dl multiplied by the wavenumber (k). dl in our case is the spacing between stress data points in the imported COMSOL data.

An example map of the phase change that was generated though the x slice of the ZBLAN sample as shown in Fig. B.4. It can be seen that the phase difference rapidly varies, especially in the centre out area of interest. Thus we must ensure we have enough points to accurately model these effects.

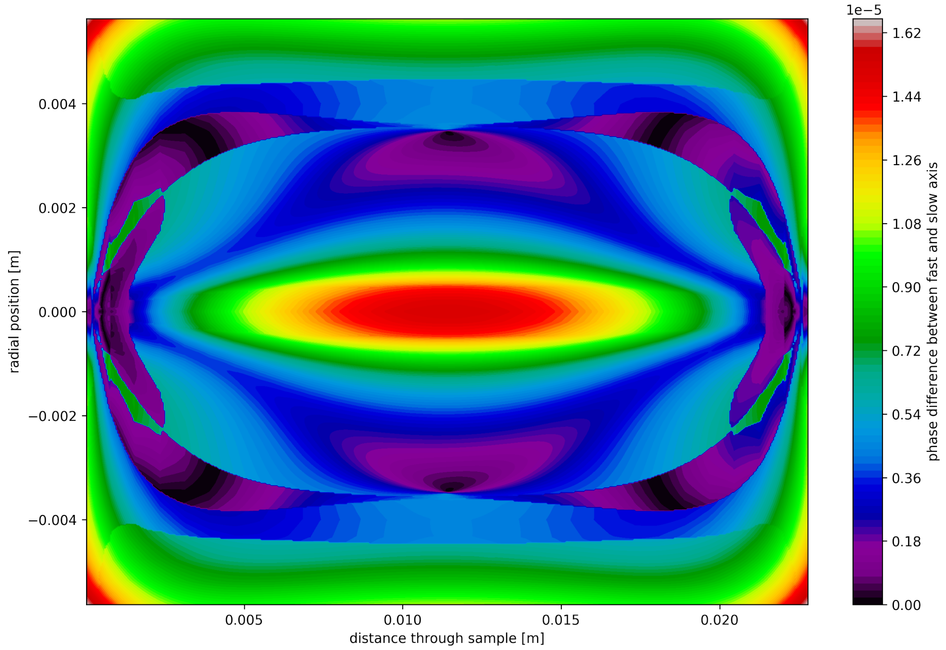

Fig. B.4 Map of phase difference between fast and slow axis throughout the sample for $\alpha = 1\neg m^{-1}$. It can be seen that it shows fluctuation of high magnitude over very small distances and the largest phase difference occurs at the centre of heating, in the centre of the sample.

Angle between fast axis and incident beam

The probe beam is propagating in the XZ plane with a rotation Ω around the y axis. The k vector of the probe beam k is defined as,

$$k = Rk_z \tag{B.37}$$

where k_z is the unit vector in the z direction and R is a rotation matrix describing a rotation Ω around the y axis

$$R = \begin{bmatrix} \cos\Omega & 0 & \sin\Omega \\ 0 & 1 & 0 \\ -\sin\Omega & 0 & \cos\Omega \end{bmatrix} \tag{B.38}$$

Using the M transformation matrix created from the principal stress vectors k can by rotated into the stress tensor frame, X' at anyone point,

$$k_{X'} = Mk \tag{B.39}$$

The angle between the x component of the probe beam and the fast axis was found using,

$$\theta = \arccos\left(\frac{k_f \cdot k_{X'}}{|k_f||k_{X'}|}\right) \tag{B.40}$$

where k_f is the direction vector of the fast axis determined above.

As all of the required variables are determined the Jones matrices can be calculated.

For the path of any one ray the Jones matrices at each point was calculated and multiplied by a Jones vector that represents the initial polarisation of the beam using Equation (B.35). In this experiment a SLED beam is used as a probe beam which is randomly polarised. To approximate this we assume that the beam is a 50:50 mix of [1,0] and [0,1] polarisation's and evaluated the phase change for both polarisation.

The resultant polarisation vector is in the form,

$$\mathbf{J}_f = \mathrm{e}^{i\phi_f} \tag{B.41}$$

Thus, to determine the optical path length changes first we need to extract the subject of the imaginary part of the exponential which is the cumulative phase change (ϕ_f) throughout the sample, then convert it to Δ OPL . ϕ_f is extracted using the following equation Equation (B.42)

$$\phi = \arctan\left(\frac{\mathbb{I}\phi_f}{\mathbb{R}(\phi_f)}\right) \tag{B.42}$$

and then is converted to Δ OPL by dividing by the wavenumber. The result will be a 2 component vector corresponding to the s and p polarisation components. Thus to determine the total Δ OPL the two final s components and the two final p components should be averaged to see the overall change.

B.1.4 Calculated OPL for the ZBLAN sample

Let us first consider the case where $\Omega = 0$. The piezo-optic coefficient used in this study were taken from literature to be $\pi_{11} = 4.07 \times 10^{-12}\,\mathrm{m}^2/\mathrm{N}$ and $\pi_{21} = 6.86 \times 10^{-13}\,\mathrm{m}^2/\mathrm{N}$ [58] and a ZBLAN sample with parameters from Table 3.1 and Table 2.2 were used. Using the methods outlined in the sections above the thermal-stress induced birefringence was quantified and the total optical path length changes of the s and p-polarisation was calculated for both the x and y slices of the probe beam as shown in Fig. B.5 and Fig. B.6 respectively. In this plot it can be seen that some of the polarisation initially in the s-polarisation has been shifted to the p-polarisation and the opposite effect is seen for the initially p-polarised light. Thus, to determine the final phase the sum of the total s-polarised light and total p-polarised light should be computed. This gives the total phase change each polarisation component.

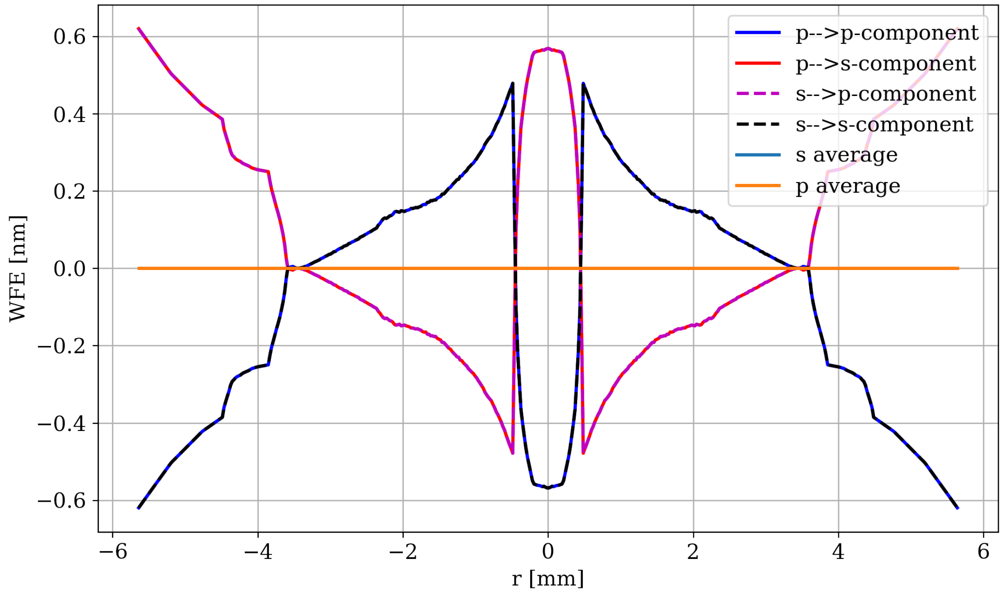

Fig. B.5 Δ OPL_{EO} with co-linear heating and probe beam in the P_{ip} slice. The dashed lines correspond to the light that on incident was in the s polarisation. The solid lines correspond to light initially in the P polarisation. The blue and orange line correspond to the average of the final s and p polarisation components

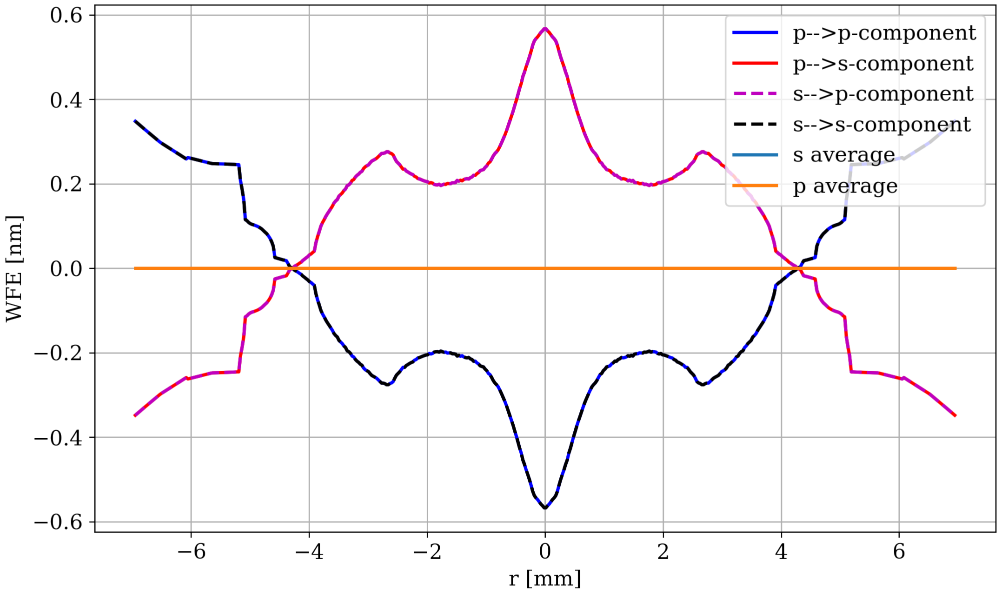

Fig. B.6 Δ OPL$_{EO}$ with co-linear heating and probe beam in the P$_{ip}$ slice. The dashed lines correspond to the light that on incident was in the s polarisation. The solid lines correspond to light initially in the P polarisation. The blue and orange line correspond to the average of the final s and p polarisation components

It can been seen that when the beam is normally incident that the final phase change between the the 2 final components of p and s polarisation thus the Δ OPL$_{EO}$ is 0.

Now we repeat this analysis us consider the angle of incidence, Ω, to be 0.0744 rad as shown in Fig. B.7 and Fig. B.8 respectively.

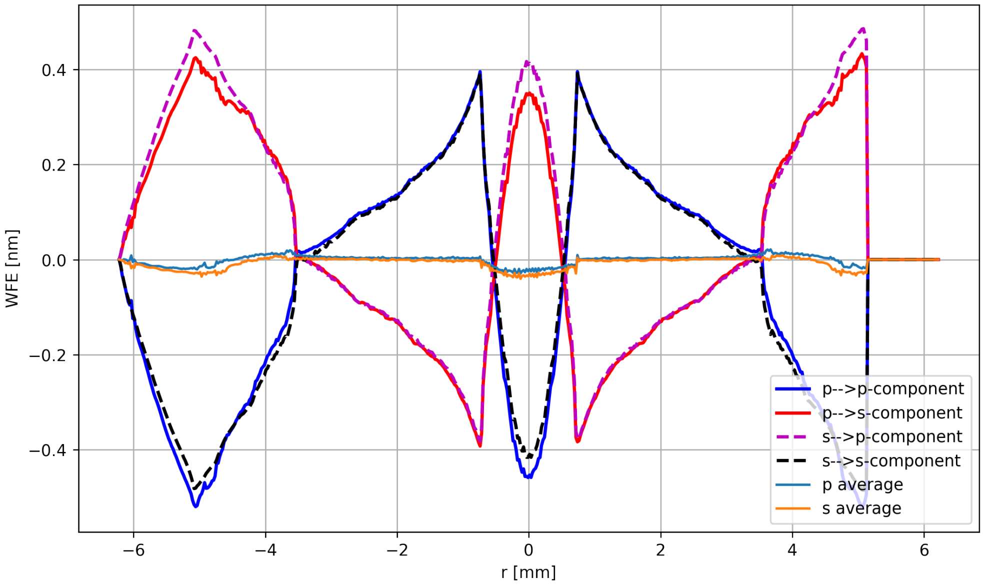

Fig. B.7 ∆ OPL_{EO} an off axis probe beam in the plane of incidence. The dashed lines correspond to the light that on incident was in the s polarisation. The solid lines correspond to light initially in the P polarisation. The blue and orange line correspond to the average of the final s and p polarisation components.

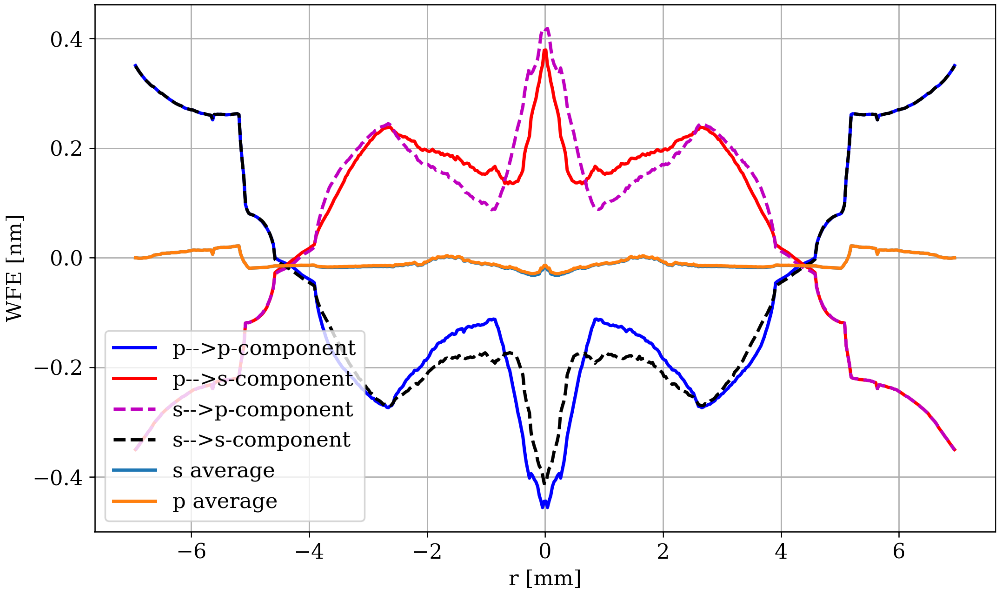

Fig. B.8 Δ OPL_{EO} an off axis probe beam in a plane perpendicular to the plane of incidence. The dashed lines correspond to the light that on incident was in the s polarisation. The solid lines correspond to light initially in the P polarisation. The blue and orange line correspond to the average of the final s and p polarisation components.

The total deformation of any one of the 4 polarisation cases identified reaches a maximum of approximately 0.4nm within the area of interest. This would effect the value of absorption calculated. However, the deformation can be seen to be largely symmetric with p and s components cancelling which means this effect would not be observed as it is below the noise floor of the DHWS. In both cases it can be seen that the p and s averages are incredibly small reaching maximums of 0.03nm for both the x and y slices.

APPENDIX C

EFFECT OF ELLIPTICAL PUMP BEAM ON WAVEFRONT DISTORTION

An elliptical pump beam will cause the wavefront distortion to be elliptical in profile. This was experimentally confirmed by measuring the WFD in a N-BK7 sample with the experimental parameters listed in Section 4.6.3. Two pump beam sizes (w_x, w_y) were used; w_1 = 1.33 mm,1.26 mm and w_2 1.64 mm,1.26 mm such that $w_{1x} \approx w_{1y}$, in comparison to that caused by a elliptical beam of w_{2y}, $1.25w_{2x}$, shown in Fig. C.1.

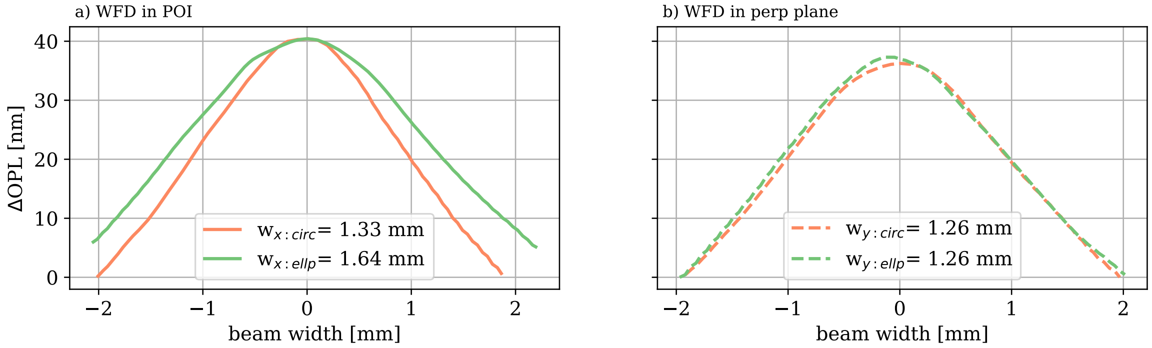

Fig. C.1 Plot of the measured WFD in the x (a) and y (b) cross sections of a measured WFD where one measurement has a beam size w_x, w_y of 1.33 mm,1.26 mm and the other w_x, w_y of 1.64 mm,1.26 mm. This demonstrates that increasing the ellipticity will cause broadening of the WFD in the axis aligned with the major axis of the beam but not significantly effect the other axis.

The cross-section of the distortion in the same plane as w_y is unchanged between these two scenarios, shown in Fig. C.1 b). Whereas there is significant difference in the imaged wavefront slices in the same plane as w_{1x} or w_{2x}, caused by the different pump beam size. Consequently, if the elliptical beam is not well characterised and the major and minor axis are not located the wavefront measured on the DHWS will differ significantly from that modelled for a symmetric beam.

APPENDIX D

SOURCES OF UNCERTAINTY

D.1 Uncertainty in ZBLAN measurements

The accuracy of the α and β values are dependant on the quality of the fit to the model. Any uncertainties in the system parameters which change the modelled wavefront profile and magnitude will ultimately cause a variance in α and β. Below each source of uncertainty and how it was measured is listed and the magnitude is tabulated in Table 5.4 for the cases 1 and 3 respectively.

- **Power**: There is a systematic inaccuracy due to calibration in the thermal power heads used to quantify the power of 5% as given by the manufacturer. Additionally, a random drift over the measurement time of 2 minutes was measured in section 4.3.2 to be 0.4%.

- **Angle**: The angle is determined by measuring the lengths of the probe beam and pump beams from the last steering mirror to the point of intersection and the distance between the mirrors. The angle is then determined using the cosine law. Variance between repeated measurements of length allowed the uncertainty to be propagated through to the angle.

- **Pump beam size**: The beam size was determined though a knife edge measurement using a razor blade mounted on a translation stage and a photodiode to record the change in power. The resulting error function was fit to using,

$$V_{pd} = b + \mathrm{erf}[\frac{-\sqrt{2}(x - x_o)}{w}] \tag{D.1}$$

  where x is the translated distance of the knife-edge, V_{pd} is the voltage measured on the photodiode, w is the beam size, x_o is the beam centre and the other factors allow for a dc shift in voltage and act as scaling factors for the real data. The variance in x was taken as half the smallest increment, 5 μm, and the power variation was measured to be 0.5% over the measurement period. Using Monte Carlo methods, noise was added to the measured data by simulating both variables as a Gaussian noise distributions where the mean was the measured value and the standard deviation was given by the variances. The uncertainty in w was taken as the standard deviation in the best fit w over the 10000 iterations.

- **Length, Radius**: Sample dimensions were measured 10 times over the length of each face using calipers and taken as the mean. The variance is the standard error in the mean.

- **Pump beam offset**: Estimated variation in pump beam position from centre of sample for each realignment was 0.5 mm as precise measurement of beam position in sample is difficult for 2 μm beam. As pointing noise was measured to be small it was not considered in this error.

- **Magnification**: Magnification is quantified by placing targets of known size in the object plane and measuring the size at the sensor/imaging plane. The variation was determined by realigning the imaging telescope 10 times and determining the maximum change.

(a) C1

Parameter	**Units**	**Value**	**Variance**	**% change in α [%]***
Power calibration, P	[w]	7.40	0.37	10
Power variation, P	[w]	7.40	0.037	1
Angle, θ_i	[rad]	0.0744	0.01	4
Pump beam size, w	[mm]	0.7	0.040	1.9
Length, h	[mm]	22.803	0.052	1.1
x radius, a_x	[mm]	11.31	0.022	1.2
y radius, a_y	[mm]	13.91	0.130	1.2
x pump beam offset	[mm]	0	0.500	1.4
y pump beam offset	[mm]	0	0.500	1
Magnification	-	2	1.000%	1

(b) C3

Parameter	**Units**	**Value**	**Variance**	**% change in α [%]***
Power calibration, P	[w]	7.40	0.37	10
Power variation, P	[w]	7.40	0.037	1.0
Angle, θ_i	[rad]	0.284	0.015	2.0
Pump beam size, w	[mm]	0.7	0.040	1.9
Length, h	[mm]	11.31	0.022	1.1
x radius, a_x	[mm]	22.803	0.052	1.2
y radius, a_y	[mm]	13.91	0.130	1.2
x pump beam offset	[mm]	0	0.500	2.2
y pump beam offset	[mm]	0	0.500	2.2
Magnification	-	2	1.000%	1.0

Table D.1 Table listing the variance in each system parameter and the % change in the best fit α due to this variance for C1 and C3 in ZBLAN. * signifies that this the total of the upper and lower variances in α.

D.2 Uncertainty in N-BK7 measurements

For the N-BK7 the uncertainties were calculated as described in section above and listed in Section D.2.

Parameter	**Units**	**Value**	**Variance**	**% change in α [%]***
Power calibration, P	[w]	2.20	0.11	10
Power variation, P	[w]	2.20	0.011	1
Angle, θ_i	[rad]	0.284	0.015	1.2
Pump beam size, w	[mm]	1.06	0.040	4.5
Length, h	[mm]	9.88	0.022	1.1
Magnification	-	2	1.000%	1.0

Table D.2 Table listing the variance in each system parameter and the % change in the best fit α for N-BK7. * signifies that this the total of the upper and lower variances in α.

In this case we do not consider the effect of random noise due to the large SNR. Additionally due to the large radius the uncertainty in this length has a negligible effect on absorption. Similarly, the effects of the pump beam being offset from the centre of the sample are small.

APPENDIX E

CODE

Below are the codes written in python used to convert the temperature distribution and end face displacements taken from the FEM into ΔOPL and complete a least squares fit to the experimental data.

E.1 Code used to fit predicted wavefront distortions to measured wavefront distortions

```
def fit_funcIP(pos,ab,beta,a,parameter,bparam, sparam=None):

"""calculate the optical path length in IP slice

pos = coordinate vector in the x_h plane [mm]

ab = bulk absorption coefficient [m-1]

beta = surface absorption coefficient

a = dc offset for fitting

parameters = dictionary of sample parameters

bparam = dictionary containing bulk absorption data such as :angle
                                 of incidence, temperature
                                 distribution, OPLTE all data
                                 values are normalised by
                                 absorption
```

```
sparam = dictionary containing surface absorption data such as :
                                angle of incidence, temperature
                                distribution, OPLTE  all data
                                values are normalised by
                                absorption
x,y = position coordinates corresponding to dis


OUTPUT: position vector in x_h, OPL_ip due to bulk and surface
                                absorption

"""



if beta==0:   # if surface absorption is zero  set contribution to
                                0
bparam['pos_surf_x']= bparam['x_surf_x'] = np.zeros(np.shape(pos))
dis_x_surf_x = np.zeros(np.shape(pos))
else:
dis_x_surf_x = fit_funcIP(pos,beta,0,a,parameter, sparam)*1e-9  #
                                calculate surface absorption OPL
#       print('restart')

pos_x, dis_TR_x = OPL_TR_IP( parameter,bparam['Tx']*ab , bparam['
                                angle'])   #calculate TR OPL
pos_TE_x, dis_TE_x = bparam['TER_x'],bparam['TE_x'] * ( ab )     #
                                calculate TE OPL
dis_TR_in_terms_of_wf_x = interp(pos, pos_x*1e3, dis_TR_x)     #
                                inteprolate to same coordinates
dis_TE_in_terms_of_wf_x = interp(pos, pos_TE_x*1e3, dis_TE_x)
dis_TR_in_terms_of_wf_x -=dis_TR_in_terms_of_wf_x.min()
dis_TE_in_terms_of_wf_x -=dis_TE_in_terms_of_wf_x.min()
dis_x = dis_TR_in_terms_of_wf_x + dis_TE_in_terms_of_wf_x +
                                dis_x_surf_x    #find total OPL
return ( dis_x-dis_x.min())*1e9+a #convert to nm and add offset if
                                required





        ###### Y #######
```

```
def fit_funcPP(pos,ab,beta,a,dic,param, sparam=None,BK = False):




"""calculate the optical path length in PP slice

pos = coordinate vector in the y_h plane [mm]

ab = bulk absorption coefficient [m-1]

beta = surface absorption coefficient

a = dc offset for fitting

parameters = dictionary of sample parameters

bparam = dictionary containing bulk absorption data such as :angle of
                                      incidence, temperature
                                     distribution, OPLTE  all data
                                     values are normalised by
                                     absorption

sparam = dictionary containing surface absorption data such as :angle
                                      of incidence, temperature
                                     distribution, OPLTE  all data
                                     values are normalised by
                                     absorption
x,y = position coordinates corresponding to dis


OUTPUT: position vector in y_h, OPL_pp due to bulk and surface
                                     absorption

"""
# if surface absorption is zero  set contribution to 0
if beta==0:
bparam['pos_surf_y']= bparam['y_surf_y'] = np.zeros(np.shape(pos))
dis_x_surf_y = np.zeros(np.shape(pos))

else:
```

```
dis_x_surf_y = fit_funcPP(pos,beta,0,a,parameter,sparam)*1e-9  #
                                   calculate surface absorption OPL

pos_y, dis_TR_y = OPL_Y(parameter,bparam['Ty']*ab,bparam['angle'])
pos_TE_y, dis_TE_y = bparam['TER_y'] , bparam['TE_y'] * ( ab )  #
                                   calculate TE OPL
dis_TR_in_terms_of_wf_y = interp (pos , pos_y*1e3, dis_TR_y ) #
                                   inteprolate to same coordinates
dis_TE_in_terms_of_wf_y = interp (pos, pos_TE_y*1e3, dis_TE_y )
dis_TR_in_terms_of_wf_y -=dis_TR_in_terms_of_wf_y.min()
dis_TE_in_terms_of_wf_y -=dis_TE_in_terms_of_wf_y.min()
dis_y = dis_TR_in_terms_of_wf_y + dis_TE_in_terms_of_wf_y +
                                   dis_x_surf_y  #find total OPL

return ( dis_y-dis_y.min())*1e9+a   #convert to nm and add offset if
                                   required


def lsfit(coeff,pos,data,parameters,bparam,sparam):



"""calculate least squares fit to IP and PP

coeff = vec array for best fit parameters [bulk absorption
                                   coefficient,surface absorption
                                   coefficient, dc offset ]


pos = 2 X N vector of [x_h coordinates, y_h coordinates] [mm]

data = 2 X N vector of [measured WFD_ip, Measured WFD_pp] [nm]

parameters = dictionary of sample parameters

bparam = dictionary containing bulk absorption data such as :angle of
                                    incidence, temperature
                                   distribution, OPLTE  all data
                                   values are normalised by
                                   absorption
```

```
sparam = dictionary containing surface absorption data such as :angle
                                                 of incidence, temperature
                                                distribution, OPLTE  all data
                                                values are normalised by
                                                absorption
x,y = position coordinates corresponding to dis





"""

from scipy.linalg import norm
from scipy.optimize import minimize


return norm(fit_funcxs(ypos[0],coeff[0],coeff[1],0,dic,param,sp )-
                                                ydata[0])**2+ norm(fit_funcys(ypos
                                                [1],coeff[0], coeff[1],0,dic,param
                                                ,sp) -ydata[1])**2
```

E.2 Code to determine optical path length change in P_{ip} and P_{pp}

```
def OPL_TR_IP(parameters,data,angle,no=500):

"""calculate the optical path length change in the OPLip slice

parameters = dictionary of sample parameters

data = 2D array of change temperature distribution in the x slice/
                                                plane of incidence of the sample

angle  = angle of incidence

no =  defines how many points along the Z axis the probe ebam path is
                                                 evaluated at
```

```
OUTPUT: coordinate vector and OPL_TR for IP slice

"""

# loading in required sample parameters
rad=parameters['a']
length= parameters['h']
dndt = parameters['dndt']
n= parameters['n_ref']


angle_t=np.arcsin(1/n*np.sin(angle))          # calculating
                                               transmitted angle

x=np.linspace(-rad ,rad ,len(data[0,:]))        # creating a vector of
                                                xin

z = np.linspace(0, length, len(data[:,0])       # creating a vector
                                               of zin

X,Z= np.array(np.meshgrid(x,z))                      # creating a mesh
                                               of coordinates for 2d array

xz = np.c_[X.flatten(),Z.flatten()]                #create x and z
                                               coordinates as list

T_vec=np.matrix.flatten(data)                      #flatten temp
                                               distribution into 1d array

F = LinearNDInterpolator(xz, T_vec, fill_value=0)    #Create function
                                                of temperature distribution


def ang(x0, alpha,no):                             #define integration
                                               over beam path
s=np.linspace(0,1,no)
x_ = x0 - s * length * np.tan(alpha)
z_ = s * length
integrand=F(x_, z_)
#find temperature dist
return integrate.trapz(integrand, x=s*length/np.cos(angle_t))
```

```
F_intT = np.vectorize(lambda x0: ang(x0, angle_t,no))        #create
                                   vector function

intT= np.array(F_intT(x))
intT =(intT-intT.max())*dndt

#defining output array with x shift due to angled propogation through
                                   the sample
x_vec = np.linspace(-rad -length * np.tan(angle_t)/2,rad- length * np
                                   .tan(angle_t)/2,r_len)

return x_vec*np.cos(angle), intT



def OPL_TR_PP(parameters,TD_Y,angle):

"""calculate the optical path length change in the OPLpp slice

parameters = dictionary of sample parameters

data = 2D array of change temperature distribution in the PP plane,
                                   the Y slice rotated by the
                                   specified
theta_t around the Y axis

angle  = angle of incidence

no =  defines how many points along the Z axis the probe ebam path is
                                   evaluated at
OUTPUT: coordinate vector and OPL_TR for PP slice

"""
#     loading glass parameters
a = dic["ay"]
h = dic["h"]
n_ref= dic['n_ref']
dndT = dic['dndt']
```

```
angle_T=np.arcsin(1/n_ref*np.sin(angle))                    #find
                                            transmitted angle
x_new=np.linspace(-a,a,len(TD_Y[:,1]))                      #define
                                            radial vector
z_new=np.linspace(0,h/np.cos(angle_T),len(TD_Y[1]))         #define
                                            length vector
integr=sci.trapz(TD_Y,z_new,axis=1)*dndT                    #
                                            integrate over path length anf
                                            multiply
#by thermo-optic coefficient
return  x_new, integr


def OPL_TE_slice(parameters, x,y,dis,angle, outx,outy, xe=None,ye=
                                            None, dise = None):


"""calculate the optical path length change due to thermal expansion
                                            of rays starting at coordinates
                                            outx,outy

parameters = dictionary of sample parameters

x,y = position coordinates corresponding to dis

dis = array of displacment of input  face at position x,y,

angle  = angle of incidence

outx,outy = X and Y coordinates to evaluated OPL_TE at

xe,ye = output face deformation position coordinates. If None assumes
                                             front andd back faces have the
                                            same  deformation

dise= array of displacement of output face at position x,y.  If None
                                            assumes front andd back faces have
                                             the same  deformation

OUTPUT: coordinate vector and OPL_TE for any set of coordinates
"""
```

```
a=0                                                     #determine if output face
                                                  data inputted
if(dise is None):                                       #if no output face data
                                                  set input =output
dise=dis
xe=x
ye=y
a=1


angle_t=np.arcsin(1/parameters['n_ref']*np.sin(angle))     # calculate
                                                   transmission angle

#     Interpolate the additional distance passed through the endface
                                                  deformation for rays at given
                                                  coordinates. The front face is
                                                  shifted by the distance translated
                                                   over the sample
front =(griddata((x*1e-3+parameters['h']*np.tan(angle_o),y*1e-3),dis*
                                                  1e-3/np.cos(angle),(outx,outy),
                                                  method ='linear',fill_value=np.nan
                                                  ))
back = (griddata((xe*1e-3,ye*1e-3),dise*1e-3/np.cos(angle),(outx,outy
                                                  ), method ='linear',fill_value=np.
                                                  nan))
if a ==0:   #invert output face data if given
back= -1*(nonan(back)-nonan(back).max())
tot= nonan((front+back))*(parameters["n_ref"]-1)    #Add addditional
                                                  distances travelled by each ray
                                                  and convert to OPL
if tot[-1]> tot[int(len(tot)/2)]:      #ensure OPL is positive
tot=-1*(tot-tot.max())
return (outx-parameters['h']*np.tan(angle_o)/2)*np.cos(angle),outy,(
                                                  tot)  #Output OPLTe translated to
                                                  plane conjugate to HES







def TE_IP_PP(parameters, x,y,dis,angle, xe=None,ye=None, dise = None)
                                                  :
```

```
"""calculate the optical path length change due to thermal expansion
                                   of rays in the ip and pp plane

parameters = dictionary of sample parameters

x,y = position coordinates corresponding to dis

dis = array of displacment of input  face at position x,y,

angle  = angle of incidence


xe,ye = output face deformation position coordinates. If None assumes
                                    front andd back faces have the
                                   same   deformation

dise= array of displacement of output face at position x,y.  If None
                                   assumes front andd back faces have
                                    the same  deformation

OUTPUT: coordinate vector and OPL_TE for IP and PP slices

"""

angle_t=np.arcsin(1/dic['n_ref']*np.sin(angle))    #find angle of
                                   transmission

surf_pos = dic['h']/2 *np.tan(angle_t)               #find position
                                   probe beam is incidence on the
                                   surface in the x axis


x_new = np.linspace(( y_te).min(), (y_te).max(),500)   #x coord for
                                   IP
y_new = np.zeros(500)    # Y coord for IP
x1,_,xted = TEdata(y_te,x_te,dis_vec,x_new,y_new,angle, dic)  #
                                   determine OPL for IP

y_newy =  np.linspace(( x_te).min(), (x_te).max(),500)   #y coord for
                                    PP
x_newy=np.linspace(surf_pos,surf_pos,500)               # x coord for
                                    PP
```

```
_,y1,yted = TEdata(y_te,x_te,dis_vec,x_newy,y_newy,angle, dic) #
                                   determine OPL for PP

return x1,xted,y1,yted  #output IP coord, IP:OPLTE, output PP coord,
                                   PP:OPLTE,


\end{pyverbatim}

\begin{pyverbatim}

  def fit_funcIP(pos,ab,beta,a,parameter,bparam, sparam=None):

  """calculate the optical path length in IP slice

  pos = coordinate vector in the x_h plane [mm]

  ab = bulk absorption coefficient [m-1]

  beta = surface absorption coefficient

  a = dc offset for fitting

  parameters = dictionary of sample parameters

  bparam = dictionary containing bulk absorption data such as :angle
                                   of incidence, temperature
                                   distribution, OPLTE  all data
                                   values are normalised by
                                   absorption

  sparam = dictionary containing surface absorption data such as :
                                   angle of incidence, temperature
                                   distribution, OPLTE  all data
                                   values are normalised by
                                   absorption
  x,y = position coordinates corresponding to dis


  OUTPUT: position vector in x_h, OPL_ip due to bulk and surface
                                   absorption
```

```
"""



if beta==0:    # if surface absorption is zero  set contribution to 0
bparam['pos_surf_x']= bparam['x_surf_x'] = np.zeros(np.shape(pos))
dis_x_surf_x = np.zeros(np.shape(pos))
else:
dis_x_surf_x = fit_funcIP(pos,beta,0,a,parameter, sparam)*1e-9  # calculate surface absorption OPL
#        print('restart')

pos_x, dis_TR_x = OPL_TR_IP( parameter,bparam['Tx']*ab , bparam['angle'])   #calculate TR OPL
pos_TE_x, dis_TE_x = bparam['TER_x'],bparam['TE_x'] * ( ab )     # calculate TE OPL
dis_TR_in_terms_of_wf_x = interp(pos, pos_x*1e3, dis_TR_x)     # inteprolate to same coordinates
dis_TE_in_terms_of_wf_x = interp(pos, pos_TE_x*1e3, dis_TE_x)
dis_TR_in_terms_of_wf_x -=dis_TR_in_terms_of_wf_x.min()
dis_TE_in_terms_of_wf_x -=dis_TE_in_terms_of_wf_x.min()
dis_x = dis_TR_in_terms_of_wf_x + dis_TE_in_terms_of_wf_x + dis_x_surf_x    #find total OPL
return ( dis_x-dis_x.min())*1e9+a #convert to nm and add offset if required
```